STABILITY OF BOTTOM ARMORING UNDER THE ATTACK OF SOLITARY WAVES

by

Ehud Naheer

W. M. Keck Laboratory of Hydraulics and Water Resources
Division of Engineering and Applied Science
CALIFORNIA INSTITUTE OF TECHNOLOGY
Pasadena, California

Report No. KH-R-34 January 1977

STABILITY OF BOTTOM ARMORING UNDER THE ATTACK OF SOLITARY WAVES

by

Ehud Naheer

Project Supervisor:

Fredric Raichlen
Professor of Civil Engineering

Supported by
National Science Foundation
Grant Nos. GK-31802X, ENG71-02367 A03, and ENG75-15786 A01

W. M. Keck Laboratory of Hydraulics and Water Resources
Division of Engineering and Applied Science
California Institute of Technology
Pasadena, California

Report No. KH-R-34

January 1977

ACKNOWLEDGMENTS

The writer wishes to express his gratitude to his thesis advisor, Professor Fredric Raichlen, who suggested this research problem and offered his advice throughout every phase of the investigation. The advice and encouragement of Professors Vito A. Vanoni, Norman H. Brooks, and Peter S. Eagleson are also deeply appreciated.

The writer also wishes to thank Dr. Robert C. Y. Koh and Dr. Sasson R. Somekh for the long discussions which helped in developing the procedures used in the experimental investigation.

A special thanks is owed to Mr. Elton F. Daly, supervisor of the shop and laboratory, whose assistance during the design, construction, and maintenance of the experimental equipment made it possible to solve almost any problem in the laboratory phase of the investigation. Thanks are also due to Mr. Joseph J. Fontana, Mr. Robert Shultz, Mr. William G. Stone, Mr. Robert L. Greenway, and Mr. Carl A. Green who assisted in the construction and maintenance of the experimental equipment; to Mr. Walter Beckmann and Miss Sally Weaks, who helped in reducing the experimental data; to Mr. Gregory Gartrell and Mr. Philip J. W. Roberts, who reviewed the original manuscript, and to Mrs. Joan L. Mathews, Mrs. Shirley A. Hughes, and Mrs. Linda Rorem who typed it; and to Mr. David Byrum who performed the drafting of the figures appearing in this manuscript.

The writer also wishes to thank the California Institute of Technology for financial assistance and for providing the facilities for this study. The experiments were conducted in the W. M. Keck Laboratory of Hydraulics and Water Resources. Thanks are also due to

the Humanities Fund, Inc., for the Boris Bakhmeteff Research Fellowship which was awarded to the writer in 1972. The research was supported by National Science Foundation Grants GK-31802X, ENG71-02367 A03, and ENG75-15786 A01.

The deepest gratitude is expressed by the writer to his wife, Daphna, for her understanding, patience, and encouragement during the period of his graduate study.

This report was submitted by the writer on May 5, 1976 as a thesis with the same title to the California Institute of Technology in partial fulfillment of the requirements for the degree of Doctor of Philosophy; it is reproduced here unchanged.

ABSTRACT

An empirical relationship is presented for the incipient motion of bottom material under solitary waves. Two special cases of bottom material are considered: particles of arbitrary shape, and isolated sphere resting on top of a bed of tightly packed spheres.

The amount of motion in the bed of particles of arbitrary shape is shown to depend on a dimensionless shear stress, similar to the Shields parameter. The mean resistance coefficient used in estimating this parameter is derived from considerations of energy dissipation, and is obtained from measurements of the attenuation of waves along a channel. A theoretical expression for the mean resistance coefficient is developed for the case of laminar flow from the linearized boundary layer equations and is verified by experiments.

For the case of a single sphere resting on top of a bed of spheres, the analysis is based on the hypothesis that at incipient motion the hydrodynamic moments which tend to remove the sphere are equal to the restoring moment due to gravity which tends to keep it in its place. It is shown that the estimation of the hydrodynamic forces, based on an approach similar to the so-called "Morison's formula", in which the drag, lift, and inertia coefficients are independent of each other, is inaccurate. Alternatively, a single coefficient incorporating both drag, inertia, and lift effects is employed. Approximate values of this coefficient are described by an empirical relationship which is obtained from the experimental results.

A review of existing theories of the solitary wave is presented and an experimental study is conducted in order to determine which theory should be used in the theoretical analysis of the incipient motion of bottom material.

Experiments were conducted in the laboratory in order to determine the mean resistance coefficient of the bottom under solitary waves, and in order to obtain a relationship defining the incipient motion of bottom material. All the experiments were conducted in a wave tank 40 m long, 110 cm wide with water depths varying from 7 cm to 42 cm. The mean resistance coefficient was obtained from measurements of the attenuation of waves along an 18 m section of the wave tank. Experiments were conducted with a smooth bottom and with the bottom roughened with a layer of rock. The incipient motion of particles of arbitrary shape was studied by measuring the amount of motion in a 91 cm x 50 cm section covered with a 15.9 mm thick layer of material. The materials used had different densities and mean diameters. The incipient motion of spheres was observed for spheres of different diameters and densities placed on a bed of tightly packed spheres. The experiments were conducted with various water depths, and with wave height-to-water depth ratios varying from small values up to that for breaking of the wave.

It was found that: (a) The theories of Boussinesq (1872) and McCowan (1891) describe the solitary wave fairly accurately. However, the differences between these theories are large when used to predict the forces which are exerted on objects on the bottom, and it was not established which theory describes these forces better. (b) The mean resistance coefficient for a rough turbulent flow under solitary waves can be described as

a function of D_s, h, and H, where D_s is the mean diameter of the roughness particles, h is the water depth, and H is the wave height. (c) Small errors in the determination of the dimensionless shear stress for incipient motion of rocks result in large errors in the evaluation of the diameter of the rock required for incipient motion. However, it was found that the empirical relationship for the incipient motion of spheres can be used to determine the size of rock of arbitrary shape for incipient motion under a given wave, provided the angle of friction of the rock can be determined accurately.

TABLE OF CONTENTS

TABLE OF CONTENTS (Cont'd)

TABLE OF CONTENTS (Cont'd)

LIST OF FIGURES

LIST OF FIGURES (Cont'd)

LIST OF FIGURES (Cont'd)

LIST OF FIGURES (Cont'd)

LIST OF FIGURES (Cont'd)

LIST OF TABLES

CHAPTER 1

INTRODUCTION

Offshore structures such as sewage outfalls and thermal discharge pipes which pass from the shore into the ocean are exposed to ocean waves that shoal on the beach and break in the surf zone. These waves tend to undermine the pipes by removing the sand and can cause structural failures due to differential settling or by acting directly on the pipes. The pipes are usually protected by placing them in a trench and armoring their tops with pavements of loose rocks. However, if not designed properly, these rocks can be removed by big storm waves. In order to determine the size of the rocks required for adequate protection at a given site it is important to be able to predict the forces and moments exerted on them by the waves. Accordingly, the rocks should be designed such that they will resist these hydrodynamic forces and moments.

The design of the rocks includes considerations of their size, weight, shape, grading and placement. It is conceivable that large and heavy rocks are more stable than small and light ones. Angular rocks of arbitrary shape are apparently more stable than spherical particles because they tend to interlock better with each other. A well-graded rock covering a limited range of sizes is possibly better than a single-sized rock, as the small particles of a well-graded rock fill in the holes among the big rocks and provide a stronger interlocking structure. Finally, rocks which are placed individually, usually with the help of a diver, are more stable than rocks which are dumped.

An understanding of the relationship between the various parameters representing the rock at actual conditions (i.e., size, weight, shape, grading and placement) and the characteristics of the design wave is therefore required for a proper design of bottom armoring.

1.1 OBJECTIVE AND SCOPE OF THE PRESENT STUDY

The objective of the present study is to investigate, both theoretically and experimentally, the conditions required for incipient motion of a bed of rocks under solitary waves. The incipient motion of a particle is defined as the event in which the particle barely moves, as the hydrodynamic moments forcing the particle from its place are equal to the restoring moment due to the weight of the particle. Solitary waves were chosen for three reasons. First, the theory of the solitary waves is well-known, so the hydrodynamics of the flow can readily be evaluated. Second, long waves shoaling on a beach have wide troughs and narrow crests which resemble solitary waves. Third, by employing solitary waves in the experimental study the problem of interaction between reflected and incident waves is avoided.

As the motion of the rocks results from hydrodynamic forces and moments which are exerted on them by the flow, it is necessary to be able to determine these forces and moments. The resistance coefficient of the bottom under solitary waves is therefore investigated, and the stresses exerted on the bed are determined from this study. The investigation of the incipient motion amounts to the study of the relationship between the hydrodynamic stresses and the characteristics of the rock

which cause the bed to be in a state of incipient motion.

The problem of incipient motion which includes consideration of all the characteristics of the rock, i.e., size, weight, shape, gradation, and placement, is quite complex. The following simplifications have been used in the present study: a. The considered rock has a narrow size distribution, i.e., all the particles are fairly uniform in diameter; b. All the rocks used in the experimental study are angular, i.e., have fairly sharp corners, and they all have approximately the same shape factor; c. All the rocks are placed in the experimental model using the same method of placement. The investigation is thus limited to the problem of incipient motion of particles of arbitrary shape characterized only by weight (or density) and mean diameter.

It is conceivable that if some motion is expected to occur under a given wave, the moving rock particles will be those which emerge above their neighbors and protrude into the flow. A similar model of a simple geometrical shape can be described by a single sphere resting on top of a bed of similar spheres. The incipient motion of such a model is also studied in the present investigation, and the results of this study are compared to those obtained with particles of arbitrary shape.

A review of previous studies of the resistance coefficient and of the initiation of motion of particles under waves is presented in Chapter 2. A theoretical analysis is presented in Chapter 3 in which three theoretical presentations of the solitary wave are compared. Theoretical considerations of the incipient motion and of the resistance coefficient are also presented in Chapter 3. The experimental equipment

and procedures are described in Chapter 4. The results of the investigation are presented and discussed in Chapter 5, and conclusions are stated in Chapter 6.

CHAPTER 2

LITERATURE SURVEY

2.1 THE INCIPIENT MOTION OF A BED OF ROCKS

There is a large number of studies in the literature dealing with the problem of the initiation of motion of bed material. However, most of these studies are concerned with the problem as it occurs in steady flows in streams and channels. The conditions required for initiation of motion for these cases are usually described by the so-called "Shields diagram", or the "Shields curve", which is named after Shields (1936) whose investigation of the problem was based on similarity principles. The Shields diagram describes a relationship between a dimensionless shear stress, τ_*, and a boundary-particle-Reynolds number, Re_*. The dimensionless shear stress, which is also called the "Shields parameter", is given by

$$\tau_* = \frac{\tau_b}{(\rho_s - \rho_w) g D_s} \quad , \tag{2.1}$$

where τ_b is the bottom shear stress, ρ_w is the density of the fluid, g is the acceleration due to gravity, and ρ_s and D_s are the mean density and size (diameter), respectively, of the particles. The boundary-particle-Reynolds number is given by

$$Re_* = \frac{u_* D_s}{\nu} \quad , \tag{2.2}$$

where ν is the kinematic viscosity of the fluid, and $u_* = \sqrt{\tau_b / \rho_w}$ is called the boundary shear velocity.

Studies applying the Shields parameter to problems of initiation

of motion under waves are quite limited. Komar and Miller (1973) used the data obtained experimentally by Bagnold (1946) and Manohar (1955) to show that the Shields diagram as it is used for steady flows cannot be used for oscillatory flows. However, Madsen and Grant (1975) used Bagnold's data to show that Shields diagram can be applied to oscillatory flows. They noted that the error in Komar and Miller's results was due to a wrong definition of the bottom shear stress. Komar and Miller (1975) independently recognized the mistake in their preceding (1973) study.

Bagnold (1946) and Manohar (1955) simulated the oscillatory flow in their experiments by oscillating a granular bed in still water. They neglected the inertia forces acting on the particles in the oscillating bed, assuming that hydrodynamic drag was dominant. However, it should be noted that for cases where inertia forces cannot be neglected, the forces acting on the oscillating particles are different from those acting on stationary particles in an oscillating fluid. This is due to the different masses associated with these forces.

The dimensionless shear stress given by Eq. (2.1) represents the ratio between the hydrodynamic forces acting on the bed particles and the gravitational force that tend to keep the particles in their at-rest positions. In cases of flows in streams and channels the hydrodynamic forces are considered to consist of drag and they are assumed to be proportional to the shear stresses which are exerted on the bed by the flow. Lift forces acting in a direction perpendicular to the direction of the flow are usually either neglected or assumed to be included in the proportionality factor relating the hydrodynamic forces to Shields

parameter (e.g., see Vanoni (1975) p. 92). Inertia forces (due to the acceleration of the fluid particles relative to the bed particles) do not exist in steady flows over stationary particles.

In cases where inertia forces cannot be neglected, e.g., under waves, the most common approach to the problem consists of an examination of the forces acting on a single bed particle. The particle itself is usually considered to be a sphere, and the hydrodynamic forces acting on it consist of some combination of drag, inertia, and lift effects. Grace (1974) presented a few of the formulae which are most commonly used to evaluate the hydrodynamic forces acting on a sphere under waves.

The formula which is most commonly used in coastal engineering practice is that due to O'Brien and Morison (1952). They assumed that the force acting on a sphere resting on the bottom in an unsteady flow can be expressed as a linear combination of drag and inertia forces, i.e.,

$$F = \frac{1}{2} \rho_w C_D A u^2 + \rho_w C_M V \frac{du}{dt} \quad , \tag{2.3}$$

where C_D and C_M are the drag and inertia coefficients respectively, assumed to be constant; A and V are the projected area and the volume of the sphere respectively; and u and $\frac{du}{dt}$ are the free stream velocity and acceleration of the fluid particles respectively, estimated at the level of the sphere in its absence. The direction of the velocity and acceleration near the bottom is parallel to the bottom plane and so is the force given by Eq. (2.3). An equation similar to Eq. (2.3) was first applied by Morison et al. (1950) to forces on piles. O'Brien and Morison did not consider lift forces in the study. They evaluated C_D

and C_M experimentally by measuring the wave profile and the forces acting on the sphere simultaneously. The fluid particle velocity and acceleration were estimated from the wave theory (using the linearized equation of motion), and the value of C_D was estimated from Eq. (2.3) at the point of zero acceleration. Similarly, C_M was evaluated at the point of zero velocity.

Eagleson, Dean and Peralta (1958) investigated the forces acting on spherical particles on a sloping beach at both incipient motion and established motion conditions. In their theoretical developments they recognized both drag, inertia and lift effects. However, they assumed that lift effects were negligible. The major differences between their analysis and that of O'Brien and Morison are that they considered a higher order wave theory (Stokes waves), and that they also considered the velocity distribution inside the boundary layer for the cases where the boundary layer thickness, δ, was greater than the diameter of the sphere. O'Brien and Morison applied only the free stream velocity distribution to their calculations.

Iversen and Balent (1951) and Bugliarello (1956) studied the resistance of an unbounded fluid to the accelerated motion of disks and spheres (respectively) moving in a unidirectional motion. They suggested that inertia and viscous effects be combined into one coefficient C_D^* . This resistance coefficient is then expressed in the form

$$C_D^* = f\left(\frac{uD_s}{\nu} , \frac{D_s}{u^2}\frac{du}{dt}\right) , \qquad (2.4)$$

and the force acting on the moving object is written in the form

$$F = \frac{1}{2} \rho_w C_D^* A u^2 \quad . \tag{2.5}$$

However, Basset (1888) showed that the force acting on a sphere accelerating in a viscous fluid depends also on the history of the flow. This means that the forces acting on two identical spheres moving in the same fluid at the same velocity and acceleration may be different for different initial conditions of their motion. Keulegan and Carpenter (1958) argued that attempts to correlate the resistance coefficient, C_D^*, to the instantaneous Reynolds number, uD/ν, and the dimensionless acceleration, $D \frac{du}{dt}/u^2$, between different types of flows (i.e., unidirectional, oscillatory, etc.) were unsuccessful for this reason.

In their investigation of the forces acting on cylinders and plates in an oscillating fluid, Keulegan and Carpenter (1958) assumed average values for the drag and inertia coefficients which remain constant throughout the period of oscillation. They considered the force to be given by an equation similar to Eq. (2.3), but with an additional term:

$$F = \frac{1}{2} \rho_w C_D A u^2 + \rho_w C_M V \frac{du}{dt} + \Delta R \quad , \tag{2.6}$$

where the function ΔR is used to account for the fact that the instantaneous values of C_D and C_M are different from their assumed average values. Keulegan and Carpenter found correlations between the average values of the coefficients and a dimensionless period, $T_* = Tu_{max}/D$, where T is the period of oscillation, u_{max} is the maximum orbital velocity of the fluid, and D is a characteristic length (diameter) of the object. They noted that the dimensionless period, T_*, could be replaced by a dimensionless length, ξ/D. A similar parameter, ξ/k_s,

where k_s is the equivalent surface roughness (k_s is proportional to the mean diameter, D_s, of the particles on a rough surface), was found to be significant in studies of the resistance coefficient of rough surfaces under oscillatory flows. These studies are presented in the following section.

2.2 THE RESISTANCE COEFFICIENTS UNDER WAVES

A significant amount of work has been done in the past in order to estimate the shear stresses exerted by waves on both smooth and rough bottoms. In most of these studies the flow was considered to be oscillatory, and only a few investigators considered solitary waves. A comprehensive review of studies on boundary layers and friction factors under oscillatory flows was given by Jonsson (1966). The present review of such flows will therefore be limited and will only demonstrate the various methods used by different investigators.

Of the theoretical treatments of laminar boundary layers under oscillatory flows, that due to Lin (1957) is often used in comparison with experimental studies of boundary layers under waves. Lin considered an oscillatory motion superimposed on a steady stream, where the amplitude of oscillation and the magnitude of the stream may vary with the x coordinate. By averaging the equations of motion over the period of oscillation and assuming high frequency of oscillations, he derived a linear boundary layer equation for the oscillatory component of the flow. The analytical solution of this equation was then introduced into the averaged equations of motion which yielded an analytical solution to the mean flow in the boundary layer. For the limiting case of zero

mean stream velocity the problem is reduced to that of the oscillatory wave, and the analytical solution of the linearized equations adequately describes the behavior of the boundary layer.

Turbulent boundary layers under oscillatory flows over both smooth and rough surfaces were investigated theoretically by Kajiura (1968). He subdivided the boundary layer into three regions, namely the inner, the overlap, and the outer layers, and considered different forms of the eddy viscosity for each of them. The values of the eddy viscosity were assumed to remain constant throughout the period of oscillation, and they were obtained from measurements of steady turbulent flows. Substituting the assumed forms of the eddy viscosities into the linearized boundary layer equations (neglecting convective terms), Kajiura obtained the solution for each subdivided region in the boundary layer. The constants of integration in his solution were eliminated by matching the solutions at the boundaries between these regions.

Experimentally, the shear stresses can be evaluated from measurements of shear forces exerted on a plate, or by measuring the velocity profiles in the vicinity of the boundary and applying some theoretical considerations which relate the velocity profile to the shear stresses. Now, since the shear stresses are the main reason for the wave energy dissipation, and as the wave energy can be expressed in terms of the wave height, the shear stresses can also be estimated from measurements of the attenuation of waves along a channel.

In a theoretical study of the attenuation of waves, Biesel (1949) used the linear equations of the laminar boundary layer to show that the height, H, of an oscillatory progressive wave decays exponentially

along the channel, i.e.,

$$H = H_o \, e^{-kx/h} \tag{2.7}$$

where H_o is the wave height at the coordinate x = 0, k is the decay coefficient, and h is the water depth. The decay coefficient was shown to be a function of a form of a Reynolds number, defined in terms of the wave length and the wave speed.

Eagleson (1962) measured the forces exerted on a plate under oscillatory progressive waves. Defining the bottom resistance coefficient, C_{f_b}, to be given by

$$C_{f_b} = \frac{\tau_b}{\frac{1}{2} \rho_w u^2} \quad , \tag{2.8}$$

where τ_b is the bottom shear stress, ρ_w is the density of the fluid, and u is in the free stream velocity evaluated near the bottom, he obtained a relationship between the decay coefficient, k, and the average resistance coefficient (averaged over a wave period). The decay coefficients which he obtained were larger than those predicted by Biesel (1949). Accordingly, the experimental values of the average resistance coefficient were larger than the theoretical ones.

Iwagaki et al. (1965) also measured the forces exerted on a plate. They noted that the discrepancies in Eagleson's results were probably due to measurement errors. They also measured the attenuation of waves along a channel. The experimental values which they obtained for the decay coefficient were also larger than the predicted ones. This discrepancy is probably due to energy dissipation at the free surface in addition to the dissipation near solid boundaries. Van Dorn (1966)

showed that such a dissipation was possible as a free-surface boundary layer could develop due to contamination.

The most common procedures applied to experimental investigations of shear stresses in turbulent oscillatory flows are those which were used by Kalkanis (1957), Jonsson (1963), and Kamphuis (1975). Kalkanis measured the velocity profile of a fluid near a smooth oscillating plate, where the fluid was otherwise at rest. In his experiments, he found that the amplitude of the fluid particle velocity in the turbulent boundary layer varied according to a power law with a coordinate z which measures the vertical distance from the plate. The phase shift between the fluid particle velocity and the velocity of the plate varied according to a logarithmic law with the coordinate z. These results enabled him to determine the distribution of the eddy viscosity in the turbulent boundary layer. However, he did not investigate the laminar sub-layer and did not provide matching conditions between the laminar and turbulent regions, thus, it appears that his study is incomplete, as far as the determination of the boundary shear stresses are concerned.

Jonsson (1963) and Kamphuis (1975) used a closed water tunnel in which the fluid oscillated in a sinusoidal manner with respect to time. Such an apparatus could be described as a fluid oscillating in a "U" shaped tube. Jonsson measured the velocity profile near the bottom of his tank and fitted the data to logarithmic curves, assuming that steady state turbulent boundary layer considerations were valid. The constants obtained from the curve fitting enabled him to estimate the shear stresses exerted on the bottom.

Dimensional analysis considerations indicate that for smooth plates

the average wave resistance coefficient is a function of a wave Reynolds number, which Kamphuis (1975) defined as $Re = a_\delta u_{max}/\nu$, where a_δ is the amplitude of a fluid particle displacement just outside the boundary layer, u_{max} is the maximum velocity of such a fluid particle, and ν is the kinematic viscosity of the fluid. For rough plates the average resistance coefficient is a function of a_δ/k_s, where k_s is the equivalent surface roughness. Kamphuis (1975) obtained empirical relationships for the resistance coefficients for both smooth and rough plates, and compared his results to those obtained experimentally by Jonsson (1963), and the theoretical ones predicted by Kajiura (1968). Considering the experimental uncertainties due to measurement errors, and the theoretical uncertainties due to the approximations considered by Kajiura in his analysis, the results of the three studies appear to agree reasonably well.

The resistance of solid boundaries to the flow of solitary waves was studied theoretically by Keulegan (1948) and Iwasa (1959) for the case of laminar flow. So far as turbulent boundary layers are concerned, the author has no knowledge of theoretical studies of the cases of flows under solitary waves. Experimental studies of the resistance coefficient under solitary waves were conducted by Ippen, Kulin and Raza (1955), and by Ippen and Mitchell (1957).

Keulegan (1948) considered the linearized equations of motion and developed an expression for the velocity distribution in the viscous boundary layer for the general case of non-uniform distribution of the free stream velocity along a solid horizontal boundary. He then obtained the bottom shear stress, τ_b, applying Newton's law of friction,

namely

$$\tau_b = \mu \left(\frac{\partial u_\ell}{\partial z} \right)_{z=o} \quad , \tag{2.9}$$

where μ is the dynamic viscosity of the fluid, u_ℓ is the horizontal velocity component in the boundary layer, and z is a vertical coordinate with its origin at the boundary. For the special case of solitary waves he assumed that the free stream velocity distribution along the wave, u, was given by

$$u(X) = \frac{C\eta(X)}{h} \quad , \tag{2.10}$$

where C is the wave speed, η is the free surface elevation above still water level, h is the water depth and X = x-Ct is a horizontal coordinate moving with the wave, and where x and t are the stationary horizontal coordinate and time respectively. He also developed a relationship between the shear stresses and the rate of wave height attenuation (due to energy losses) along a channel, and used the experimental data which was observed by Scott-Russell (1844) to verify his theoretical developments. The accuracy of his results is, however, doubtful. The reason is that the approximate expression of the velocity (Eq. (2.10)), is good only for small amplitude waves, i.e., $\eta/h << 1$. For waves of large height-to-depth ratio Eq. (2.10) does not describe the velocity accurately. Furthermore, for waves of large height-to-depth ratio the convective terms in the equations of motion are not small enough to be neglected compared to the linear terms, and the full, nonlinear equations have to be solved for a more accurate description of the boundary layer.

Iwasa (1959) used a higher approximation (than Eq. (2.10)) for the free stream velocity. In order to solve the complete (nonlinear) boundary layer equations he considered the cases where he assumed either a linear or a parabolic velocity profile in the boundary layer. However, these assumptions were not verified experimentally.

Ippen, Kulin, and Raza (1955) used the relationships which were developed by Keulegan (1948) and measured the attenuation of waves over both smooth and rough bottoms. Their results for smooth bottoms were inconclusive, apparently due to measurement uncertainties. For rough bottoms they found that the resistance coefficient depended on the absolute value of the roughness size in addition to the wave Reynolds number, Re, which they defined as

$$\mathrm{Re} = \int_0^{\xi} \frac{u\,d\xi}{\nu} \quad , \tag{2.11}$$

where ξ is the displacement of a fluid particle in the free-stream near the bottom. Ippen and Mitchell (1957) obtained the resistance coefficient from direct measurement of the forces exerted on a plate. In their analysis they considered higher approximation for the velocity than that used by Ippen et al. (1955)(i.e., Eq. (2.10)). They also found that the resistance coefficient for rough beds depends on the absolute value of the roughness. Their results seem to be independent of the Reynolds number, and since the values of the Reynolds numbers in their experiments were larger than those in the investigation of Ippen et al. (1955), they assumed that the two different studies were conducted at different flow regimes (i.e., that their experiments were conducted in the rough turbulent regime, while the experiments of Ippen et al. (1955) were conducted

in the transition to rough turbulent regime).

Results which show dependence on the absolute value of the roughness cannot be used in cases where the roughnesses are different from those tested. In order to obtain a more general relationship for the resistance coefficient, these results should be examined from other aspects such as dimensional analysis. However, neither study provided an analysis and explanation for the relationships which they found.

CHAPTER 3

THEORETICAL CONSIDERATIONS

In the course of investigation of the incipient motion of bed material under solitary waves it is first necessary to study the fluid mechanics of these waves. Second, the hydrodynamic forces exerted on the bed particles by the flow under solitary waves must be determined and, finally, the properties of the bed particles have to be chosen such that they will resist the hydrodynamic forces exerted on them.

A review of three existing theories of the solitary wave is presented in Section 3.1. Theoretical consideration for the forces exerted on bed material under solitary waves are presented in Section 3.2, and the conditions required for incipient motion of bed particles are discussed in Section 3.3.

3.1 THE SOLITARY WAVE

The existence and the formulations of the solitary wave are very well known, therefore theoretical developments will not be analyzed here. Three theoretical solutions of the solitary wave equations which are often referred to in the literature are those due to Boussinesq (1872), McCowan (1891), and Laitone (1963). The surface profile, the wave celerity, and the fluid particle velocity which are derived from these theories are presented here for the convenience of reference. They will later be compared to those of experimentally generated waves in order to determine which of the three theories is most suitable for use in conjunction with the experimental study of stability of armored bottoms.

The wave motion is considered in a two-dimensional space and is illustrated in Fig. 3.1. The wave consists of a single surface elevation of height H traveling with a speed C over a body of water of constant depth h. The x coordinate is located along the bottom of the fluid with the z coordinate directed upward. The fluid is unbounded in the x direction. The wave induces a flow field $\vec{q}(x,z,t) \equiv (u,v)$ where $\vec{q}$ is the velocity vector ($\vec{}$ denotes vectorial quantity), u and v are the horizontal and vertical velocity components respectively and t is the time. The surface elevation above still water level is denoted by $\eta(x,t)$. The water away from the wave is considered to be at rest.

Considering an incompressible homogeneous fluid and an irrotational flow, the flow field can be represented by the velocity potential Φ (such that $\vec{q} = \nabla\Phi$) satisfying Laplace's equation:

$$\nabla^2\Phi = 0 \ , \tag{3.1}$$

with the boundary condition at the bottom:

$$\frac{\partial\Phi}{\partial z} = 0 \quad (\text{at } z = 0). \tag{3.2}$$

The kinematic condition at the free surface is

$$\frac{\partial\eta}{\partial t} + \frac{\partial\Phi}{\partial x}\frac{\partial\eta}{\partial x} - \frac{\partial\Phi}{\partial z} = 0 \quad (\text{at } z = h + \eta(x,t)), \tag{3.3}$$

and the dynamic condition, neglecting surface tension, is

$$\frac{\partial\Phi}{\partial t} + \frac{1}{2}(\nabla\Phi)^2 + g\eta = 0 \quad (\text{at } z = h + \eta(x,t)), \tag{3.4}$$

where g is the gravitational acceleration. The pressure at the free

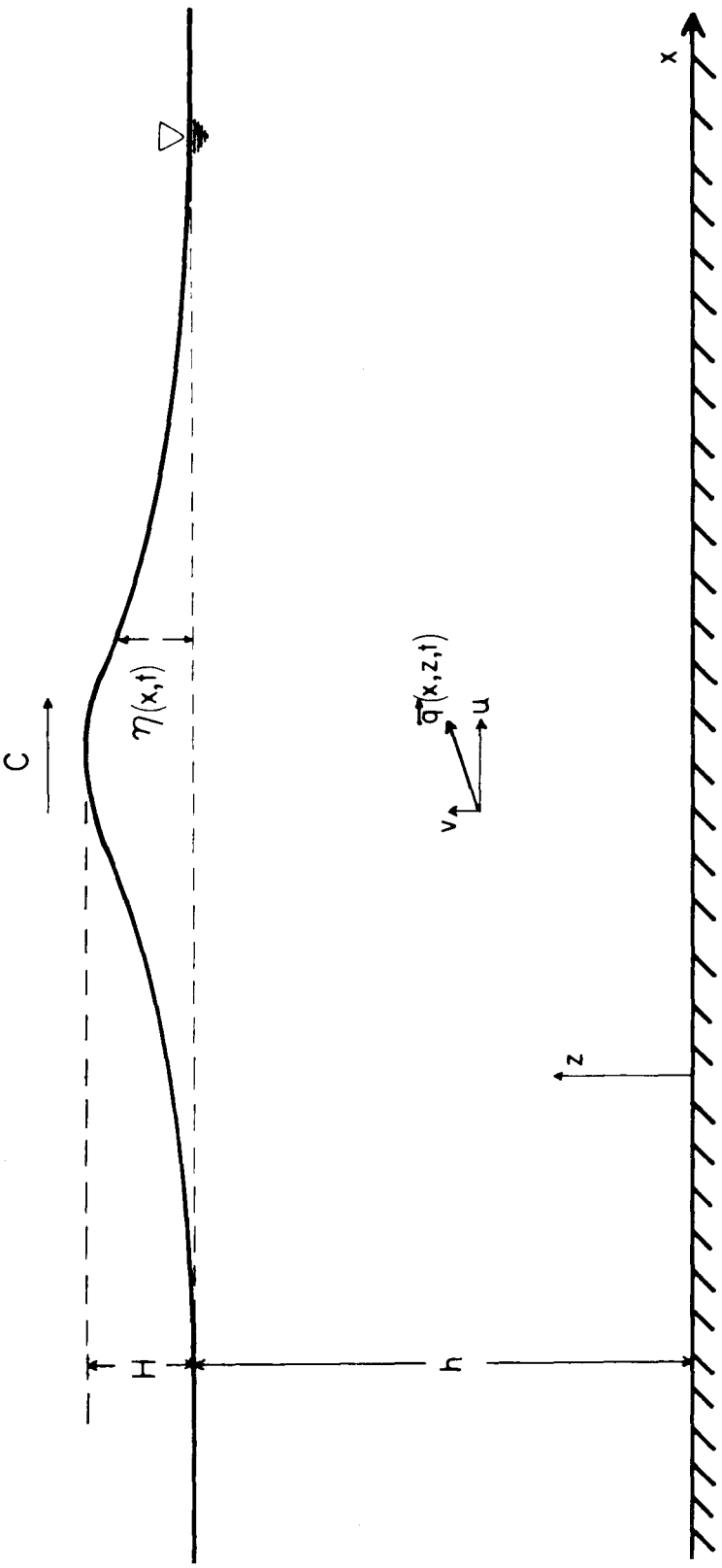

Fig. 3.1 Definition sketch for the solitary wave.

surface is taken to be zero for convenience. The difficulty of the problem lies in the nonlinearity of the boundary conditions at the free surface, the elevation of which is unknown *a priori* and must be determined from the solution of the problem.

Expanding the velocity potential in a power series:

$$\Phi = \sum_{j=o}^{\infty} \Phi_j z^j \quad , \tag{3.5}$$

Boussinesq's (1872) solution to Eq. (3.1) with the boundary conditions (Eqs. (3.2), (3.3), and (3.4)) can be considered as the first term in the series. McCowan (1891) carried the solution to the first term choosing different functions Φ_j that represent the velocity potential. The solution of Laitone (1963) is similar to that of Boussinesq but contains higher order terms. Expressions for the surface profile, wave celerity, and fluid particle velocity of the solitary wave which were derived from these solutions are presented in Table 3.1 in terms of the coordinate system (X,z) where X = x-Ct is a coordinate system moving with the wave transforming it to a stationary form. McCowan's solution is shown (in Table 3.1) in dimensionless terms as presented by Munk (1949).

As can be seen in Table 3.1, Boussinesq's presentation of the wave profile and the wave speed are the same as the lowest order terms in Laitone's formulation. The horizontal velocity as expressed by Boussinesq is derived from continuity considerations assuming a uniform velocity distribution over the depth. The first order terms in the expansion of this expression for the velocity in a power series of H/h are the same as those appearing in Laitone's presentation. The

Table 3.1 Solutions of the solitary wave due to Boussinesq, McCowan, and Laitone.

	Boussinesq	McCowan	Laitone
Wave profile η =	$H\,\mathrm{sech}^2\sqrt{\frac{3H}{4h}}\,\frac{X}{h}$	$\frac{h\,N\,\sin M(1+\eta/h)}{M\left[\cos M(1+\eta/h)+\cosh M\frac{X}{h}\right]}$ (3	$H\,\mathrm{sech}^2\left(\alpha\,\frac{X}{h}\right)\left[1-\frac{3}{4}\,\frac{H}{h}\left(1-\mathrm{sech}^2\,\frac{\alpha X}{h}\right)\right]$ (4
Wave speed C =	$\sqrt{gh(1+H/h)}$	$\sqrt{\frac{gh}{M}\tan M}$	$\sqrt{gh}\left[1+\frac{1}{2}\,\frac{H}{h}-\frac{3}{20}\left(\frac{H}{h}\right)^2+0\left(\frac{H}{h}\right)^3\right]$
Fluid particle velocities horizontal u =	(1 $\frac{C\eta}{h+\eta}$	$\frac{CN\left(1+\cos M\frac{z}{h}\,\cosh M\frac{X}{h}\right)}{\left(\cos M\frac{z}{h}+\cosh M\frac{X}{h}\right)^2}$	$\sqrt{gh}\left\{\frac{H}{h}\left[1+\frac{H}{h}\left(\frac{1}{4}-\frac{3z^2}{2h^2}\right)\right]\mathrm{sech}^2\left(\alpha\,\frac{X}{h}\right)+\left(\frac{H}{h}\right)^2\left(\frac{9z^2}{4h^2}-1\right)\mathrm{sech}^4\left(\alpha\,\frac{X}{h}\right)\right\}$
vertical v =	(2	$\frac{CN\,\sin M\frac{z}{h}\,\sinh M\frac{X}{h}}{\left(\cos M\frac{z}{h}+\cosh M\frac{X}{h}\right)^2}$	$-\sqrt{gh}\left[\frac{z}{h}\,\frac{d\eta}{dX}+0\left(\frac{H}{h}\right)^{5/2}\right]$
Notes	1) u is averaged over the depth applying continuity consideration 2) expression for the vertical velocity was not presented by Boussinesq for solitary waves	3) the relationships for N and M are $N=\frac{2}{3}\sin^2\left[M\left(1+\frac{2}{3}\,\frac{H}{h}\right)\right]$ $\frac{H}{h}=\frac{N}{M}\tan\left[\frac{1}{2}\,M\left(1+\frac{H}{h}\right)\right]$	4) $\alpha=\sqrt{\frac{3H}{4h}}\left(1-\frac{5}{8}\,\frac{H}{h}\right)+0\left(\frac{H}{h}\right)^{5/2}$

similarity and differences between the presentations of Boussinesq and McCowan are not immediately seen because of the complexity of the expressions involving the parameters M and N in McCowan's formulation. However, McCowan himself noted that the two solutions are similar to each other. A comparison between the surface profile, the wave celerity, and the velocity distribution of an experimentally generated wave and the three theoretical formulations shown in Table 3.1 are presented in Section 5.1. The interested reader is referred to that section for a more detailed discussion.

3.2 THE HYDRODYNAMIC FORCES EXERTED ON BED MATERIAL UNDER SOLITARY WAVES

The investigation of hydrodynamic forces exerted on solid surfaces usually consists of boundary layer considerations, where the conditions of interaction between the surface and the flow are taken into account (i.e., smooth or rough surface, laminar or turbulent flow, etc.). Solutions of the equations of motion in the bottom boundary layer under solitary wave may provide a direct estimation of the shear stresses exerted on the bottom. Approximate solutions of this kind are known for the case of smooth laminar flow (e.g., Keulegan (1948), Iwasa (1959)). The writer has no knowledge of theoretical solutions to the cases of turbulent boundary layers under solitary waves. Experimental investigation of the velocity profile in the turbulent boundary layer (see Section 5.1.3) was unsuccessful. For these cases the shear stresses in the boundary layer are studied here based on considerations of wave energy dissipation.

3.2.1 The Damping of Solitary Waves

Consider the solitary wave in a channel as presented by Boussinesq (1872)(see Table 3.1):

$$\eta(X) = H \operatorname{sech}^2 \alpha X \quad , \tag{3.6}$$

where η is the surface elevation above still water level, H is the wave height, $\alpha=\sqrt{3H/4h^3}$, with h being the water depth, and X = x-Ct is a horizontal coordinate moving with the wave, in which x is a stationary horizontal coordinate, C is the wave celerity, and t is the time. The wave celerity is given by:

$$C = \sqrt{gh(1+H/h)} \quad , \tag{3.7}$$

where g is the acceleration due to gravity. The horizontal component of the fluid particle velocity, u, is expressed as:

$$u(X) = \frac{C\eta(X)}{h+\eta(X)} = \frac{C}{1+\frac{h}{H}\cosh^2 \alpha X} \quad . \tag{3.8}$$

Boussinesq (1872) did not present an expression for the vertical velocity component under the solitary wave. The total wave potential energy per unit channel width, E_{p_1}, can be described by:

$$E_{p_1} = \frac{1}{2} \rho_w g \int_{-\infty}^{\infty} \eta^2 dX = \frac{4}{\sqrt{27}} \rho_w g h^3 \left(\frac{H}{h}\right)^{3/2} , \tag{3.9}$$

where ρ_w is the density of the fluid. The total kinetic energy per unit width, E_{k_1}, is given by:

$$E_{k_1} = \frac{1}{2}\rho_w \int_{X=-\infty}^{X=+\infty} dX \int_{z=0}^{z=h+\eta(X)} u^2 dz =$$

$$= \frac{2\rho_w g h^3 (1+H/h)}{\sqrt{3H/h}} \left(\frac{H}{h} - \frac{1}{2}\sqrt{\frac{H/h}{1+H/h}}\ \ell n \frac{1+\sqrt{\frac{H/h}{1+H/h}}}{1-\sqrt{\frac{H/h}{1+H/h}}} \right). \qquad (3.10)$$

Eqs. (3.9) and (3.10) are similar to the expressions developed by Iwasa (1959). The differences between Iwasa's expressions and Eqs. (3.9) and (3.10) are due to the differences between his presentation of the solitary wave and the solitary wave due to Boussinesq (1872) which is considered here. Iwasa's solitary wave is of higher order approximation and includes expressions for the vertical component of the fluid particle velocity. However, his results show that the kinetic energy due to this velocity component is negligible compared to the potential energy and the kinetic energy due to the horizontal velocity component.

The total wave energy per unit channel width, E_1, is obtained by adding the potential energy to the kinetic energy, i.e., Eqs. (3.4) and (3.10):

$$E_1 = E_{p_1} + E_{k_1} = \frac{2}{\sqrt{3}}\rho_w g h^3 \left[\left(1+\frac{5}{3}\frac{H}{h}\right)\sqrt{\frac{H}{h}} - \frac{1}{2}\sqrt{1+\frac{H}{h}}\ \ell n \frac{1+\sqrt{\frac{H/h}{1+H/h}}}{1-\sqrt{\frac{H/h}{1+H/h}}} \right]. \qquad (3.11)$$

The total wave energy, E, in a channel of finite width, B, is given by:

$$E = BE_1 \quad . \qquad (3.12)$$

As can be seen in Eqs. (3.11) and (3.12), the total wave energy of a given fluid (given ρ_w) in a channel of constant depth and constant width is a function of the wave height-to-water depth ratio only (considering

the gravitational acceleration to be constant).

As the wave propagates along a channel, the bottom and the walls exert stresses on the fluid. These stresses are the main cause for the dissipation of wave energy. The rate of energy dissipation, $\frac{dE}{dt}$, can be obtained as follows:

$$\frac{dE}{dt} = \frac{\partial E}{\partial (H/h)} \frac{d(H/h)}{dt} \quad . \tag{3.13}$$

During the time increment dt the wave travels a distance dx = Cdt, thus, Eq. (3.13) becomes:

$$\frac{dE}{dt} = C \frac{\partial E}{\partial (H/h)} \frac{d(H/h)}{dx} \quad . \tag{3.14}$$

Substituting Eq. (3.7) for C in Eq. (3.14), and substituting Eq. (3.12) into Eq. (3.11) and differentiating it with respect to H/h yields

$$\frac{dE}{dt} = \frac{1}{\sqrt{3}} B\rho_w g^{3/2} h^{5/2} \left[5\sqrt{\frac{H}{h}\left(1+\frac{H}{h}\right)} - \frac{1}{2} \ln \frac{1+\sqrt{\frac{H/h}{1+H/h}}}{1-\sqrt{\frac{H/h}{1+H/h}}} \right] \frac{d(H/h)}{d(x/h)} \quad . \tag{3.15}$$

The rate of energy dissipation is obtained experimentally from measurements of the attenuation of waves along the channel and substitution of the measured value of $\frac{d(H/h)}{d(x/h)}$ in Eq. (3.15).

Consider a shallow wide channel such that the width is much greater than the depth, hence the shear forces exerted on the walls are negligible compared to those exerted on the bottom. For this case the rate of energy dissipation is equal to the rate of work done by the fluid on the bottom (considering no energy sources or sinks in the flow domain). Assuming that the bottom shear stresses are uniformly distributed across

the channel, this is expressed as:

$$\frac{dE}{dt} = -B \int_{-\infty}^{\infty} \tau_b u dX \quad , \tag{3.16}$$

where τ_b denotes the shear stresses exerted on the bottom. Eq. (3.16) describes a simple mechanical law that the rate of energy change of a body is equal to the inner product of the force applied on the body and its velocity. The minus sign on the right-hand side of Eq. (3.16) accounts for the fact that τ_b is considered as the shear stress exerted on the bottom rather than that exerted by the bottom on the fluid. The bottom shear stress is defined by means of a bottom friction coefficient, C_{f_b}, such that

$$\tau_b = \frac{1}{2} C_{f_b} \rho_w u^2 \quad . \tag{3.17}$$

Substitution of Eq. (3.17) into Eq. (3.16) yields:

$$\frac{dE}{dt} = -\frac{1}{2} B \rho_w \int_{-\infty}^{\infty} C_{f_b} u^3 dX \quad . \tag{3.18}$$

Considering C_{f_b} as a mean resistance coefficient for a wave, it can be taken out of the integral in Eq. (3.18). It is then evaluated by equating Eq. (3.18) to Eq. (3.15), i.e.,

$$\overline{C_{f_b}} = \frac{-\frac{1}{\sqrt{3}} g^{3/2} h^{3/2} \left[5\sqrt{\frac{H}{h}\left(1+\frac{H}{h}\right)} - \frac{1}{2} \ln \frac{1+\sqrt{\frac{H/h}{1+H/h}}}{1-\sqrt{\frac{H/h}{1+H/h}}} \right] \frac{d(H/h)}{d(x/h)}}{\frac{1}{2} \int_{-\infty}^{\infty} u^3 dX} \quad , \tag{3.19}$$

where the bar over C_{f_b} denotes a mean value (averaged over the wave).

It has to be noted that substitution of the value of $\overline{C_{f_b}}$ as given by Eq. (3.19) into Eq. (3.17) may not necessarily yield the correct distribution of bottom shear stresses under solitary wave, since the local values of the friction coefficient may be different from the mean resistance coefficient defined by Eq. (3.19). In fact, application of the mean resistance coefficient to Eq. (3.17) implies that the maximum shear stress occurs under the wave crest, where the velocity is maximum. However, Kajiura (1968), in his investigation of turbulent boundary layers under oscillatory waves, showed that there is a phase lag between the bottom shear stress profile and the free-stream velocity profile. Keulegan (1948) showed that the maximum bottom shear stress in the smooth laminar boundary layers under solitary waves occurs under the wave front near the crest, but not directly under the crest. Therefore, application of the mean resistance coefficient may be inaccurate when used to estimate local shear stresses and it can only be applied to problems where wave attenuation is concerned. Nevertheless, for two channels of the same width and depth with waves of equal heights, the stresses in the channel of stronger wave attenuation are larger than the stresses in the channel of weak attenuation. Therefore, the application of the mean resistance coefficient, although it may not describe the correct distribution of the shear stresses, can be used qualitatively. When considering a representative shear stress to be given by substitution of the mean resistance coefficient and the maximum velocity under the wave in Eq. (3.17), it is expected that the true stresses

under the waves with large representative shear stresses are larger than those under waves with small representative stresses.

Since the mean resistance coefficient will be evaluated from experimental measurements of wave attenuation, it is necessary to establish a functional relationship between the resistance coefficient and other parameters involved in the problem. Thus, a relationship obtained under certain experimental conditions will be used for cases other than those tested.

In most studies of the resistance coefficient under oscillatory flows (e.g., Jonsson (1966), Kajiura (1968), and Kamphuis (1975)), it was shown that the resistance coefficient of a smooth bottom depends on a so-called "wave Reynolds number" which is defined by the maximum velocity, u_{max}, and the displacement amplitude of a fluid particle just outside the boundary layer. For rough bottom in the transition regime the resistance coefficient depends also on the ratio between a_δ and the surface roughness size (considered here as given by the mean diameter of the roughness particles, D_s). For fully developed rough turbulent flows the resistance coefficient depends only on D_s/a_δ. Note that the maximum displacement of a fluid particle just outside the boundary layer, ξ, is equal to $2a_\delta$ for oscillatory flows. Ippen, Kulin and Raza (1955) defined the Reynolds number for the solitary wave, R_e, as

$$R_e = \int_o^\xi \frac{ud\xi}{\nu} \,. \tag{3.20}$$

Since $u = d\xi/dt$, and with $dX = - Cdt$, Eq. (3.20) becomes

$$R_e = \int_{-\infty}^{\infty} \frac{u^2}{C\nu} dX \quad , \tag{3.21}$$

where it is noted that $\xi = 0$ at $X = + \infty$. Introducing the solitary wave equations due to Boussinesq (1872)(i.e., Eqs. (3.6), (3.7), and (3.8) into Eq. (3.21) yields

$$R_e = \frac{2\sqrt{gh}\ h}{\nu\sqrt{3}} \sqrt{\frac{H/h}{1+H/h}} \left[-1 + \frac{1}{2} \left(\sqrt{\frac{H/h}{1+H/h}} + \sqrt{\frac{1+H/h}{H/h}} \right) \ell n \frac{1+\sqrt{\frac{H/h}{1+H/h}}}{1-\sqrt{\frac{H/h}{1+H/h}}} \right] . \tag{3.22}$$

The displacement of a fluid particle can be described by the volume of fluid confined by the wave profile (per unit channel width) divided by the water depth. This is expressed as

$$\xi = \int_{-\infty}^{\infty} \frac{\eta}{h} dX \quad , \tag{3.23}$$

where η is the surface elevation above still water level. Substituting Eq. (3.6) into Eq. (3.23) yields

$$\xi = \frac{4h}{\sqrt{3}} \sqrt{\frac{H}{h}} \quad . \tag{3.24}$$

The studies of the resistance coefficient in oscillatory flows which were mentioned above deduced the dependence of the resistance coefficient on the wave Reynolds number and on the relative fluid particle displacement (ξ/D_s) from dimensional analysis considerations assuming similarity to flows over a flat plate. (For details of the resistance

coefficient of a flat plate see, for example Schlichting (1968)). The fluid particle displacement was considered to be equivalent to the length of the plate. Thus, as the resistance coefficient is a function of the ratio between the boundary layer thickness and the roughness size, and as the boundary layer thickness is a function of the length of the plate and the roughness size, then the resistance coefficient is a function of ξ/D_s due to the similarity between the length of the plate and ξ. However, for rough surfaces in oscillatory flows, the forces on the roughness particles include also inertia components due to the unsteadiness of the flow. Hence the shear stresses include also inertia effects as they are defined as the forces on the particles in a unit bed area. Ippen and Mitchell (1957) showed that the local resistance coefficient under solitary waves depends on a dimensionless acceleration $\frac{D_s}{u^2}\frac{du}{dt}$. Inertia forces are usually defined as being proportional to the fluid particle acceleration, and they are canceled out when integrated over the wave. Hence it seems that the mean resistance coefficient (as opposed to the local resistance coefficient) does not include inertia forces. Yet it is expected that acceleration has effects on the drag forces. Keulegan and Carpenter (1958), for example, showed that the drag coefficient of a cylinder in an oscillating fluid is different from the drag coefficient in a steady flow.

The fluid particle acceleration is given by

$$\frac{du}{dt} = \frac{\partial u}{\partial t} + u\frac{\partial u}{\partial x} = (-C+u)\frac{\partial u}{\partial X} \quad , \tag{3.25}$$

where the transformation X=x-Ct is employed. Substituting Eqs. (3.6),

(3.7), and (3.8), which describe the solitary wave, into Eq. (3.25) yields:

$$\frac{du}{dt} = \frac{2C^2 h\eta \sqrt{\frac{3H}{4h}} \tanh\left(\sqrt{\frac{3H}{4h}} \frac{X}{h}\right)}{(h+\eta)^3} \tag{3.26}$$

and the dimensionless acceleration becomes

$$\frac{D_s}{u^2} \frac{du}{dt} = \frac{2D_s h \sqrt{\frac{3H}{4h}} \tanh\left(\sqrt{\frac{3H}{4h}} \frac{X}{h}\right)}{\eta(h+\eta)} \tag{3.27}$$

The values of the dimensionless acceleration as given by Eq. (3.27) vary from zero under the crest, to infinity as x tends to infinity. In order to describe the inertia effects on the mean resistance coefficient it is necessary to estimate a characteristic dimensionless acceleration for the wave. Such a parameter may be chosen in the form

$$\left(\frac{D_s}{u^2} \frac{du}{dt}\right)_{char} = \frac{D_s}{u^2}_{max} \left(\frac{du}{dt}\right)_{max} , \tag{3.28}$$

in which $\left(\frac{D_s}{u^2} \frac{du}{dt}\right)_{char}$ denotes a characteristic dimensionless acceleration, u_{max} and $\left(\frac{du}{dt}\right)_{max}$ are the maximum velocity and maximum acceleration (respectively) of a fluid particle. As the forces on a roughness particle consist of drag, inertia, and lift components (see Section 3.2.3, Eqs. (3.51) and (3.52)), the dimensionless acceleration given by Eq. (3.28) represents the ratio of maximum inertia force to the maximum drag under the wave, assuming that the drag and inertia coefficients are constant along the wave. The dimensionless acceleration given by Eq. (3.28)

is therefore assumed to describe the inertia effects on the resistance coefficient. Note that a characteristic dimensionless acceleration may also be defined in the following way. A characteristic time scale, T_c, for the solitary wave is defined by considering the solitary wave as given in Eq. (3.6), and rewriting it in the form,

$$\eta = H \operatorname{sech}^2\left(\frac{x}{L_c} - \frac{t}{T_c}\right) , \tag{3.29}$$

in which L_c is a characteristic length scale of the wave. From Eq. (3.6) it follows that

$$T_c = \frac{h}{C\sqrt{\frac{3H}{4h}}} , \tag{3.30}$$

A characteristic fluid particle velocity, u_c, is described as the displacement of a fluid particle divided by the time scale of this displacement, i.e.,

$$u_c \sim \frac{\xi}{T_c} , \tag{3.31}$$

and a characteristic fluid particle acceleration, $\left(\frac{du}{dt}\right)_c$, is given by

$$\left(\frac{du}{dt}\right)_c \sim \frac{\xi}{T_c^2} . \tag{3.32}$$

It follows from Eqs. (3.31) and (3.32), that a characteristic dimensionless acceleration is given by

$$\left(\frac{D_s}{u^2}\frac{du}{dt}\right)_{char} = \frac{D_s}{u_c^2}\left(\frac{du}{dt}\right)_c \sim \frac{D_s}{\xi} . \tag{3.33}$$

A correlation between the experimentally measured resistance coefficient and the characteristic dimensionless acceleration is presented in Section 5.2, and the significance of Eq. (3.33) is discussed in that section.

The values of the characteristic dimensionless acceleration which describe the ratio of maximum inertia force to maximum drag exerted on the roughness particle are largely dependent on the theory by which they are estimated. The ratio of inertia to drag forces as predicted by Boussinesq's (1872) theory (see Section 5.3.2, Figs. 5.21 and 5.22). Hence, the interpretation of the inertia effects consists of uncertainties due to possible errors in estimating the actual dimensionless acceleration. In order to obtain a functional relationship which is independent of such uncertainties, it is necessary to obtain a correlation between the resistance coefficient and wave parameters which can be measured or evaluated accurately. From dimensional analysis it may be shown that if the density and the viscosity of the fluid are given, then the resistance coefficient is uniquely defined by the water depth, h, the wave height, H, and the roughness size, D_s. Hence, if it is assumed that the resistance coefficient is independent of the Reynolds number (assuming, for example, that the flow is rough-turbulent), then the resistance coefficient, $\overline{\overline{C_{f_b}}}$, may be defined by

$$\overline{\overline{C_{f_b}}} = f\left(\frac{D_s}{h}, \frac{H}{h}\right) . \tag{3.34}$$

Note that Eq. (3.34) may be deduced from the assumption that the resistance coefficient is a function of ξ/D_s and the dimensionless

acceleration, as both parameters are functions of H/h and D_s/h. An empirical relationship between $\overline{C_{f_b}}$, $\frac{D_s}{h}$, and $\frac{H}{h}$ is presented in Section 5.2.

When considering the forces exerted on bed particles under waves, the shear stresses are defined as the horizontal forces acting on the individual particles per unit projected area of the bed. However, as noted earlier in this section, these forces consist of inertia forces (due to the unsteadiness of the flow), in addition to the drag forces which account for the energy dissipation. The inertia forces, which are usually assumed to be proportional to the fluid particle acceleration, are non-dissipative, and they cancel out when integrated over the wave, hence, they cannot be estimated from considerations of energy dissipation. Furthermore, the forces acting on bed particles include also lift components which act in a direction perpendicular to the bed plane, and they are not included in the shear forces. The lift forces are usually either neglected or assumed to be proportional to the drag forces, when considered in sedimentation problems in streams and channel (e.g., see Vanoni (1975), p. 92).

It is concluded that the mean resistance coefficient as obtained from measurements of wave attenuation is inadequate as far as the estimation of the actual forces on bed particles is concerned. It can only be used as a qualitative measure for the magnitude of these forces when inertia and lift effects are either negligible or assumed to be proportional to drag effects. For cases where inertia and lift forces cannot be neglected and are not proportional to the drag, the forces

acting on the bed particles have to be determined from a different approach. A simple model of the forces acting on a bed particle protruding into the flow from the bed surface is described by considering the forces acting on a single sphere resting on a bed of similar spheres. Such a model is presented in Section 3.2.3.

3.2.1.1 Correction for Wall Effects

As the mean resistance coefficient is evaluated from measurements of wave attenuation in the laboratory, and since experiments are performed in channels of finite width, it is necessary to correct the values of $\overline{C_{f_b}}$ as obtained from Eq. (3.19) for wall effects. Assuming that the total energy dissipation can be described as a linear combination of dissipations due to wall and bottom shear stresses, a corrected form of Eq. (3.16) is given by:

$$\frac{dE}{dt} = -B\int_{-\infty}^{\infty}\tau_b u dX - 2\int_{X=-\infty}^{X=+\infty} dX \int_{y=0}^{y=h+\eta(X)} \tau_w u dy \quad , \tag{3.35}$$

where τ_w denotes the wall shear stress and y is a coordinate along the wetted perimeter of the cross-sectional area of the channel. The bottom resistance coefficient then has the form

$$\overline{C_{f_b}} = \frac{-\frac{g^{3/2}h^{5/2}}{\sqrt{3}/5}\left[\sqrt{\frac{H}{h}\left(1+\frac{H}{h}\right)} - \frac{1}{10}\ln\frac{1+\sqrt{\frac{H/h}{1+H/h}}}{1-\sqrt{\frac{H/h}{1+H/h}}}\right]\frac{d(H/h)}{d(x/h)} - \frac{2}{B\rho_w}\int_{X=-\infty}^{X=+\infty} dX \int_{y=0}^{y=h+\eta(X)} \tau_w u dy}{\frac{1}{2}\int_{-\infty}^{\infty} u^3 dX} \tag{3.36}$$

where the second term in the numerator on the right-hand side of Eq. (3.36) represents the wall correction for the bottom resistance coefficient in a channel of finite width. Theoretical evaluation of this term is presented in the following section for the case of laminar flow.

3.2.2 Shear Stresses in the Laminar Boundary Layer

The present analysis is based on ideas that were developed by Keulegan (1948) from the linearized boundary layer equations which were presented by Boussinesq (1878). Keulegan's theory was developed assuming solitary waves of small heights. His development is extended here for flows induced by large amplitude solitary waves. The difference between the present definition of small and large amplitude solitary waves lies in the expression of the fluid particle velocity (see Table 3.1, Boussinesq's presentation), $u = C\eta/(h+\eta)$. For small amplitude waves $\eta \ll h$ and $u \simeq C\eta/h$, but for large waves η cannot be neglected compared to h.

The loss of energy of laminar flow of a homogeneous fluid is due to viscous shear stresses in the boundary layer. For thin boundary layers, the rates of change of quantities along the layers are much smaller than across them, i.e., $\frac{\partial}{\partial x} \ll \frac{\partial}{\partial z}$ and $\frac{\partial^2}{\partial x^2} \ll \frac{\partial^2}{\partial z^2}$ where x is a coordinate along the layer, and z is a coordinate perpendicular to it. Also, the vertical velocity component (in the z direction) is small compared to the horizontal velocity. Neglecting quadratic terms with no body forces in the x direction, the equations of motion become:

$$\frac{\partial u_\ell}{\partial t} = -\frac{1}{\rho_w}\frac{\partial p}{\partial x} + \nu \frac{\partial^2 u_\ell}{\partial z^2} \quad , \tag{3.37a}$$

and

$$0 = -\frac{1}{\rho_w}\frac{\partial p}{\partial z} - g \quad , \tag{3.37b}$$

where u_ℓ is the horizontal velocity component in the boundary layer, ρ_w is the density of the fluid, p is the pressure, ν is the kinematic viscosity of the fluid, and g is the acceleration due to gravity. Eq. (3.37b) implies that the pressure across the boundary layer is hydrostatic, hence variations of the pressure in the x direction are the same as those outside the layer and next to it. The linearized equations of motion in the x direction outside the boundary layer have the form:

$$\frac{\partial u}{\partial t} = -\frac{1}{\rho_w}\frac{\partial p}{\partial x} \quad . \tag{3.38}$$

The free stream velocity, u(x,z,t), is approximately equal to the velocity at the bed evaluated from potential flow theory, u(x,0,t), since the boundary layer is assumed to be very thin. Subtracting Eq. (3.38) from Eq. (3.37a) yields, since u is independent of z:

$$\frac{\partial}{\partial t}(u_\ell - u) = \nu \frac{\partial^2 (u_\ell - u)}{\partial z^2} \quad , \tag{3.39}$$

with the boundary conditions

$$u_\ell - u = -u \quad (\text{at } z = 0) \quad , \tag{3.40a}$$

and

$$u_\ell - u = 0 \quad (\text{at } z \to \infty) \quad . \tag{3.40b}$$

Introducing the coordinate system X = x-Ct which is stationary with respect to the wave, Eq. (3.39) becomes:

$$\frac{\partial}{\partial X}(u_\ell - u) = -\frac{\nu}{C}\frac{\partial^2(u_\ell - u)}{\partial z^2} \quad , \tag{3.41}$$

subject to the boundary conditions (3.40), it should be noted that $u(x,0,t)$ transforms to $u(X,0)$ and is denoted by $u(X)$.

The solution of Eq. (3.41) with the boundary conditions (3.40) is obtained using a Fourier integral. Following Keulegan (1948) it has the form:

$$u_\ell - u = -\frac{2}{\sqrt{\pi}}\int_o^\infty u\left(X + \frac{Cz^2}{4\nu\beta^2}\right)e^{-\beta^2}d\beta \ . \tag{3.42}$$

The boundary shear stress is defined as

$$\tau = \mu\left(\frac{\partial u_\ell}{\partial z}\right)_{z=o} \quad , \tag{3.43}$$

where μ is the dynamic viscosity of the fluid. Differentiating Eq. (3.42) with respect to z and substituting it in Eq. (3.43) will provide an expression for the boundary shear stress. The procedure is performed for the solitary wave as follows.

Consider a solitary wave as presented by Boussinesq (1872) (see Table 3.1; also see Eqs. (3.6), (3.7), and (3.8)). Introducing Eq. (3.8) into Eq. (3.42) gives:

$$u_\ell - u = -\frac{2C}{\sqrt{\pi}}\int_o^\infty \left[1+\frac{h}{H}\cosh\left(\alpha X + \frac{\alpha C z^2}{4\nu\beta^2}\right)\right]^{-1} e^{-\beta^2}d\beta. \tag{3.44}$$

Differentiating Eq. (3.49) with respect to z:

$$\frac{\partial u_\ell}{\partial z} = \frac{2C}{\sqrt{\pi}}\int_o^\infty \frac{\frac{h}{H}\sinh 2\left(\alpha X + \frac{\alpha C z^2}{4\nu\beta^2}\right)}{\left[1+\frac{h}{H}\cosh\left(\alpha X + \frac{\alpha C z^2}{4\nu\beta^2}\right)\right]^2}\frac{\alpha C z}{2\nu\beta^2}e^{-\beta^2}d\beta \ . \tag{3.45}$$

Let $\sqrt{\frac{\alpha C}{4\nu}}\frac{z}{\beta} = \kappa$, hence $d\kappa = -\sqrt{\frac{\alpha C}{4\nu}}\frac{z}{\beta^2}d_\beta$. Introducing this into Eq. (3.45) and letting z=0 yields:

$$\left(\frac{\partial u_\ell}{\partial z}\right)_{z=o} = 2C\sqrt{\frac{\alpha C}{\pi\nu}}\int_o^\infty \frac{\frac{h}{H}\sinh 2(\alpha X+\kappa^2)d\kappa}{\left[1+\frac{h}{H}\cosh^2(\alpha X+\kappa^2)\right]^2} \quad . \tag{3.46}$$

Eq. (3.46), when multiplied by the dynamic viscosity μ, represents the distribution of the smooth bottom shear stresses under a solitary wave for a laminar boundary layer. At the rear of the wave the direction of the flow is against an adverse pressure gradient. Separation of the boundary layer is therefore expected to occur, and laminar boundary layer considerations do not hold behind this point. In fact, it can be seen that the integral on the right-hand side of Eq. (3.46) may have negative values at negative values of X, since the integrand is an odd function of $\alpha X+\kappa^2$. Separation is expected to take place at the coordinate X where the integral in Eq. (3.46) equals zero, as this is the point where the velocity profile in the boundary layer reaches a point of inflection. Behind this point Eq. (3.46) is invalid for the estimation of the bottom shear stresses.

The local friction coefficient, $C_f(X)$, which is related to the shear stress by

$$\tau(X) = \frac{1}{2}\rho_w C_f(X)u^2(X) \tag{3.47}$$

can be evaluated by substitution of Eq. (3.46) into Eq. (3.43) and equating it to Eq. (3.47). The values of the friction coefficient obtained in this way vary along the wave. A mean resistance coefficient

may be obtained from energy dissipation considerations as described in Section 3.2.1 (Eqs. (3.16) through (3.19)), i.e.,

$$\overline{C_f} = \frac{\int_{-\infty}^{\infty} \tau u dX}{\frac{1}{2} \rho_w \int_{-\infty}^{\infty} u^3 dX} \tag{3.48}$$

Substitution of Eq. (3.43) into Eq. (3.38) yields:

$$\overline{C_f} = \frac{\int_{-\infty}^{\infty} \mu u \left(\frac{\partial u_\ell}{\partial z}\right)_{z=o} dX}{\frac{1}{2} \rho_w \int_{-\infty}^{\infty} u^3 dX} \tag{3.49}$$

and with the aid of Eq. (3.43) the mean resistance coefficient for a smooth bottom in a laminar flow can be evaluated theoretically.

As described in Section 3.2.1, experimental values of the mean resistance coefficient can be obtained from measurements of wave attenuation along a channel. However, a discrepancy between the theoretical and experimental results should be expected due to the separation of boundary layer at the rear of the wave. Experimental values of the resistance coefficient should be somewhat larger than the theoretical ones since the separation is usually accompanied by generation of turbulence and larger shear stresses. However, if the point of separation occurs at the rear of the wave far from the crest, the

contribution of the stresses behind this point to the energy dissipation is small, since the fluid particle velocity away from the crest is small. In this case the differences between the theoretical and experimental values of $\overline{C_f}$ should be small.

A discrepancy between the theoretical and measured values of the resistance coefficient may also be expected due to the approximations assumed in the theoretical solution of the boundary layer equations, where the linearized form of the equations was considered. This was done in order to make it possible to solve these equations analytically. However, the convective (nonlinear) terms in the equations of motion under solitary waves of large amplitudes may not be small enough to be neglected. Considering the transformation of coordinates, X=x-Ct, the linear and convective terms of the acceleration become

$$\frac{\partial u}{\partial t} + u \frac{\partial u}{\partial x} = (-C+u) \frac{\partial u}{\partial X} \quad . \tag{3.50}$$

Consider, for example, a solitary wave with a height-to-depth ratio H/h = 0.5. For this wave the fluid particle velocity (calculated from Eq. (3.8)) has the values $u \leq C/3$. Thus the value of u on the right hand side of Eq. (3.50) may not be negligible compared to C, and neglecting the quadratic term $u\frac{\partial u}{\partial x}$ in the equations of motion introduces an error to the solution.

A comparison between the theoretical and experimental values of the mean resistance coefficient of a smooth bottom is presented in Section 5.2.

Corrections for wall effects of the coefficient $\overline{C_{f_b}}$, obtained experimentally in a channel of finite width with smooth walls, can now be estimated for the case of laminar flow. This is done by substitution of the value of τ from Eq. (3.43) into τ_w in Eq. (3.36). As noted earlier, this correction may not be valid, since laminar boundary layer considerations do not hold behind the point of separation, and due to the error which may result from the approximation to the solution. However, if agreement is found between theoretical and measured values of the resistance coefficient of a smooth bottom, this will justify the correction for wall effects, and the error will be considered negligible.

3.2.3 The Forces Exerted on a Single Sphere Resting on a Bed of Spheres

As noted earlier, the mean bottom resistance coefficient under solitary waves, evaluated from considerations of energy dissipation, is inadequate when it is needed to estimate the instantaneous forces exerted on bottom material. When the bed is formed of a rough surface with the roughness particles protruding into the flow, the forces on the particles consist of drag and inertia force components in a direction parallel to the bed (considered here as being horizontal), and a lift force perpendicular to it. The bottom shear stress is defined as the sum of the horizontal forces in a unit projected area of the bed, and the rate of energy dissipation is obtained by integrating the product of the bottom shear stress and the fluid particle velocity over the wave. Lift forces do not contribute to the shear stress, and the

(non-dissipative) inertia forces cancel out as the shear stresses are integrated over the wave. Hence the mean resistance coefficient, as estimated from measurements of wave attenuation (i.e., from measurements of energy dissipation rate), cannot be used to estimate the forces exerted on the bed since it does not include the inertia and lift forces. As noted in Section 3.2.1, the fact that inertia forces cancel out when the shear stresses are integrated over the wave does not mean that there are no inertia effects on the mean resistance coefficient, since the drag force in an unsteady flow is not necessarily the same as that in a steady flow, even if the instantaneous Reynolds numbers in both flows are the same. A discussion of possible inertia effects on the mean resistance coefficient is presented in Section 5.2.

An approach incorporating considerations of both drag, inertia, and lift effects is described by the following model, shown in Fig. 3.2, in which the forces exerted on a single isolated sphere with diameter D_s and density ρ_s, resting on a bed of tightly packed spheres with diameters D_B, are considered. Consideration of a sphere resting on top of the bed rather than a sphere embedded in the surface seems to represent the problem of interest since it models those particles in the bed which protrude into the flow higher above their neighbors. The forces exerted on these particle are larger than those exerted on their neighbors, and as far as incipient motion is concerned, it is expected that they will be the first particles to move.

A wave of height H travels with a speed C over the surface of

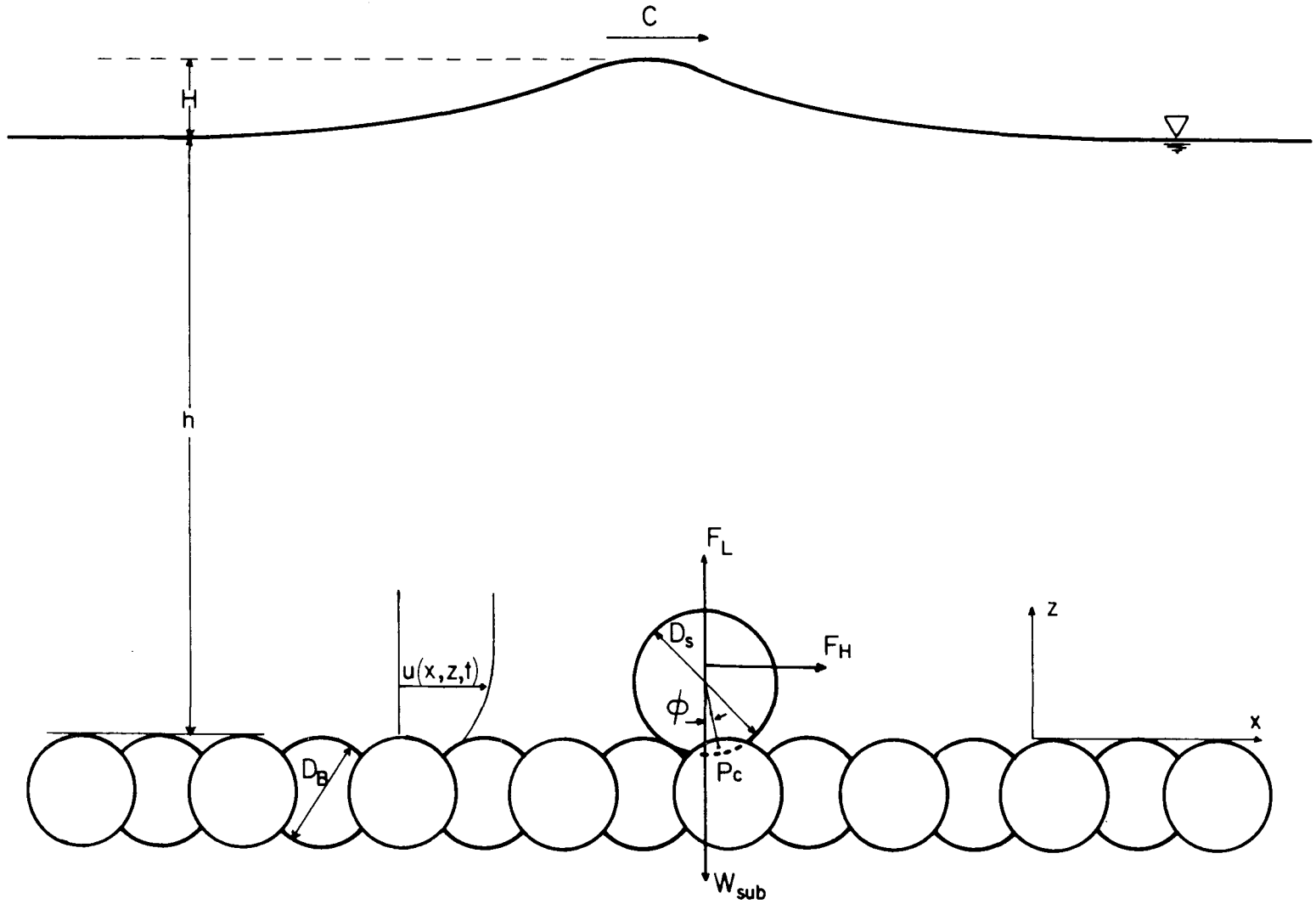

Fig. 3.2 Definition sketch for the forces exerted on a sphere under solitary waves.

water of constant depth h and induces a flow field u(x,z,t), in which u is the horizontal velocity component, x is a horizontal coordinate located at the bottom, z is a vertical coordinate directed upward, and t is the time. The wave also induces a vertical velocity component, v(x,z,t). However, the vertical velocity is small compared to the horizontal component, particularly near the bottom (see the expressions for the velocity due to McCowan (1891) and Laitone (1963), Table 3.1). As shown in Table 3.1, the vertical distribution of the free stream velocity (the horizontal component) in the vicinity of the bottom is uniform. The non-uniform velocity distribution which is shown schematically in Fig. 3.2 is that which exists in the boundary layer near the bottom. The flow which is induced by the wave causes hydrodynamic forces and moments which tend to remove the sphere from its place.

O'Brien and Morison (1952) investigated the forces acting on a sphere located at the bottom under oscillatory waves. They proposed that the hydrodynamic forces exerted on the sphere can be described as a linear combination of drag (F_D) and inertia forces (F_I), i.e.,

$$F_H = \frac{1}{2} \rho_w C_D A u^2 + \rho_w C_M V \frac{du}{dt} , \qquad (3.51)$$

in which F_H is the hydrodynamic force, considered as being horizontal, ρ_w is the density of the fluid, $A = \frac{\pi D_s^2}{4}$ and $V = \frac{\pi D_s^3}{6}$ are the projected area and the volume of the sphere respectively, C_D is the drag coefficient, and C_M is the inertia coefficient. The first term on the right hand side of Eq. (3.51) represents the drag force, F_D, and

the second term represents the inertia force, F_I. The fluid particle velocity and acceleration are given from the wave theory, and they are evaluated near the bottom in the absence of the sphere. O'Brien and Morison neglected the effect of the boundary layer on the magnitude of the velocity at the level of the sphere, and they did not consider lift forces, in a direction perpendicular to the bottom. However, it can be shown that in a proximity to the bottom there exists a lift force, F_L, which may be expressed as

$$F_L = \frac{1}{2} \rho_w C_L A u^2 \quad , \tag{3.52}$$

where C_L is the lift coefficient. Eagleson et al. (1958) noted that due to the velocity distribution in the boundary layer, the velocity at the top of the sphere is larger than the velocity at the bottom, hence a circulation is introduced around the sphere, which results in a force perpendicular to the direction of the flow. Furthermore, even if the boundary layer thickness is small compared to the diameter of the sphere, such that the velocity distribution at the level of the sphere is practically uniform, or when assuming that the fluid is ideal, such that there is no boundary layer at all, there still exists a lift force which is described by Eq. (3.52). The calculation of the lift coefficient for such a (potential) flow is given in Appendix I.

The hydrodynamic forces exerted on the sphere can readily be estimated from Eqs. (3.51) and (3.52) provided the coefficients C_D, C_M, and C_L are known. Assuming that the drag coefficient is independent of the unsteadiness of the flow, it can be estimated from charts as a

function of Reynolds number (e.g., see Rouse (1950), p. 122). Also, if it is assumed that the lift coefficient is independent of the viscosity of the fluid and that the boundary layer thickness is small compared to the diameter of the sphere such that the lift coefficient is independent of the velocity profile, and, furthermore, if it is assumed that the inertia coefficient is independent of the Reynolds number, then C_L and C_M can be evaluated from potential flow theory (as shown in Appendix I). The above assumptions are considered only as an approximation to the problem, since the flow field (and hence the inertia and lift forces) of a viscous fluid is different from that of an ideal fluid. Furthermore, the development of a boundary layer and wakes around the sphere (and hence the drag force) in an unsteady flow is different from that in a steady flow. It seems that the instantaneous drag, inertia, and lift coefficients under the wave depend on both the Reynolds number and some dimensionless form of the acceleration. However, the above approximations are employed due to the lack of knowledge of such a dependence. Iversen and Balent (1951) and also Bugliarello (1956) proposed to present the force in a form of a drag force and to include inertia and viscous effects in the drag coefficient. However, their experiments were conducted in an essentially unbounded fluid and their results did not include lift effects. The idea of combining drag, inertia, and lift effects into one coefficient will be discussed later in this section.

The hydrodynamic forces cause a moment which tends to roll the

sphere around an axis passing through the point of contact, P_c (see Fig. 3.2), between the isolated sphere and the bed spheres. In order to evaluate the hydrodynamic moment exerted on the sphere it is necessary to determine the points at which the forces act with respect to the point of contact P_c. The lift and the inertia forces are assumed to act at the center of the sphere. However, since the bottom of the sphere is partially blocked from the flow by the supporting bed spheres, and due to the velocity distribution in the boundary layer where the top of the sphere is exposed to larger velocities than the bottom, the forces at the top of the sphere are expected to be larger than the forces at the bottom. In this case the resultant hydrodynamic force acts above the center of the sphere. Yet, the exact point of force action is not known. When the thickness of the boundary layer is small compared to the diameter of the sphere and when the portion of the sphere sheltered from the flow is small, the forces may be assumed to act at the center of the sphere. The following analysis is based on the assumption that all the forces act at the center of the sphere. Experimental investigation (to be presented in Chapter 5) should indicate how good the assumptions considered in this analysis are.

With the above considerations, and with the aid of Eqs. (3.51) and (3.52), the hydrodynamic moment, M_H, that would cause motion of the sphere is given by

$$M_H = \left(\frac{1}{2}\rho_w C_D A u^2 + \rho_w C_M V \frac{du}{dt}\right) \frac{\alpha_m D_s}{2} \cos\phi + \frac{1}{2}\rho_w C_L A u^2 \frac{\alpha_m D_s}{2} \sin\phi \quad , \quad (3.53)$$

in which $\frac{\alpha_m D_s}{2}$ is the distance between the axis of motion, P_c, and the center of the sphere, and ϕ is the angle between the moment arm and a normal to the bed (see Fig. 3.2). The angle ϕ and the proportionality coefficient α_m depend on the ratio of the isolated sphere diameter to the bed sphere diameter D_s/D_B, and on the direction of hydrodynamic force with respect to the placement of the isolated sphere on top of the bed. The two extreme values of ϕ (minimum and maximum) for a given value of D_s/D_B are described in Sections 4.4.2 and 5.3.2. Denoting the minimum value of ϕ for a given D_s/D_B as ϕ_1, and the maximum value as ϕ_2 (see Fig. 5.19), it can be shown that

$$1 \geq \alpha_m \geq \frac{\cos\phi_2}{\cos\phi_1} \quad . \tag{3.54}$$

Eq. (3.53) can be used to determine the hydrodynamic moment exerted on the sphere assuming that the drag, inertia, and lift coeffients are known, and that the forces act at the center of the sphere. However, as noted before, it seems reasonable to believe that these assumptions are inaccurate. Hence, the problem is considered here in a similar way to that proposed by Iversen and Balent (1951) and Bugliarello (1956) who combined inertia and viscous effects into one coefficient. In the following analysis lift effects are also considered in this coefficient, in addition to inertia and viscous effects.

Consider the hydrodynamic moment given by Eq. (3.53) and rewrite it as

$$M_H = \left(C_D + C_L \tan\phi + \frac{4}{3} C_M \frac{D_s}{u^2} \frac{du}{dt} \right) \frac{1}{2} \rho_w A u^2 \frac{\alpha_m D_s}{2} \cos\phi \ , \qquad (3.55)$$

where $\frac{\pi D_s^2}{4}$ and $\frac{\pi D_s^3}{6}$ are substituted for A and V respectively. The bracketed term on the right hand side of Eq. (3.55) may be considered as a moment-resistance coefficient, C_D^*, such that

$$C_D^* = C_D + C_L \tan\phi + \frac{4}{3} C_M \frac{D_s}{u^2} \frac{du}{dt} \ , \qquad (3.56)$$

and the combined hydrodynamic forces exerted on the sphere are expressed in a form of a drag force, i.e.,

$$F = \frac{1}{2} \rho_w C_D^* A u^2 \ . \qquad (3.57)$$

Note that the force given by Eq. (3.57) is not an actual force exerted on the sphere. It is an equivalent horizontal force which, when applied to the sphere, introduces the same moment as that introduced by the actual (horizontal and lift) forces. The introduction of C_D^* into Eq. (3.57) will not give the true force exerted on the sphere unless C_D^* is decomposed into its original components which describe the horizontal and lift forces separately. It seems that the use of a single coefficient, C_D^*, is disadvantageous as compared to the use of drag, inertia, and lift coefficients, since it results in a loss of information about the actual forces exerted on the sphere. However, with the lack of knowledge of the values of these coefficients it has the advantage that it requires one to estimate only one coefficient rather than three. As far as incipient motion is concerned, this coefficient adequately describes the hydrodynamic moments exerted on the sphere, and the manner in which the hydrodynamic force is divided into horizontal and

lift components is unimportant. Empirical values of the resistance coefficient C_D^*, as obtained from measurements of incipient motion, will be presented in Section 5.3.

In addition to the hydrodynamic forces exerted by the flow, the sphere is also subjected to a gravitational force given by its submerged weight. This force is expressed as

$$W_{sub} = (\rho_s - \rho_w) g V \ , \tag{3.58}$$

in which W_{sub} is the submerged weight and g is the acceleration due to gravity. While the hydrodynamic forces cause a moment which tends to remove the sphere, the submerged weight causes a restoring moment, M_R, expressed as

$$M_R = W_{sub} \frac{\alpha_m D_s}{2} \sin\phi \ , \tag{3.59}$$

which tends to keep it in its place. Incipient motion occurs when the hydrodynamic moment is equal to the restoring moment, i.e.,

$$\frac{M_H}{M_R} = 1 \ . \tag{3.60}$$

A discussion of the relationships which define the incipient motion of bed material under solitary waves, and which is based on the relationship described by Eq. (3.55) is presented in the following section.

3.3 THE INCIPIENT MOTION OF BED MATERIAL UNDER SOLITARY WAVES

The incipient motion of a particle is described as the event in which the particle begins to move. Mathematically, it is defined by Eq. (3.60) which states that at incipient motion the hydrodynamic moment which tends to remove the particle is equal to the restoring moment which tends to keep it in its at-rest position. The use of Eq.

(3.60) to determine the state of the particle with respect to incipient motion is feasible provided the hydrodynamic and the restoring moments are accurately estimated. However, the evaluation of these moments as presented in the preceding sections is probably inaccurate, since it is based on some assumptions whose validity is questionable. Hence, in the following analysis, the problem is approached by combining the considerations that resulted in Eq. (3.60) with dimensional analysis in order to determine the relationships which define the incipient motion of bottom material under solitary waves.

3.3.1 The Incipient Motion of Particles of Arbitrary Shape

The parameter which is most often used in problems of initiation of motion of bottom material in streams and channels is the Shields parameter τ_*, expressed as

$$\tau_* = \frac{\tau_b}{(\rho_s - \rho_w) g D_s} , \tag{3.61}$$

where τ_b is the bottom shear stress, ρ_s and D_s are the density and the mean diameter of the bed particles respectively, ρ_w is the density of the fluid, and g is the acceleration due to gravity. The dimensionless shear stress given by Eq. (3.61) represents the ratio between the hydrodynamic and the gravitational forces exerted on the particles, assuming that the hydrodynamic forces are proportional to the shear stress. As noted in Section 3.2.3, incipient motion is defined by the ratio between hydrodynamic and restoring moments rather than by ratio between forces. However, if the ratio between the moment arms of the hydrodynamic and

gravitational moments is assumed to be constant for a material of specified angularity and shape, then the ratio between the moments is reduced to the ratio between the forces (i.e., Eq. (3.61)) multiplied by a constant. Shields (1936) noted that the right-hand side of Eq. (3.61) should be divided by a parameter describing the friction coefficient between the uppermost particles in the bed and the particles supporting them. This parameter is similar to the term $\tan\phi$ appearing in Eq. (3.64) which describes the ratio of the hydrodynamic moment to the restoring moment acting on a sphere at incipient motion (see the following section). Shields assumed that this parameter is a function of the shape of the particles, and for beds consisting of particles of practically similar shapes this parameter is constant. Hence he assumed that the dimensionless shear stress as described by Eq. (3.61) can be applied to problems of incipient motion. Although the Shields parameter is mostly applied in sedimentation problems in steady flows, its application in problems under waves are rather limited. Only recently, Madsen and Grant (1975), and Komar and Miller (1975) have shown that it may also be applied to oscillatory flows.

As the bed is composed of particles of arbitrary shape which are scattered and packed randomly on the bottom surface, it is conceivable that not all the particles require the same hydrodynamic forces to be removed. Thus it is expected to observe some motion in the bed if a wave exerts a large enough shear stress. As a larger wave passes, it exerts larger shear stresses, and a larger amount of motion is expected

to be observed. Defining the amount of motion as the ratio between the number of moving particles in a given bed area, N_p, and the total number of particles on the bed surface in the same area, N_{p_T}, it appears that N_p/N_{p_T} is an increasing function of τ_*. Hence, if a relationship is found between N_p/N_{p_T} and τ_*, the extrapolation of this relationship to the point where $N_p/N_{p_T} = 0$ will yield the value of the dimensionless shear stress which defines the incipient motion of particles of arbitrary shape.

So far as the shear stresses are concerned, it was shown in Section 3.2.1 that they can be obtained indirectly from measurements of attenuation of waves along the channel. As noted in that section, the shear stresses obtained in this way are inaccurate as they employ a mean resistance coefficient rather than a local friction coefficient and they exclude inertia and lift forces. Considerations of the incipient motion based on parameters which can be measured directly are presented in the following section.

3.3.2 The Incipient Motion of a Single Sphere

Consider the model of a single sphere resting on top of a bed of well packed spheres (see Section 3.2.1, Fig. 3.2). The important parameters which define the incipient motion are the diameter, D_s, and the density, ρ_s, of the isolated sphere; the diameter of the bed spheres, D_B; the moment angle, ϕ; the water depth, h; the wave height, H; the gravitational acceleration, g; and the density, ρ_w, and the dynamic viscosity, μ (or the kinematic viscosity, $\nu = \mu/\rho_w$), of the fluid. The above considerations mean, for example, that if the fluid

properties (i.e., ρ_w and μ) and the gravitational field (g) are given, then the water depth, the density, and the geometry of the sphere at the bottom define a unique value of the wave height that would cause the sphere to be in a state of incipient motion. The relationship for incipient motion is expressed in dimensionless form as

$$f\left(\frac{D_s}{h}, \frac{D_B}{h}, \frac{H}{h}, \frac{\rho_s}{\rho_w}, \frac{\sqrt{gh}\,h}{\nu}, \phi\right) = 0 \ . \tag{3.62}$$

The applicability of Eq. (3.62) for predicting incipient motion of a sphere is rather limited, unless a relationship between the parameters appearing in this equation is given explicitly. Development of such a relationship based on the considerations expressed by Eq. (3.60) which states that at incipient motion the hydrodynamic moment exerted on the sphere is equal to the restoring moment due to gravity are presented as follows.

Consider the definition of the incipient motion as expressed by Eq. (3.60). Substitution of Eqs. (3.55) through (3.59) into Eq. (3.60) yields, at incipient motion,

$$\frac{\frac{1}{2}\rho_w C_D^* A u^2 \frac{\alpha_m D_s}{2}\cos\phi}{(\rho_s-\rho_w)gV\frac{\alpha_m D_s}{2}\sin\phi} = 1 \ , \tag{3.63}$$

where C_D^* is called the moment-resistance coefficient, A and V are the projected area and the volume of the sphere respectively, u is the fluid

particle velocity, estimated at the level of the sphere in its absence, and $\frac{\alpha_m D_s}{2}$ is the distance between the point of force action and the axis over which the hydrodynamic forces tend to roll the sphere. The numerator of Eq. (3.63) is the hydrodynamic moment, M_H, which tends to remove the sphere, and the denominator is the restoring moment, M_R due to gravity, which tends to keep it in its place. Note that the assumption considered in Section 3.2.3 that the hydrodynamic forces act at the center of the sphere is retained in Eq. (3.63). An additional assumption is made that the velocity u in Eq. (3.63) is given by the free stream velocity, evaluated from the wave theory near the bottom (i.e., neglecting boundary layer effects on the actual velocity distribution at the level of the sphere). The discrepancies which result from the above assumptions can be accommodated by the definition of the resistance coefficient C_D^*. As expressed in Eqs. (3.56) and (3.47), C_D^* is defined such that when it is substituted in Eq. (3.55), it yields the actual hydrodynamic moment exerted on the sphere. This definition may be carried further by saying that C_D^* is a coefficient that, when combined with the free stream velocity, and when assuming that the forces act at the center of the sphere, it yields the actual hydrodynamic moment exerted on the sphere.

Considering Boussinesq's (1872) presentation of the solitary wave (see Table 3.1, and also Eqs. (3.6), (3.7), and (3.8)), Eq. (3.63) becomes

$$\frac{3C_D^* h(\eta/h)^2(1+H/h)}{4\left(\frac{\rho_s}{\rho_w}-1\right)D_s(1+\eta/h)^2\tan\phi} = 1 \ , \qquad (3.64)$$

in which η is the elevation of the water surface above still water level, and where $\pi D_s^2/4$ and $\pi D_s^3/6$ were substituted for A and V respectively. A characteristic value of the surface elevation is given by its maximum, i.e., by the wave height. Substitution of H for η in Eq. (3.64) will result in an error, since due to inertia effects the incipient motion is expected to occur under the wave front near the crest, where η is smaller than H (see Section 5.3.2, Figs. 5.21 and 5.22). However, as the resistance coefficient, C_D^*, is unknown beforehand, the discrepancy may be absorbed in C_D^*. Substituting H for η in Eq. (3.64) yields

$$\frac{(H/h)^2}{(1+H/h)} = \frac{4}{3} \frac{(\rho_s-\rho_w)D_s \tan\phi}{\rho_w C_D^* h} \quad , \tag{3.65}$$

or, separating unknown parameters from measurable quantities:

$$\left(\frac{H}{h}\right)^2 = f\left[C_D^* , \frac{(\rho_s-\rho_w)}{\rho_w} \frac{D_s}{h} \tan\phi\right] , \tag{3.66}$$

in which f[ ] denotes a function of the terms enclosed in the brackets.

By applying the physical consideration, that at incipient motion the hydrodynamic moment exerted on the sphere is equal to the restoring moment due to gravity, the relationship for incipient motion, as derived from dimensional analysis in Eq. (3.62), was transformed to the relationship given by Eq. (3.65). The advantage of Eq. (3.65) is that it provides an explicit relationship for incipient motion. However, since it includes an unknown parameter, C_D^*, it will have to be obtained experimentally, as shown in Section 5.3.2.

CHAPTER 4

EXPERIMENTAL EQUIPMENT AND PROCEDURES

4.1 THE WAVE TANK

A recirculating tilting flume measuring 130 ft (40 m) long, 43 in. (110 cm) wide and 2 ft (61 cm) deep was modified for the purpose of water-wave experiments. Complete details of this flume are given by Vanoni, Brooks and Raichlen (1967). Its important features are briefly stated here and shown in Fig. 4.1. The bottom of the flume and short sections of the wall at the ends are made of stainless steel plate; the remaining portion, 110 ft (33.53 m) long, has glass sides 1/2 in. (12.7 mm) thick in panels 5 ft (152.4 cm) long. Two stainless steel rails, 1.5 in. (38.1 mm) in diameter, are mounted along the flume on top of its frame by studs spaced at about 2 ft ($\sim$ 60 cm). The rails support an instrument carriage that can be driven to any location along the flume. The wave generator is a piston type mounted on the tank at one of the ends and is described in Section 4.2. A wave dissipator consisting of two 2 in. (5 cm) thick layers of rubberized hair (commonly used in the manufacture of furniture) was tied to a 23% slope and installed at the other end of the tank. Reflection coefficients for this system were not tested since its only purpose was to minimize waiting time between experiments.

The flume is supported by eight power-driven screw-jacks and can be tilted to a maximum slope of 2%. When the waves travel up the slope they increase in amplitude and get to extreme heights (up to breaking).

The recirculating pipes under the flume (shown in Fig. 4.1) were

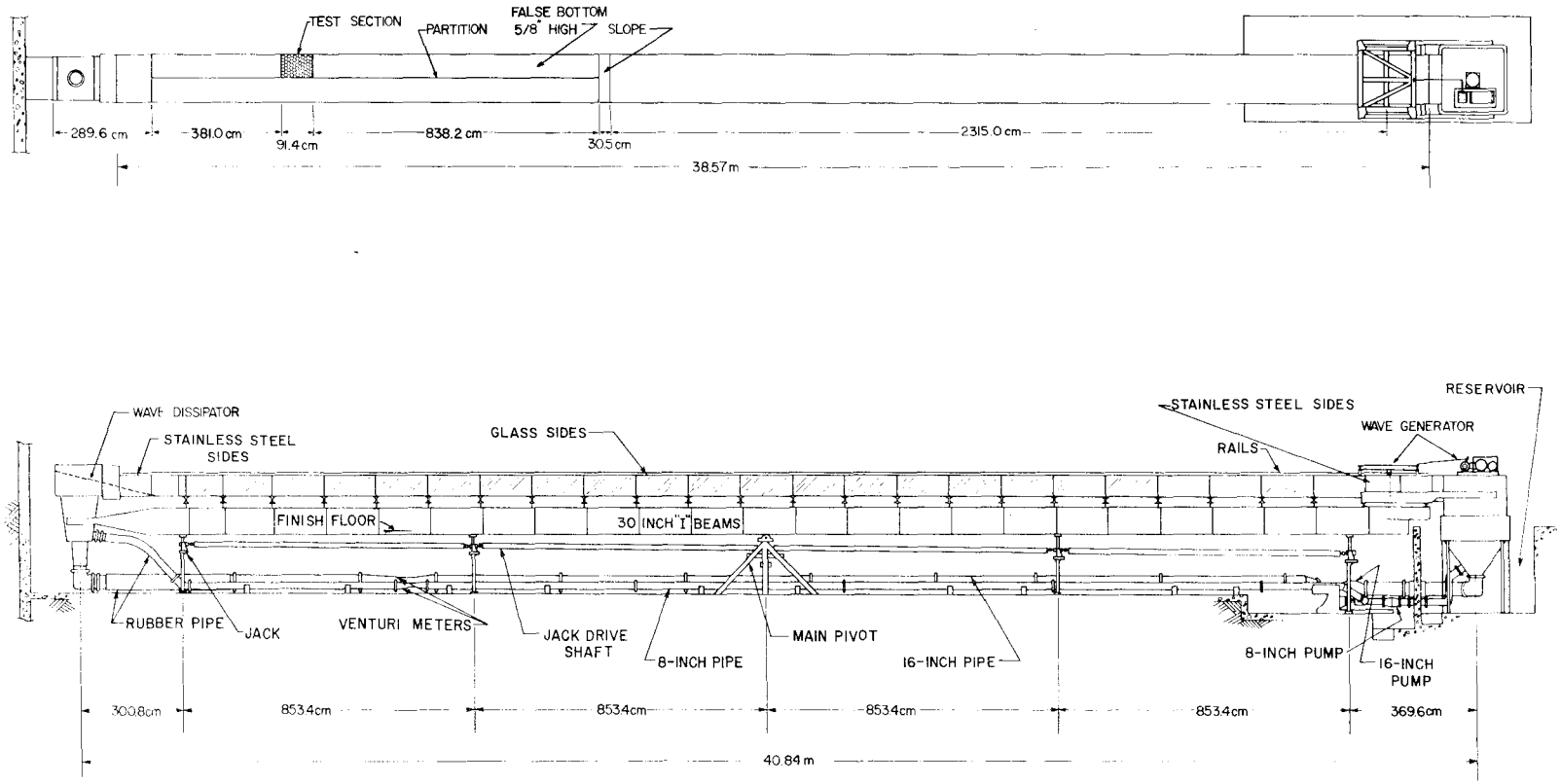

Fig. 4.1 Details of 40-meter precision tilting flume modified for wave experiments.

blocked to prevent oscillations in the flume due to transient currents in addition to the waves.

4.2 THE WAVE GENERATOR

A piston type wave generator was installed at the upstream end of the wave tank. The generator, shown in Fig. 4.2, consisting of an aluminum plate 1/4 in. (6.35 mm) thick, 27.2 in. (69 cm) high was slightly narrower than the wave tank so that it could move freely between the walls. The plate was mounted on an aluminum frame with linear ball bushings that traveled on two steel rails 1.5 in. (38.1 mm) in diameter. The frame was connected by a 1.5 in. (38.1 mm) steel pipe 6 ft (1.83 m) long to an adjustable eccentric arm which was mounted on a rotating shaft driven by an electric motor such that the maximum stroke was about 1 ft (30 cm). The stroke was adjusted with a screw and was calibrated by a counter.

The motor driving the wave generator had a variable speed gear with an RPM indicator. However, for precision adjustment of the motor speed, a measuring device was installed on the shaft. A circular aluminum plate with 200 holes equally spaced near its perimeter was mounted on the shaft. A source emitted a light beam through the holes into a photo-cell that generated electric pulses. A Beckman counter (Model 7351) counted the number of pulses during 10 seconds. If the number of pulses in a counting time T_{co} is N_{co} and the number of holes in the plate is N_h, then the period T of one revolution is $T = \frac{N_h T_{co}}{N_{co}}$.

In order to generate solitary waves it was necessary to drive the wave generator in such a way that it would follow the motion of the

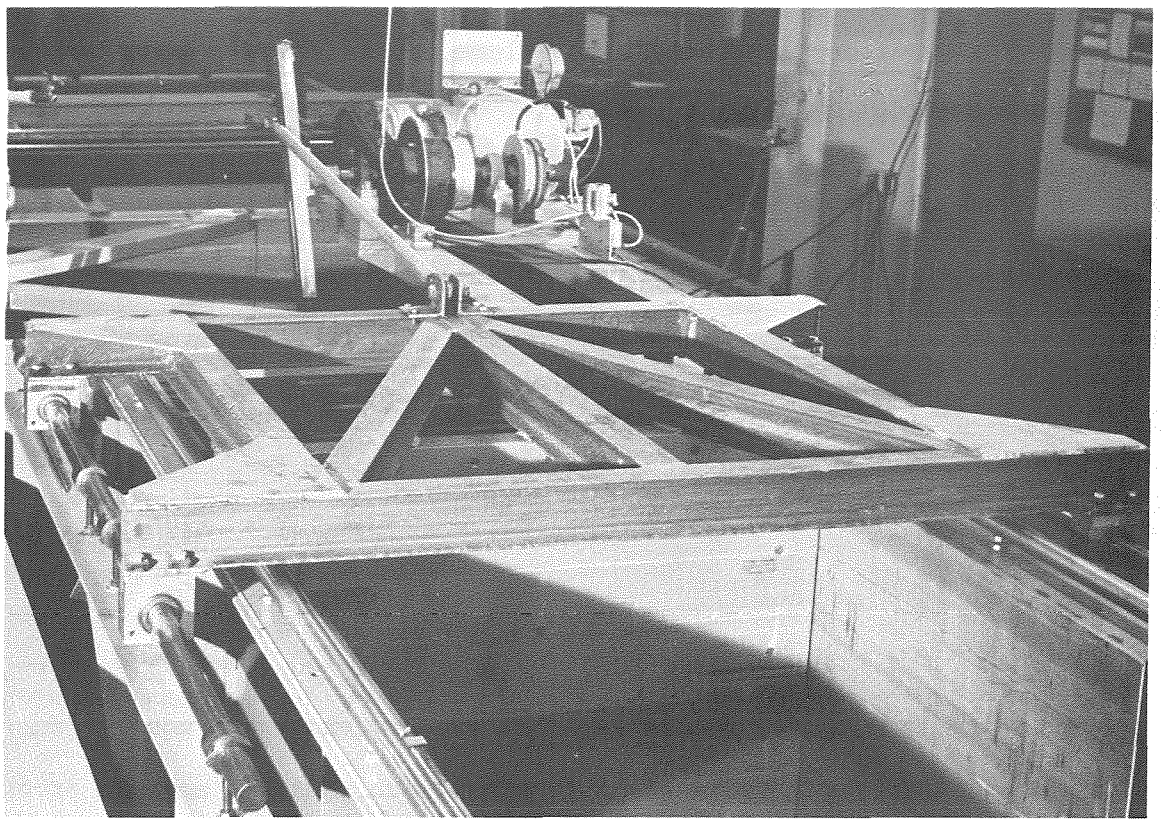

Fig. 4.2 Overall view of the wave generator.

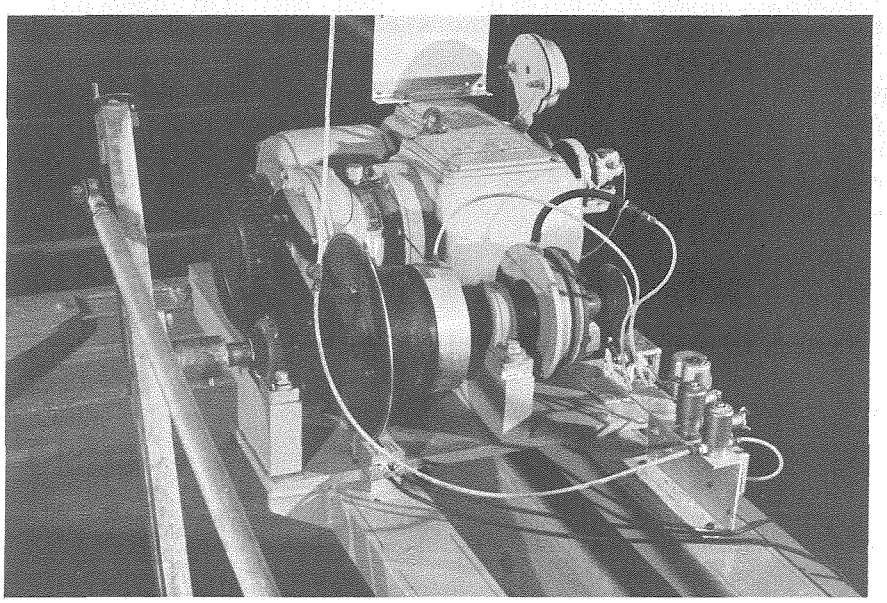

Fig. 4.3 View of the system controlling the motion of the wave generator.

fluid particles under solitary waves. The motion of the wave generator was controlled by a pneumatic clutch and brake system (Horton "Air Champ" models with air pressure controlled by Norgren valves). The system is shown in Fig. 4.3. To generate a wave, the plate of the wave generator was placed at its maximum negative position and the stroke set. The brake was then engaged to hold the generator in place. The clutch was engaged and the brake disengaged simultaneously, enabling the shaft to turn half a revolution, driving the generator plate to its most forward position. At this point a microswitch was automatically activated to stop the motion. The system was also capable of generating oscillatory waves by driving the plate continuously. The calculated displacement of the wave generator (shown in Fig. 4.4) followed approximately a sinusoidal motion of half a cycle when generating solitary waves. As can be seen in Fig. 4.4 the calculated motion of the wave generator does not follow exactly the fluid particle displacement under the solitary wave. The importance of this is discussed in Section 5.1. Note that the actual motion of the wave generator was not measured.

4.3 THE MEASUREMENT OF WAVE AMPLITUDE

Resistance type wave gages were used in conjunction with a Sanborn (150 Series) recorder in order to measure wave profiles as a function of time at a specific location in the wave tank. The wave gage (shown in Fig. 4.5) consisted of two stainless steel wires 0.01 in. (0.254 mm) in diameter, 13 in. (33 cm) long and spaced at 1/8 in. (3.18 mm) apart. The wires were stretched taut and parallel in a frame constructed of 3/16 in. (4.76 mm) stainless steel rod. The wires are electrically insulated from the frame and from each other. When the gage is immersed

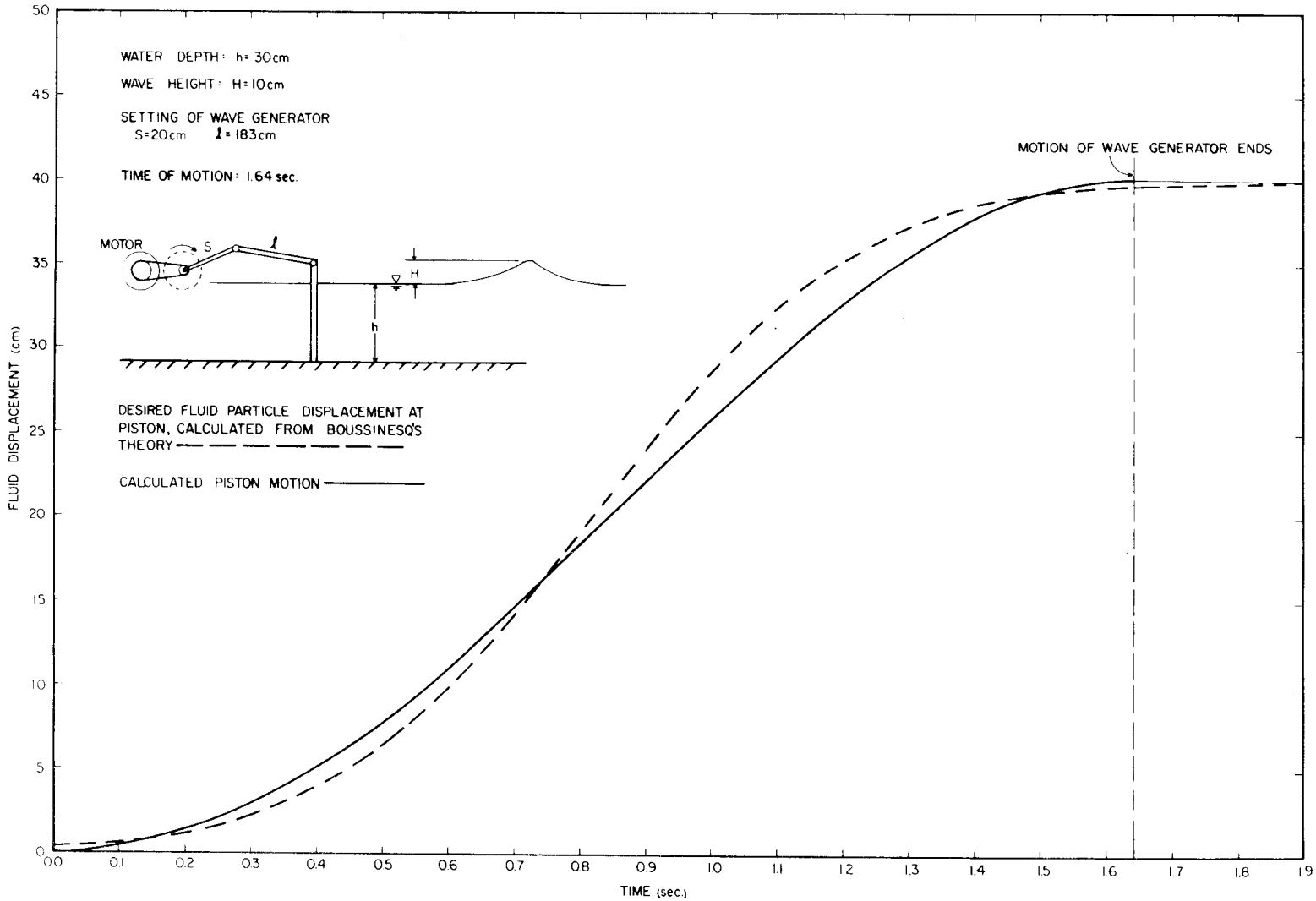

Fig. 4.4 The displacement of fluid particles under a solitary wave and at the wave generator piston.

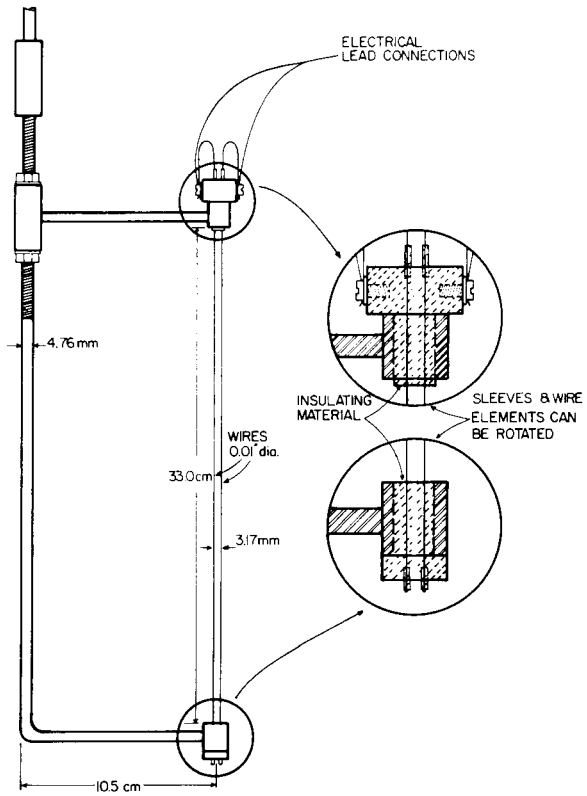

Fig. 4.5 Drawing of a typical wave gage.

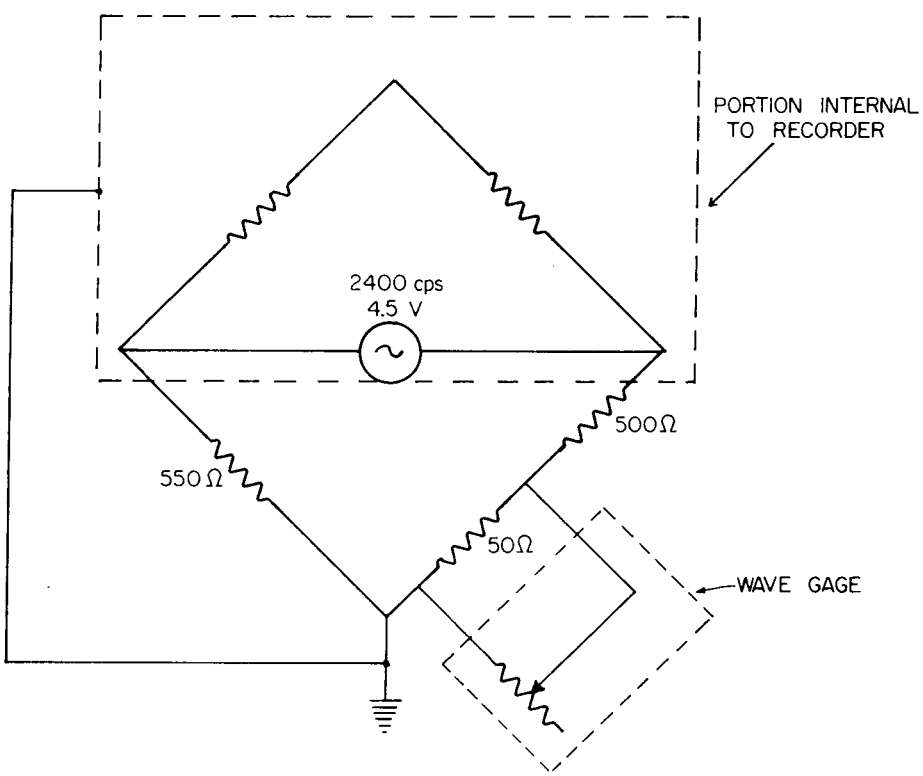

Fig. 4.6 Circuit diagram for wave gages.

in a conducting fluid a current which varies with the depth of immersion passes between the wires. The wave gage was mounted on a point gage supported by the instrument carriage on top of the tank. A Sanborn carrier preamplifier was used to supply 4.5 volts at 2400 cps excitation to the wave gage as indicated by the circuit diagram in Fig. 4.6. The output signal from the wave gage was also received by the carrier preamplifier which after demodulation and amplification was displayed on the recording unit. As the immersion of the wave gage varied in the conducting fluid, the resistance in the circuit changed proportionally, causing an imbalance in the full bridge circuit shown in Fig. 4.6. This imbalance was recorded as a change from the balanced position.

Before each set of experiments the bridge circuit was balanced at a fixed wave gage immersion. The gage was calibrated by immersing it in water to various depths, noting the corresponding deflections of the recording stylus, and returning the gage to its original position. A typical calibration curve is shown in Fig. 4.7. No calibration was done after completing the experiments since each experiment was completed within a few minutes after each calibration.

During calibration of the wave gage, a drift of the recording stylus was noted. In order to estimate the error which resulted from this drift, four wave gages were mounted on a rack on the instrument carriage and simultaneously recorded a wave at the same location in the wave tank. The differences between the four records indicated a measurement error of approximately 5% of the wave height. The reasons for the drift during calibration are not completely understood and were not investigated. It was found, however, that the error was somewhat reduced by

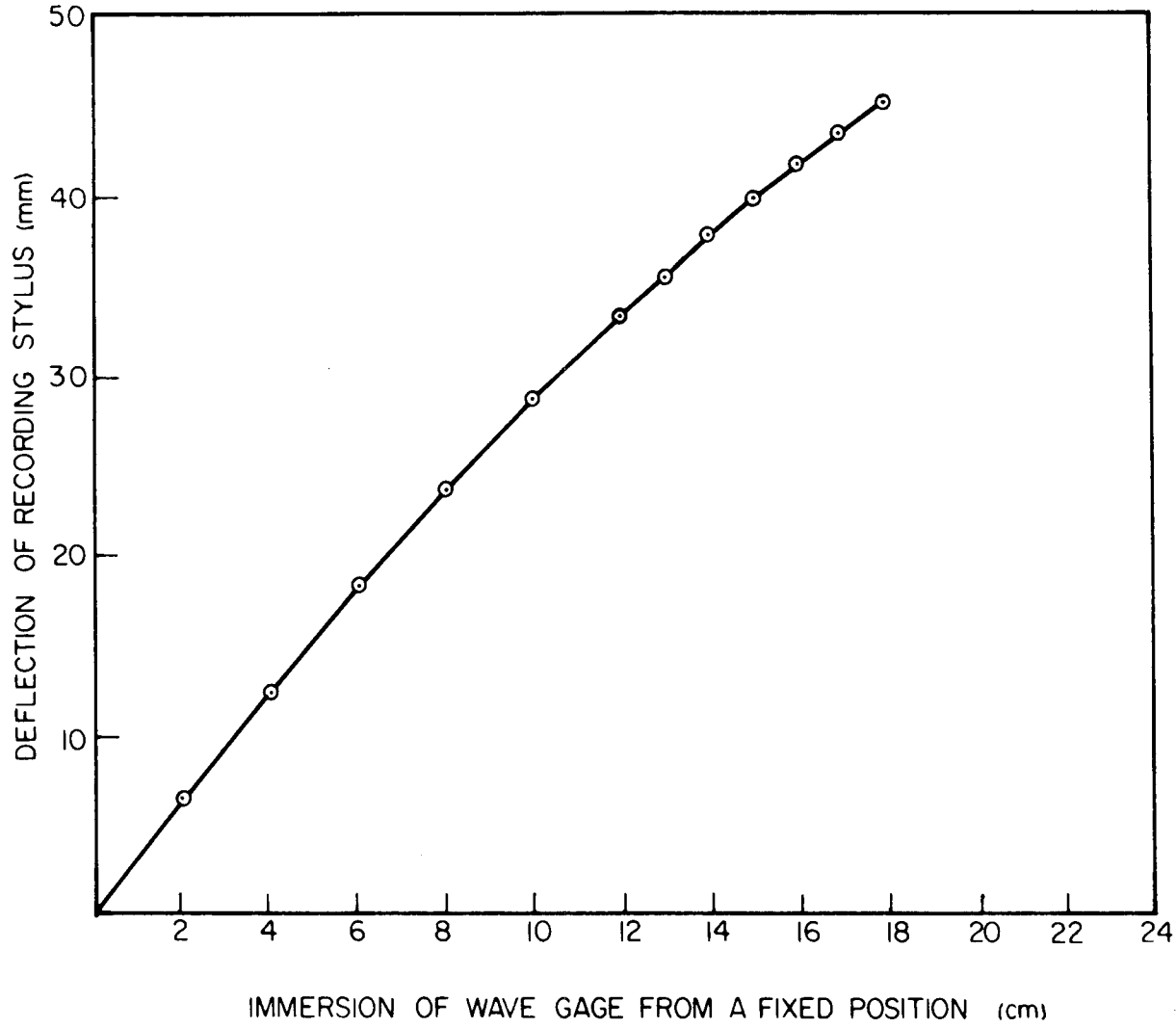

Fig. 4.7 Typical calibration curve for a wave gage.

dynamic calibration. This was done by moving the gage to its prescribed depth and returning it to its original position as rapidly as possible. Thus the calibration curve was obtained before the stylus began to drift. In the process of this rapid motion, however, the reading of the wave gage immersion from the point gage scale became less accurate, introducing another error. The estimated error of dynamic calibration was approximately 3% of the wave height. The differences between dynamic and static calibrations are illustrated in Fig. 4.8. This error was acceptable for most of the experiments but not for the experiments on wave damping.

In some of the experiments on wave damping the wave amplitude decreased approximately 1% when the wave traveled over a distance from one gage to another. In order to improve the performance of the wave gages, the stainless steel wires were replaced by 0.01 in. (0.254 mm) platinum wires. The wires were cleaned with chromic sulfuric acid and then platinized. The platinizing solution consists of 1 gr chloroplatinic acid (platinum chloride) and 12 mg lead acetate in 100 mℓ of water. The wires (already mounted on the wave gage frame) were immersed in the solution and connected to the negative terminal of a 3V dry cell battery. A piece of platinum was connected to the positive terminal and dipped in the solution. The platinizing was completed when the wires were completely coated with black. When the wave gages were not in use they were kept in distilled water. They were cleaned and platinized again whenever the black coating peeled off, or when erratic readings were noted. The drift which had been noticed during static calibration of wave gages with stainless steel wires (see Fig. 4.8a) was eliminated by using gages with platinum wires. The relative error of this type of wave gage was estimated at less than 1%.

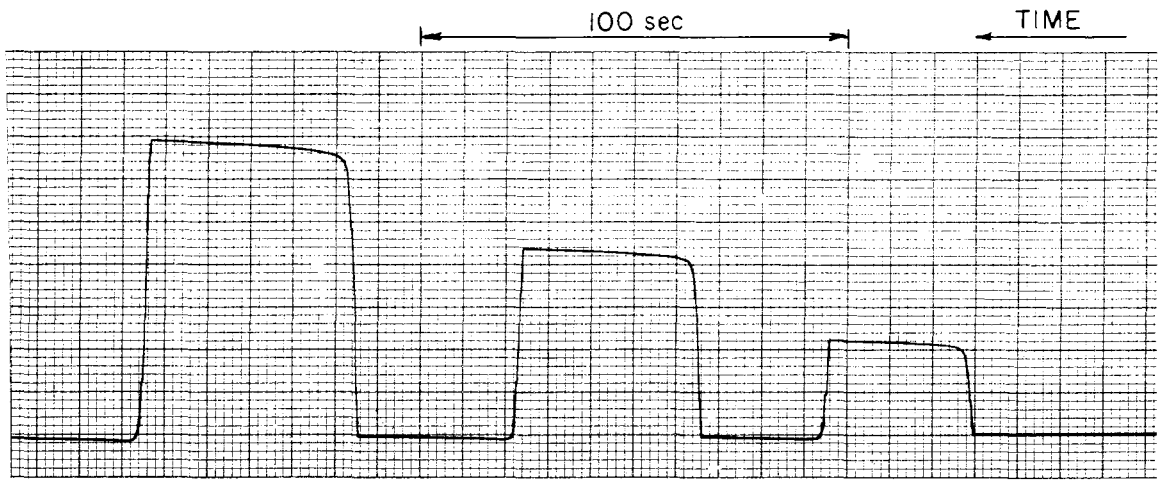

a. STATIC CALIBRATION

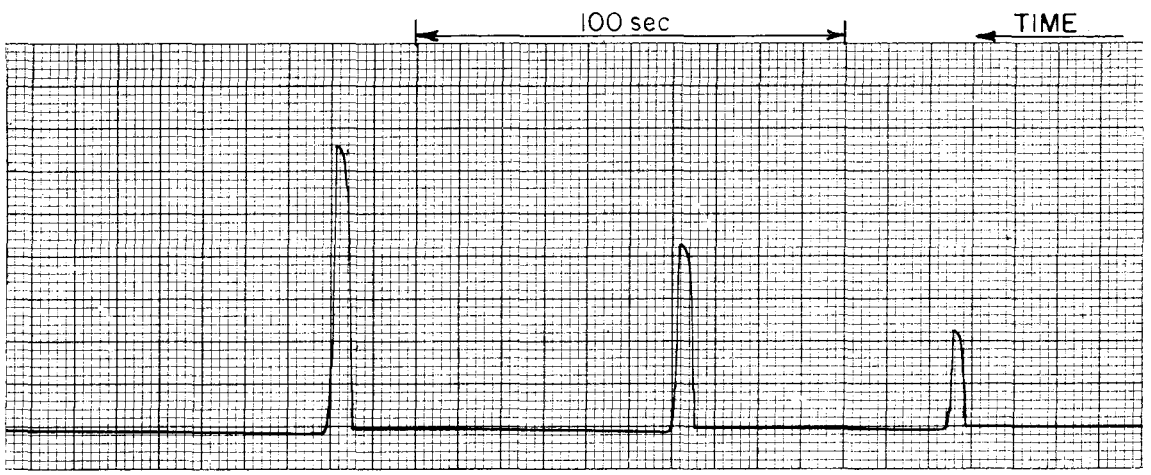

b. DYNAMIC CALIBRATION

Fig. 4.8 Typical records of static and dynamic calibration (wave gage constructed with stainless steel wires).

4.4 TEST SECTIONS AND EXPERIMENTAL METHODS FOR INCIPIENT MOTION EXPERIMENTS

4.4.1 The Working Area

The investigation of incipient motion of spheres and the stability of rocks required a false bottom in front and behind the spheres (or the rocks) in order to provide a smooth transition and a uniform depth over the entire working area. The working area with the rock section in place is shown in Fig. 4.9. The false bottom was made of 5/8 in. (15.9 mm) thick plates of anodized aluminum. The plates were slightly narrower than the tank to reduce possible damage to the glass walls during installment. A continuous smooth surface was attained by attaching the plates one to another with dowel pins.

The false bottom started 76 ft (23.15 m) from the wave generator. A sloping sheet of galvanized steel 1 ft (31 cm) long provided a smooth transition from the bottom of the tank to the top of the false bottom. The total length of the false bottom is 44 ft (13.41 m), ending with the wave dissipator at the downstream end of the tank. The tank was divided in half longitudinally over the entire length of the false bottom in order to compare the characteristics of solitary waves over a smooth bottom and over the spheres. The section with the spheres was placed at one side of the dividing wall (as shown in the plan view of Fig. 4.1) while the other side was kept smooth. The dividing wall was made of anodized aluminum plates 1/4 in. (6.35 mm) thick, 8 ft (2.44 m) long and 2 ft (61 cm) high. The plates were placed in a groove 1/16 in. (1.6 mm) deep along the center line of the bed, and were held at the top by cross bars fastened to the top of the side-walls of the tank.

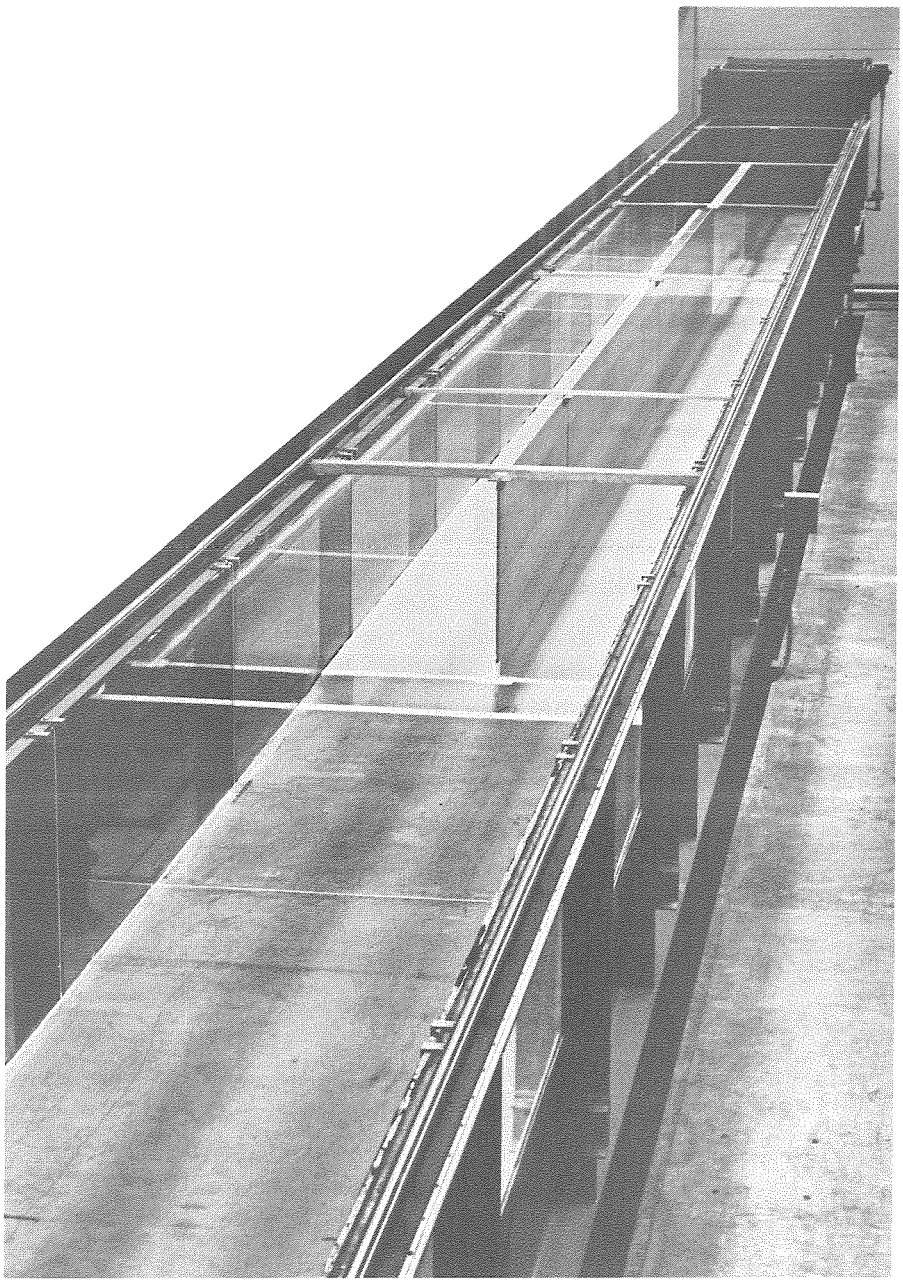

Fig. 4.9 Overall view of the working area in the wave tank.

The experiments of the incipient motion of spheres required a free path for a laser beam across the tank. (The details of the laser equipment are described in Section 4.4.2.) In order to provide this path, a portion of the partition at the working section was made of a 1/4 in. (6.35 mm) transparent lucite plate.

During the experiments the waves were recorded simultaneously over both the spheres and the smooth side in order to examine the effect of the bed of spheres on the wave height.

4.4.2 Incipient Motion of Spheres

4.4.2.1 The Test Section

The test section was located 28.5 ft (8.69 m) from the beginning of the false bed and was 3 ft (91.4 cm) long. A layer of well-packed spheres was glued to a 3 ft x 21-1/4 in. (91.4 cm x 54.0 cm) plate and placed in the tank. Two sizes of spheres were used. One bed consisted of 1/2 in. (12.7 mm) nylon spheres glued to an 1/8 in. (3.18 mm) anodized aluminum plate and the other, shown in Fig. 4.10, of 3/8 in. (9.53 mm) nylon spheres glued to a 1/4 in. (6.35 mm) plate. The thicknesses of the plates were chosen such that when they were placed in the test section, the tops of the spheres were leveled flush with the false bottom. A special epoxy (Epoxilite #211 with catalyst #C301) was used to hold the spheres to the plate under water. The plate provided enough weight against possible movement of the total unit under extremely high waves. Four precision stainless steel spheres glued at the center of the plate supported a precision sphere whose incipient motion was investigated (see Fig. 4.11).

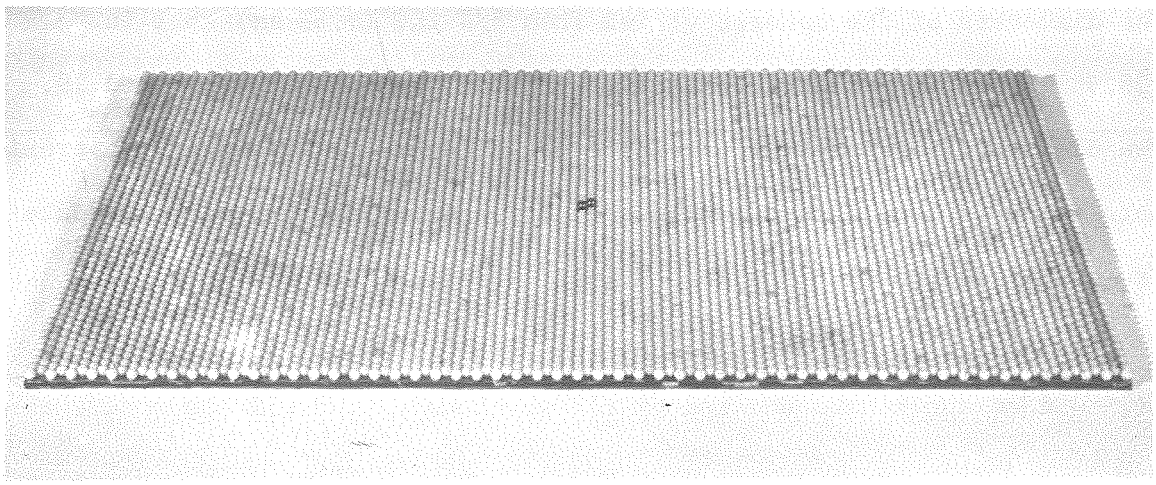

Fig. 4.10 View of the bed of spheres.

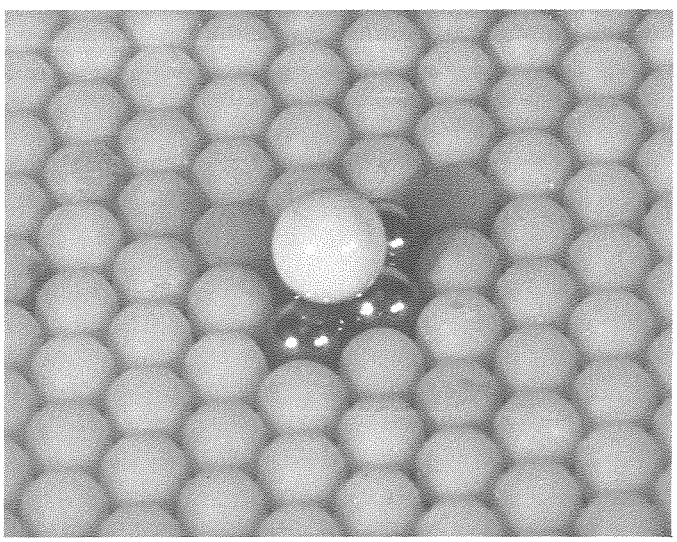

Fig. 4.11 View of an isolated precision sphere supported on top of the bed by precision stainless steel spheres.

The test spheres used in the investigation are shown in Fig. 4.12. The diameters of the spheres varied from 3/8 in. (9.53 mm) to 1 in. (25.4 mm) and the values of specific gravity varied from 1.15 to 2.79. The diameters and specific gravities noted in Fig. 4.12 are only approximate values. More accurate values are given with the experimental data presented in Appendix II, Table A.2.1. The incipient motion of each sphere was tested in two positions. In position I, which is shown in Fig. 4.13a, the moment exerted by the wave tended to roll the sphere over and between two spheres, while in position II, which is shown in Fig. 4.13b, it was forced above a single sphere.

Experiments were conducted with water depths of 10, 20, 22.5, 30 and 42 cm. A few experiments were conducted under breaking waves at depths different from those mentioned above in order to investigate the incipient motion under waves of limiting heights.

4.4.2.2 The Measurement of Incipient Motion

The incipient motion is defined experimentally as the conditions under which the sphere barely moves under the wave. A technique was developed to measure infinitesimal displacements of the sphere. The system, shown schematically in Fig. 4.14, also indicated the time at which the motion began.

A laser beam, about 0.040 in. (1 mm) in diameter, was transmitted across the tank in front of the sphere into a photo-cell which generated an electronic signal (voltage) proportional to the amount of light it received. The laser was mounted on a rack connected to a micrometer such that it could be positioned with an accuracy of 0.001 in. (1/40 mm).

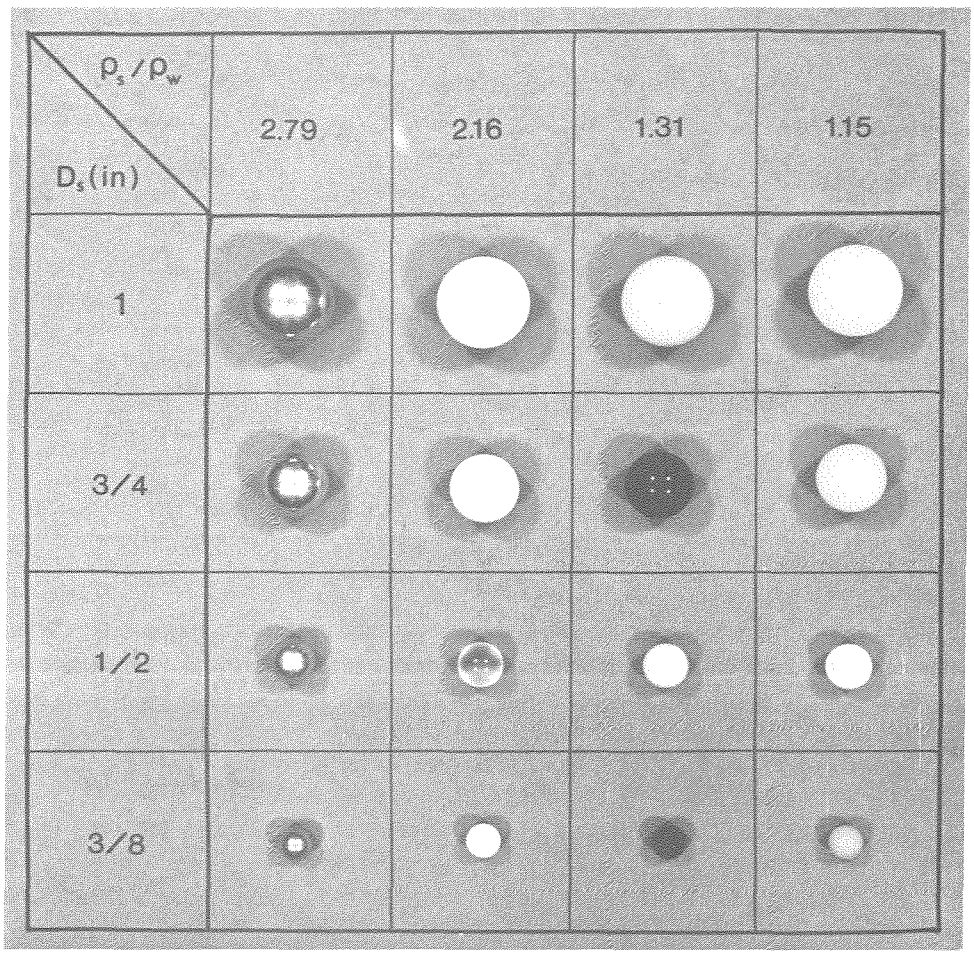

Fig. 4.12 The precision spheres whose incipient motion was investigated.

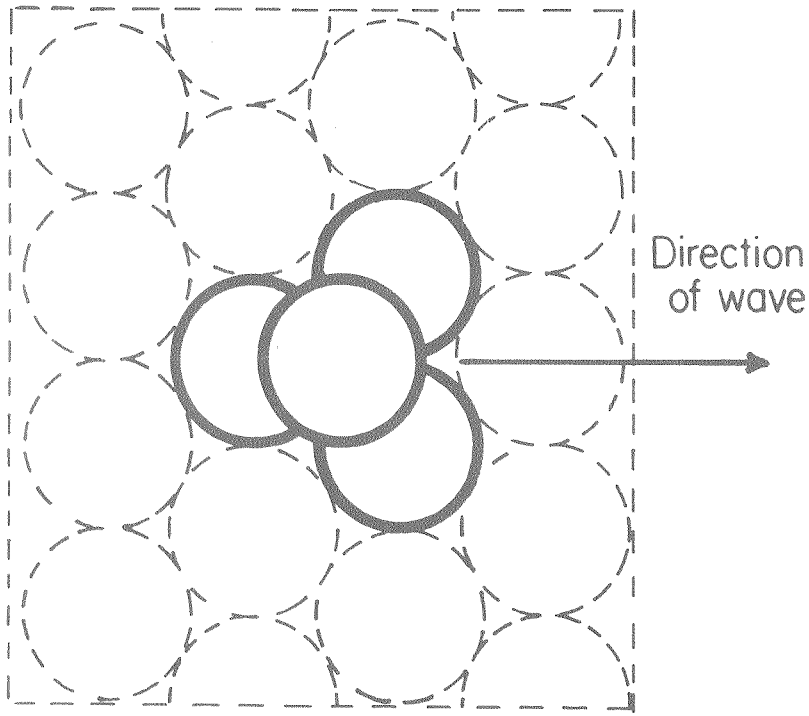

a. Position I

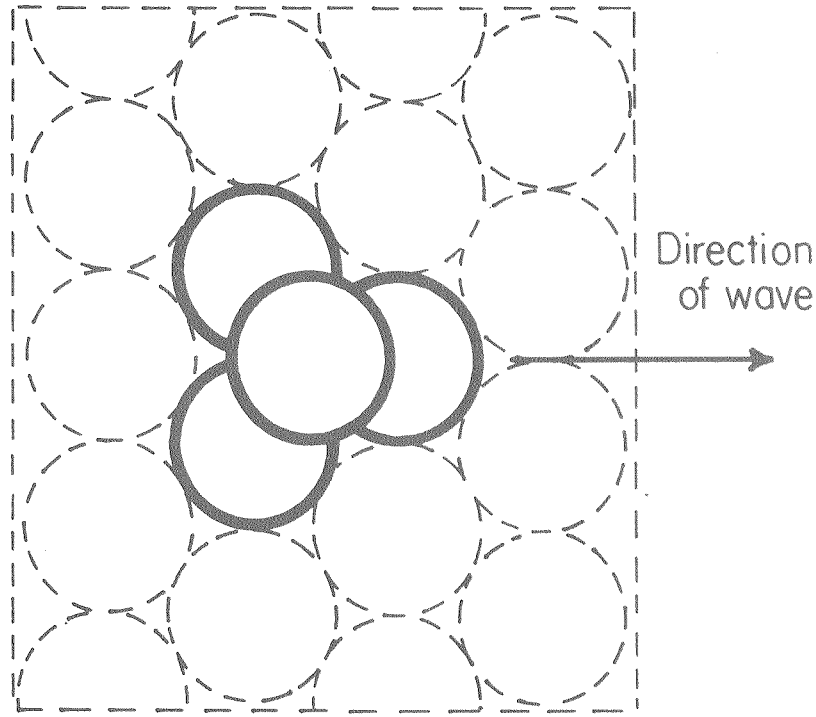

b. Position II

Fig. 4.13 Plan view of the two positionings of an isolated sphere on top of the bed of spheres.

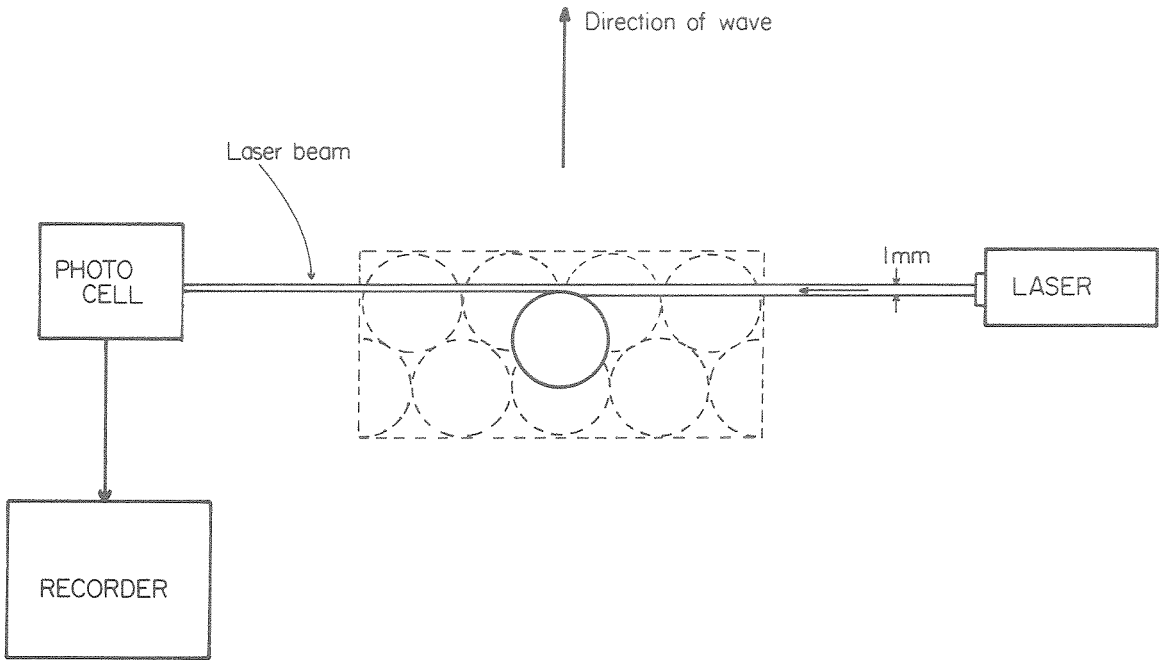

Fig. 4.14 Schematic drawing of the system used to detect infinitesimal displacements of a sphere.

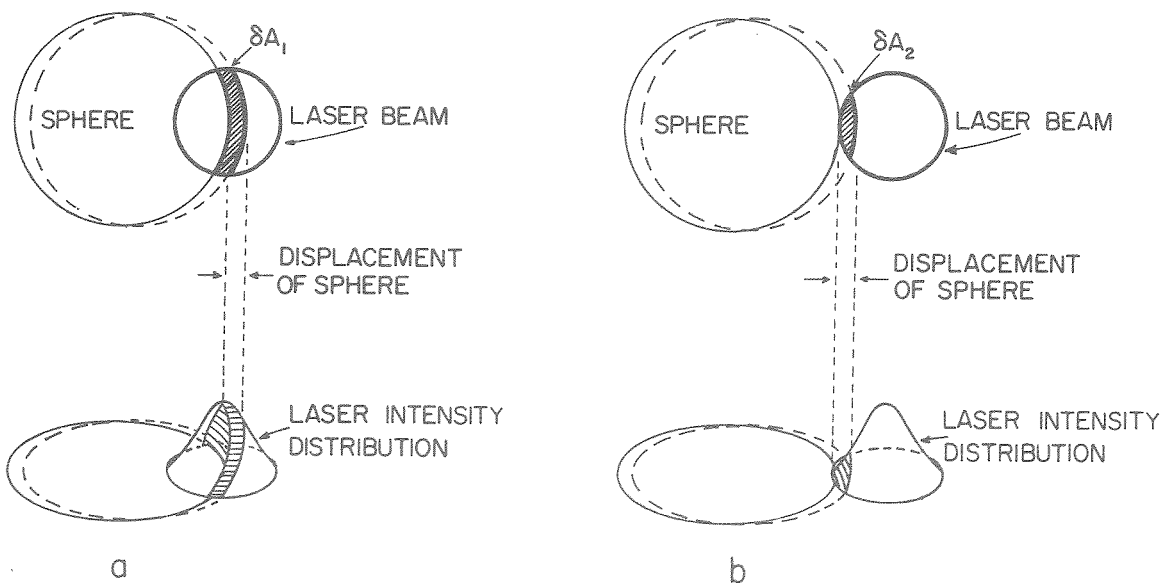

Fig. 4.15 Schematic drawing of a typical positioning of the laser beam with respect to the sphere; (a) large output signal of the system; (b) small output signal of the system (for the same displacement of the sphere).

It was positioned such that the path of the laser beam was partially blocked by the sphere. Displacement of the sphere in a direction across the laser beam caused a change in the amount of light received by the photo-cell and the change of voltage was indicated on a Sanborn (150 Series) recorder. The system was calibrated by moving the laser with the micrometer screw in steps of 0.005 in. relative to the sphere, and recording the corresponding changes in voltage. An example of a calibration record is shown in the lower right portion of Fig. 4.17.

In order to maximize sensitivity of the measurements, the laser was positioned such that the sphere blocked approximately half of the beam. The reasons for this are illustrated schematically in Fig. 4.15. The light intensity has a Gaussian distribution over the beam cross section so the maximum intensity is at the center of the beam. Also, the change in beam area δA_1 (see Fig. 4.15a) is maximum for a given displacement of the sphere when the sphere covers half the beam. As the amount of light is defined by the product of the light intensity and the area which it covers, the change of the amount of light (and hence the change of the output voltage of the photo cell) is maximum for a given displacement of the sphere when the sphere covers half of the beam.

During the experiment a wave gage was placed directly above the sphere as shown in Fig. 4.16. The motion of the sphere and the wave were recorded simultaneously on two channels. An example of a record is shown in Fig. 4.17. The record indicates the amount of motion and the time it took place with respect to the wave.

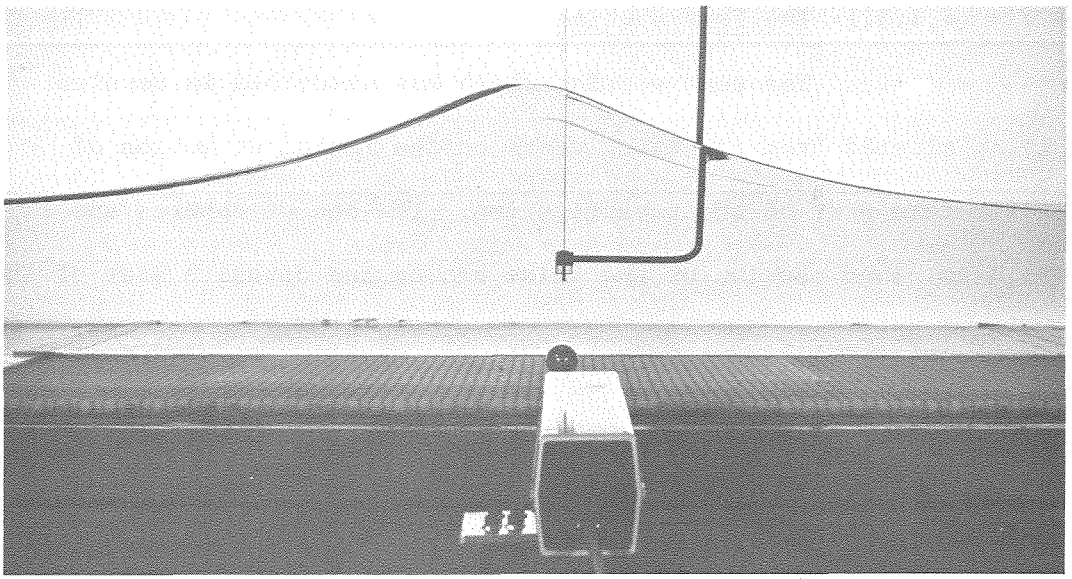

Fig. 4.16 View of the test section during an experiment.

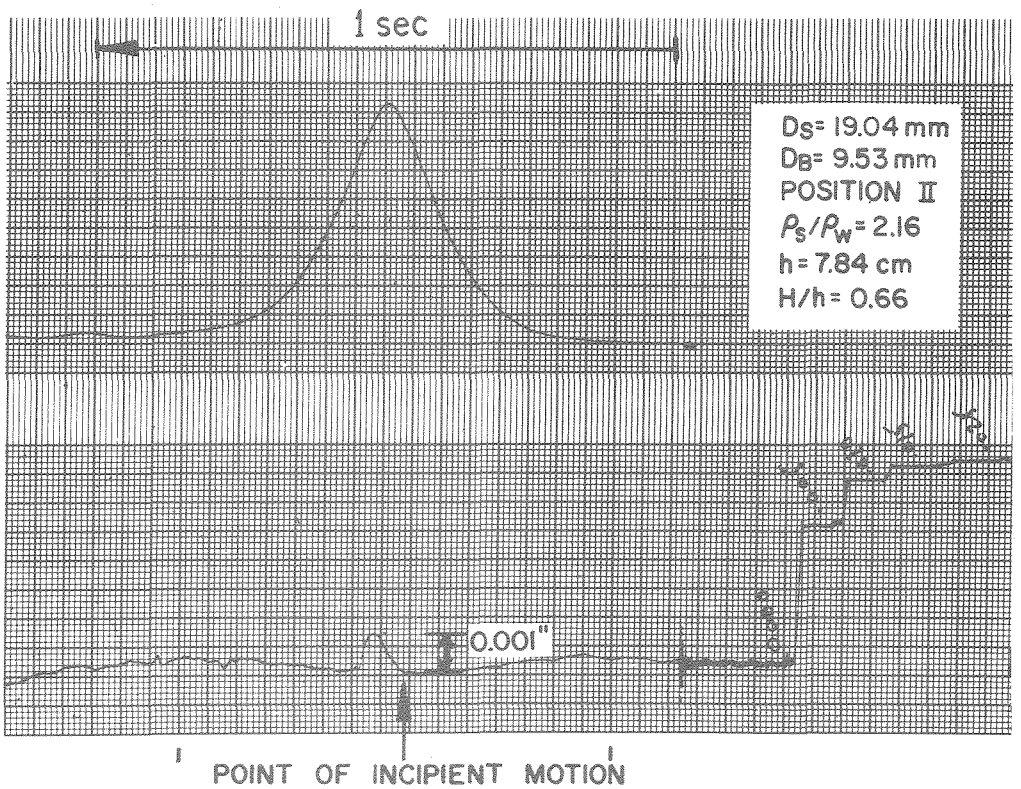

Fig. 4.17 Typical record of the motion of the sphere. Upper curve displays the wave record; lower curve displays the calibration and the motion of the sphere.

4.4.3 The Incipient Motion of Particles of Arbitrary Shape

4.4.3.1 The Test Section

The test section which was described in Section 4.4.2.1 was altered from the experiments on the incipient motion of spheres for this part of the investigation. The bed of spheres and a 3 ft (91.4 cm) long section of the false bed on the opposite side of the dividing wall were removed. The two gaps in the bottom on both sides of the partition were filled with two different size particles of arbitrary shape, resulting in layers 5/8 in. (15.9 mm) thick. The particles were leveled flush with the false bed using a straight edge. The test section is shown in Fig. 4.18. It seemed plausible to utilize both sides of the tank without being concerned about possible changes in the wave due to the bed effects since the experiments on solitary waves over spheres indicated no significant damping over the relatively short (3 ft) rough bed. The simultaneous use of two different size particles on both sides of the tank resulted in two experimental data points from the run of a single wave. Experiments were conducted with natural rock and with coal particles. During the experiments it was found that the wave reflected from the wave dissipator, although very small, was large enough to disturb the bed of the very light coal particles, hence two gates were constructed in front and behind the bed. The gates were closed immediately after the wave passed thus preventing the trailing and reflected waves from disturbing the bed.

4.4.3.2 The Characteristics of the Particles

The experiments were conducted using natural rock and anthracite coal. Two different size particles were used from each material.

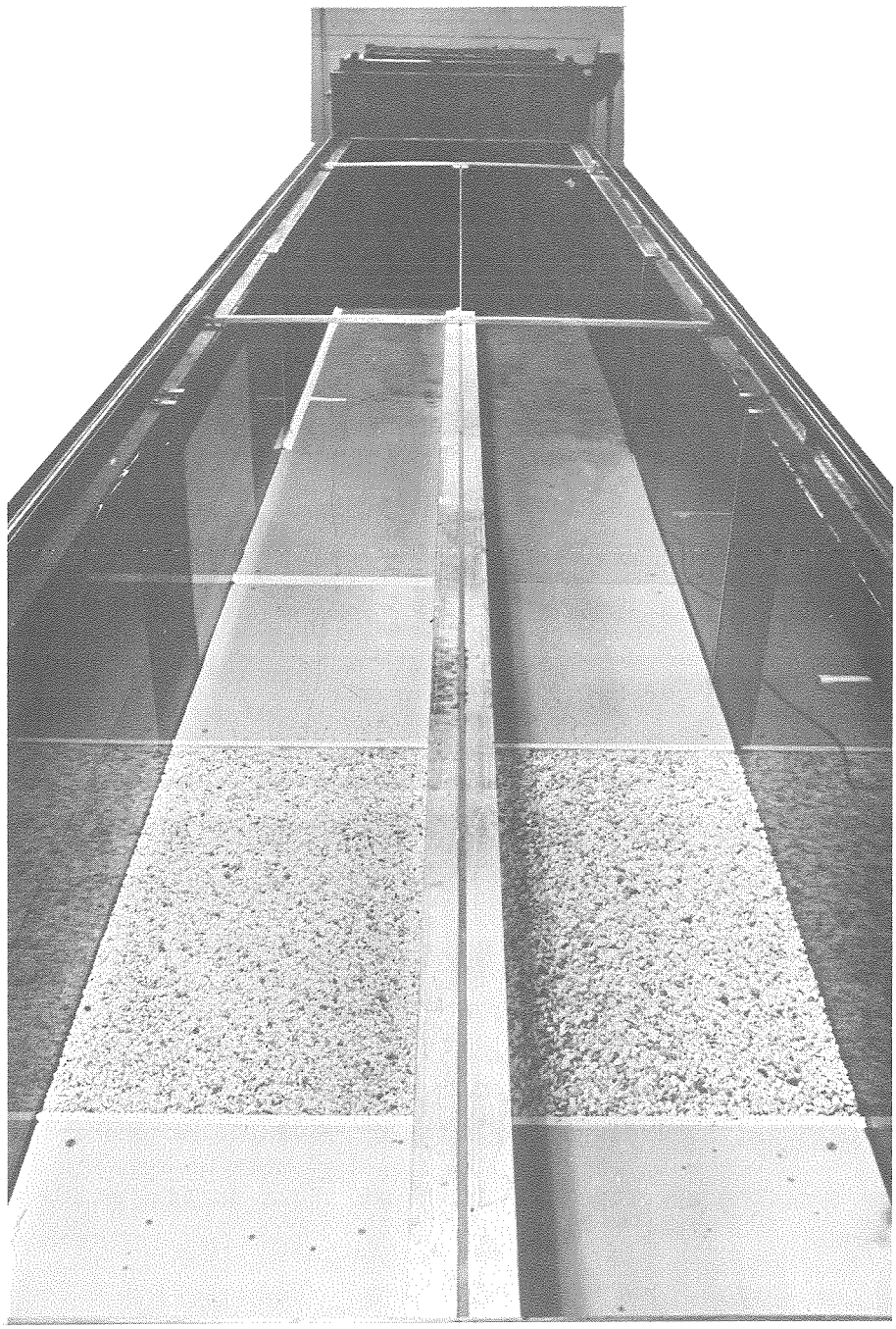

Fig. 4.18 View of the particles of arbitrary shape placed in the test section.

Eqs. (3.61) and (3.64) imply that the important characteristics of the rock are its mean diameter, D_s, its density, ρ_s, and its angle of friction, ϕ. The characteristics of each sample used in the experiments were measured as follows.

1. Diameter. The natural rock was purchased in a gravel form with a wide range of particle sizes. The coal was purchased in a form of large lumps and was crushed into a form similar to that of the natural rock. The particles were sorted by sieving them through a stack of screens. Each size fraction was used separately thus an approximately uniform size distribution was achieved. Each sample was sieve analyzed following the procedure described by Vanoni, Brooks and Kennedy (1961). The size distribution curves of the materials are shown in Fig. 4.19.

2. Density. The specific gravity of an object is obtained by dividing its weight in air by the difference between its weight in air and in water. A sample of 120 particles was chosen arbitrarily from the natural rock and their specific gravity was measured yielding a mean value of $\left(\frac{\rho_s}{\rho_w}\right)_{rock} = 2.68$ and a standard deviation of 0.036. The same procedure was repeated with 21 coal particles and the results were $\left(\frac{\rho_s}{\rho_w}\right)_{coal} = 1.283$ and a standard deviation of 0.023. The probability distributions of the specific gravities are shown in Fig. 4.20a and 4.20b.

3. Angle of repose. A special method was developed in order to measure the angle of friction of materials under water. The idea for this method was presented by Iribarren Cavanilles (1965) who measured the angle of friction of materials placed on a slope of a breakwater model. The system used here is shown in Fig. 4.21 and Fig. 4.22. A

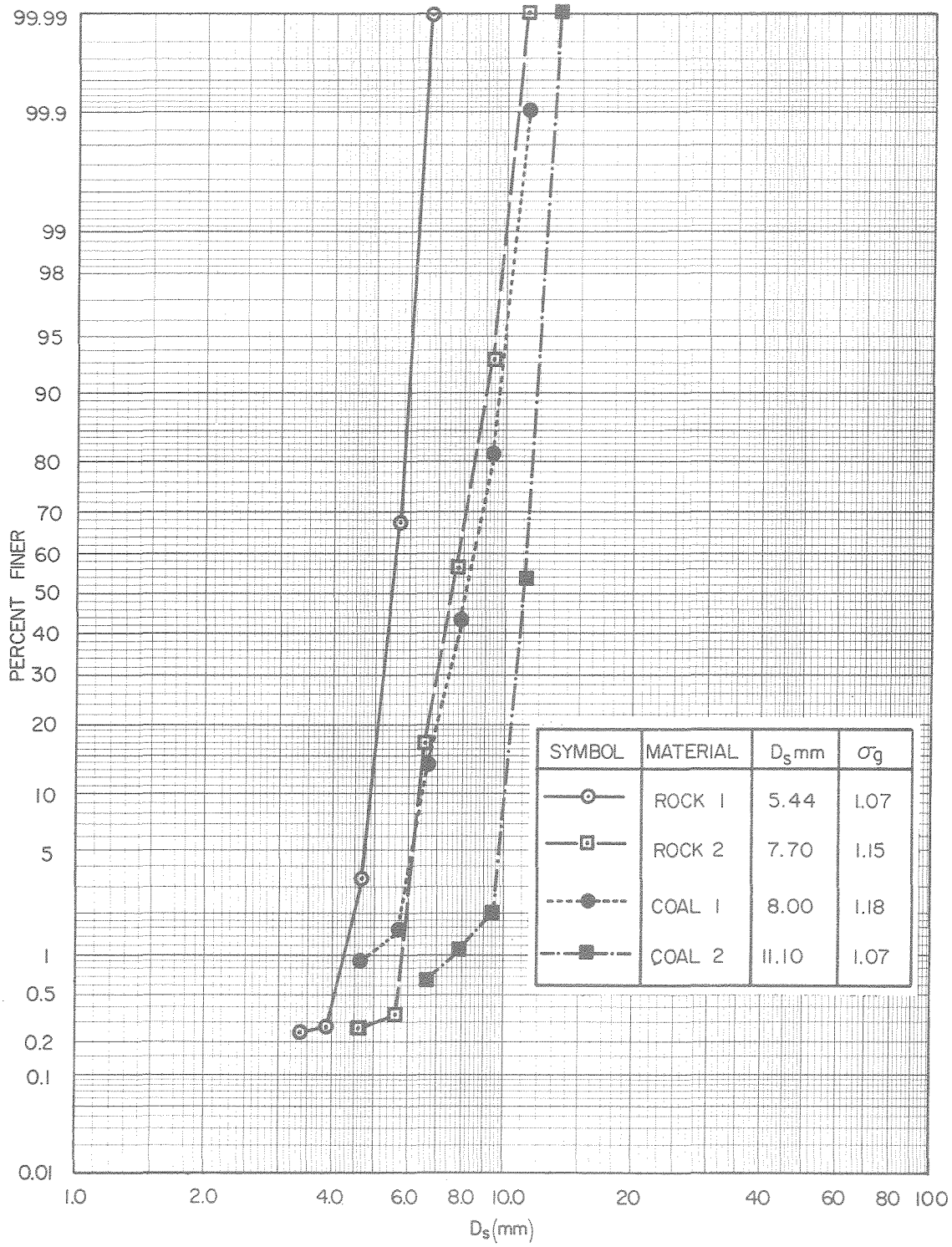

Fig. 4.19 Sieve size distribution curves of the particles of arbitrary shape used in the experiments of incipient motion.

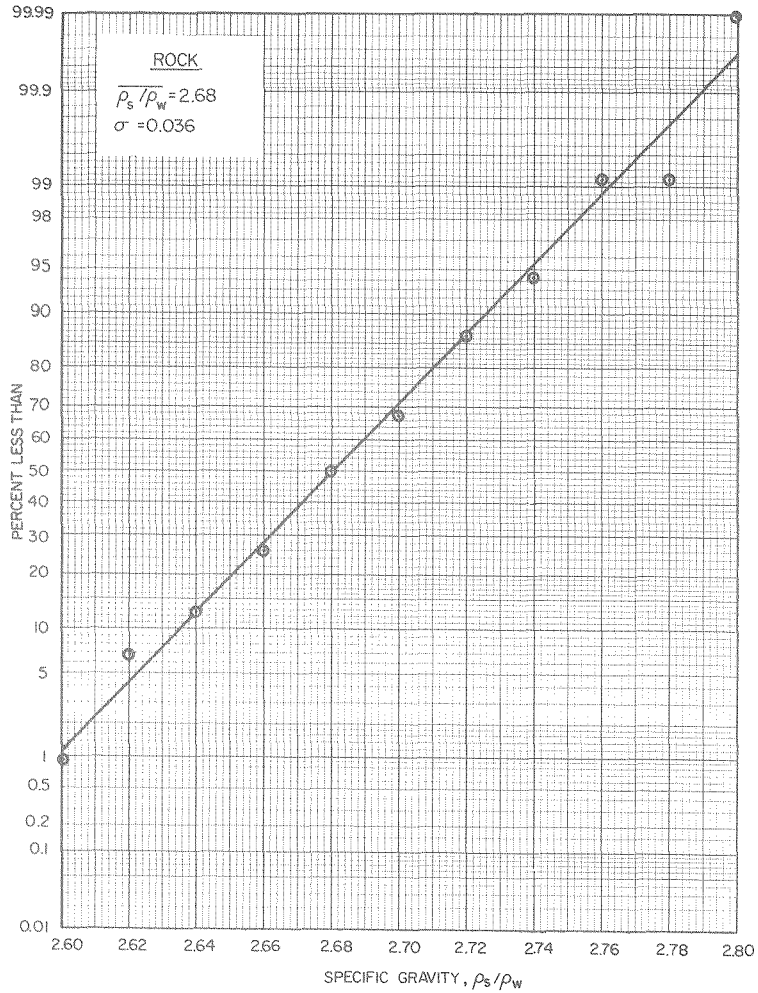

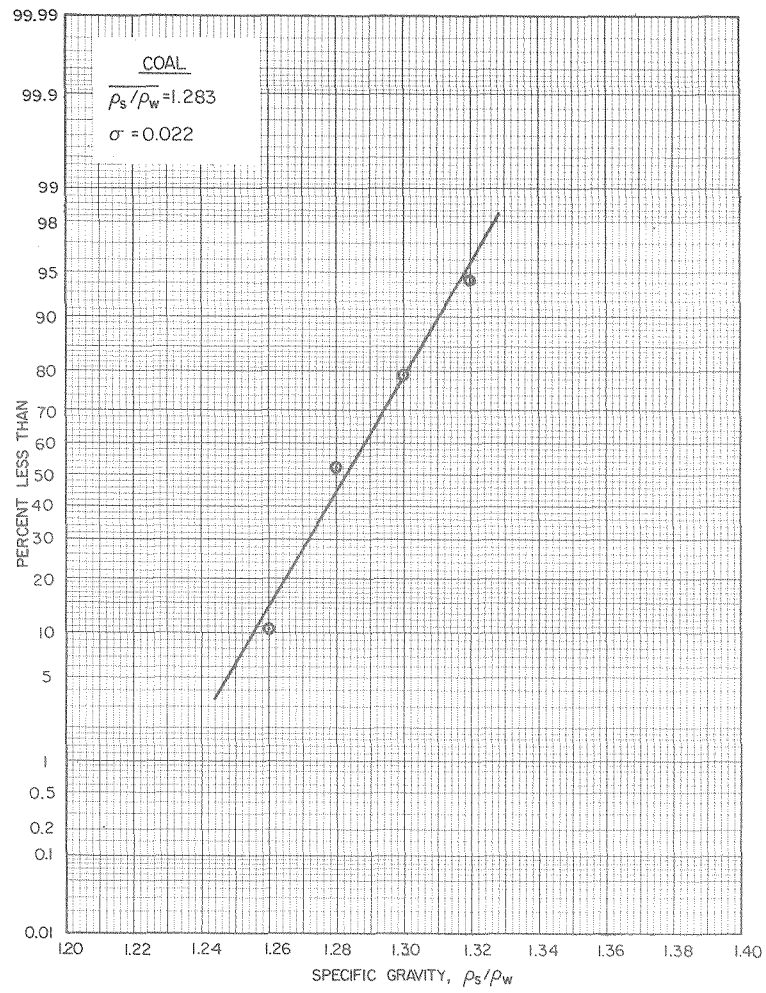

Fig. 4.20 Specific gravity distribution curves of the materials used in the experiments; (a) Natural rock, (b) Coal.

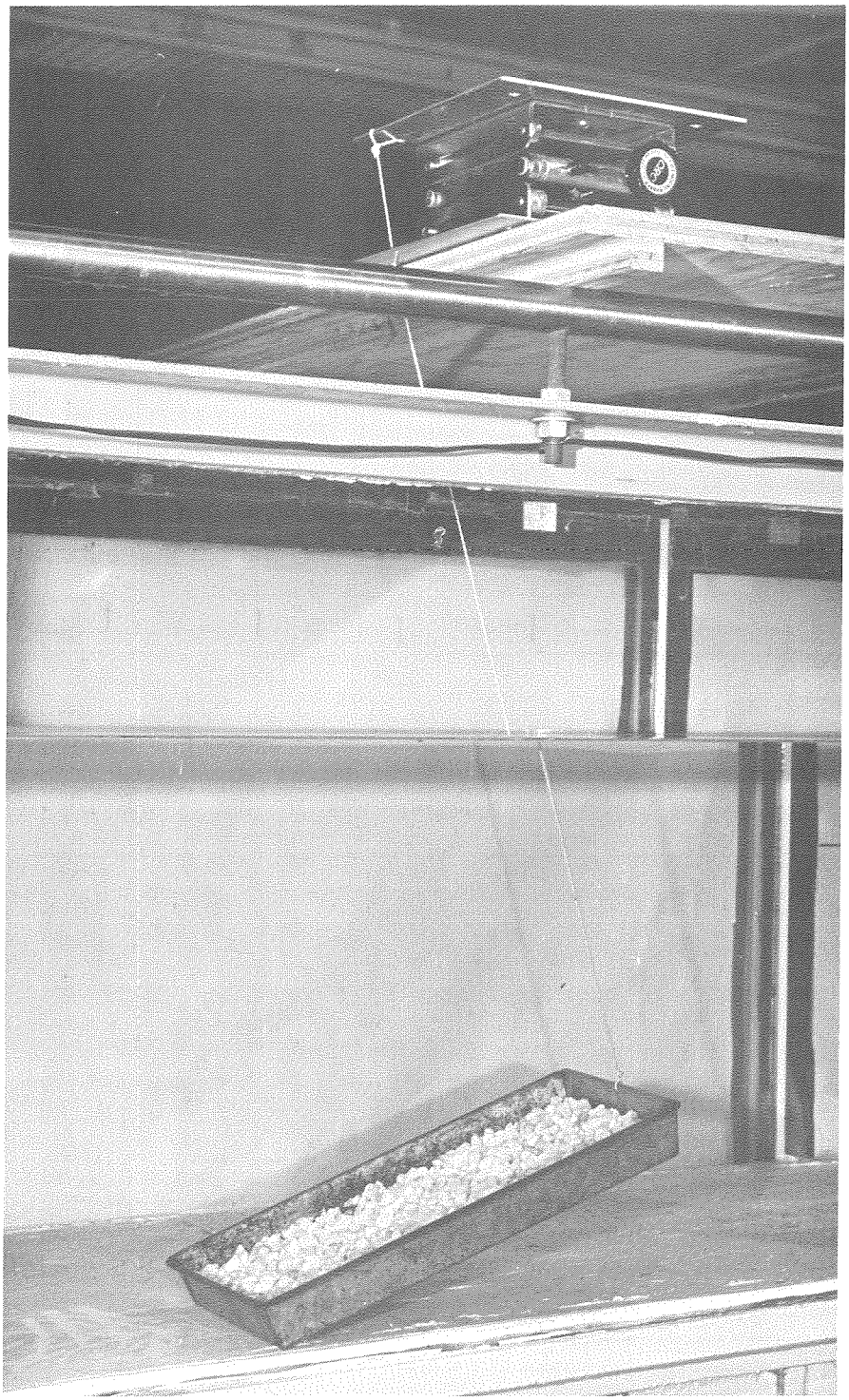

Fig. 4.21 Overall view of the system used to measure the angle of friction.

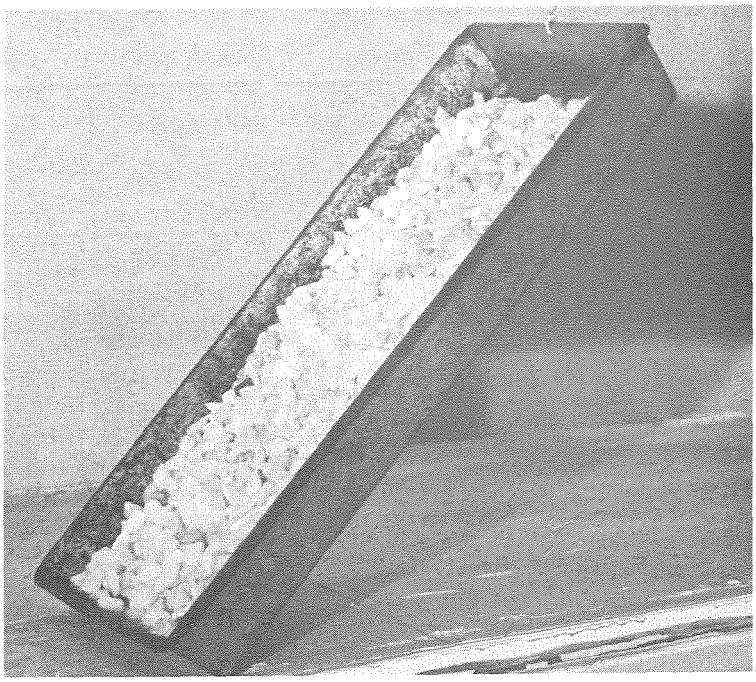

(a)

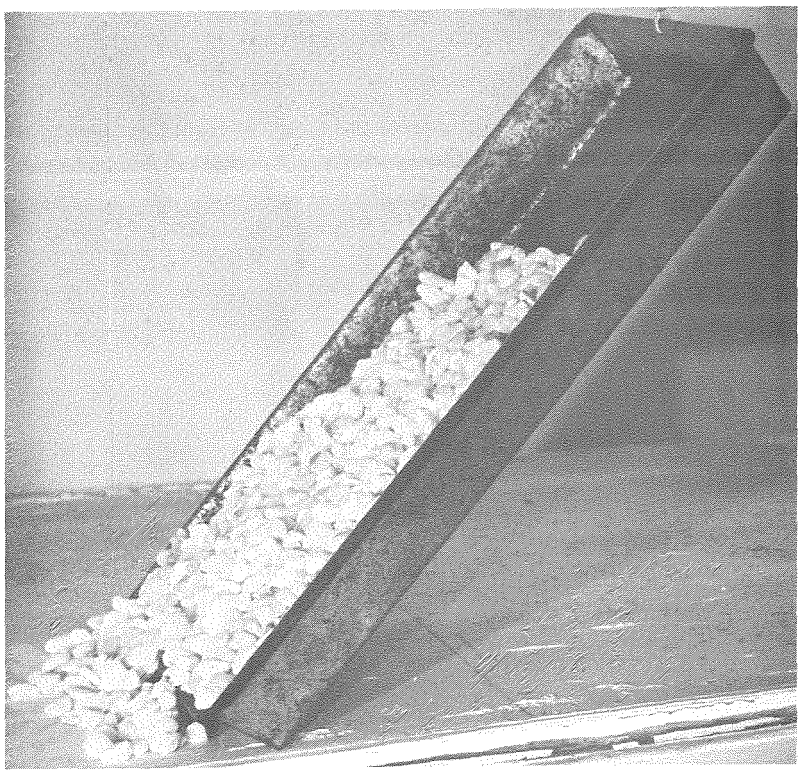

(b)

Fig. 4.22 View of the system used to measure the angle of friction at (a) the "packing" angle, and (b) the angle of "collapse".

tin tray measuring 13.5 x 8.5 x 1.5 in. (34.3 x 21.6 x 3.8 cm) was filled with a layer of gravel 5/8 in. (15.9 mm) deep and placed in a water tank next to its glass side wall. A string was tied to one of the 8.5 in. walls of the tray and was slowly pulled up by means of a crank-driven screw jack. The opposite side of the tray was kept in contact with the bottom of the water tank. The jack was used in order to provide a smooth uniform pull of the tray. The tray was pulled up until some motion of the particles was observed. At first the particles just seemed to pack up into a formation tighter than the loosely packed gravel (see Fig. 4.22a). The angle of the tray with respect to the horizon was noted for this case as the "packing angle". The tray was tilted more until the entire slope of gravel collapsed and the particles rolled down (see Fig. 4.22b). The angle of the tray was noted as the "angle of collapse". The measured angles of packing and collapse for the materials used in the investigation of incipient motion are presented in Table 4.1. The value of the angle of friction was identified here with some value between the packing and the collapse angles. This was based on the assumption that nondestructive waves traveling over a horizontal granular bed tend to pack the grains, but the packing is not as tight as that obtained by tilting the bed.

Table 4.1. The measured angles of packing and collapse for the materials used in the investigation of incipient motion.

Material	ρ_s/ρ_w Specific Gravity	D_s Mean Diameter (mm)	Packing Angle (deg)	Angle of Collapse (deg)
Natural Rock #1	2.68	5.44	40	50
Natural Rock #2	2.68	7.70	42	49
Coal #1	1.283	8.00	39	51
Coal #2	1.283	11.10	41	50

As can be seen in Table 4.1, all four materials used yielded a packing angle at approximately 40° and they collapsed at approximately 50°. Hence the angle of friction was assumed to be 45° throughout the investigation of incipient motion of arbitrary shape particles.

Shields (1936) noted that the dimensionless shear stress exerted on the bed involves a proportionality factor similar to the term $\tan\phi$ in Eq. (3.64). This term was assumed to be a function of the shape of the particles. The shape factor is defined as $S_f = d_a/\sqrt{d_b d_c}$ where d_a, d_b and d_c are three diameters of the particle in three orthogonal directions with d_a being the smallest and d_c being the largest possible diameters. All four materials used in the experiments consisted of angular particles. Fifty particles were randomly picked up from each sample and their shape factor was calculated after measuring them with a micrometer. The probability distributions of the shape factors are shown in Fig. 4.23 for all four samples. As can be seen in Fig. 4.23 all of the four materials had approximately the same mean value of the shape factor and about the same variance. This supports the employment of the same angle ϕ for all the materials used in the investigation of the incipient motion of particles of arbitrary shape.

4.4.3.3 The Measurement of the Motion of the Particles

The motion of the particles of arbitrary shape was measured using a photographic technique. The photographic equipment is shown in Fig. 4.24. A 4x5 in. Graphic camera with a back for 70 mm non-perforated roll film was mounted on a wooden frame supported by an instrument carriage on top of the wave tank. The camera was placed about 8 ft (2.4 m) above the bed at the center of the tank such that the complete

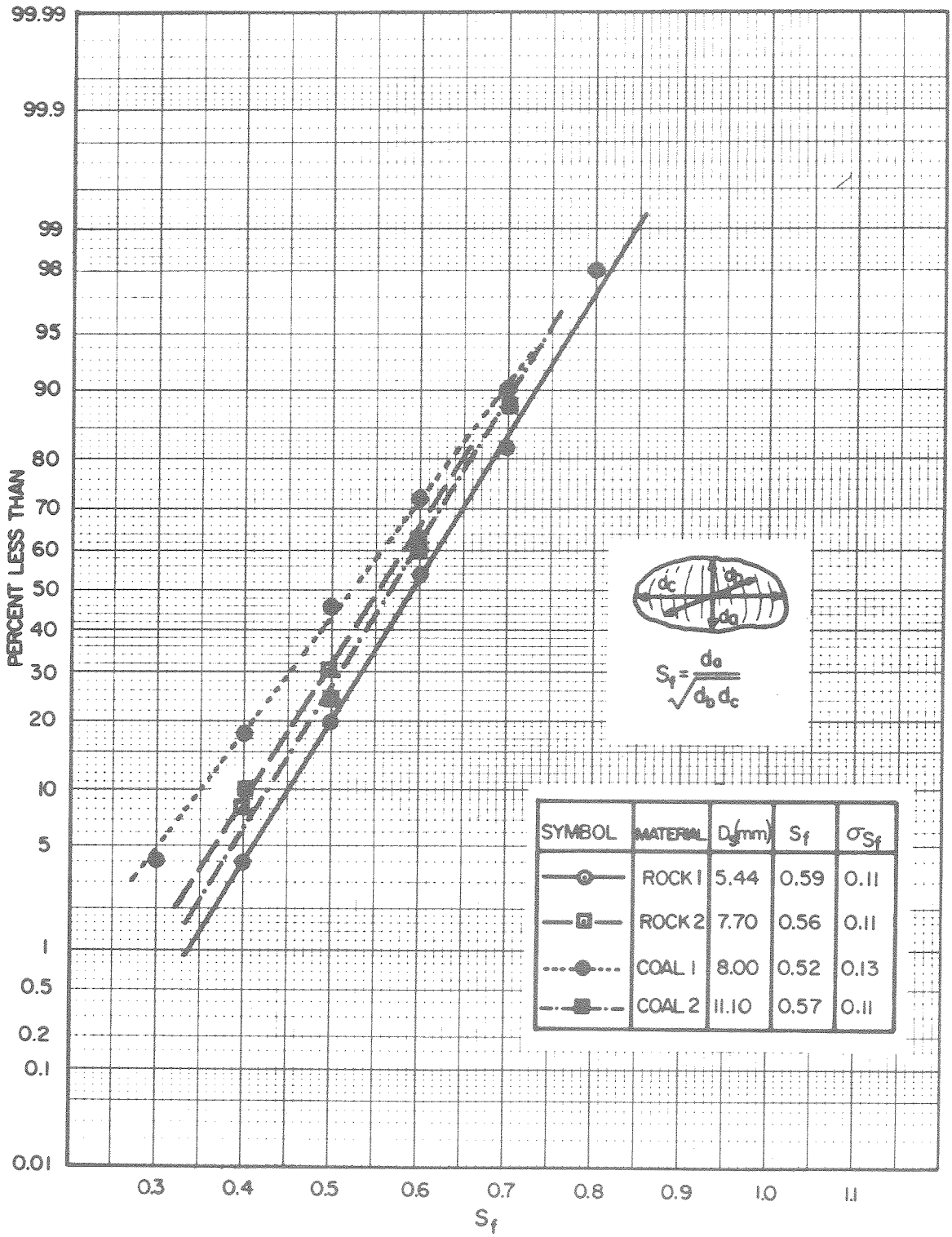

Fig. 4.23 Shape-factor distribution curves of the particles used in the experiments of incipient motion of particles of arbitrary shape.

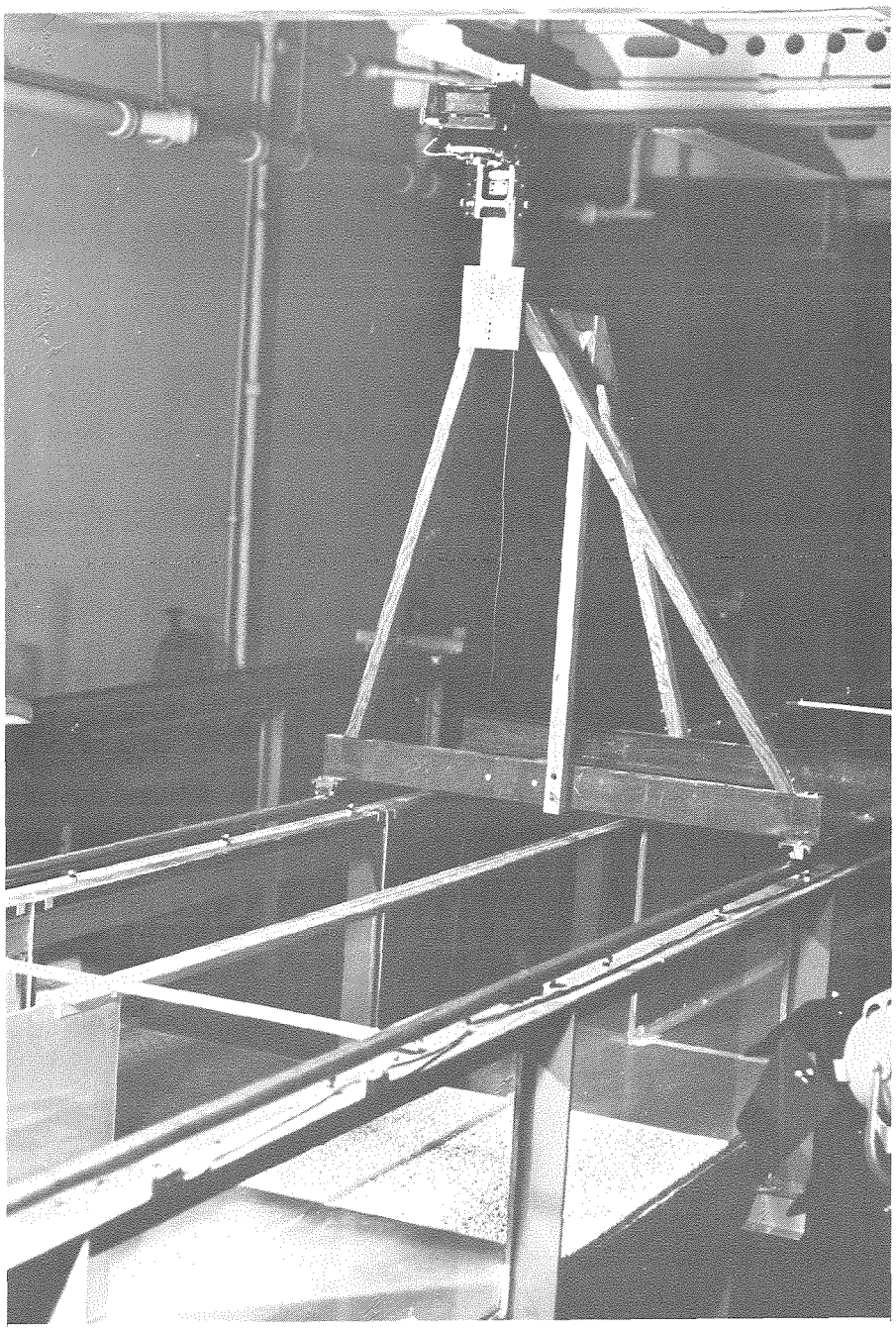

Fig. 4.24 View of the photographic equipment installed at the test section.

area on both sides of the bed was photographed simultaneously to a maximum magnification. Four studio lights were placed on both sides of the tank. Each light had photographic "barn doors" in front of its housing in order to attain even illumination.

A photograph of the bed was taken before running the wave, then an instrument carriage carrying a wave gage was brought above the bed and a wave was generated and recorded. Another picture was taken after the carriage with the wave gage was removed and the water was quiet again. The two pictures were compared to each other in order to indicate the motion of the particles. The comparison of the pictures was performed as follows.

A positive transparency was made from the negative with a 1:1 magnification (utilizing contact printing technique). The negative of the picture taken before the wave (Fig. 4.25a) was taped to a light table. The positive transparency taken after the wave (Fig. 4.25b) was taped to a piece of glass plate and placed on top of the negative forming a "sandwich". The two transparencies were aligned manually until a uniform dark surface was seen with only the particles that moved showing up. The method is based on the idea that a white particle with surrounding dark shadows forms a dark image with bright surroundings on the negative and a positive image on the transparency. When the positive and negative are aligned the dark image of the negative completes the bright positive picture and the bright negative surroundings complete the positive shadows, thus a continuous dark gray surface is obtained. If a particle is removed during the period between the two photographs, it appears in the negative in its place, but it does not

appear in the positive picture to complete the negative image. Hence only the particles that moved show up. Each particle can be seen twice; once as a dark image from the negative part and once as a bright spot from the positive part of the combination. The alignment of the two transparencies, whose pictures are shown in Figs. 5.25a,b, is shown in Fig. 5.25c. An enlargement of Fig. 4.25c is shown in Fig. 4.25d.

As can be seen in Fig. 4.25d, the two transparencies were not well aligned over the entire area. In fact, it was never possible to match the transparencies well throughout. There are probably two reasons for this: first, the pictures were taken through the water surface and a slight movement of the water could cause distortion due to refraction. To minimize this distortion, the second picture was taken when the water surface seemed still, at least 20 min. after running the wave. Each picture was used twice; once for the previous wave and once for the next one. The second reason is uneven shrinking of the film. The film used was ILFORD FP4 with acetate base which shrinks slightly after processing. Only glass plates are shrink-free, but the film was preferred because it was easier to handle. Films with estar thick base like KODAK EKTAPAN shrink much less than acetate base films, but they tend to buckle when dry, thus they cause another distortion since they do not keep flat while processing the transparencies and during the alignment process.

The transparencies were made of Dupont aerial film. Both the negative and the positive were tested for exposure and processing to provide good contrast that made it easier to see the particles that moved.

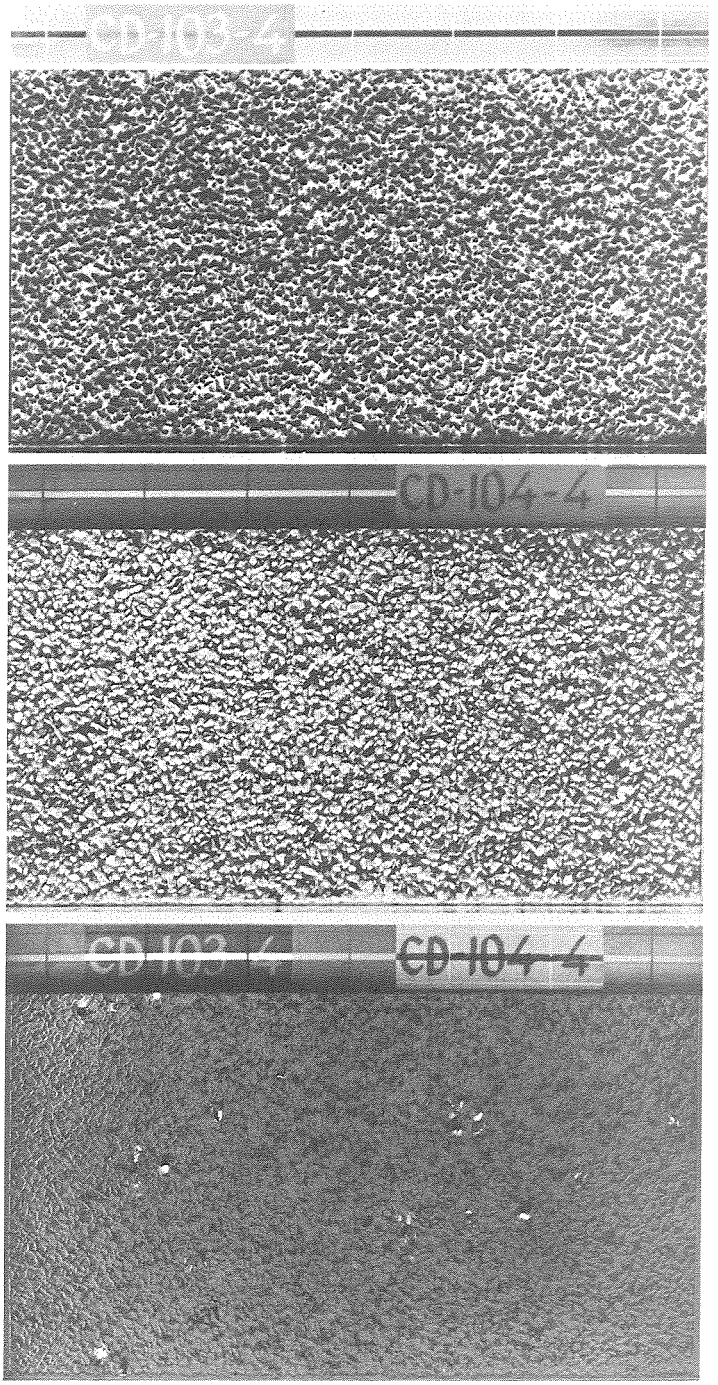

Fig. 4.25 Overhead photographs of the bed of particles of arbitrary shape; (a) negative picture of the bed before running the wave, (b) positive picture of the bed after running the wave, (c) alignment of pictures (a) and (b).

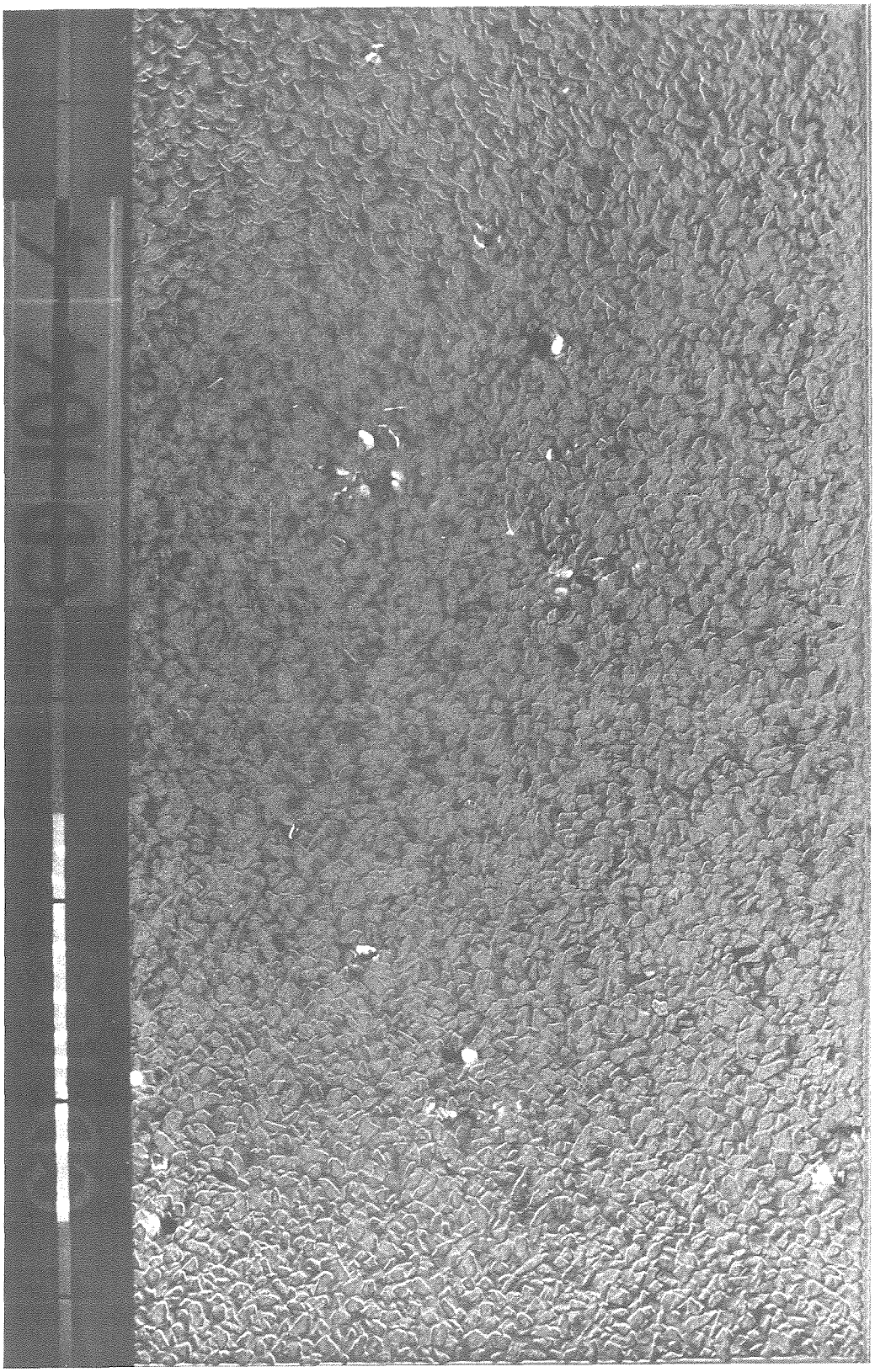

Fig. 4.25d Alignment of Figs. 5.25a and 5.25b (enlarged).

In order to avoid the problem of misalignment, the entire picture of the negative-positive combination was divided into small squares, each square occupying a small portion of the picture. Each square was aligned separately and inspected with a magnifying glass to maximize resolution. The amount of motion was obtained by counting the number of particles that moved in the entire picture.

The amount of motion was normalized by dividing the number of particles that moved by the total number of particles at the upper layer of the bed. In order to estimate the total number of particles, three screws, 5/8 in. (15.9 mm) long were glued to the bottom of the tank on either side of the partition wall. The heads of the screws (leveled with the surface of the bed) were marked with crosses and they were placed at three corners of a square measuring 10 x 10 cm. A portion of the picture of the bed including the screws was enlarged to the maximum magnification allowed by the available darkroom facilities, as shown in Fig. 4.26. An area of the picture was outlined and the number of particles N_{p_r} seen in this area was counted. The area A_{p_r} containing these particles was measured with a planimeter which was calibrated using the square outlined by the screws. The total area of the bed A_T that was covered by the camera was measured from the picture of the full bed (Fig. 4.25) which was scaled by its length (91.4 cm). The total number of particles N_{p_T} exposed to the flow was estimated as $N_{p_T} = \frac{A_T N_{p_r}}{A_{p_r}}$. The values of N_{p_T} for the materials used in the investigation are presented in Appendix II, Table A.2.3.

4.5 THE MEASUREMENT OF FLUID PARTICLE VELOCITY

Motion picture photography was applied in the measurement of the

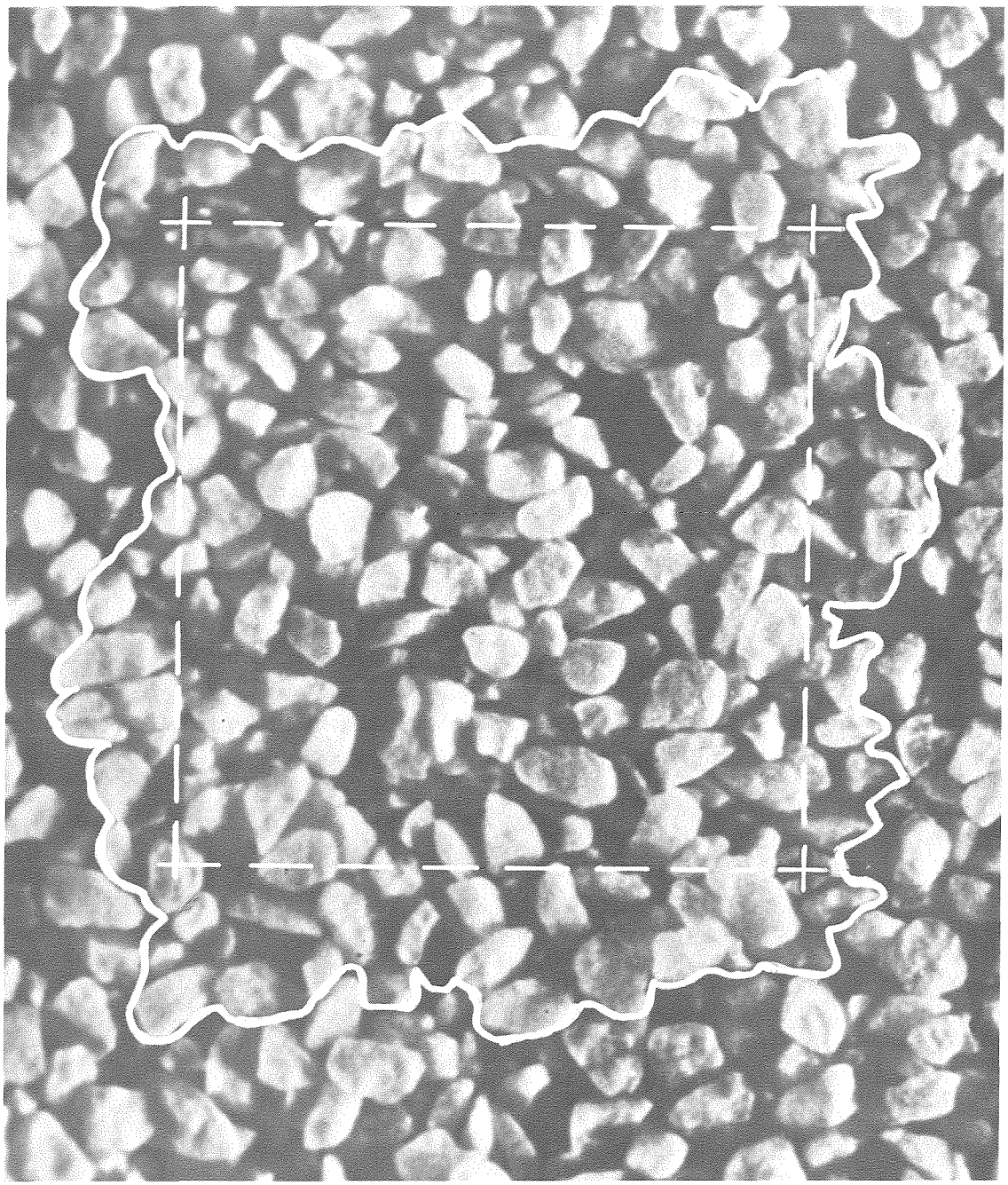

Fig. 4.26 Photograph of the section of the bed used to estimate the total number of particles seen in the overhead view of the entire test section.

fluid particle velocity over a rough bed under solitary waves. The flow was visualized using neutrally buoyant particles produced from a mixture of carbon-tetrachloride, mineral oil and blue oil dye. The proportions of the three ingredients were adjusted by trial so that a droplet of liquid tracer would neither rise nor settle in a sample of water from the wave tank. The mixture was injected instantaneously using a hypodermic syringe with a needle inner diameter of 0.0225 in. (0.57 mm). The impulsive injection broke the liquid into small droplets ranging in size from a fraction of a millimeter to approximately 3 mm. The droplets formed a cloud that was photographed under the wave.

The photography equipment consisted of a 16 mm motion picture camera with seven filming speeds ranging from 12 to 64 frames per second. The camera, shown schematically in Fig. 4.27, was mounted on a tripod next to the tank approximately 1.5 ft (45 cm) from its side wall at the level of the bed. The wall on the other side of the tank was covered with translucent paper and illuminated with two studio lights in order to have a good distinction of the particles against the background. The test section in the tank was also illuminated with two lights.

The filming speed was set at 64 frames/sec. However, this figure was inconsistent and inaccurate. In order to precisely measure the filming speed the timing component shown schematically in Fig. 4.27 was added to the system. A Beckman counter (Model 7351) was used to generate electric pulses at a rate of 100 pulses per second. The pulses were counted and displayed by a Hewlett-Packard (Series 5300A) counter, and the display was transmitted to the camera by a set of mirrors. If the counter display showing in one picture is t_1 and after N_f frames it shows t_2, and the pulse rate is P_r pulses/sec, then the time interval

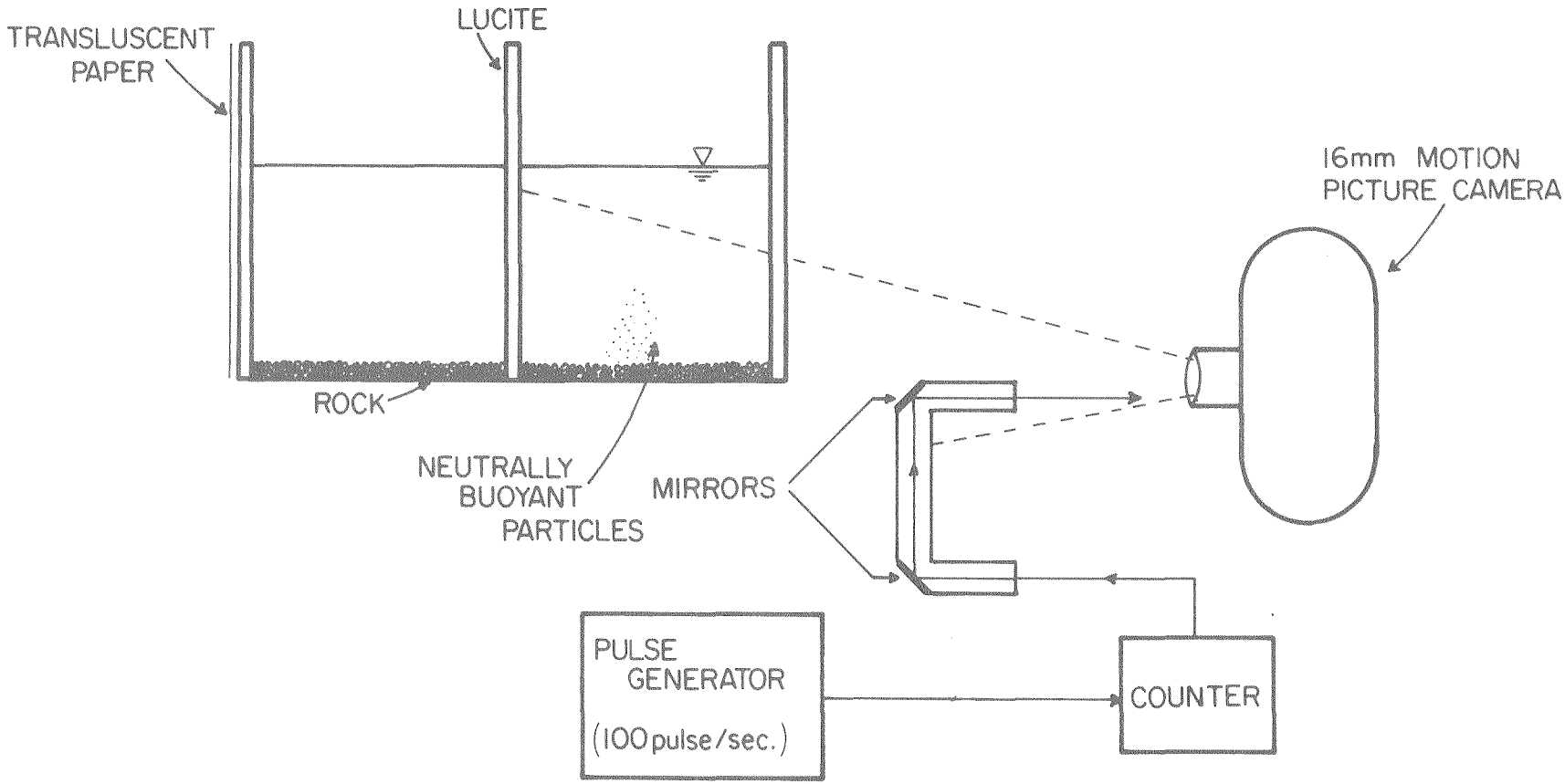

Fig. 4.27 Schematic drawing of the system used to measure the fluid particle velocity.

between two frames is $\Delta t = \frac{t_2 - t_1}{N_f P_r}$.

Another component was added to the systems in order to synchronize the film with the wave record. A flash bulb was mounted beside the camera aiming at the wave tank. An electric switch activated the flash bulb and at the same time recorded a mark on the wave record. The film frame at which the flash bulb flashed was easily identified since it was much brighter than the rest of the film. The time of this frame was identified with the mark on the wave record. Thus any film frame could be related to the instant at which it took place under the wave.

The experimental procedure was as follows. The two scales shown in Fig. 4.28, one horizontal and one vertical, were inserted in the tank and photographed before the experiment. The reason for having both horizontal and vertical scales was to account for possible distortion in the picture. After taking the picture of the scales they were removed and the wave gage was calibrated. The liquid tracer was injected into the water after the wave gage was calibrated, and the wave was generated immediately afterwards. The reason for following the procedure in this order was that the mixture of the tracer was not absolutely homogeneous. There usually were some particles in the cloud of buoyant tracer that rose up and settled on the wires of the wave gage thus interfering with its calibration. With the above procedure the experiment was completed before this process could take place. The injection of the tracer particles did not seem to disturb the flow field, since by the time that the wave arrived at the test section, the disturbance had been damped, as the tracer appeared to be quiescent.

The velocity measurements were conducted as follows. Two 8 x 10 in.

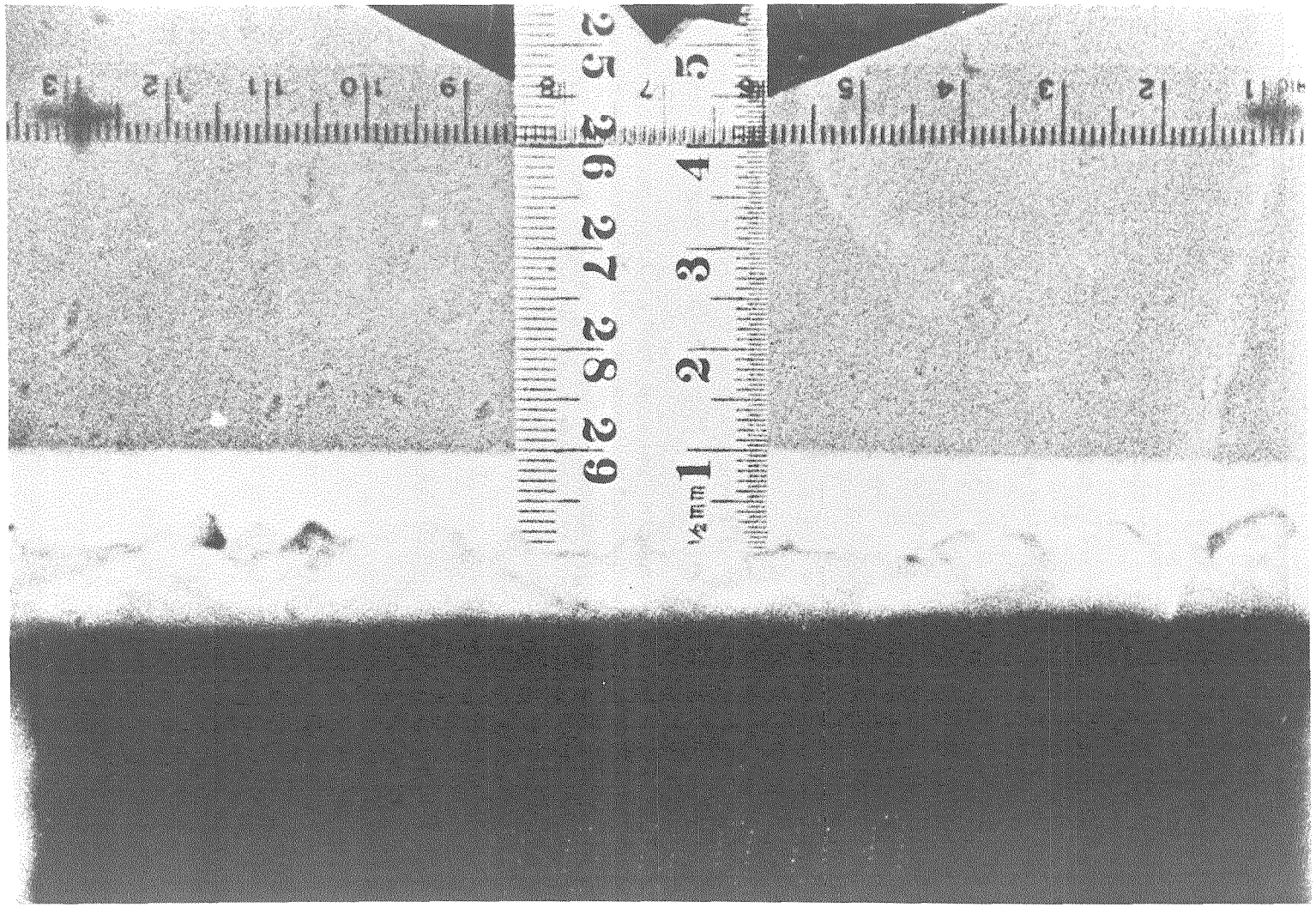

Fig. 4.28 The scale used to measure the displacements of tracer particles.

(20 x 25 cm) transparencies (shown in Fig. 4.29a,b reduced in size) were made from two adjacent frames of the 16 mm film. The transparencies were aligned on a light table to form the picture shown in Fig. 4.29c. An enlargement of Fig. 4.29c, to scale with Fig. 4.28, is shown in Fig. 4.29d. Each tracer droplet was seen twice; once on one transparency and once on the other. The displacement $\Delta\xi$ that this particle had moved was measured using a grid produced from the photograph of the scales (Fig. 4.28). The time Δt between the two transparencies was calculated from the digital display and the fluid particle velocity $u = \frac{\Delta\xi}{\Delta t}$ was calculated. The calculated value of u was an average over the period Δt. However, when the film speed was large enough (64 frames/sec), the time increment Δt was small enough to approach the instantaneous value of $u = \frac{d\xi}{dt}$.

The coordinate X of a particle was evaluated from measurement of the distance x of the particle from the center of the picture (using the photograph of the scales) and the time t with respect to the wave crest (using the digital time display and the synchronization with the wave record). Measurement of the wave speed C provided $X = x-Ct$. The vertical coordinate z of each particle was noted using the vertical scale.

Experiments were conducted in water 30 cm deep and a wave 15 cm high. The roughness of the bed consisted of the 7.70 mm white rock that was used in the investigation of incipient motion of rocks (presented in Section 4.4.3).

4.6 MEASUREMENTS OF BOTTOM RESISTANCE COEFFICIENT UNDER SOLITARY WAVES

The experiments were performed in the wave tank with a smooth bottom and with rough bottoms of two different size roughnesses. The

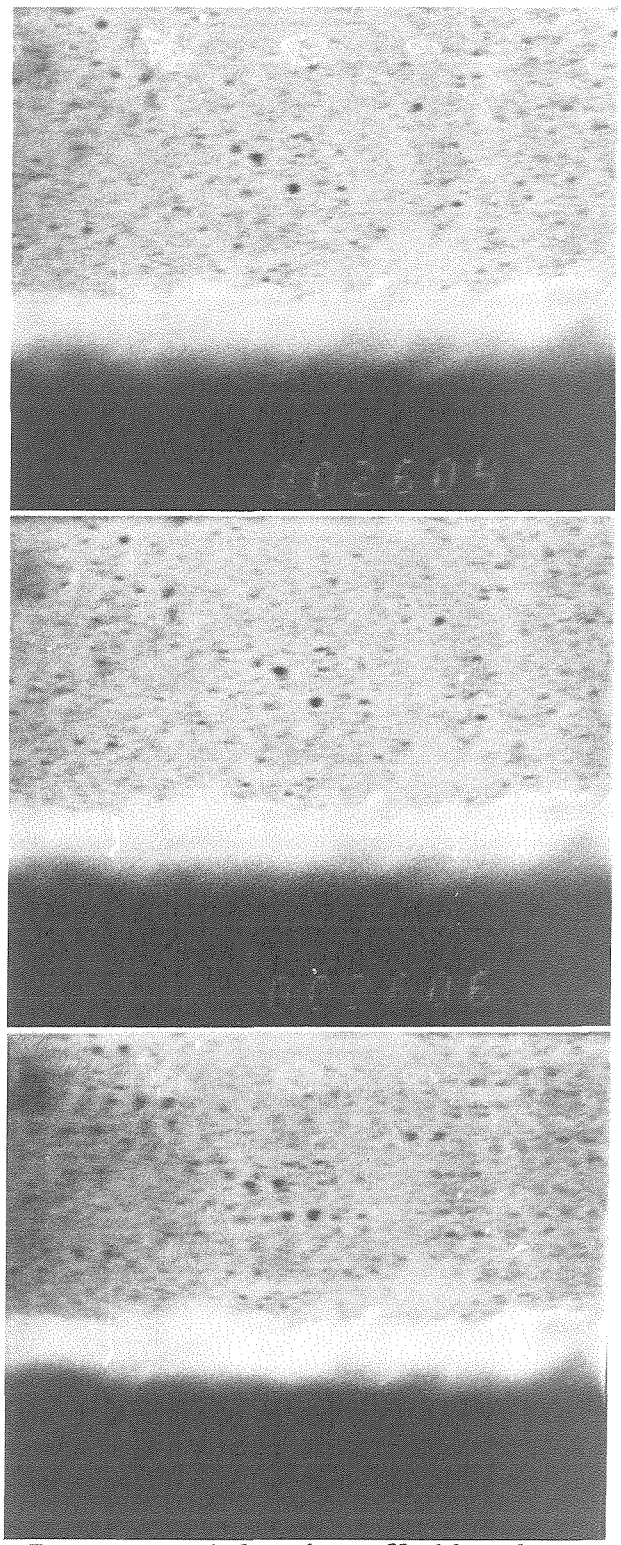

(a)

(b)

(c)

Fig. 4.29 Tracer particles in a fluid under a solitary wave; (a) at t=26.04 sec; (b) at t=26.06 sec; (c) alignment of (a) and (b).

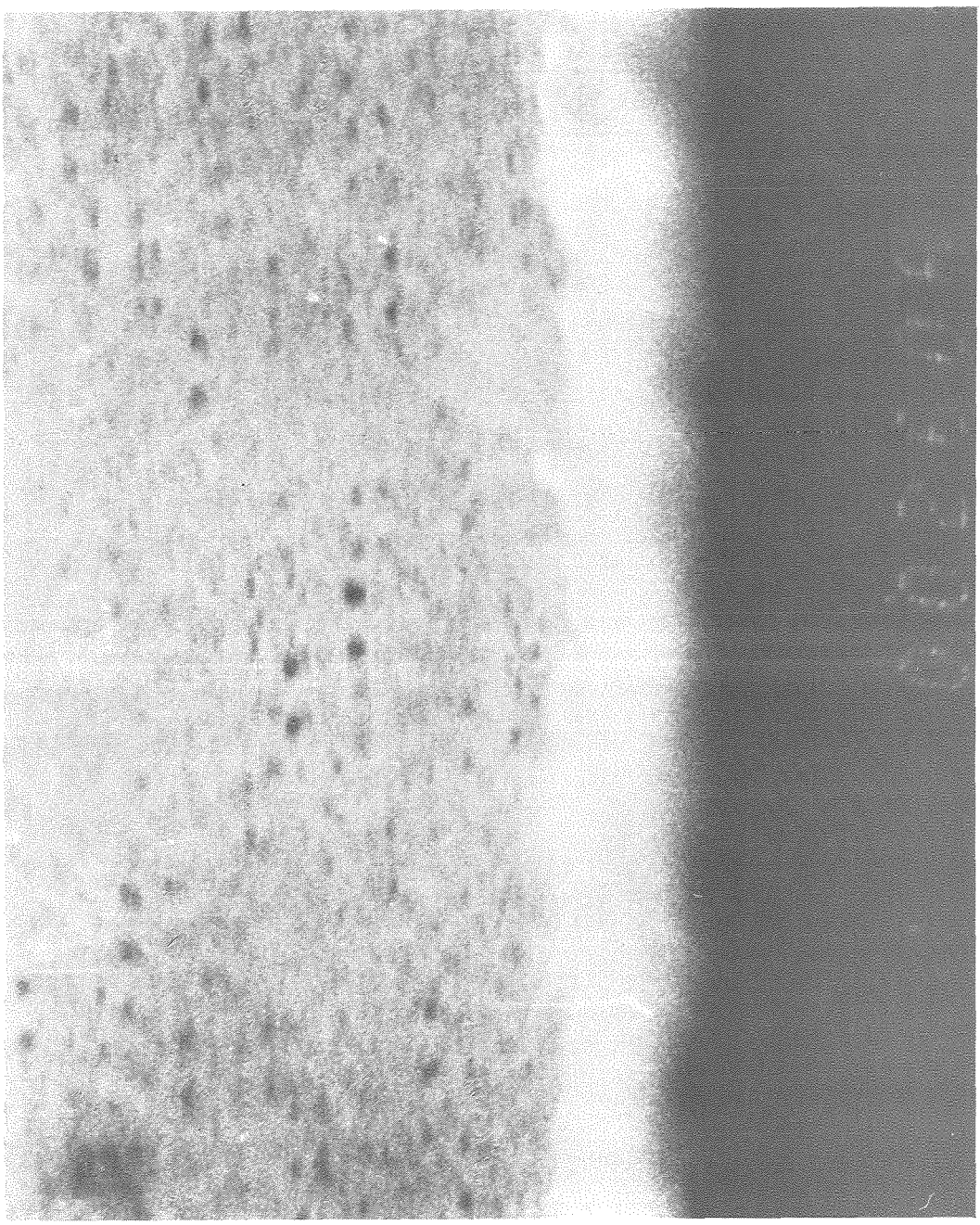

Fig. 4.29d Alignment of Figs. 4.29a and 4.29b (enlarged to scale with Fig. 4.28).

experiments with a smooth bottom were conducted in the tank as described in Section 4.1. The rough bottom consisted of a 5/8 in. (15.9 mm) layer of gravel placed between two sections of the false bottom described in Section 4.4.1. A 36 ft (10.97 m) long section of the false bottom was placed in the tank 3 ft (75 cm) from the wave generator and a 5 ft (1.52 m) section was placed at the wave dissipator. The remaining 76.5 ft (23.32 m) portion of the tank between the false bottom sections was filled with gravel. The gravel was leveled flush with the false bottom applying the following procedure: two pieces of plywood 5/8 in. (15.9 mm) high and 42.5 in. (109 cm) long were placed across the tank on its bottom spaced at about 3 ft (90 cm). The gravel was placed between the plywood bars and was leveled with their tops using a straight edge. The next step was to level an additional section approximately 3 ft long using the same technique. When two adjacent sections were leveled, the plywood bar between them was removed and the space it had occupied was manually filled and leveled to provide a continuous surface of the rough bed. The process continued step by step until the entire space between the false bottoms was covered with rocks.

The gravels used were size fractions obtained from sieving a large amount of graded rock. The two size fractions used were sieve analyzed. Their size distributions are shown in Fig. 4.30.

Four wave gages with platinum wires (as described in Section 4.3) were used to record the wave at four stations over the rough bed in order to measure the reduction of wave height along the tank. The gages were mounted on instrument carriages starting 11 ft (3.30 m) downstream from the beginning of the rough bed and spaced approximately at 20 ft

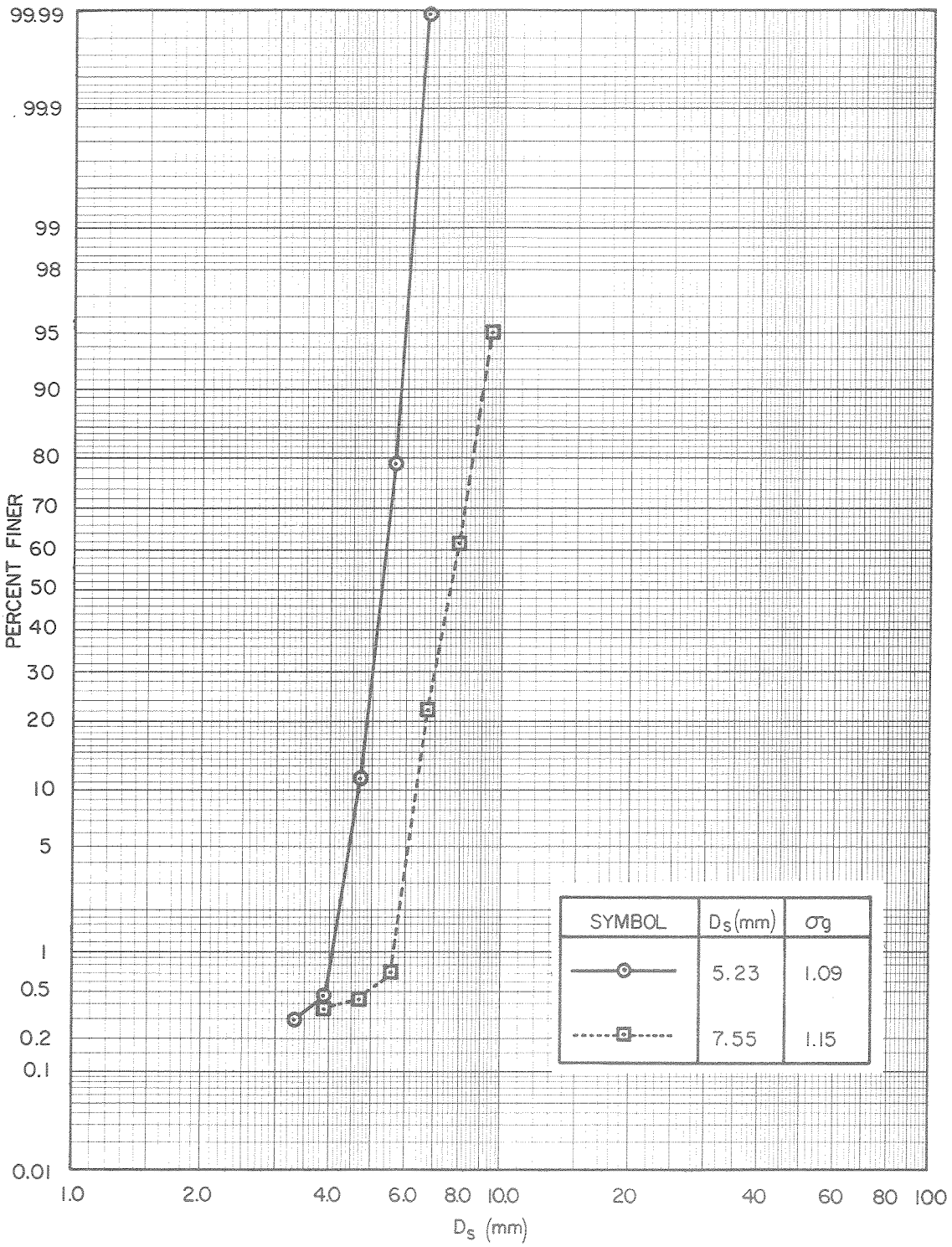

Fig. 4.30 Sieve size distribution curves of the rock used in the experiments of wave attenuation.

(6.10 m), with the distances between them carefully measured. The wave height at each of the four stations was used to evaluate the value of $\frac{d(H/h)}{d(x/h)}$ required (in Eq. 3.36) to calculate the bed friction factor.

All the experiments were performed with the wave tank in a horizontal position.

CHAPTER 5

PRESENTATION AND DISCUSSION OF RESULTS

5.1 THE SOLITARY WAVE

5.1.1 The Wave Profile

The surface profiles, the wave celerities, and the fluid particle velocities of solitary waves were measured in the laboratory to determine which of the three theories presented in Section 3.1 (i.e., Boussinesq (1872), McCowan (1891), and Laitone (1963)) should be used in conjunction with the investigation of incipient motion of bed material. Results of the measurements of the surface profile are presented in this section. The results of the measurements of the wave celerity and the fluid particle velocity are presented in Sections 5.1.2 and 5.1.3 respectively.

The wave tank was divided longitudinally into two. The test section of a bed of spheres was placed on one side of the partition, while the other side was kept smooth. A description of the bed of spheres is given in Section 4.4.2, and the smooth bottom is described in Section 4.4.1. Wave profiles which were measured over the test section with the wave tank in a horizontal position were compared to waves measured over the other side of the partition in order to test the effects of the rough bed section on wave damping. Wave profiles were obtained also over a sloping bottom. Comparisons of the measured wave profiles to the theoretical profiles are presented in Figs. 5.1, 5.2, and 5.3 for waves over a horizontal bottom, and in Figs. 5.4, 5.5, and 5.6 for waves propagating over a slope of 0.5% (1 vertical to 200 horizontal).

The profile of a wave with a height-to-depth ratio of 0.086 traveling over a bed of spheres (D_B = 12.7 mm) in a depth of 10 cm with the wave tank in a horizontal position is shown in Fig. 5.1. The abscissa is $\frac{X}{h}\sqrt{\frac{3H}{4h}}$ and the ordinate is η/h, where X is a coordinate system moving with the wave (X = x-Ct, where x is a stationary horizontal coordinate, C is the wave speed, and t is the time), h is the water depth, H is the wave height, η is the elevation of the water surface above still water level, and D_B is the diameter of the bed spheres. As can be seen in Fig. 5.1, the differences among the wave profiles obtained from the theories of Boussinesq, McCowan, and Laitone are negligible for the value of H/h in this figure. The experimental wave profile agrees well with the theories over the major part of the wave, from $\frac{X}{h}\sqrt{\frac{3H}{4h}} = -1.0$ to $\frac{X}{h}\sqrt{\frac{3H}{4h}} \cong 3.0$, and it deviates from the theories near the trailing edge of the wave. This disagreement is probably due to the trailing wave system which is generated by the type of the wave generator used. The (calculated) time displacement history of the wave generator does not follow exactly the fluid particle displacement under a solitary wave (see Fig. 4.4), thus generating additional oscillatory waves. Under these conditions, where H/h is small, the celerity of the solitary wave is not great enough to leave the oscillatory waves too far behind by the time it travels over the test section.

The profiles of the solitary waves over smooth bottoms are compared to the profiles over rough beds in Fig. 5.2 for a wave of H/h = 0.34 in 30 cm of water, and in Fig. 5.3 for a wave of H/h = 0.64 in water 10 cm deep. The experimental results show no significant difference between

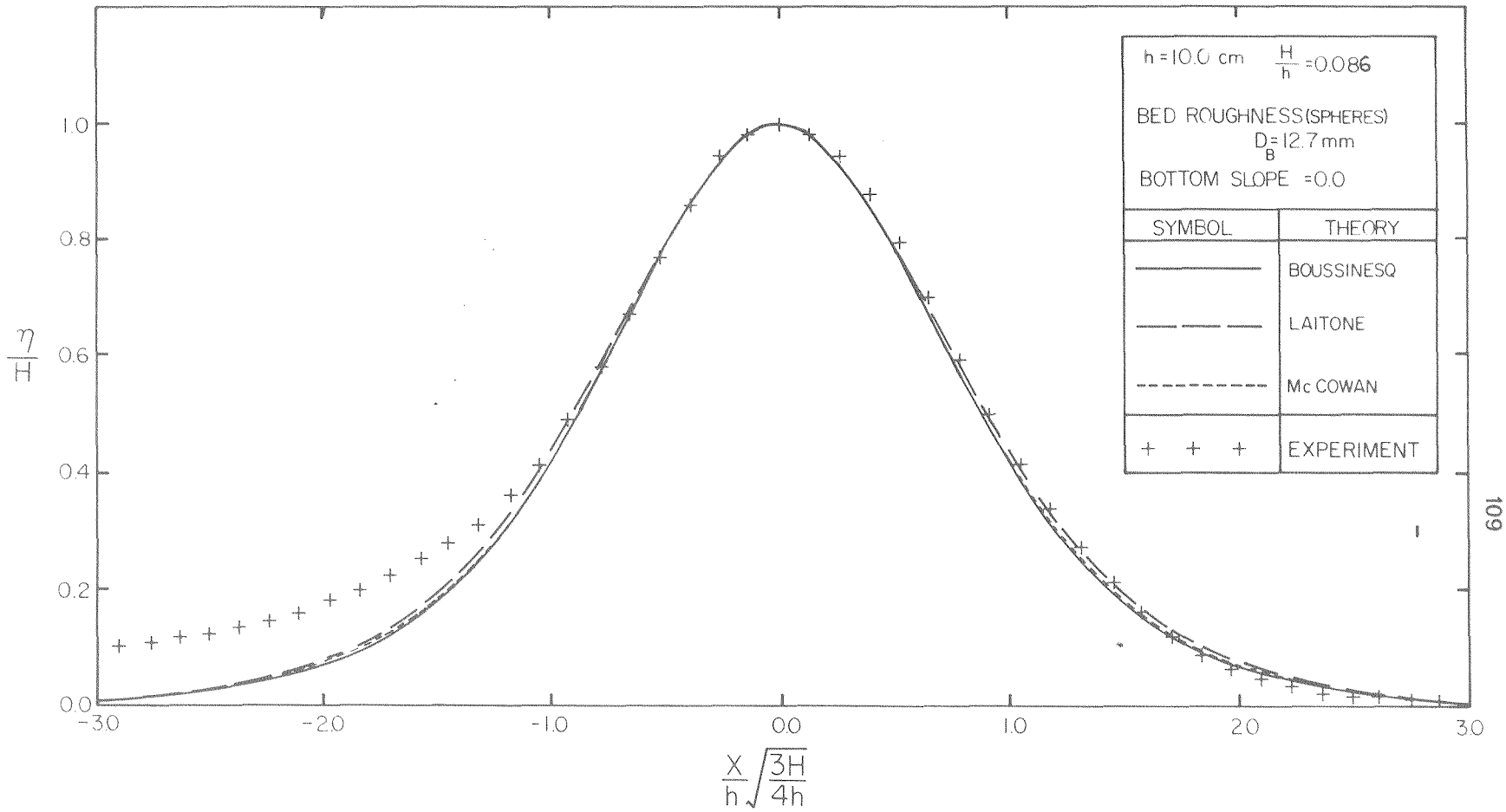

Fig. 5.1 Comparison between a measured solitary wave and between the theories of Boussinesq, McCowan, and Laitone; h=10.0 cm; H/h=0.086; bottom slope=0.0.

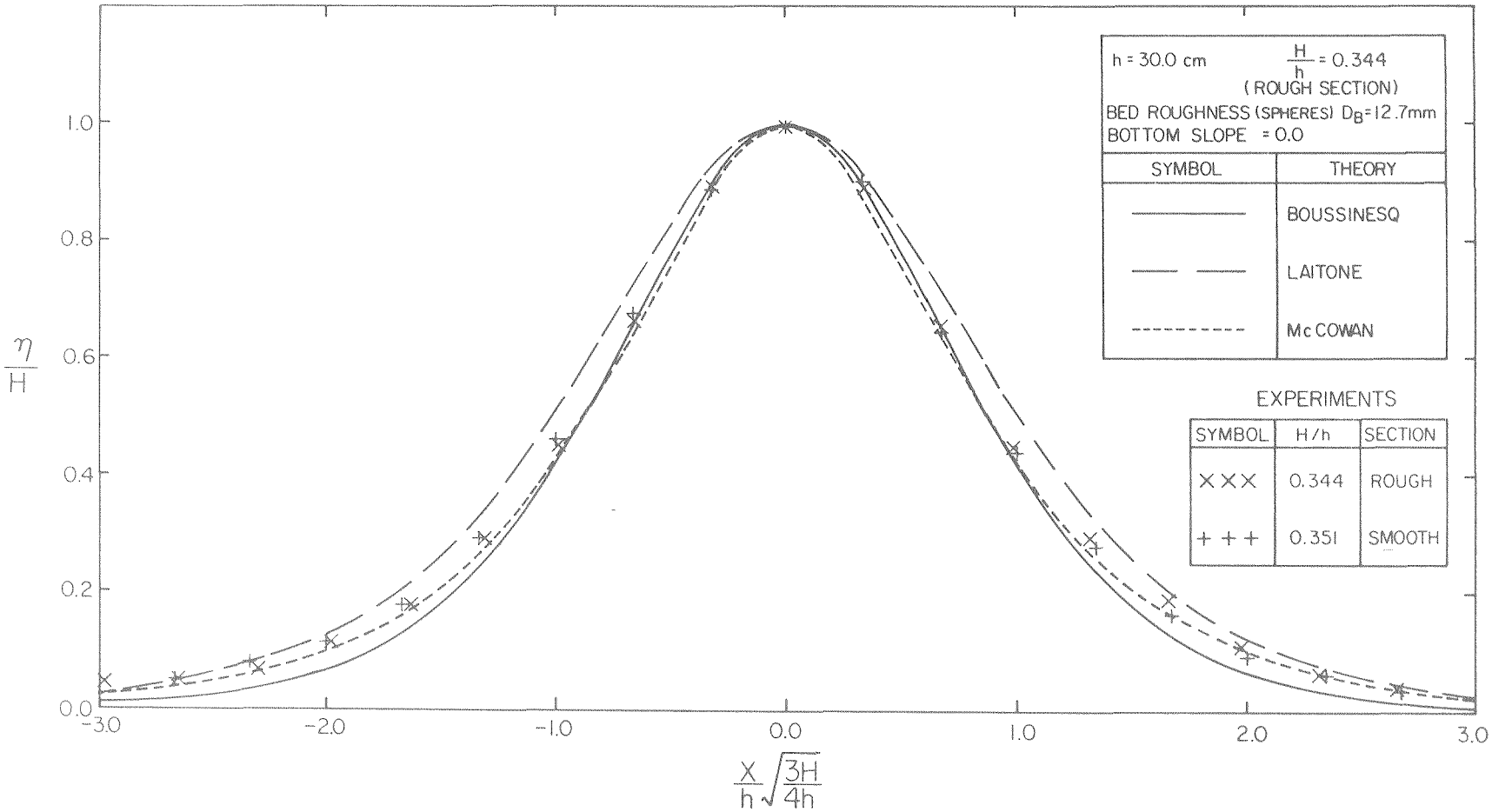

Fig. 5.2 Comparison between the solitary waves measured over the smooth and rough bed sections and between the theories of Boussinesq, McCowan, and Laitone; h=30.0 cm; bottom slope=0.0; H/h=0.351 (over the smooth section); H/h=0.344 (over the rough section).

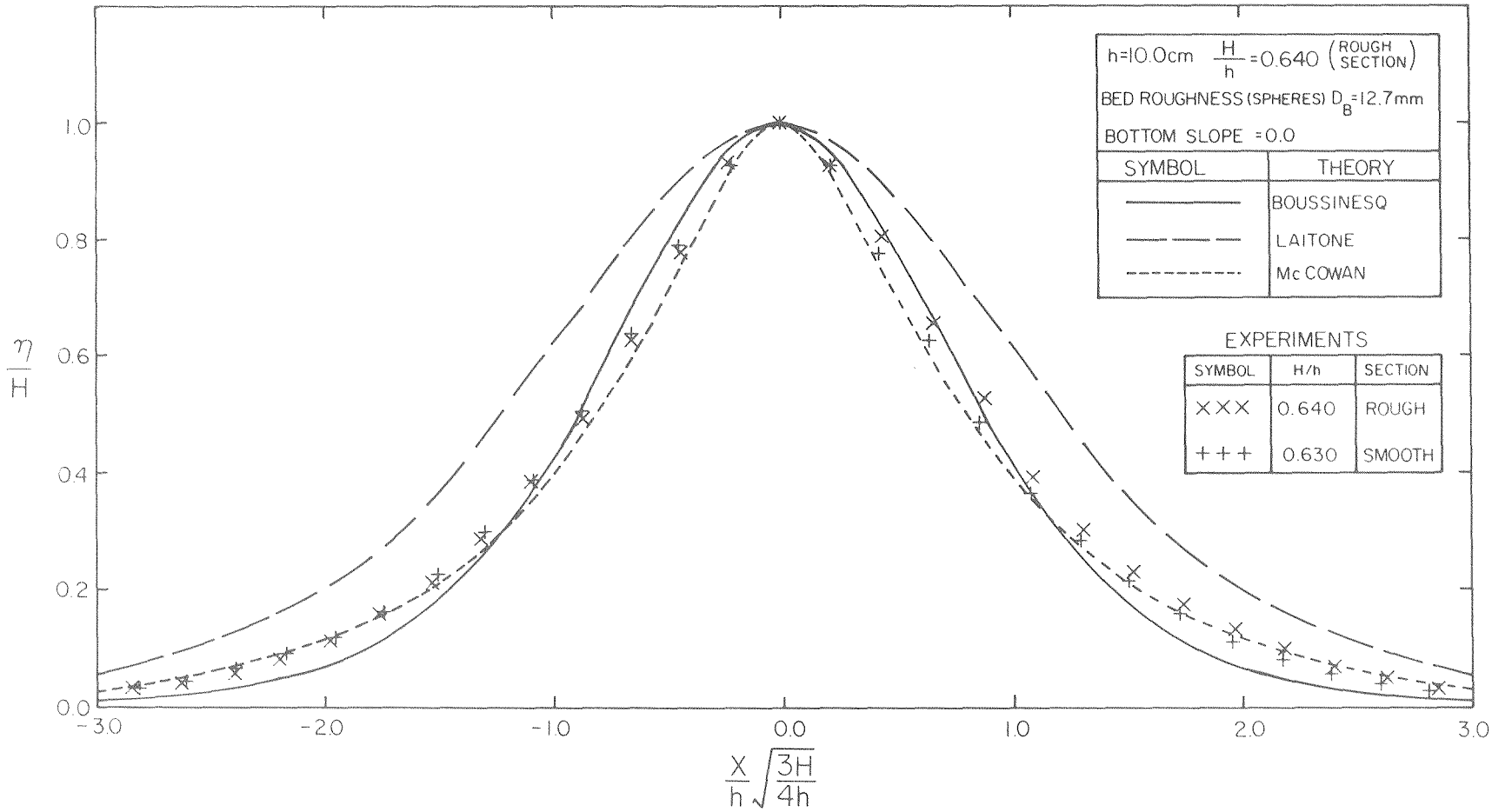

Fig. 5.3 Comparison between the solitary waves measured over the smooth and rough bed sections and between the theories of Boussinesq, McCowan, and Laitone; h=10.0 cm; bottom slope=0.0; H/h=6.30 (over the smooth section); H/h=0.640 (over the rough section).

the waves over the smooth and rough sections, as the approximately 2% difference of the measured wave heights is within the measurement error. The wave gages used to measure the wave profile had stainless steel wires, and their measurement error was estimated to be approximately 3% of the wave height (see description of the wave gages in Section 4.3). There are appreciable differences among the theoretical wave profiles of Boussinesq, McCowan, and Laitone for both cases, i.e., for H/h = 0.34 and H/h = 0.64, and these differences appear to increase with H/h. The experimental profiles of the waves over the smooth and rough beds are between the theoretical profiles of Boussinesq and McCowan near the crest, and they coincide with McCowan's as the distance from the crest increases in both directions. The absence of trailing waves in Figs. 5.2 and 5.3 compared to their presence in Fig. 5.1 is due to the relative height of the waves shown in these figures. Trailing oscillatory waves were generated by the imperfect wave generator in all of these cases. However, solitary waves of large relative height (i.e., large H/h) have a great speed, thus leaving the trailing waves far behind. By the time of the measurement of the wave profiles shown in Figs. 5.2 and 5.3 the trailing waves had not arrived at the test section.

The surface profiles of waves traveling over a slope of 1:200 are presented in Figs. 5.4, 5.5, and 5.6. The depth at the measurement station is 26.2 cm. A wave of H/h = 0.25 is plotted in Fig. 5.4, a wave of H/h = 0.60 in Fig. 5.5, and a wave near breaking, of H/h = 0.87 is shown in Fig. 5.6. The reason for conducting the experiments over a sloping bottom was that it was impossible to generate extremely large

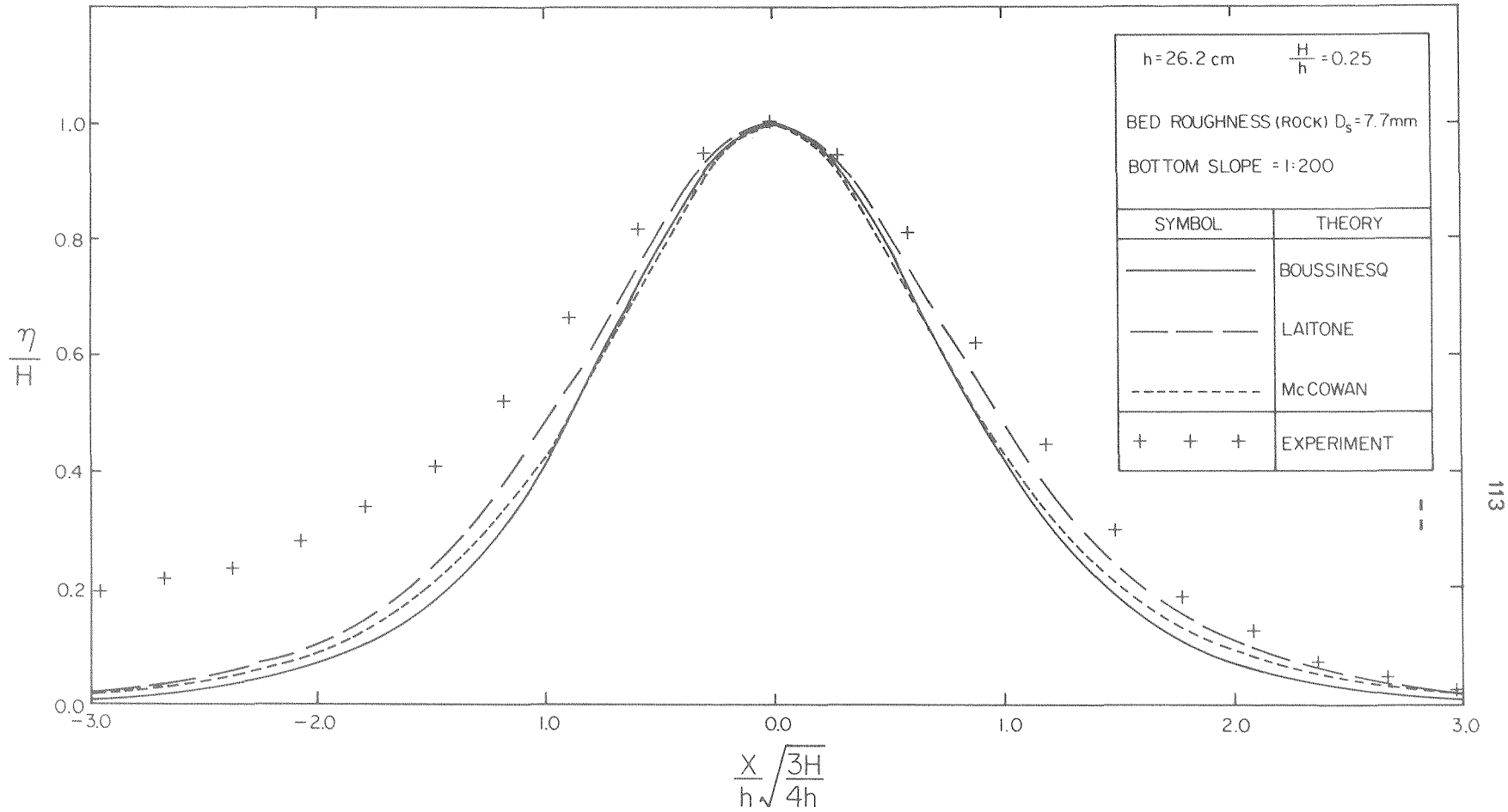

Fig. 5.4 Comparison between a measured solitary wave and between the theories of Boussinesq, McCowan, and Laitone; h=26.2 cm; H/h=0.25; bottom slope=1:200.

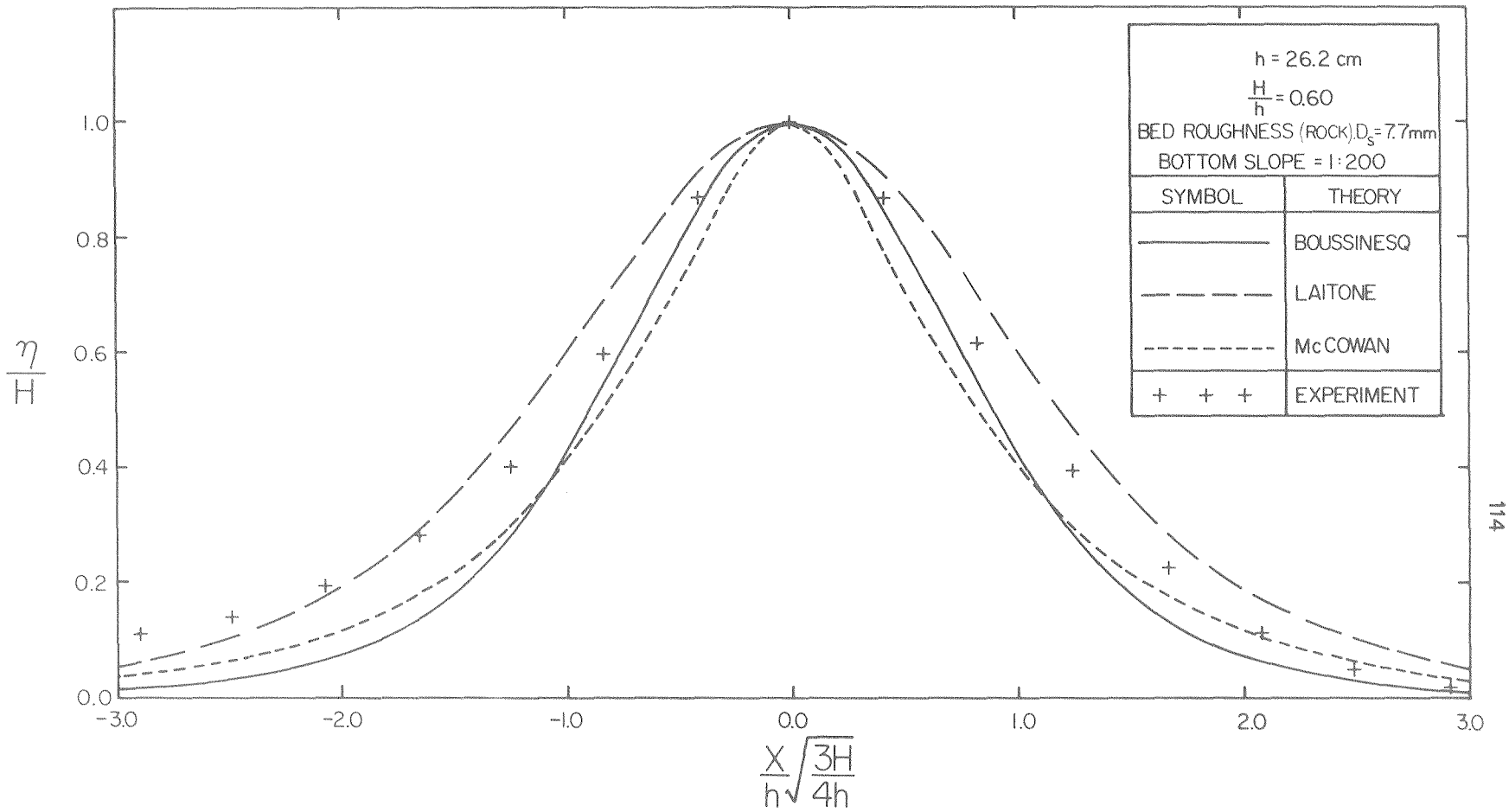

Fig. 5.5 Comparison between a measured solitary wave and between the theories of Boussinesq, McCowan, and Laitone; h=26.2 cm; H/h=0.60; bottom slope=1:200.

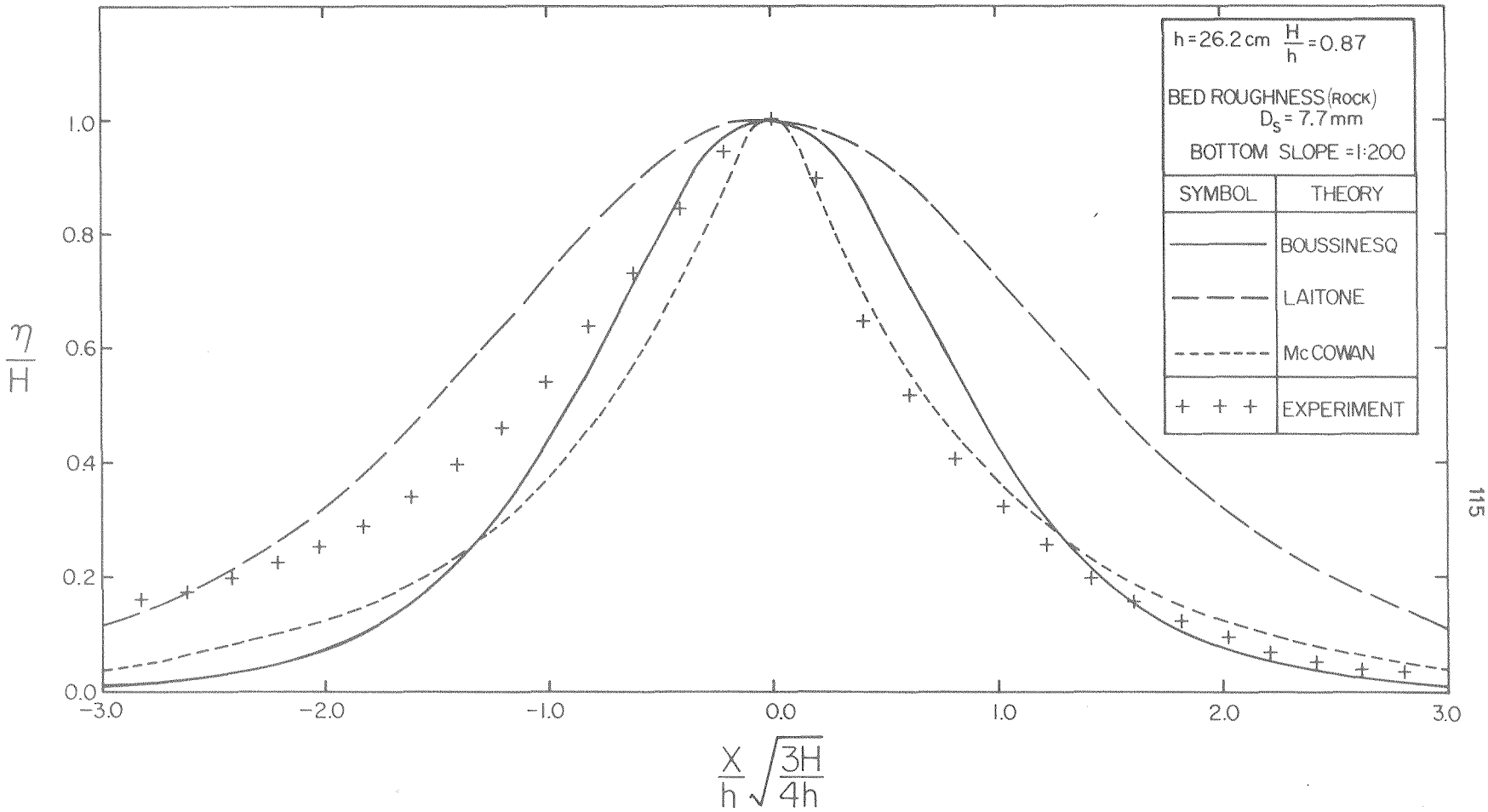

Fig. 5.6 Comparison between a measured solitary wave and between the theories of Boussinesq, McCowan, and Laitone; h=26.2 cm; H/h=0.87; bottom slope=1:200.

waves over a horizontal bottom with the available equipment. While the surface elevation of the experimentally generated wave with H/h = 0.25 is higher than Laitone's theoretical curve, a wave of H/h = 0.60 lies between the theoretical profiles of Laitone and Boussinesq, and the front of a wave near breaking is even steeper than the theoretical wave due to McCowan. The trailing edge of a breaking wave is still closer to the theories of Boussinesq and Laitone. However, the front of the wave, which appears to agree with the theoretical profiles better than the rear of the wave, is of major concern for practical purposes, since this is where the forces which are exerted on objects reach their maximum values (as will be shown later in this chapter). The asymmetric profiles of waves of large relative height, in which the wave front is steeper than the rear of the wave, are probably due to the shoaling effects of the slope over which the waves travel. Large waves shoaling on sloping beaches are known to have such (asymmetric) profiles.

The results of profile measurements indicate that for waves of small relative height over a horizontal bottom the three theories are close to each other and the experimental wave profile agrees with the theories. The experiments also indicate that for waves of larger relative height over a horizontal bottom the theories of either Boussinesq or McCowan should be used. For sloping bottoms, the front of the experimentally measured wave is represented well by Laitone's theory for relatively small and intermediate waves, by Boussinesq's theory for relatively large waves, and by McCowan's theory for extremely large waves. The rear of the wave in all of the studied cases of sloping bottom is better represented by the theories of Laitone and Boussinesq.

The conclusions presented in the preceding paragraph are incomplete since they result from measurements of only the surface profile of the solitary wave. In order to conclusively determine which theory (i.e., Boussinesq's, McCowan's, or Laitone's) to use in the present research, comparisons between the measured and the theoretical wave celerities, and between the measured and the theoretical fluid particle velocities are presented in the following sections.

5.1.2 The Wave Celerity

The speed of the solitary wave was measured over a horizontal bottom in the following way. Two wave gages were placed at two stations approximately 4 m apart along the wave tank. The distance between them was carefully measured, and it varied from one experiment to another. The wave was recorded simultaneously by the gages on two channels as shown in Fig. 5.7. If p_s is the speed of the recording paper, in mm/sec, and d_r is the distance, in mm, between the recorded peaks (the wave crests), then the time t, in seconds, during which the wave propagated from one wave gage to another is

$$t = \frac{d_r}{p_s} \quad , \tag{5.1}$$

and the speed, C, at which it traveled is

$$C = \frac{\ell}{t} = \frac{\ell p_s}{d_r} \quad , \tag{5.2}$$

where ℓ is the distance between the wave gages.

The wave celerity was measured in water depths of 10 cm, 20 cm, 22.5 cm, and 30 cm over a horizontal bottom. A comparison between the

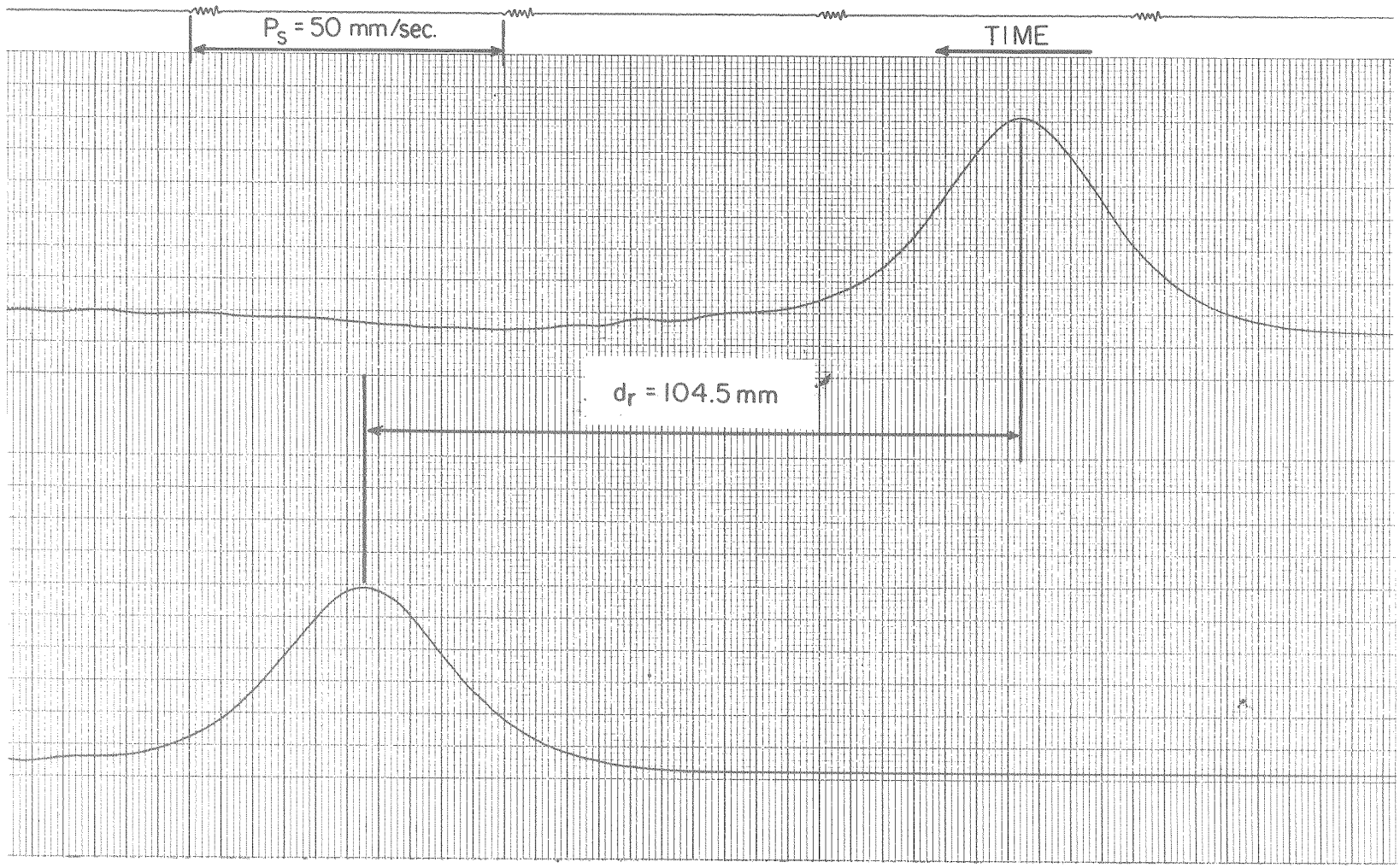

$$\ell = 421.3\ \text{cm.}; \qquad t = \frac{d_r}{P_s} = 2.090\ \text{sec.}; \qquad C = \frac{\ell}{t} = 201.6\ \text{cm/sec.}$$

Fig. 5.7 An example of a wave record used to evaluate the wave celerity.

experimentally measured wave celerities and the theories of Boussinesq (1872), McCowan (1891), and Laitone (1963) is shown in Fig. 5.8. The abscissa in this figure is H/h and the ordinate is $C/\sqrt{gh}$, where H is the wave height, h is the water depth, and g is the gravitational acceleration. Also shown in this figure are experimental data which were obtained by Daily and Stephan (1952) and by French (1969). The theoretical curves in Fig. 5.8 were calculated from the formulae presented in Table 3.1. The results indicate that the theories of Boussinesq, McCowan and Laitone are very close to each other for waves of small relative height ($H/h < 0.2$). For higher waves ($H/h > 0.2$), the theories of Boussinesq and Laitone are still close to each other where the theoretical values of the celerity given by Boussinesq are larger than those given by Laitone, and McCowan's theory predicts much smaller values of the celerity. The experimental results of the present study agree well with the theory of Boussinesq, while the experimental results of Daily and Stephan (1952) and of French (1969) agree better with Laitone's theory. The reasons for the differences between the present measurements and those conducted by Daily and Stephan and by French are not understood. However, although these differences appear to be systematic and not a result of random experimental scatter, they appear to be too small to be significant in practical use. Boussinesq's expression for the wave speed is given in a closed form (see Table 3.1), while Laitone's expression is given in a power series of H/h carried to order of $(H/h)^2$. Additional terms, i.e., of higher order of H/h, might be significant, particularly for large values of H/h. For this reason, and because the differences between the wave celerities due to Boussinesq

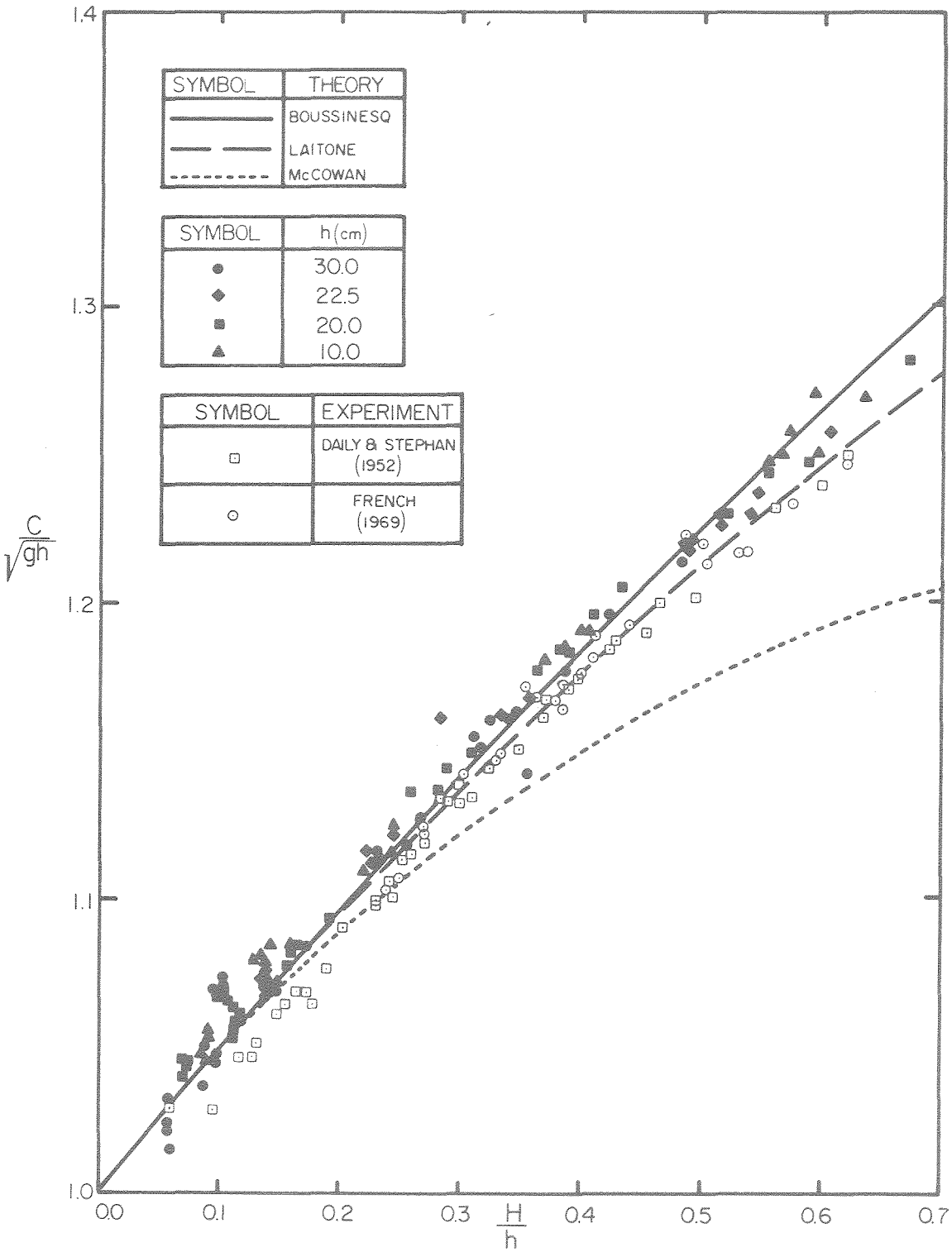

Fig. 5.8 The celerity of solitary waves.

and Laitone are small, Boussinesq's expression for the wave speed, i.e.,

$$C = \sqrt{gh\left(1+\frac{H}{h}\right)} \tag{5.3}$$

is apparently the best one to use.

5.1.3 The Fluid Particle Velocity

The fluid particle velocity near the bed and the water surface profile of a solitary wave with a height-to-depth ratio of 0.492 were measured in water 30 cm deep with the wave tank in a horizontal position. The test section consisted of a layer of rocks with a mean diameter (D_s) of 7.70 mm and a geometric standard deviation (σ_g) of 1.15 (this material was used in the experiments of incipient motion). The results are shown in Figs. 5.9a,b, where the abscissa is $\frac{X}{h}\sqrt{\frac{3H}{4h}}$, the ordinate in Fig. 5.9a is η/H, and in Fig. 5.9b u/C. The horizontal coordinate moving with the wave is denoted by X, h is the water depth, H is the wave height, η is the elevation of the water surface above still water level, u is the fluid particle velocity, and C is the measured value of the wave celerity.

Fig. 5.9a indicates that the experimental water surface profile agrees with Boussinesq's theory near the wave crest, and with Laitone's theory away from the crest. The measured fluid particle velocities which are shown in Fig. 5.9b lie between the theories of Boussinesq and McCowan near the crest, and they agree with McCowan's theory away from the crest. The scatter of data at the rear of the wave is larger than that at the wave front. This is probably due to the development of turbulence during the passage of the wave. Boussinesq's expression for the

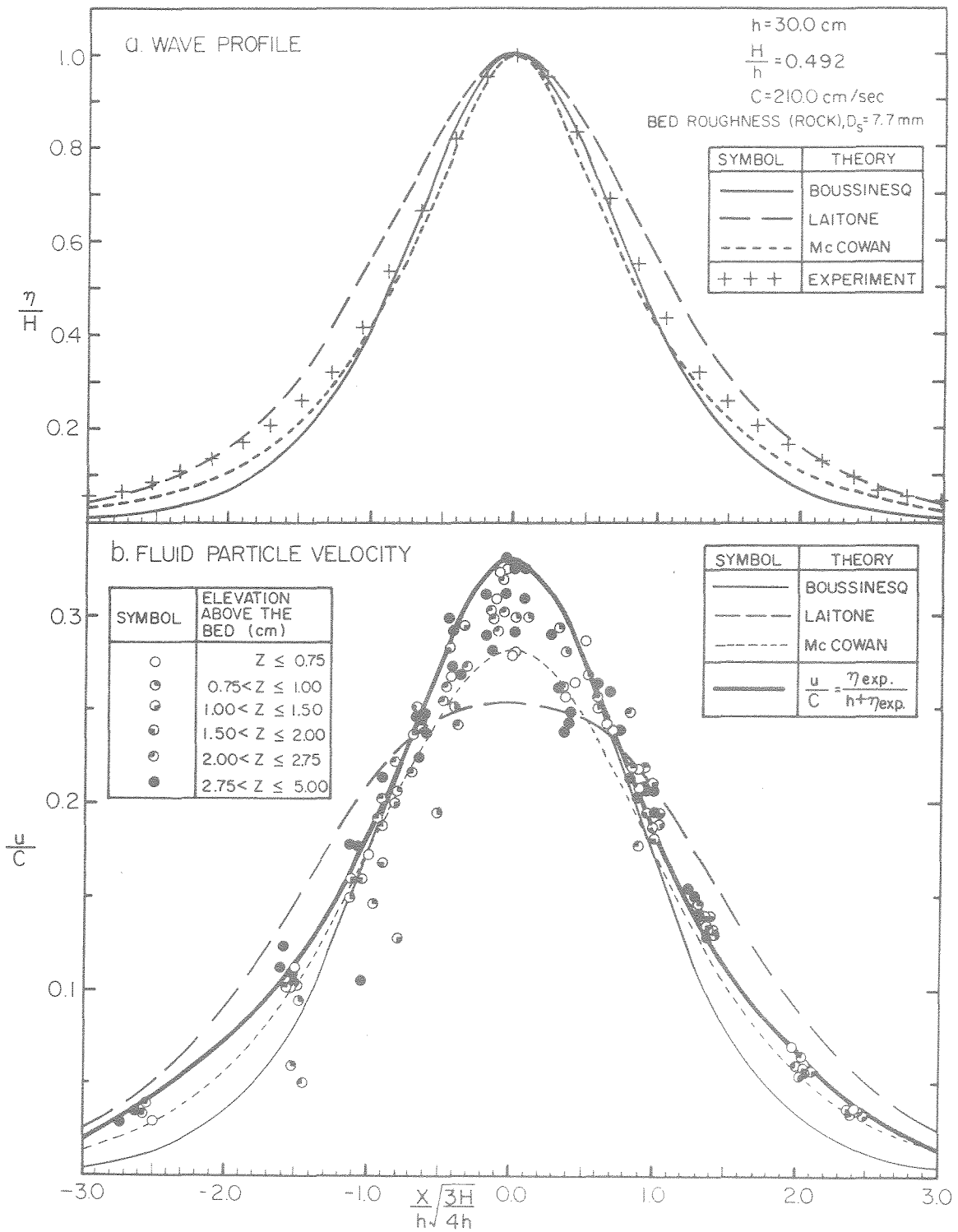

Fig. 5.9 (a) The surface profile of a solitary wave; (b) The fluid particle velocity near the bottom under a solitary wave.

velocity, $\frac{u}{C} = \frac{\eta}{h+\eta}$, was derived from continuity considerations assuming uniform velocity distribution over the depth. This relationship employed his expression for the surface profile (see Table 3.1). The same relationship employing the measured surface profile is also shown in Fig. 5.9b in order to study the validity of the assumption of vertically uniform velocity distribution combined with continuity considerations. The curve representing this relationship (i.e., $\frac{u}{C} = \frac{\eta_{exp}}{h+\eta_{exp}}$, where η_{exp} is the experimentally measured surface profile) agrees with Boussinesq's theory near the crest and with McCowan's theory away from the crest. It is indicated from the figure that the assumption from which Boussinesq's expression for the velocity was derived is valid over the major part of the wave, and only near the crest does it predict velocities somewhat larger than the measured ones. Yet, both Boussinesq's theory and the curve representing the velocity evaluated from measurements of the surface profile are within the range of scatter of the measured velocities. McCowan's theory predicts velocities smaller than the measured ones under the crest, and is also within the measurement scatter. Only Laitone's theory appears to disagree with the velocity measurements over the full range of the abscissa in Fig. 5.9b. The conclusions from these results are that the fluid particle velocity under solitary waves in the laboratory is best presented by employing the measured surface profile combined with continuity considerations (i.e., $\frac{u}{C} = \frac{\eta_{exp}}{h+\eta_{exp}}$). As far as theoretical formulations are concerned, the velocity may be presented by either Boussinesq's theory or McCowan's theory, and it appears that Laitone's theory does not predict the fluid particle velocity well.

The velocity profile in the boundary layer near the bed was investigated by measuring the fluid particle velocity at different levels (up to 5 cm) above the bed. Data points which were obtained in regions of different heights above the bed are indicated in Fig. 5.9b by different symbols. As can be seen in this figure, the velocity profile in the boundary layer could not be determined within the accuracy of measurements. Note from the following considerations that the boundary layer was expected to be rough turbulent. Iwasa (1959) investigated the smooth laminar boundary layer under solitary waves based on the assumption that the velocity profile in the boundary layer is either linear or parabolic. For the linear velocity profile he obtained

$$\delta^2_{X=0} = \frac{16h^{5/2}}{3\sqrt{3H}\ R_c} \quad , \tag{5.4}$$

and for the parabolic profile

$$\delta^2_{X=0} = \frac{16h^{5/2}}{\sqrt{3H}\ R_c} \quad , \tag{5.5}$$

in which $\delta_{X=0}$ is the boundary layer thickness under the wave crest, and R_c is a wave Reynolds number, defined by Iwasa as

$$R_c = \frac{\sqrt{gh}\ h}{\nu} \quad , \tag{5.6}$$

where g is the gravitational acceleration, and ν is the kinematic viscosity of the fluid. Assuming the velocity profile in the boundary layer as being parabolic, then for the example shown in Fig. 5.9, where h = 30 cm, and H/h = 0.492, the thickness of the smooth laminar boundary layer under

the wave crest should be

$$\delta_{X=0} = \left[\frac{16h\nu}{\sqrt{3gH}}\right]^{1/2} = 0.15 \text{ cm} \quad , \tag{5.7}$$

in which the kinematic viscosity assumed the value $\nu = 0.01$ cm^2/sec, and the gravitational acceleration is $g = 981$ cm/sec^2. Assuming linear velocity profile in the boundary layer, its thickness under the crest can be shown from Eq. (5.4) as having the value of 0.05 cm. Since in the present example the mean diameter of the roughness particle was 7.7 mm and they protruded approximately 4 mm above the bed mean level into the flow, they prevented the development of a laminar boundary layer. Therefore, it was expected that the boundary layer under the wave should be rough turbulent. A study of the velocity profile in this boundary layer was necessary in order to determine the shear stresses exerted on the bottom. However, since such a profile could not be indicated from the measurements of the fluid particle velocity, local shear stress (and local friction coefficients) could not be determined from this study, and a further investigation of the boundary layer under solitary waves is needed. A different method of estimating the bottom shear stresses, based on measurements of wave attenuation, is presented in the following section.

5.2 THE RESISTANCE COEFFICIENT UNDER SOLITARY WAVES

The problem of the friction coefficient under solitary waves was investigated in order to estimate the bottom shear stresses caused by the waves. Theoretical estimation of local shear stresses is given only for laminar flows (see Section 3.2.2). For the general case (i.e.,

either laminar or turbulent flows) an approximate evaluation of stresses is given by the use of the mean resistance coefficient under the wave, which was estimated as follows. The theoretical estimates of the mean resistance coefficient of smooth laminar flows were obtained from Eq. (3.49), while experimental values were obtained for both smooth and rough beds by substitution of the experimentally measured values of $\frac{d(H/h)}{d(x/h)}$ (where H is the wave height, h is the water depth, and x is a stationary coordinate along the wave tank) into Eq. (3.36). The values of $\frac{d(H/h)}{d(x/h)}$ were measured as follows. Four wave gages recorded the wave at four different stations along a 60 ft (18.3 m) section of the wave tank and the values of $(H/h)_i$ (i = 1,2,3,4) were evaluated from the record. The ratio of the wave height to the water depth was found to decrease exponentially along the wave tank, i.e.,

$$\frac{H}{h} = \left(\frac{H}{h}\right)_o e^{-k\frac{x}{h}} \quad , \tag{5.8}$$

where k is the decay coefficient. The origin of x is chosen arbitrarily, and $(H/h)_o$ is the value of H/h at x=0. The values of $(H/h)_o$ and k were evaluated employing the experimental values of $(H/h)_i$ and using a least-squares fit technique, i.e.,

$$\sum_{i=1}^{4} \left[\left(\frac{H}{h}\right)_i - \left(\frac{H}{h}\right)_o e^{-k\left(\frac{x}{h}\right)_i}\right]^2 = \text{minimum} \ . \tag{5.9}$$

The value of $\frac{d(H/h)}{d(x/h)}$ was then obtained from the exponential decay relationship,

$$\frac{d(H/h)}{d(x/h)} = -k \frac{H}{h} \quad . \tag{5.10}$$

During the experiment, the variation of the wave height resulted in a variation of $\frac{d(H/h)}{d(x/h)}$ along the channel. In order to obtain a representative experimental data point from the experiment, a representative value, $\left[\frac{d(H/h)}{d(x/h)}\right]_{rep}$, was estimated as follows. The ratio of the wave height to the water depth which occurs at approximately midway along the tank, i.e., between the second and third measurement stations, was considered as a representative value, $\left(\frac{H}{h}\right)_{rep}$. Substitution of $\left(\frac{H}{h}\right)_{rep}$ into Eq. (5.10) yields:

$$\left[\frac{d(H/h)}{d(x/h)}\right]_{rep} = -k\left(\frac{H}{h}\right)_{rep} \quad . \tag{5.11}$$

An example of an experimental result for a rough bed is shown in Fig. 5.10a, and for a smooth bottom in Fig. 5.10b. The abscissa is x/h, and the ordinate is H/h in both figures. The figures indicate that the wave attenuation is indeed exponential since the deviations of the measured values of H/h from the fitted exponential curves are negligible.

The decay coefficient, however, is not constant for the entire range of wave amplitudes. This is illustrated by the different curves in Fig. 5.10, where the slopes of the lines, and hence the values of k, vary for different ranges of H/h at the same water depth. This means that if the wave tank were long enough for the wave to decrease in height considerably, the decay would not be exponential over the entire length of the tank, and Eq. (5.8) would be invalid. It seems sufficient, however, to use the decay coefficient, k, evaluated for each experiment

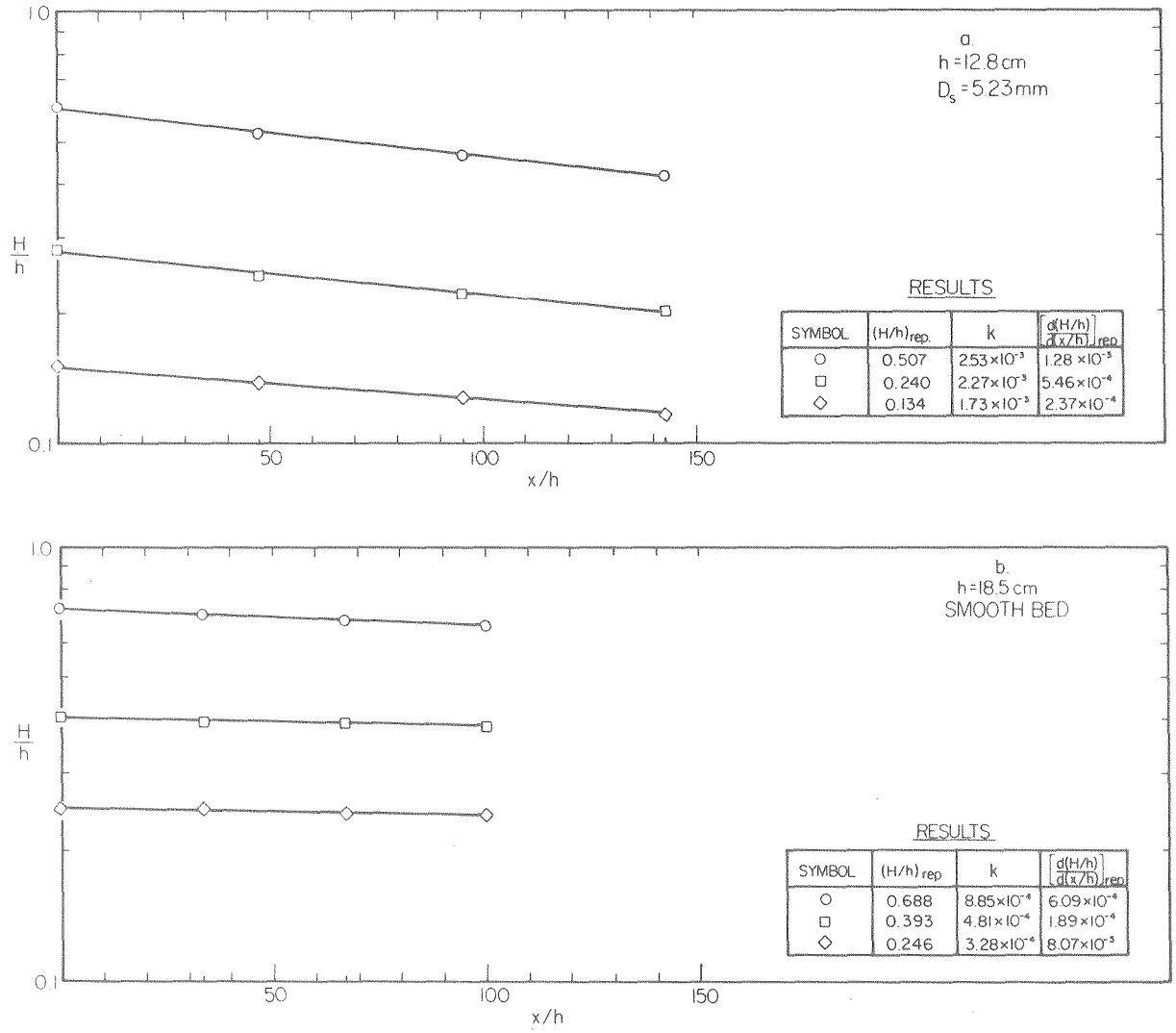

Fig. 5.10 Attenuation of solitary waves along a channel; (a) over a rough bed; (b) over a smooth bed.

from the relatively short (60 ft) distance, over which the wave height did not decrease appreciably.

Ippen et al. (1955) artificially increased the distance over which the wave traveled by measuring the wave reflected from vertical walls at the ends of the wave tank. Their procedure was not used in the present investigation since the transient trailing waves might interfere with the measurements of the reflected wave.

Experiments were conducted over a smooth bottom and over rough beds of 15.9 mm thick layers of material with mean diameters, D_s, of 5.23 mm and 7.55 mm. The experiments with the smooth bottom and the 5.23 mm roughness were conducted with water depths of 12.8 cm, 14.5 cm, 18.5 cm, and 26.2 cm, and over the 7.55 mm roughness with 14.5 cm, 18.5 cm, and 26.2 cm water depths. These values provided a range of roughness-to-depth ratios (D_s/h) from 0.020 to 0.052. Some values of D_s/h were repeated with the two different roughnesses. The reason for running the experiments at the same depths over both smooth and rough bottoms was to obtain results which could be used to correct the values of the resistance coefficient of rough beds for wall effects. The experimental data are presented in Appendix II, Table A.2.2.

The results showing the mean resistance coefficient, $\overline{C_{f_b}}$, as a function of the flow Reynolds number, Re, are plotted in Fig. 5.11. The theoretical estimates of the mean resistance coefficient of a smooth bottom were obtained for waves of given height and depth by numerical evaluation of Eq. (3.49). The corresponding values of the flow Reynolds number were obtained from Eq. (3.22). The theoretical curve

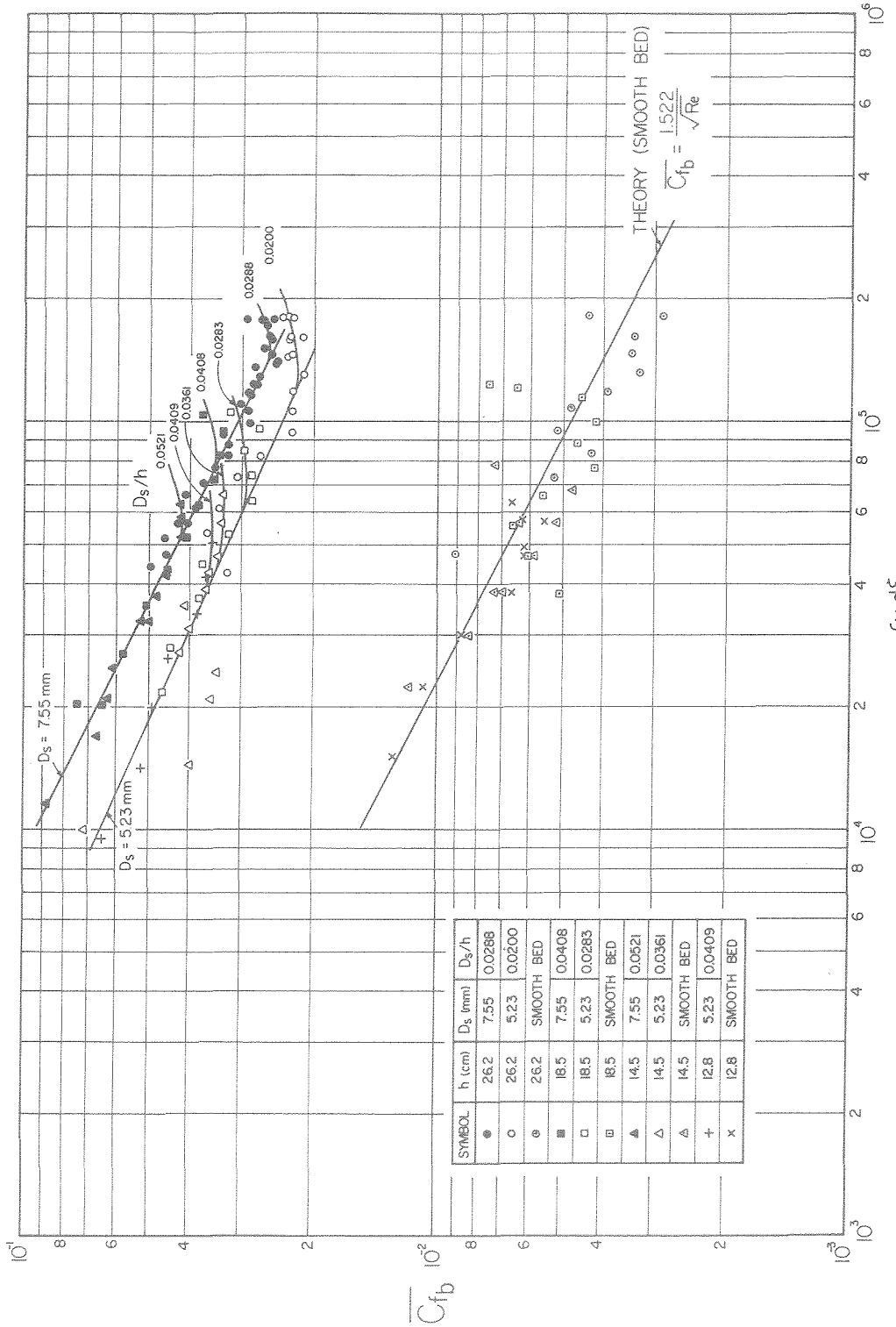

Fig. 5.11 The mean resistance coefficient as a function of the flow Reynolds number.

was found to have the form

$$\overline{C_{f_b}} = \frac{1.522}{\sqrt{Re}} \quad . \qquad (5.12)$$

This expression may be compared to $\overline{C_{f_b}} = 1.33/\sqrt{Re}$ found theoretically by Blasius (e.g., see Schlichting (1968)) for a steady flow over a flat plate, and also experimentally by Ippen and Kulin (1957) for solitary waves, or to $\overline{C_{f_b}} = 2/\sqrt{Re}$ found by Jonsson (1966) for oscillatory flows. Blasius defined the Reynolds number as $Re = \frac{uL}{\nu}$, where u is the (constant) free stream velocity, L is the length of the plate and ν is the kinematic viscosity of the fluid. Jonsson defined $\overline{C_{f_b}} = \frac{\tau_{max}}{\frac{1}{2}\rho_w u_{max}^2}$ and $Re = \frac{u_{max} a_\delta}{\nu}$, where τ_{max} is the maximum shear stress, u_{max} is the maximum fluid particle velocity, ρ_w is the density of the fluid, and a_δ is the amplitude of the fluid particle displacement just outside the boundary layer. Ippen and Kulin defined the Reynolds number in a similar way to that which is used in the present investigation, i.e., $Re = \int_0^\xi \frac{ud\xi}{\nu}$, where ξ is the fluid particle displacement near the bottom under the solitary wave. The difference between the results of Ippen and Kulin and those described by Eq. (5.12) is probably due to the different expressions for the velocity used in evaluating the Reynolds numbers in these investigations, and to the different relationships used to estimate the resistance coefficient. Their original data, however, were unavailable so it was impossible to determine the exact reasons for the differences between their results and those of the present investigation.

The experimental results shown in Fig. 5.11 for a smooth bottom seem to agree reasonably well with the theoretical curve described by

Eq. (5.12). The relatively large scatter of data is believed to result from errors in measurements. The relative error of the wave gages used was estimated at approximately 1% of the wave height. This error is of the same order of magnitude as the attenuation of waves over the smooth bottom. It can be seen in Fig. 5.10b that the wave height decreased between 3% and 9% for the range of H/h considered while traveling over a distance of 18.6 m. The measurement error was of second order for the case of rough bottom, as seen in Fig. 5.10a, where the amplitude attenuation was between approximately 25% and 35%. The amplitude attenuation varied for different water depths and roughness diameters. However, in all of the experiments the attenuation was much smaller for a smooth bottom than for a rough one. This was expected because of the smaller shear stresses exerted by the smooth surfaces compared to the rough bottom. Thus the relative error in evaluating $\frac{d(H/h)}{d(x/h)}$ for a smooth bottom was much larger than for rough beds, resulting in a large scatter of data.

The reasonably good agreement between the theoretical and the experimental results for a smooth channel justifies the theoretical wall effect correction in the measurements of the mean resistance coefficient of rough bottoms. This correction is given by the second term of the numerator on the right-hand side of Eq. (3.36), and it was usually smaller than 10% of the mean resistance coefficient of the rough bed. Note that the maximum value of the flow Reynolds number observed in the experiments is approximately 1.8×10^5. This Reynolds number is defined in a similar way to that of a flat plate, where the flow is laminar

for $Re < 2.5x10^5$. This justifies the laminar boundary layer considerations in evaluating the mean resistance coefficient of smooth bottoms.

As noted in Section 3.2.2, a discrepancy between the theoretical and experimental results was expected, due to approximations in the theoretical analysis, where only the linearized form of the equations of motion was considered, and due to the possible separation of boundary layer at the rear of the wave, where laminar boundary layer considerations are no more valid. Such a discrepancy should result in a systematic deviation of the experimental data points from the theoretical curve. However, it is seen in Fig. 5.11 that the scatter of data points is random. Therefore, the inaccuracy due to the theoretical approximations is considered to be negligible.

The experimental results of the mean resistance coefficient for rough bottoms, already corrected for wall effects, are shown in Fig. 5.11 as a function of the flow Reynolds number. The mean resistance coefficient appears to depend on the flow Reynolds number and on the absolute value of the roughness diameter, D_s, for waves of small Reynolds numbers. As can be seen in Fig. 5.11, the term "small" for the Reynolds number varies for each set of data points (represented in the figure by a different symbol). It was noted in all of the experiments that this range of Reynolds numbers occurred for waves of H/h smaller than 0.45 (it varied in the experiments between 0.40 and 0.48). For waves of large relative height, i.e., for $H/h > 0.45$, the resistance coefficient seems to depend solely on the relative roughness, D_s/h. Ippen et al. (1955), and Ippen and Mitchell (1957) also found that the mean resistance coefficient is a function of the absolute value of the

bed particle diameter. However, they did not observe the dependence on D_s/h for waves of large relative height.

The dependence of the mean resistance coefficient on the absolute value of the roughness diameter, D_s, as shown in Fig. 5.11 is not practical for general use, since it cannot be applied to cases with roughnesses other than those tested. Jonsson (1966) and Kamphuis (1975) showed that for oscillatory flows over a rough bottom the resistance coefficient is a function of the wave Reynolds number, defined as $Re = \frac{u_{max} a_\delta}{\nu}$, and a roughness parameter, D_s/a_δ, in which a_δ and u_{max} are the displacement amplitude and the maximum velocity of a fluid particle just outside the boundary layer. They also showed that when the flow is rough turbulent the mean resistance coefficient depends only on D_s/a_δ. They developed their analysis from boundary layer considerations similar to those of a flat plate in a steady flow, assuming that the effect of the ratio of the roughness size, D_s, to the length of the plate, L, is analogous to the effect of the parameter D_s/a_δ. (For details about the resistance coefficient of a flat plate see, for example, Schlichting (1968)). Note that if ξ is the maximum displacement of a fluid particle just outside the boundary layer, then for oscillatory flows $\xi = 2a_\delta$. It follows that if it is assumed in the present investigation that the mean resistance coefficient is independent of the Reynolds number (this assumption will be discussed later in this section), then it should be a function of only D_s/ξ. The experimental data of the mean resistance coefficient are shown as a function of D_s/ξ in Fig. 5.12, where the fluid particle displacement, ξ, was evaluated from Eq. (3.24).

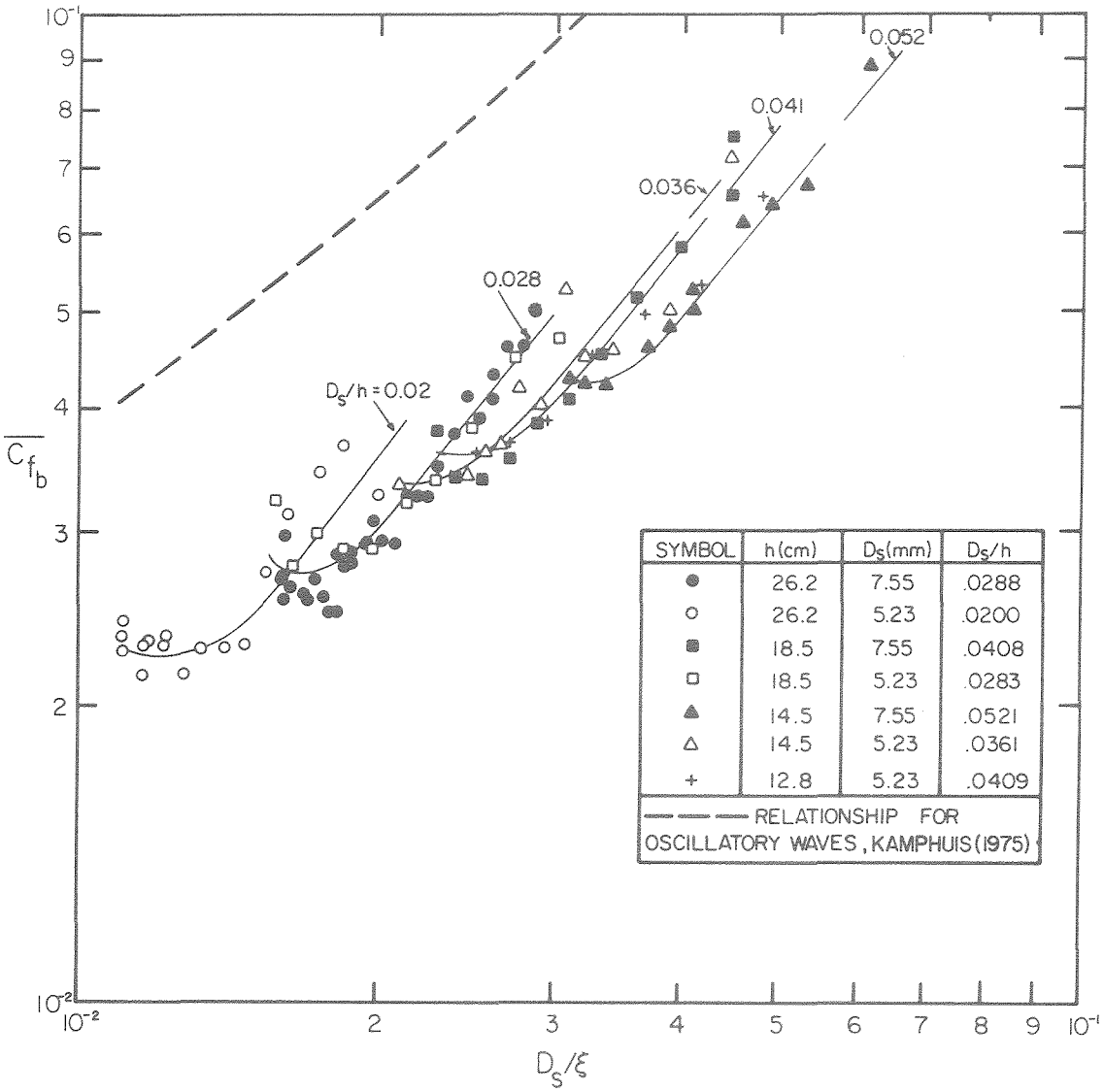

Fig. 5.12 The mean resistance coefficient as a function of the ratio of the roughness size, D_s, to the displacement of a fluid particle just outside the boundary layer, ξ.

Kamphuis' (1975) empirical relationship for the resistance coefficient under oscillatory flows is shown in Fig. 5.12 for the convenience of reference. Note that Kamphuis used a roughness parameter, k_s, which in his experiments was approximately equal to $2.6D_s$. It appears from this figure that the data of the present study display a different behavior than that found by Kamphuis, where the resistance coefficient is a function of only D_s/ξ. The experimental results of the present study show that, in addition to D_s/ξ, the mean resistance coefficient depends on the ratio of the mean roughness diameter to the water depth, D_s/h. The differences between Kamphuis' results and the results of the present study are probably due to the differences between the nature of the flows in the two studies. Kamphuis conducted his experiments by oscillating the fluid in a closed tunnel and measuring the stresses exerted on a plate, while in the present study there is a solitary wave traveling into quiescent water in an open channel, where the attenuation of the wave is measured. Yet, specific reasons for the differences between the results of the two studies (i.e., reasons which explain why the differences in the nature of the flow cause the different results) are not understood. The experimental data shown in Fig. 5.12 indicate that, in addition to the effects caused by the protrusion of the roughness particles relative to the fluid particle displacement (which is assumed here as being analogous to the parameter D_s/L in the case of a turbulent steady flow over a rough plate), there are effects which are described by the parameter D_s/h. In Section 3.2.1 it was noted that inertia effects may also be important, in addition to the effects of the parameter D_s/ξ. The inertia effects were described by the dimensionless acceleration, and a characteristic dimensionless acceleration was given by Eq. (3.28).

However, in Eq. (3.33) it was shown that the characteristic dimensionless acceleration may be represented by the parameter D_s/ξ, and indeed, the data presented in Fig. 5.13, in which the mean resistance coefficient is shown as a function of the characteristic dimensionless acceleration, $\left[\frac{D_s}{u^2}\frac{du}{dt}\right]_{char}\left(=\frac{D_s}{u^2_{max}}\left(\frac{du}{dt}\right)_{max}\right.$, as given by Eq. (3.28)$\Big)$, indicate that the effects of D_s/ξ (Fig. 5.12), are similar to the effects of the dimensionless acceleration (Fig. 5.13). Hence, since the two effects are described by the same parameter, it is impossible to point out which effect is due to acceleration and which to the effects of the rough turbulent flow. Furthermore, the data shown in Figs. 5.12 and 5.13 imply that the characteristic dimensionless acceleration as given by Eq. (3.28) probably does not describe the actual inertia effects on the mean resistance coefficient, since if all the physical effects are described by the same parameter, D_s/ξ, then the resistance coefficient should be a function of this parameter alone. Yet, it appears to be also a function of D_s/h, hence, some of the effects should be described by a different parameter. It is important to remember that the choice of the dimensionless acceleration as given by Eq. (3.28) was based on the assumption that the ratio of the maximum inertia forces to the maximum drag exerted on the roughness particles indeed represents inertia effects. On the other hand, inertia forces seem to cancel out when integrated over the waves. This implies that they may have effects on local resistance coefficients under the wave, but not on the mean resistance coefficient, which is obtained by integrating the product of the forces by the fluid particle velocity along the wave. Apparently, inertia effects should be examined considering the manner in which they

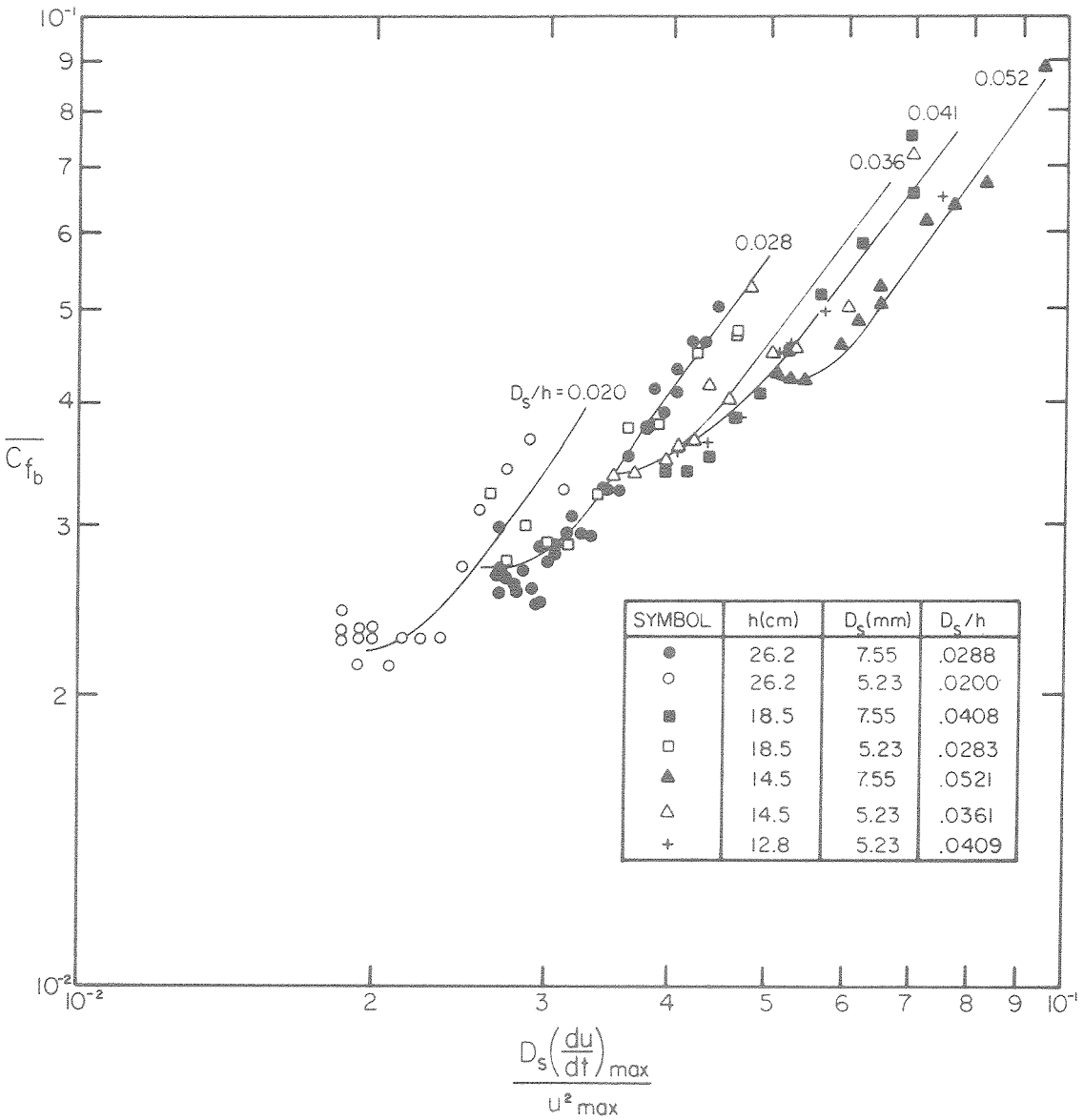

Fig. 5.13 The mean resistance coefficient as a function of the characteristic dimensionless acceleration.

affect the development of the boundary layer rather than their effects on inertia forces. In addition, it is noted that the dimensionless acceleration was evaluated using Boussinesq's (1872) theory for the solitary wave, and it might not represent the actual characteristic dimensionless acceleration. In Section 5.1.3 it was shown that the differences among the theories of Boussinesq (1872), McCowan (1891), and the measured fluid particle velocity may be considered as being small. Hence, it was assumed that the fluid particle acceleration is described fairly accurately by the two theories. However, as can be seen in Section 5.3.2, Figs. 5.21 and 5.22, the differences between the theories of Boussinesq and McCowan are quite significant when used to predict the inertia forces relative to drag forces. This means that conclusions regarding the effects of inertia, assuming that it is described by the dimensionless acceleration, depend on how accurately the dimensionless acceleration is estimated.

From the preceding discussion it follows that due to the uncertainties involved in interpreting the actual inertia effects on the mean resistance coefficient, a relationship which may be used to estimate this coefficient can be presented only empirically by fitting curves to the experimental data. The disadvantage of such an (empirical) relationship is that it may be inaccurate when used to estimate the resistance coefficient by extrapolation to values of the parameters much different from those tested, since it is not known if the physical laws that govern this relationship are still valid beyond the range of the parameter values for which it was obtained. An empirical relationship is presented graphically in Figs. 5.12 and 5.13 by the curves which

were fitted by inspection to the data. Now, since Fig. 5.12 shows a dependence on D_s/ξ and D_s/h, and since ξ is a function of h and H/h, as shown by Eq. (3.24), the mean resistance coefficient can be described as a function of D_s/h and H/h. Such a relationship was also deduced from geometrical considerations in Section 3.2.1. The disadvantage of presenting the mean resistance coefficient as a function of D_s/ξ is that it requires some theoretical relationships in order to estimate D_s/ξ from the measured parameters D_s, h, and H, while presentation of the resistance coefficient as a function of D_s/h and H/h is obtained from directly observed quantities. Essentially though, once an expression is given for D_s/ξ, there is no preference of one parameter over another.

The experimental data, showing the mean resistance coefficient as a function of D_s/h and H/h are presented in Fig. 5.14, where the abscissa is H/h and the ordinate is $\overline{C_{f_b}}$. The various values of D_s/h are noted in this figure for the different curves which were fitted (by inspection) to the data. The results shown in this figure will later be used to estimate the dimensionless shear stress employed in the investigation of the incipient motion of bottom material under solitary waves.

When presenting the experimental data in Figs. 5.12, 5.13, and 5.14, it was assumed that the resistance coefficient is independent of the Reynolds number. This assumption may be justified if it is shown that the flow was rough turbulent during the experiments. In Section 5.1.3 it was shown from laminar boundary layer considerations that the size of the bed roughness was larger than the thickness of the laminar boundary layer. Therefore, it was concluded that the roughness size was certainly much larger than the laminar sublayer if the flow was

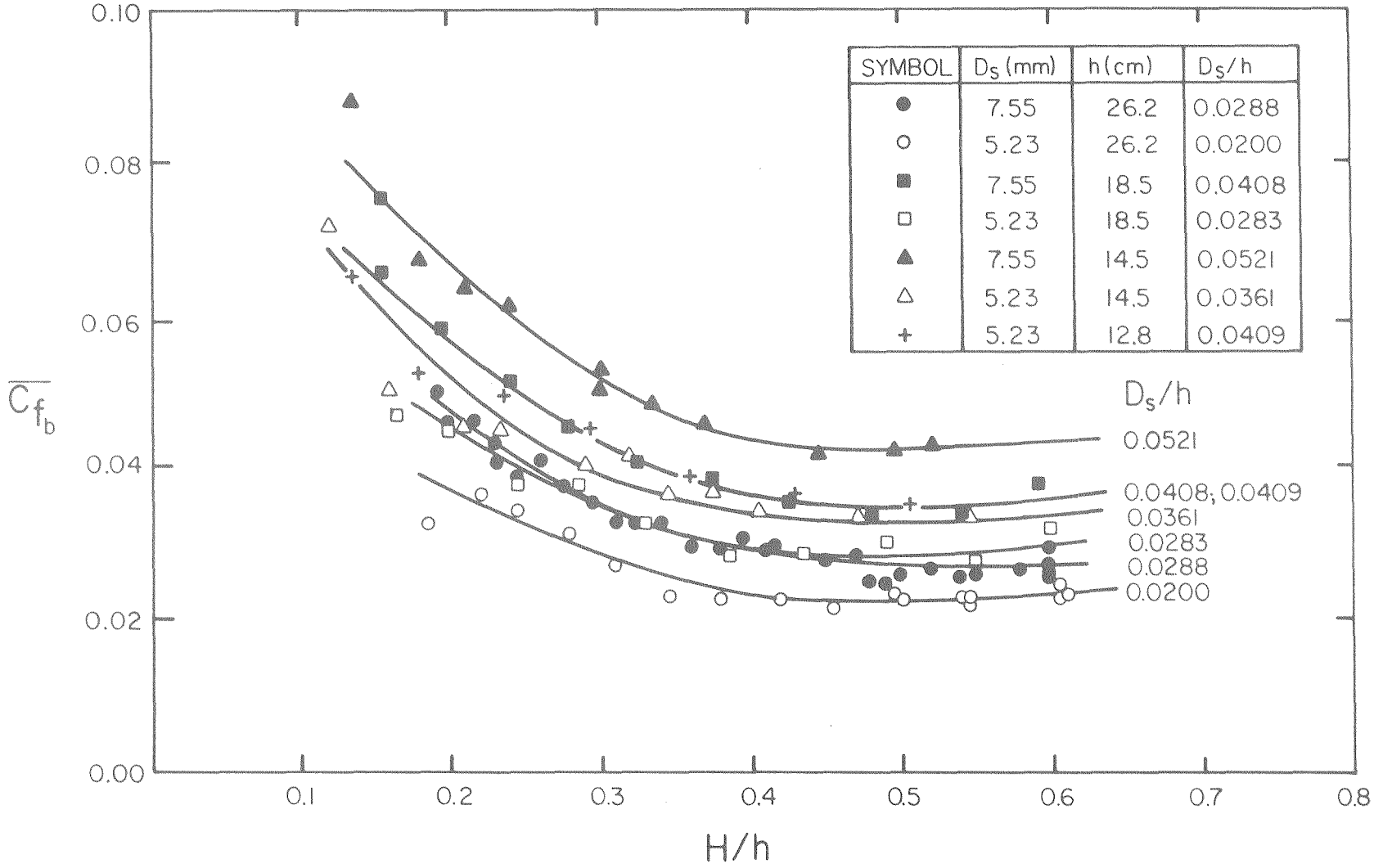

Fig. 5.14 The mean resistance coefficient as a function of the dimensionless lengths H/h and D_s/h.

considered as being turbulent. Hence, the flow must be rough turbulent. However, the example in Section 5.1.3 was given only for a single wave with H/h = 0.49 in 30 cm of water. In the following it is shown from turbulent boundary layer considerations that the flow was rough turbulent throughout the experiments.

Schlichting (1968) showed that the flow may be considered as rough turbulent if

$$\frac{u_* D_s}{\nu} > 70 \quad , \tag{5.13}$$

where $u_* = \sqrt{\tau_b/\rho_w}$ is called the shear velocity, in which τ_b is the bottom shear stress, and ρ_w is the density of the fluid. Assuming (as an approximation) that the bottom shear stress is described by the mean resistance coefficient, i.e.,

$$\tau_b = \frac{1}{2} \rho_w \overline{C_{f_b}} u^2 \quad , \tag{5.14}$$

where $\overline{C_{f_b}}$ is the mean resistance coefficient and u is the fluid particle velocity outside the boundary layer, then for rough turbulent flows, Eq. (5.13) yields

$$\frac{\sqrt{\frac{\overline{C_{f_b}}}{2}} u D_s}{\nu} > 70 \quad . \tag{5.15}$$

Considering the waves that were generated during the experiments, substitution of the fluid particle velocities of these waves (calculated from Eq. (3.8)) with the corresponding mean resistance coefficients (which are given in Appendix II, Table A.2.2) into Eq. (5.15) indicates that all the experiments in the present study were conducted in the

rough turbulent flow regime. Hence it was reasonable to assume that the mean resistance coefficient was independent of the Reynolds number.

In addition, it is noted that the independence of the resistance coefficient of the Reynolds number may also be concluded from dimensional analysis considerations. An inspection of the expressions which describe the various dimensionless parameters involved in the problem (i.e., the Reynolds number, Re (Eq.(3.22), the relative wave height, H/h, and the relative roughness, D_s/h) indicates that it is impossible to simultaneously maintain geometrical and Reynolds number similarities between two models of different geometrical dimensions. This means that if the mean resistance coefficient is the same for two differently sized models which are geometrically similar, then it must be independent of the Reynolds number, because it has the same value for two different Reynolds numbers. Furthermore, maintaining similarity due to Reynolds number implies that there is no geometrical similarity, and since the resistance coefficient is not the same in two models which are not geometrically similar, the same Reynolds number must admit two different resistance coefficients. Since in the present study the mean resistance coefficient was shown to depend only on dimensionless geometrical parameters, it was concluded that it was independent of the Reynolds number. Yet, this conclusion must be considered carefully, since the difference between the Reynolds numbers in two geometrically similar experiments in the present investigation was not large. Considering the sizes of the roughness particles and the water depths used in the experiments, it can be shown (employing Eq. (3.22) that the ratio between the Reynolds numbers in two geometrically similar experiments

was approximately 1.7. Hence, the differences between the Reynolds numbers in the experiments might not be large enough to conclude that the mean resistance coefficient is completely independent of the Reynolds number. The justification for the assumption that the resistance coefficient is independent of the Reynolds number is therefore inconclusive when it is based on dimensional analysis considerations. However, the boundary layer considerations presented earlier in this section seem to have justified this assumption.

The results of the investigation of the mean resistance coefficient under solitary waves were employed in the study of the incipient motion of bottom material which is described in the following section.

5.3 THE INCIPIENT MOTION OF BED MATERIAL

5.3.1 The Incipient Motion of Particles of Arbitrary Shape

The results of the experimental investigation of the incipient motion of material of arbitrary shape are presented in this section. The theoretical considerations presented in Section 3.3.1 suggest that the incipient motion should be a function of a dimensionless shear stress, but as no functional relationship was obtained, the results were obtained experimentally. In the experimental investigation of the incipient motion of spheres, which is presented in the following section, the procedure consisted of an observation of the motion of a single isolated sphere. However, in the investigation of the incipient motion of particles of arbitrary shape it was impractical to consider the motion of a single particle. The reason is that the motion of the particle is affected by its particular shape and placement in the bed,

and observations of the incipient motion of a single particle may not represent the entire bed. The results presented here are from observations of motion in the entire bed, pertaining to the incipient motion of rocks. The amount of motion in the bed, defined as the ratio of the number of moving particles, N_p, to the total number of particles exposed to the flow, N_{p_T}, was measured using the technique described in Section 4.4.3. The experiments were conducted over a sloping bottom with a slope of 1:200. This enabled the generation waves of extreme heights (up to breaking) over the test section. Over a horizontal bottom it was impossible to generate waves with large height-to-depth ratios at large depths. For example, the largest value of H/h obtained in the wave tank over a horizontal bottom at 25 cm of water was approximately 0.55.

Preliminary experiments indicated that the first waves passing over a newly prepared bed caused significant motion of material. This motion decreased with each consecutive wave until it appeared to reach an asymptotic value. The number of moving particles, N_p, is shown as a function of the number of waves, N_W, in Fig. 5.15 for a particular experiment. The decreasing number of moving particles with increasing number of waves is probably due to the manner in which the gravel was loosely packed and leveled in the test section. The bed became more tightly packed as the number of waves to which it was exposed increased, resulting in less motion. Eventually, a condition was reached where the amount of motion (averaged over a certain number of waves) became constant. It appears in Fig. 5.15 that some data points for the amount of motion are not randomly scattered around some optimal curve, but

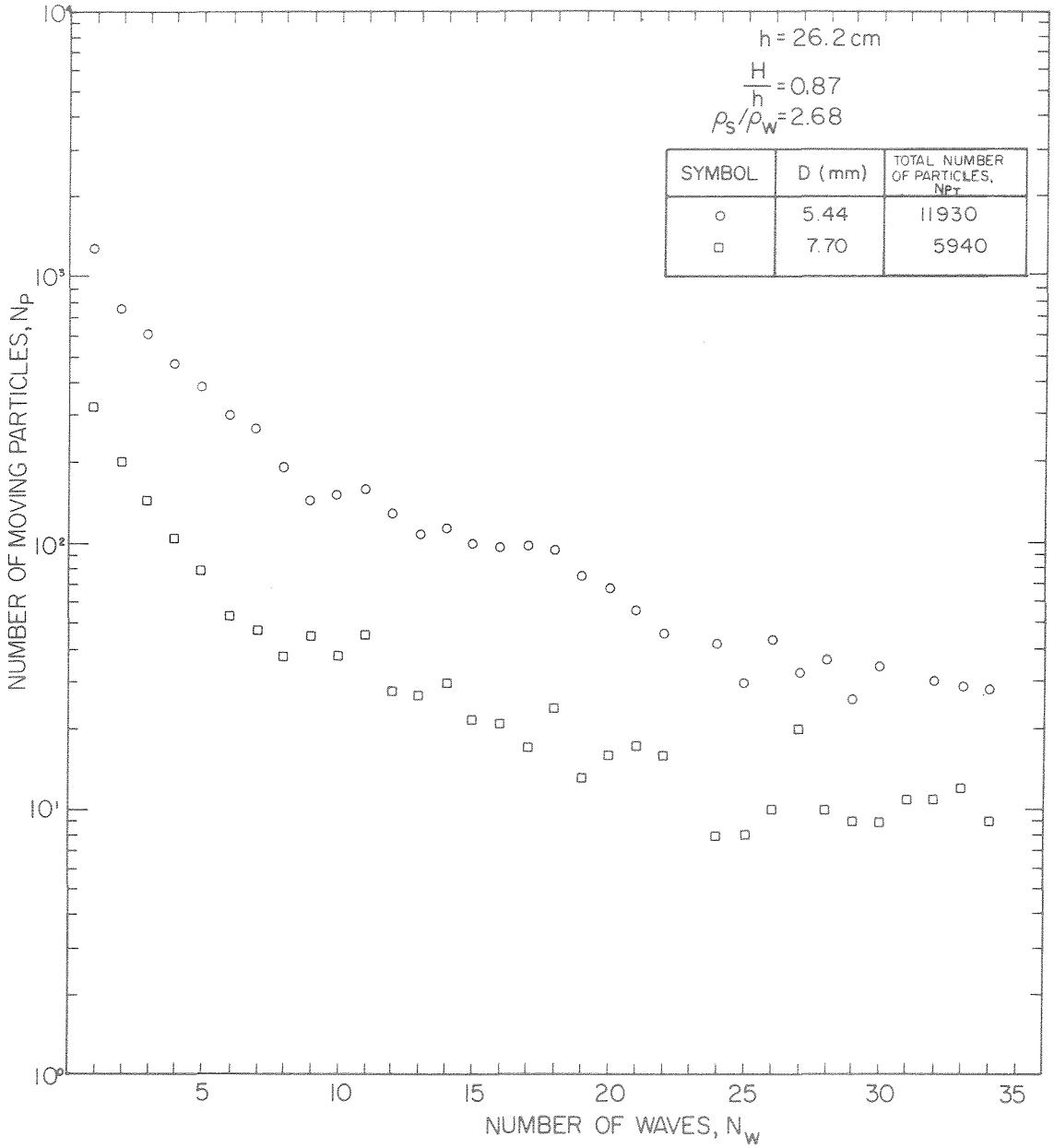

Fig. 5.15 The packing of a granular bed by waves.

oscillate with a period of about five waves. For a very small amount of motion the oscillation is small and the scatter appears more random. The reasons for the oscillatory nature of the data are not known and were not investigated here. The present research was limited to the investigation of the stability of an already packed bed, and not to the process by which the packing develops. Measurements were begun after a large number of waves (100 to 300) had passed over the bed and the packing seemed to be complete. The amount of motion was averaged over fifteen consecutive waves. The reason for having fifteen waves in a sample of measurements lies in the experimental equipment where no more than sixteen photographs (from which the motion was measured, see Section 4.4.3) could be developed in a single processing. These fifteen waves appear to give an adequate sample since they cover more than two cycles of the oscillatory nature of the amount of motion, as seen in Fig. 5.15. The procedure was repeated with a second set of fifteen waves after generating approximately thirty more waves, in order to determine whether the packing of the bed was completed. If the average amount of motion in the two sets of measurements was approximately the same, the process was considered to have reached its asymptotic value, and the bed completely packed.

As the present study consists of an attempt to model the prototype in the ocean, where loose rock pavements are used to protect offshore pipelines, outfalls, etc., it is important to note that the same packing process apparently occurs in nature. The rock is designed to remain stable under a prescribed wave of given height and depth. The design wave is usually very large, and based on statistical calculations, it is

expected to take place in a storm which occurs only once in a period of a prescribed number of years. If the rock pavement is of a limited number of rocks covering a limited area, and the design wave travels over the pavement immediately following its construction, then the wave may destroy the pavement by removing most of the rocks. However, since the design wave occurs only once in a large number of years, it is expected that by the time this wave occurs, the rock should have been exposed to a large number of smaller waves which caused only small motions, and completed the packing of the rock structure.

During the experiments it was noticed that the nature of the bed surface changed significantly while the packing process was taking place. A cross-sectional drawing of the test section in a plane parallel to the direction of the wave propagation is shown in Fig. 5.16a,b. In Fig. 5.16a the bed is shown immediately after placing and leveling the particles in the test section, before beginning the experiments, and the surface of the bed appears to be fairly smooth. During the packing process, the particles which had been removed from their positions were placed in locations where they got locked in, and their orientation with respect to the bed surface was changed. The completely packed bed is shown in Fig. 5.16b, where the bed surface appears to be rough, compared to the surface before beginning the experiments. When running more waves over the bed, the particles which protrude into the flow above their neighbors are subjected to hydrodynamic forces larger than those exerted on their neighbors. Hence, if some motion occurs in the bed, it is assumed that these particles are the first ones that move. The significance of this assumption will be discussed later in this section. It

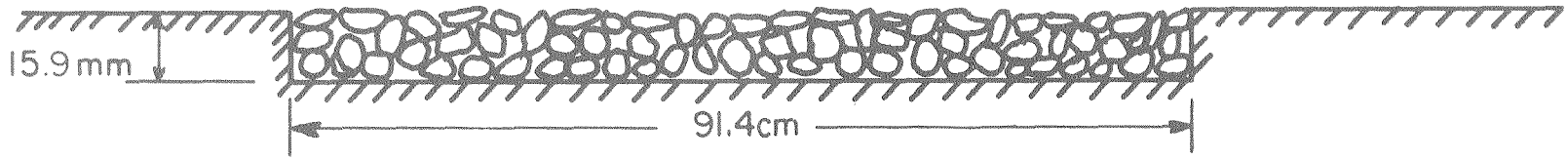

a. Loosely leveled bed (before the experiment)

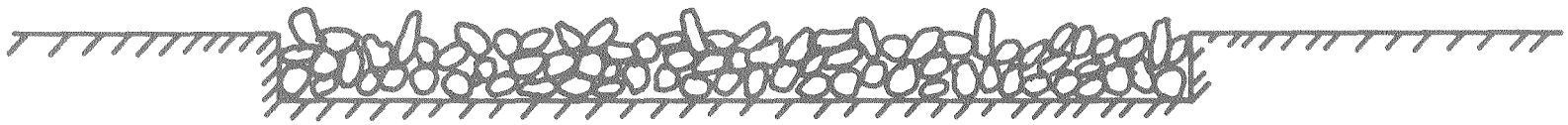

b. Bed completely packed (after the experiment)

Fig. 5.16 Schematic drawing of a cross-sectional view of the bed of particles of arbitrary shape, showing the nature of the bed surface before and after the packing of the bed.

should be noted, however, that this assumption was not verified, as during the experiments it was impossible to detect whether the moving particles indeed were those that protrude above their neighbors.

The experimental data which were obtained with the packed bed, i.e., in which the amount of motion had reached its asymptotic value, are presented in Appendix II, Table A.2.4. The test section and the characteristics of the material used in the experiments are described in Section 4.4.3. The experiments with the natural rock (specific gravity, $\rho_s/\rho_w = 2.68$) were conducted with water depths of 18.5 cm and 26.2 cm, and with wave height-to-water depth ratios (H/h) varying from 0.60 to 0.88. Over the coal ($\rho_s/\rho_w = 1.283$) H/h had values of 0.25 at water depths of 14.5 cm and 26.2 cm, and 0.34 at 14.5 cm of water. The experiments with the coal particles required relatively small waves since larger waves disturbed the structure of the bed significantly and were considered to be destructive.

As noted earlier, theoretical analysis showed that the amount of motion in the bed, N_p/N_{p_T}, is a function of a dimensionless shear stress, τ_*. This dimensionless shear stress, which is similar to the Shields parameter, has the form

$$\tau_* = \frac{\tau_b}{(\rho_s - \rho_w) g D_s} \quad , \tag{5.16}$$

where τ_b is the bottom shear stress, ρ_s and ρ_w are the densities of the bed material and the water respectively, g is the acceleration due to gravity, and D_s is the mean diameter of the particles. The shear stresses exerted on the bed by the waves were evaluated using the

results of the mean resistance coefficient presented in Section 5.2. Substituting $\tau_b = \frac{1}{2} \rho_w \overline{C_{f_b}} u^2$ in Eq. (5.16) yields

$$\tau_* = \frac{\overline{C_{f_b}} u^2}{2\left(\frac{\rho_s}{\rho_w} - 1\right) g D_s} \quad , \tag{5.17}$$

where $\overline{C_{f_b}}$ is the mean resistance coefficient, and u is the fluid particle velocity under the solitary wave, calculated from Eq. (3.8). Since the resistance coefficient used in Eq. (5.17) is only an average value (averaged over the wave), the maximum value of the right-hand side of Eq. (5.17) is obtained by substituting into it the maximum value of the velocity under the wave. For the solitary wave given by Eqs. (3.6), (3.7), and (3.8), the maximum value of Eq. (5.17) yields

$$\tau_{*max} = \frac{\overline{C_{f_b}} h (H/h)^2}{2\left(\frac{\rho_s}{\rho_w} - 1\right) D_s \left(1 + \frac{H}{h}\right)} \quad , \tag{5.18}$$

where τ_{*max} is the maximum value of the dimensionless shear stress, h is the water depth, and H is the wave height. The value of $\overline{C_{f_b}}$ to be substituted in Eq. (5.18) was estimated for given particle diameter, water depth, and wave height from Fig. 5.14. As noted in Section 3.2, this average value, $\overline{C_{f_b}}$, may not necessarily represent the actual resistance coefficient, because of inertia effects, and since the maximum shear stress does not necessarily occur under the wave crest (i.e., at the point of maximum velocity). Therefore, Eq. (5.18) may not give the actual maximum value of the dimensionless shear stress. However, it is

assumed that the actual maximum dimensionless shear stress can be represented by Eq. (5.18) on a comparative basis. This means that the actual dimensionless shear stresses are assumed to be large for cases in which the value of the expression given by Eq. (5.18) is large, and they are assumed to be smaller for smaller values of this expression. Therefore, Eq. (5.18) is considered as describing a representative dimensionless wave shear stress which may be used to define the conditions required for incipient motion of material of arbitrary shape.

The measured values of N_p/N_{p_T} are shown as a function of τ_{*max} in Fig. 5.17. The number printed next to each data point in this figure indicates the total number of experiments in which this same data point was repeated (i.e., the same amount of motion with the same τ_{*max}). These data are also presented in Appendix II, Table A.2.4. The large scatter of data seen in Fig. 5.17 is due to the random nature of the amount of motion and the limited area of the test section. The motion was observed in a total area of 91.4 cm x 50.5 cm, and the total number of moving particles was of order of 10. It was expected that the number of moving particles would vary when repeating the experiment under identical conditions (i.e., the same wave height and water depth) due to the random distribution of the motion over the bed surface. Since the number of the moving particles was small, a slight variation of this number resulted in a large variation of N_p/N_{p_T}, as seen in Fig. 5.17. Presumably, a large test section would yield a larger sampling area with less data scatter.

The experimental data shown in Fig. 5.17 appear to be scattered around some optimal curve displaying the expected trend of increasing amount of motion with the dimensionless shear stress. The optimal

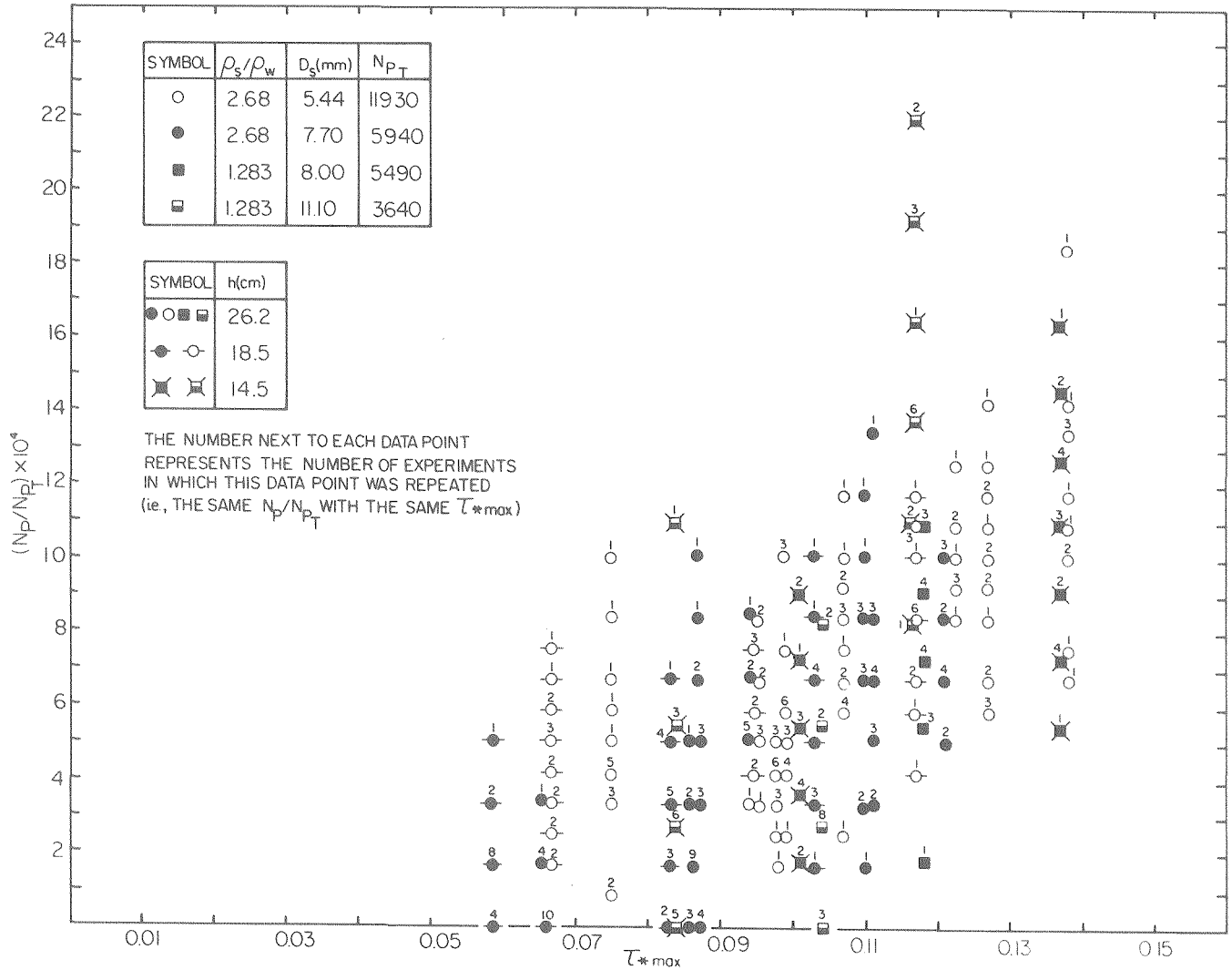

Fig. 5.17 The amount of motion of particles of arbitrary shape as a function of the dimensionless shear stress.

curve is obtained by averaging the amount of motion for each value of τ_{*max} and fitting a curve through the averaged data. The average amount of motion is shown as a function of τ_{*max} in Fig. 5.18. The data are also presented in Table 5.1.

The results of the experiments with the 11.1 mm coal particles at water depth of 14.5 cm under a wave of H/h = 0.335 are seen in Fig. 5.18 to disagree with the rest of the data, as they have a large value of N_p/N_{p_T} at a relatively small value of τ_{*max}. It is assumed that since the total thickness of the coal layer was only 5/8 in. (15.9 mm) the large coal particles could possibly slip over the smooth bottom underneath, resulting in a fairly large amount of motion. Another reason for the discrepancy could lie in the error in evaluating τ_{*max}. In Table 5.1 (Column (5)) it is seen that the range of most of the values of D_s/h is between 0.020 and 0.052 and therefore the values of $\overline{C_{f_b}}$ (Table 5.1, Column (6)) were obtained from interpolation of the curves shown in Fig. 5.14. The value of D_s/h for the 11.1 mm coal particles at h = 14.5 cm is 0.0766 which is beyond the range of the experiments from which $\overline{C_{f_b}}$ was determined. In this case $\overline{C_{f_b}}$ had to be obtained from extrapolation of the curves in Fig. 5.14, and its error is possibly larger than that of the other data points. Yet, the experimental results with the same particles (under waves with H/h = 0.25 at water depths of 14.5 cm and 26.2 cm) do not appear to disagree with the rest of the data like the result with H/h = 0.335 at 14.5 cm of water. The reason for the discrepancy is therefore not completely understood. It is possible that during the packing process, when the first waves passed over the bed, the bed structure was disturbed for some unknown reason, resulting

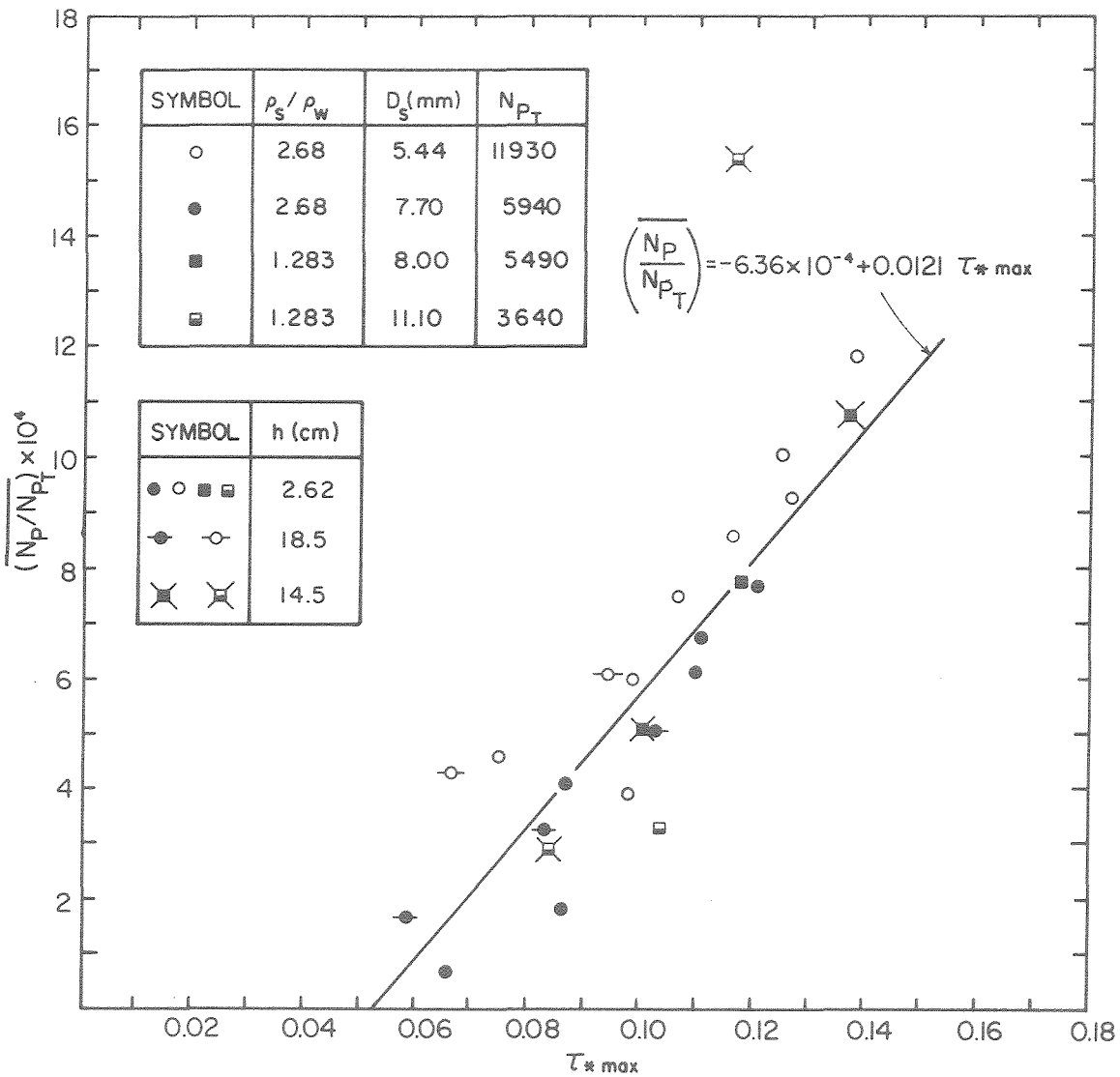

Fig. 5.18 The average amount of motion of particles of arbitrary shape as a function of the dimensionless shear stress.

Table 5.1 Experimental data of the average amount of motion of particles of arbitrary shape.

D_s (mm) (1)	ρ_s/ρ_w (2)	h (cm) (3)	H/h (4)	D_s/h (5)	$\overline{C_{f_b}}$ (6)	τ^*_{max} (7)	Average $\frac{N_p}{N_{p_T}} \times 10^4$ (8)	Std. dev. of $\frac{N_p}{N_{p_T}} \times 10^4$ (9)
5.44	2.68	26.2	0.875	0.0208	0.0235	0.138	11.81	3.30
7.70	2.68	26.2	0.875	0.0294	0.0293	0.121	7.65	1.90
5.44	2.68	26.2	0.824	0.0208	0.0235	0.125	10.06	1.34
7.70	2.68	26.2	0.824	0.0294	0.0293	0.110	6.09	3.40
5.44	2.68	26.2	0.746	0.0208	0.0235	0.107	7.49	2.23
7.70	2.68	26.2	0.746	0.0294	0.0293	0.0945	5.61	1.46
5.44	2.68	26.2	0.829	0.0208	0.0235	0.127	9.28	2.68
7.70	2.68	26.2	0.829	0.0294	0.0293	0.111	6.73	2.46
5.44	2.68	26.2	0.708	0.0208	0.0235	0.0989	5.99	2.48
7.70	2.68	26.2	0.708	0.0294	0.0293	0.0870	4.09	3.28
5.44	2.68	26.2	0.704	0.0208	0.0235	0.0980	3.89	0.96
7.70	2.68	26.2	0.704	0.0294	0.0293	0.0862	1.79	1.35
5.44	2.68	26.2	0.596	0.0208	0.0235	0.0750	4.58	2.45
7.70	2.68	26.2	0.596	0.0294	0.0293	0.0660	0.673	1.064
5.44	2.68	18.5	0.856	0.0294	0.0293	0.117	8.55	2.11
7.70	2.68	18.5	0.856	0.0416	0.0364	0.103	5.05	2.55
5.44	2.68	18.5	0.747	0.0294	0.0293	0.0946	6.09	1.60
7.70	2.68	18.5	0.747	0.0416	0.0364	0.0832	3.25	1.96
5.44	2.68	18.5	0.600	0.0294	0.0293	0.0667	4.30	1.79
7.70	2.68	18.5	0.600	0.0416	0.0364	0.0586	1.68	1.42
8.00	1.283	26.2	0.249	0.0305	0.0410	0.118	7.77	2.53
11.10	1.283	26.2	0.249	0.0424	0.0501	0.104	3.30	2.58
8.00	1.283	14.5	0.253	0.0552	0.0583	0.101	5.10	2.20
11.10	1.283	14.5	0.253	0.0766	0.0712	0.0839	2.93	3.02
8.00	1.283	14.5	0.335	0.0552	0.0487	0.137	10.71	3.15
11.10	1.283	14.5	0.335	0.0766	0.0600	0.117	15.38	4.13

in a large asymptotic value for the amount of motion. This point is ignored in fitting the curve to the data in Fig. 5.18.

The curve through the data in Fig. 5.18 was obtained using a least-squares fit technique. Assuming that $\overline{N_p/N_{p_T}}$ is described by a straight line,

$$\left(\frac{\overline{N_p}}{N_{p_T}}\right) = a + b\tau_{*max} \quad , \tag{5.19}$$

and employing the least-squares fit formulation, i.e.,

$$\sum_{i=1}^{N_d} [(\overline{N_p/N_{p_T}})_i - (a + b\tau_{*max_i})]^2 = \text{minimum} \quad , \tag{5.20}$$

in which N_d is the number of data points, the values of a and b were found to be $a = -6.36\text{x}10^{-4}$, and $b = 1.21\text{x}10^{-2}$. The curve in Fig. 5.18 is then described by

$$\left(\frac{\overline{N_p}}{N_{p_T}}\right) = -6.36\text{x}10^{-4} + 0.0121\ \tau_{*max} \quad . \tag{5.21}$$

Following the procedures of error analysis (e.g., see Bevington (1969)), it was found that the standard deviations of the coefficients a and b (due to the scatter of data shown in Fig. 5.18) are $\sigma_a = 1.27\text{x}10^{-4}$, and $\sigma_b = 1.24\text{x}10^{-3}$. These values will later be used to describe the possible errors in determining the diameter of the rock designed for incipient motion. Considering the incipient motion to be defined as the event in which $\overline{N_p/N_{p_T}} = 0$, it is found from Eq. (5.21) that at incipient motion $\tau_{*max} = 0.053$. By employing Eq. (5.18), this value can be used to design the rock for incipient motion, when the wave height, the water

depth, and the specific gravity of the rock are given. Furthermore, if some amount of motion in the bed is allowed, the corresponding value of τ_{*max} which is evaluated from Eq. (5.21) can be substituted into Eq. (5.18) to design the rock for the allowed amount of motion. In order to estimate the diameter of the rock, Eq. (5.18) is rewritten in the form

$$\frac{D_s}{h} = \frac{\overline{C_{f_b}} \, (H/h)^2}{2\tau_{*max}\left(\frac{\rho_s}{\rho_w} - 1\right)\left(1 + \frac{H}{h}\right)} \quad . \tag{5.22}$$

Note that the mean resistance coefficient in Eq. (5.22) is a function of H/h and D_s/h (see Section 5.2, Fig. 5.14). Unless the functional relationship between $\overline{C_{f_b}}$, H/h, and D_s/h is given explicitly, Eq. (5.22) will have to be solved by trial and error. A study of the variation of $\overline{C_{f_b}}$ with D_s/h for a given value of H/h as shown in Fig. 5.14 resulted in an empirical relationship, expressed as

$$\overline{C_{f_b}} = K^*\left[\left(\frac{H}{h}\right)\right]\left(\frac{D_s}{h}\right)^{0.63} \quad , \tag{5.23}$$

where $K^*\left[\left(\frac{H}{h}\right)\right]$ denotes a function of H/h. Numerical values of K* for given values of H/h were obtained from the empirical relationship. For $H/h > 0.45$ it was found that $K^* = 0.27$. This value, substituted in Eq. (5.23) is used in the following example.

Consider a rock with specific gravity, $\frac{\rho_s}{\rho_w} = 2.65$, and determine the ratio of its diameter to the water depth (D_s/h), required for incipient motion, under a wave with a height-to-depth ratio, $\frac{H}{h} = 0.75$. As noted earlier, it was found from Eq. (5.21) that $\tau_{*max} = 0.053$ at incipient motion. Substituting this value, combined with the given values of H/h, ρ_s/ρ_w, and Eq. (5.23) into Eq. (5.22) yields $D_s/h = 0.150$. In

considering this value of D_s/h for incipient motion of the rock it is necessary to point out possible errors in its evaluation. First, it was noted in Section 5.2 that the largest value of D_s/h for which the mean resistance was obtained was 0.052. Hence, the empirical relationship described by Eq. (5.23) may not be valid for $D_s/h = 0.150$, for which it was used in the present example. Second, an error in the value of τ_{*max} at incipient motion is expected due to the scatter of data shown in Fig. 5.18. Assuming that this error is defined by the standard deviation of the coefficients a and b in Eq. (5.19)(where it was found that $a = -6.36\text{x}10^{-4}$, $\sigma_a = 1.27\text{x}10^{-4}$, $b = 1.21\text{x}10^{-2}$, and $\sigma_b = 1.24\text{x}10^{-3}$), it follows that at incipient motion $\tau_{*max} = 0.053 \pm 0.011$, i.e., an error of approximately ±20%. Considering the above example (i.e., $\frac{\rho_s}{\rho_w} = 2.65$, and $\frac{H}{h} = 0.75$), for $\tau_{*max} = 0.042$, Eq. (5.22) yields $\frac{D_s}{h} = 0.282$. Thus an error of 20% in τ_{*max} (from 0.053 to 0.042) results in an approximately 90% error in estimating $\frac{D_s}{h}$ (from 0.150 to 0.282). For $\tau_{*max} = 0.064$ Eq. (5.22) yields a value of 0.090 for $\frac{D_s}{h}$. Here an error of 20% in τ_{*max} results in a 40% error in $\frac{D_s}{h}$. Again, note that the value of the mean resistance coefficient used in both of these examples may be inaccurate due to the values of D_s/h for which it was used. Consider the above example for a wave with $H/h = 0.50$. This yields $D_s/h = 0.0255$ for incipient motion. This is within the range of D_s/h used in the investigation on the resistance coefficient, hence it might be expected that the error in this value of D_s/h is smaller than that in the preceding example. However, even when D_s/h is sought for the case where $\overline{C_{f_b}}$ does not have to be found by extrapolation, it can be shown that a small error in τ_{*max} results in a large error in D_s/h for incipient motion. Substitution of Eq. (5.23) into Eq. (5.22) indicates that $\frac{D_s}{h} \sim \left[\frac{f(H/h)}{\tau_{*max}}\right]^{2.70}$ for all values of H/h and D_s/h, and an error of ±20% in τ_{*max} results in -39% and +83% error in D_s/h from this relationship.

Two conclusions can be drawn from the preceding example. First, so far as incipient motion of natural rock under waves of large relative height is concerned, it appears that the range of D_s/h which was used to estimate the mean resistance coefficient is inadequate. Second, although a discrepancy of 20% in estimating the dimensionless shear stress for incipient motion may not be considered as being too large, it results in a large error in estimating the diameter of the rock. It concludes that the results obtained from observing the motion of particles of arbitrary shape and correlating this motion to a dimensionless shear stress is inadequate when used to design the rock for incipient motion. Now, earlier in this section it was assumed that the moving particles are those which protrude above their neighbors into the flow region. Since the forces exerted on these particles are larger than those exerted on their neighbors, and as these forces include inertia and lift components which are not described by the mean resistance coefficient, it is possible that the mean resistance coefficient may not be used to represent these forces. In this case the physical conditions of a moving particle resemble those of an isolated sphere, as presented in Section 3.2.3, Fig. 3.2. The results of the investigation of the incipient motion of a single sphere resting on top of a bed of spheres are presented in the following section, and a correlation between these results and those of the incipient motion of particles of arbitrary shape are presented in this section.

5.3.2 The Incipient Motion of Spheres

The results of the theoretical and experimental investigations of the incipient motion of an isolated sphere resting on a horizontal bed of well-packed spheres are presented in this section.

The theoretical considerations have been discussed in Sections 3.2.3 and 3.3.2, and are used to predict the wave height that would cause incipient motion of a particular sphere when the water depth and the diameter of the bed spheres are given. The relationship describing the incipient motion is given by Eq. (3.60) which, with the aid of Eqs. (3.55) and (3.59), is expressed as

$$\frac{\left[\frac{3}{4}(C_D + C_L\tan\phi) + C_M \frac{D_s}{u^2}\frac{du}{dt}\right] u^2}{\left(\frac{\rho_s}{\rho_w} - 1\right) gD_s\tan\phi} = 1 \qquad (5.24)$$

in which C_D, C_L, and C_M are the drag, lift, and inertia coefficients respectively, describing the drag, lift, and inertia force components used in evaluating the hydrodynamic moment exerted on the sphere; D_s is the diameter of the isolated sphere; u is the fluid particle velocity, estimated from the solitary wave theory at the level of the sphere in its absence; t is the time; ρ_s and ρ_w are the densities of the isolated sphere and the water respectively; g (= 981 cm/sec^2) is the acceleration due to gravity; and ϕ is the angle between a normal to the bed and the moment arm passing through the point of force action and the axis around which the hydrodynamic moment tends to move the sphere. The diameter and the density of the isolated sphere, and the density and the depth of the water are considered as being given. Assuming that the hydrodynamic forces act at the center of the isolated sphere, then for a given diameter of the bed spheres, D_B, the angle ϕ is defined by the ratio D_s/D_B, and by the positioning of the isolated sphere on top of the bed with respect to the direction of the horizontal components of the

hydrodynamic force (which is assumed to be parallel to the direction of wave propagation). A description of the two positions studied in the present investigation is given in Section 4.4.2, Fig. 4.13, and is also shown in Fig. 5.19 in an isometric drawing. The geometry yields, for position I,

$$\tan\phi_1 = \frac{1}{\sqrt{3\left(\frac{D_s}{D_B}\right)^2 + 6\,\frac{D_s}{D_B} - 1}} \quad , \tag{5.25}$$

and for position II,

$$\tan\phi_2 = \frac{2}{\sqrt{3\left(\frac{D_s}{D_B}\right)^2 + 6\,\frac{D_s}{D_B} - 1}} \quad . \tag{5.26}$$

The values of ϕ_1 and ϕ_2 are plotted as a function of D_s/D_B in Fig. 5.19.

The coefficients appearing in Eq. (5.24) have the following values. The inertia and lift coefficients were calculated analytically for a sphere which is in contact with a smooth wall in an ideal fluid, and were assumed to represent the values of C_M and C_L in the present study. These calculations are presented in Appendix I, and they yield values of 1.7 for C_M (Eq. (A.1.18)), and 0.42 for C_L (Eq. (A.1.19)). In estimating the drag coefficient, it was assumed that an instantaneous Reynolds number in an unsteady flow defines an instantaneous drag coefficient by the same relationship in which the drag coefficient is defined by the Reynolds number in steady flows. Thus, when a wave height and the water depth are assumed, the distribution of the velocity, u, along the wave is calculated from the solitary wave theory (see Section 3.1, Table 3.1). An instantaneous sphere Reynolds number, $Re_s = \frac{uD_s}{\nu}$, in which ν is the

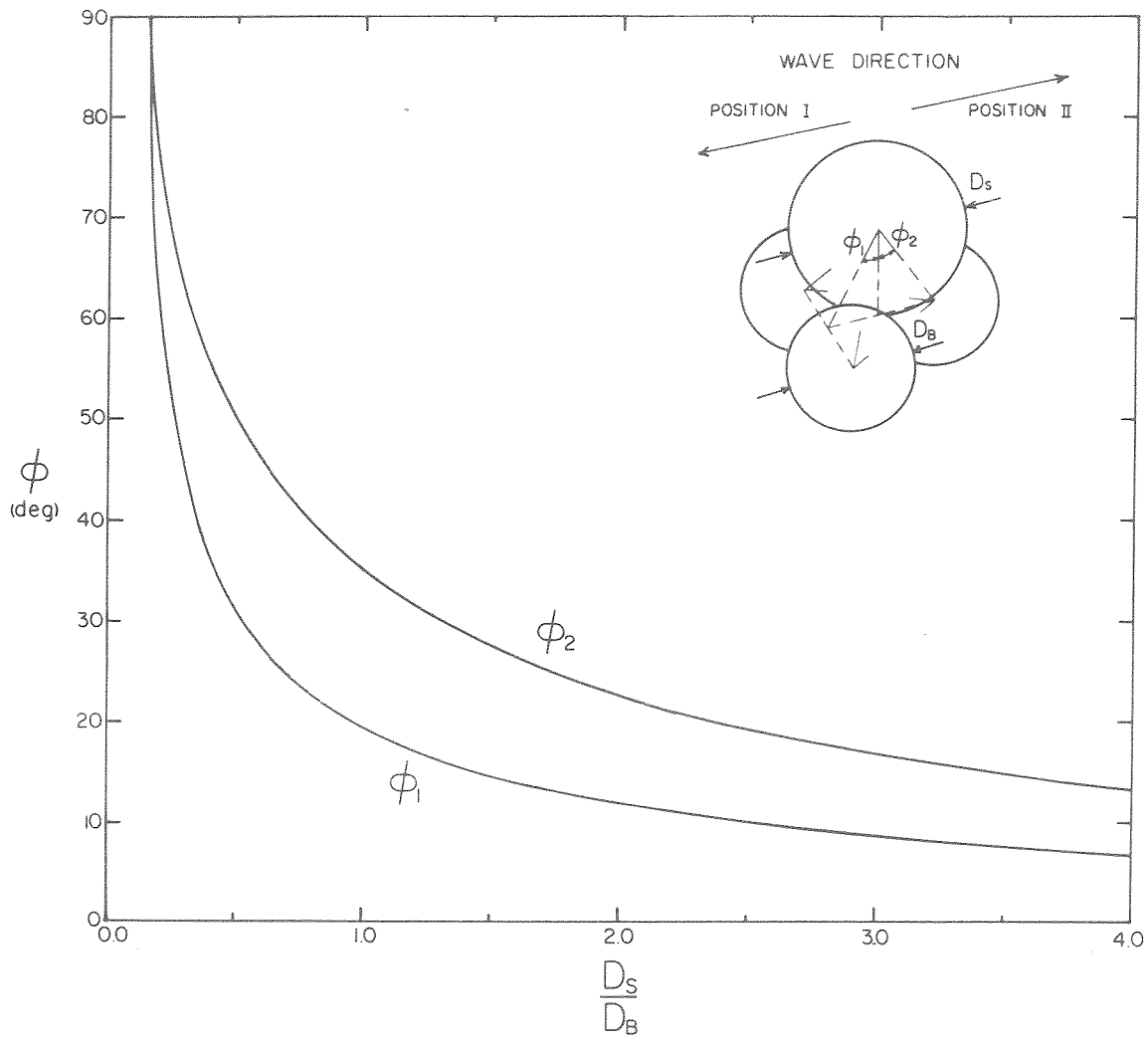

Fig. 5.19 The angles ϕ_1 and ϕ_2.

kinematic viscosity of the fluid, is evaluated from the velocity distribution, and the corresponding drag coefficient, C_D, is obtained from charts which are used for steady flows (e.g., see Schlichting (1968), p. 17).

The wave height that would cause incipient motion is obtained analytically by trial and error, as follows. A wave height is assumed (where D_s, ρ_s, ρ_w, ϕ, and h are given), and the distribution along the wave of the ratio of the hydrodynamic moment, M_H, to the restoring moment, M_R, is calculated from the left-hand side of Eq. (3.24). The maximum value of M_H/M_R is compared to unity. If $\frac{M_{H_{max}}}{M_R} > 1$, where $M_{H_{max}}$ is the maximum value of the hydrodynamic moment, the sphere will move. The procedure is repeated assuming different values of wave heights until a wave is obtained, for which $\frac{M_{H_{max}}}{M_R} = 1$. The procedure is explained schematically in Fig. 5.20, where the maximum value of M_H/M_R is shown as a function of H/h for two given spheres (given D_s and ρ_s/ρ_w) at given water depths and angles ϕ. The fluid particle velocities and accelerations for the examples shown in Fig. 5.20 were calculated using Boussinesq's (1872) theory for the solitary wave. As could be expected, Fig. 5.20 indicates that a light sphere requires a wave of small relative height for incipient motion; and a heavier sphere, posed at a larger angle ϕ, requires a higher wave for incipient motion.

The distribution of moments and forces under the waves that are predicted to cause incipient motion for the two cases shown in Fig. 5.20 presented in Fig. 5.21a,b. The abscissa is $\frac{X}{h}\sqrt{\frac{3H}{4h}}$ where X is a coordinate moving with the wave (X = x=Ct, in which x is a stationary horizontal coordinate, C is the wave celerity, and t is the time). There are three

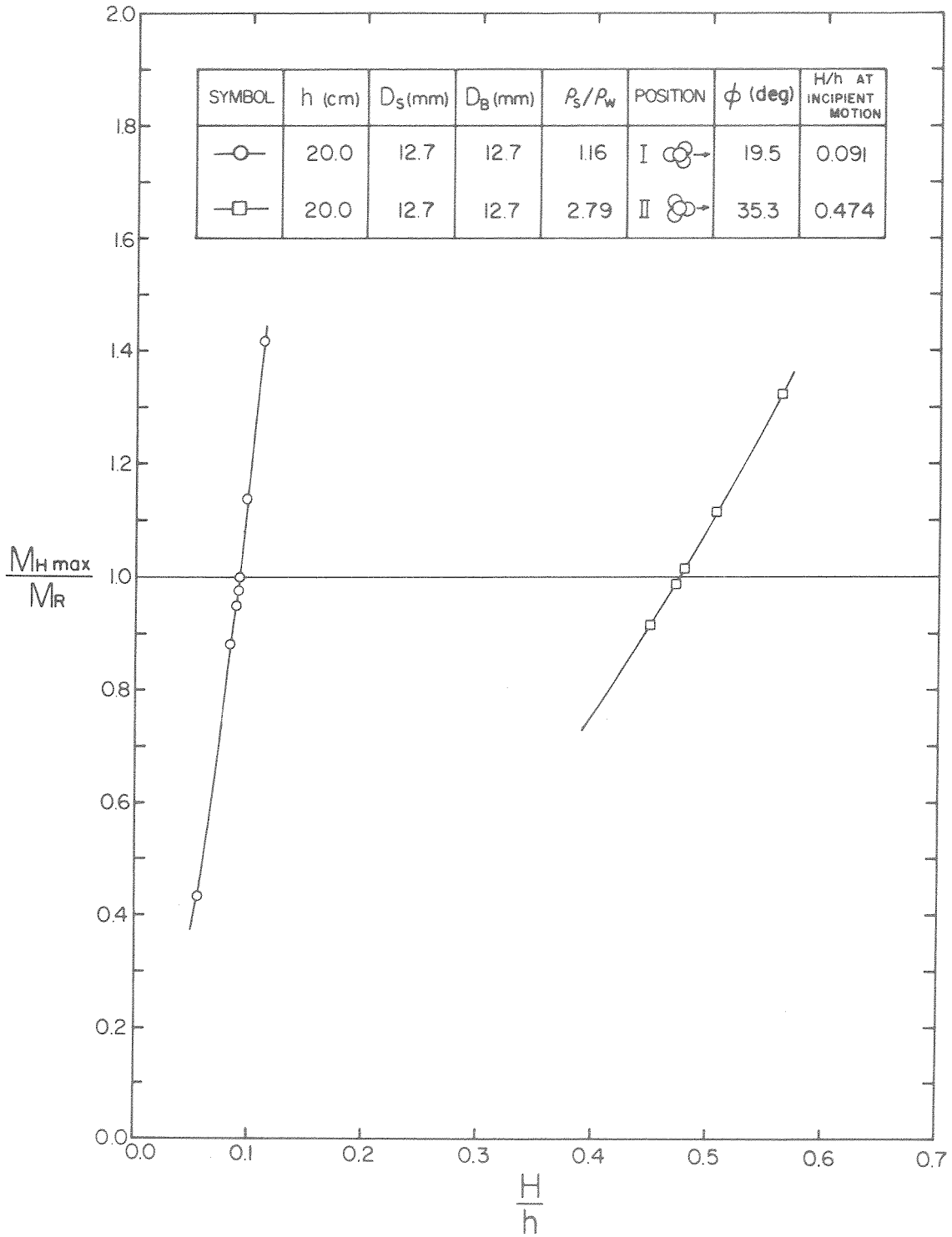

Fig. 5.20 A graphic illustration of the trial and error procedure used to determine the wave that causes incipient motion.

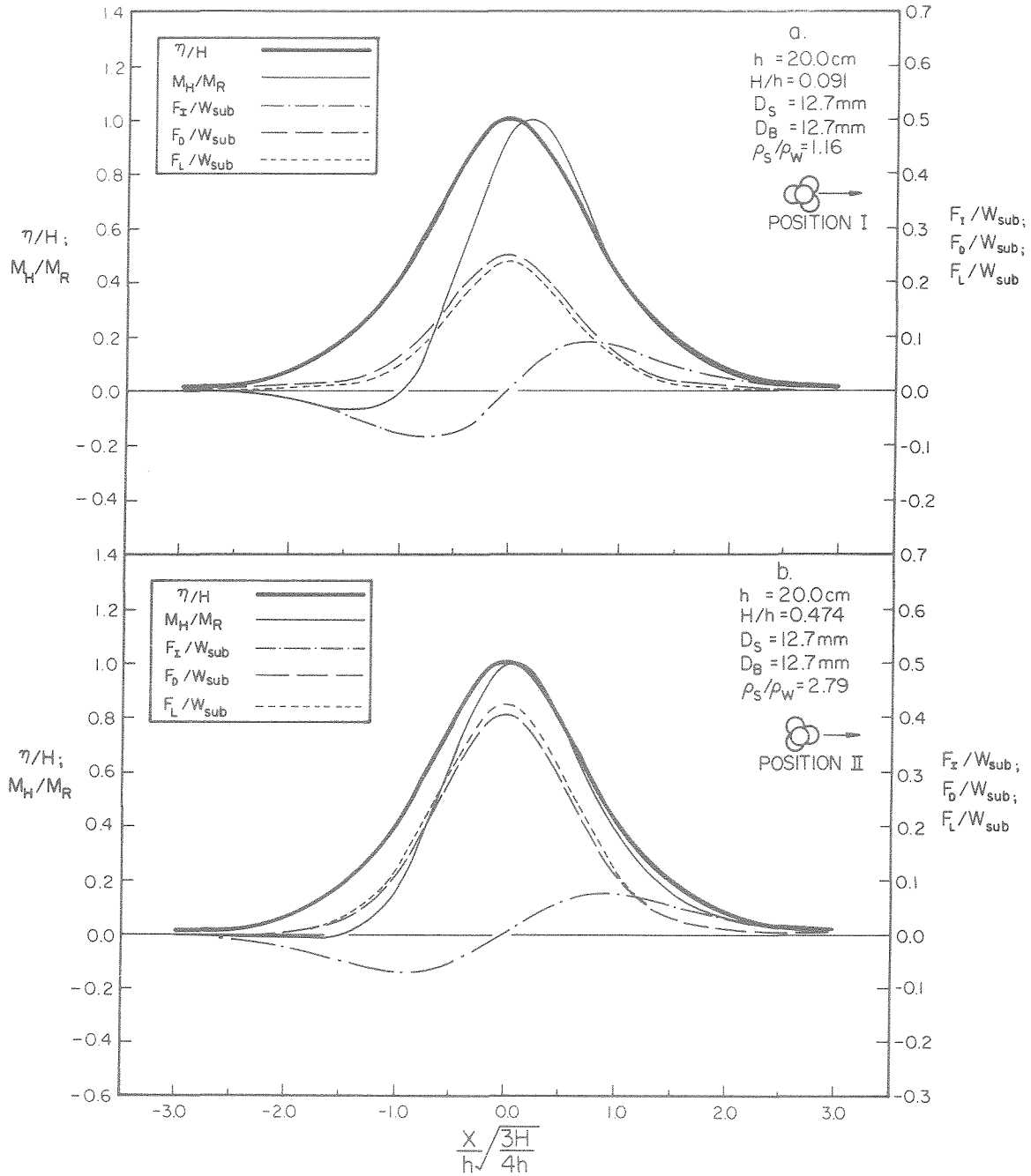

Fig. 5.21 The distribution of forces and moments exerted on a sphere under solitary waves at incipient motion of the sphere (using Boussinesq's theory).

ordinates: one ordinate represents the surface elevation normalized by the wave height (η/H); the second describes the hydrodynamic forces (calculated from Eqs. (3.51) and (3.52)) normalized by the submerged weight of the sphere, and is denoted by $\frac{F_D}{W_{sub}}$, $\frac{F_I}{W_{sub}}$, and $\frac{F_L}{W_{sub}}$, where W_{sub} is the submerged weight of the sphere, and F_D, F_I, and F_L are the drag, inertia, and lift forces respectively; the third ordinate describes the distribution of moments and is denoted by $\frac{M_H}{M_R}$. Note that the drag and lift forces are symmetrical about the centerline of the wave, and the inertia force is anti-symmetric, being positive under the wave front and negative under the rear of the wave. This is due to the distribution of the velocity, which is symmetric, and the acceleration, which is anti-symmetric, under the solitary wave. The combination of moments due to the hydrodynamic forces results in a shift of the maximum hydrodynamic moment towards the wave front. This means that incipient motion is expected to occur under the wave front, at the point where $\frac{M_H}{M_R} = 1$.

As can be seen in Figs. 5.21a,b, the hydrodynamic moment has negative values under the trailing edge of the wave. A backwards motion of the sphere could therefore be expected for cases where the angle ϕ_1, towards the negative X, is much smaller than ϕ_2 in the direction of positive X. This is particularly important for a sphere placed on a sloping bottom, where the restoring moment against motion down the slope decreases for increasing slopes. However, such cases have not been studied in the present investigation.

Note also that the lift and drag forces are of the same order of magnitude. This is because the drag and lift coefficients are

approximately equal. For the higher wave (Fig. 5.21b), the sphere Reynolds number is of order of 10^3, where $C_D = 0.4$, which is slightly smaller than the lift coefficient ($C_L = 0.42$). The lift force under the crest is therefore slightly larger than the drag. For the smaller wave (Fig. 5.21a), the sphere Reynolds number is smaller than 10^3 and the drag coefficient is greater than 0.4, resulting in drag forces slightly larger than lift.

For both cases shown in Figs. 5.21a,b the maximum value of the inertia forces is smaller than the maximum drag and lift, indicating that inertia forces are less important than lift and drag. However, the ratio between inertia and drag forces is larger for the smaller waves. This means that inertia effects relative to drag and lift are more important for smaller waves. The ratio of inertia effects to drag and lift effects is described by the dimensionless acceleration $\frac{D_s}{u^2}\frac{du}{dt}$ in Eq. (5.24). The expressions for the dimensionless acceleration which were given in Section 3.2.1 (Eqs. (3.27) and (3.28)) show that for a given sphere diameter and water depth, $\frac{D_s}{u^2}\frac{du}{dt}$ increases for decreasing wave heights.

It should be noted that the examples shown in Figs. 5.20 and 5.21 were considered applying Boussinesq's (1872) theory for the solitary wave, and the conclusions which were drawn regarding the magnitude of the inertia forces relative to drag and lift forces were based on these considerations (in addition to the assumptions regarding the magnitude of inertia, lift, and drag coefficients; these assumptions will be discussed later). These considerations were justified by measurements of surface profiles, wave celerities, and fluid particle velocities of

solitary waves (see Section 5.1). However, it was noted that McCowan's (1891) theory, combined with Boussinesq's expression for the wave celerity, also describes the solitary wave fairly accurately. In the following it is shown that the two theories are quite different when used to estimate the hydrodynamic forces and moments exerted on the sphere.

In Section 5.1.3 it was shown that the fluid particle velocity, as calculated from McCowan's theory, is smaller under the crest than that calculated from Boussinesq's theory. That was only a single example, in which a wave with h = 30 cm and H/h = 0.49 was considered. However, it can be shown that Boussinesq's theory predicts larger fluid particle velocity than McCowan's theory for all values of H/h. For small values of H/h the differences between the fluid particle velocities calculated from the two theories are small, and they increase with increasing values of H/h. It follows that for cases where drag and lift are dominant, Boussinesq's theory predicts larger hydrodynamic moments (due to larger fluid particle velocities and larger forces) than those predicted from McCowan's theory for the same wave. Hence, Boussinesq's theory predicts that incipient motion would occur under a smaller wave than that predicted by McCowan's theory.

The hydrodynamic forces and moments exerted on the same spheres, under the same waves, and at the same positionings as those considered in Fig. 5.21 are shown in Figs. 5.22a,b as calculated using McCowan's theory for the solitary wave. In Figs. 5.21b and 5.22b, where H/h = 0.474, it is seen that lift and drag forces are dominant, and indeed McCowan's theory predicts a maximum hydrodynamic moment which is

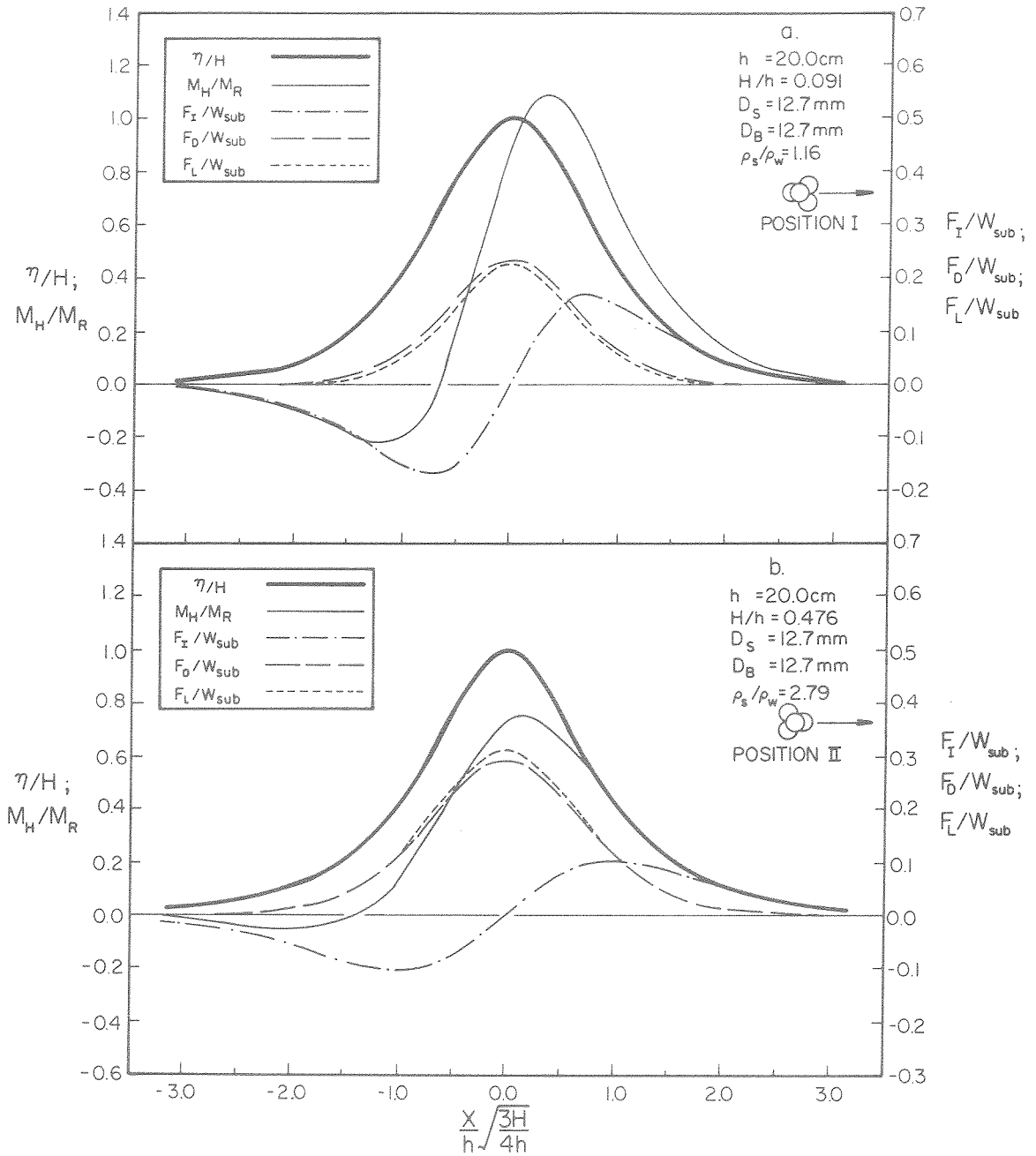

Fig. 5.22 The distribution of forces and moments exerted on a sphere under solitary waves (using McCowan's theory).

approximately 25% smaller than that predicted by Boussinesq's theory. It is important to note that while the differences between Boussinesq's and McCowan's theories may be small when used to estimate the fluid particle velocity, u, these differences are enlarged when used to describe the term u^2. Hence, large differences between these theories are expected when they are used to estimate the lift and drag forces, since the expressions for these forces contain the term u^2. For the wave of small relative height (H/h = 0.091), which is shown in Figs. 5.21a and 5.22a, it appears that the differences between the two theories in predicting drag and lift forces are small, since the differences in the estimated fluid particle velocities are small. However, the fluid particle acceleration, and hence the inertia forces, as calculated from McCowan's theory are much larger than those predicted by Boussinesq's theory. In this case the combination of drag, lift, and inertia forces result in hydrodynamic moments which are larger when calculated from McCowan's theory. For both theories the ratio of maximum inertia force to maximum drag decrease with increasing H/h. However, this ratio is much larger when calculated from McCowan's theory than from Boussinesq's, and when considering the inertia effects on the hydrodynamic forces as being described by this ratio, conclusions regarding these effects will be significantly different, depending on the theory used. It concludes that although the theories of Boussinesq and McCowan describe the fluid particle velocity and the surface profile of a solitary wave fairly accurately, it is not known how well they describe the fluid particle acceleration. Hence, they may be inadequate when used to calculate the forces exerted on bottom material and to predict its incipient motion.

It is important to note that the examples on which the preceding discussion was based were considered with the following assumptions: (a) It was assumed that all the forces exerted on the sphere act at its center; (b) It was assumed that the inertia and lift can be described by the same coefficients as those of a sphere touching a smooth wall in an ideal fluid--note that the values of these coefficients are only approximate ones, since the theoretical considerations are inaccurate when the sphere is very close to the wall (see Appendix I); (c) It was assumed that the instantaneous drag coefficient in an unsteady flow can be described by an instantaneous Reynolds number with the same relationship used for steady flows; (d) It was assumed that the drag coefficient for a sphere resting on the bottom is the same as that for a sphere in an unbounded fluid; (e) The velocity profile in the boundary layer at the bottom was neglected, assuming that the boundary layer thickness is small compared to the diameter of the sphere. Hence, the velocity, u, is given by the wave theory, as presented in Section 3.1. The validity of these assumptions will be discussed later, in view of the experimental results.

The incipient motion was determined both theoretically and experimentally for the sixteen spheres shown in Fig. 4.12. The spheres were considered at both the positions shown in Fig. 5.19 on beds with sphere diameters of 9.53 mm and 12.7 mm with water depth varying from 10 cm to 42 cm. The diameter of each sphere was measured with a micrometer and its specific gravity was evaluated by dividing its weight in air by the difference between its weight in air and in water. The wave height which caused incipient motion of the isolated sphere was found experimentally

using the technique described in Section 4.4.2. The incipient motion was defined to occur when the sphere moved 1/40 mm or less and fell back to its original position (see Fig. 4.17). Note from Fig. 4.17 that the phase under the wave at which the motion occurs is consistent with the theoretical approach that predicts maximum hydrodynamic moment under the wave front.

The observed and predicted values of H/h at incipient motion are shown in Fig. 5.23 as a function of D_s/D_B for given values of h, D_B, ρ_s/ρ_w, and position. The experimental data are also presented in Appendix II, Table A.2.1. The theoretical values were obtained to a maximum value of H/h = 0.9. Waves of limiting heights, before breaking, do not reach this value. Thus, if the sphere was predicted not to move under waves of such a relative height it was deduced that it would not move at all. The largest value of H/h recorded during the experiments was H/h = 0.67 for waves traveling over a horizontal bottom. Waves before breaking over a sloping bottom reached a maximum relative height of 0.77 over a slope of 0.1% and 0.88 over a slope of 0.5%. The theoretical results shown in Fig. 5.23 were evaluated using the theoretical velocity distribution of both McCowan and Boussinesq (see Table 3.1). The wave celerity in both cases was calculated using only Boussinesq's theory, as it was shown to agree better with experiments (see Section 5.1, Fig. 5.8). As can be seen in Fig. 5.23 the relative heights (H/h) predicted to cause incipient motion using McCowan's theory are substantially different from those predicted using Boussinesq's theory, particularly for large values of H/h. For spheres made of light materials (nylon and phenolic), which require waves of small relative

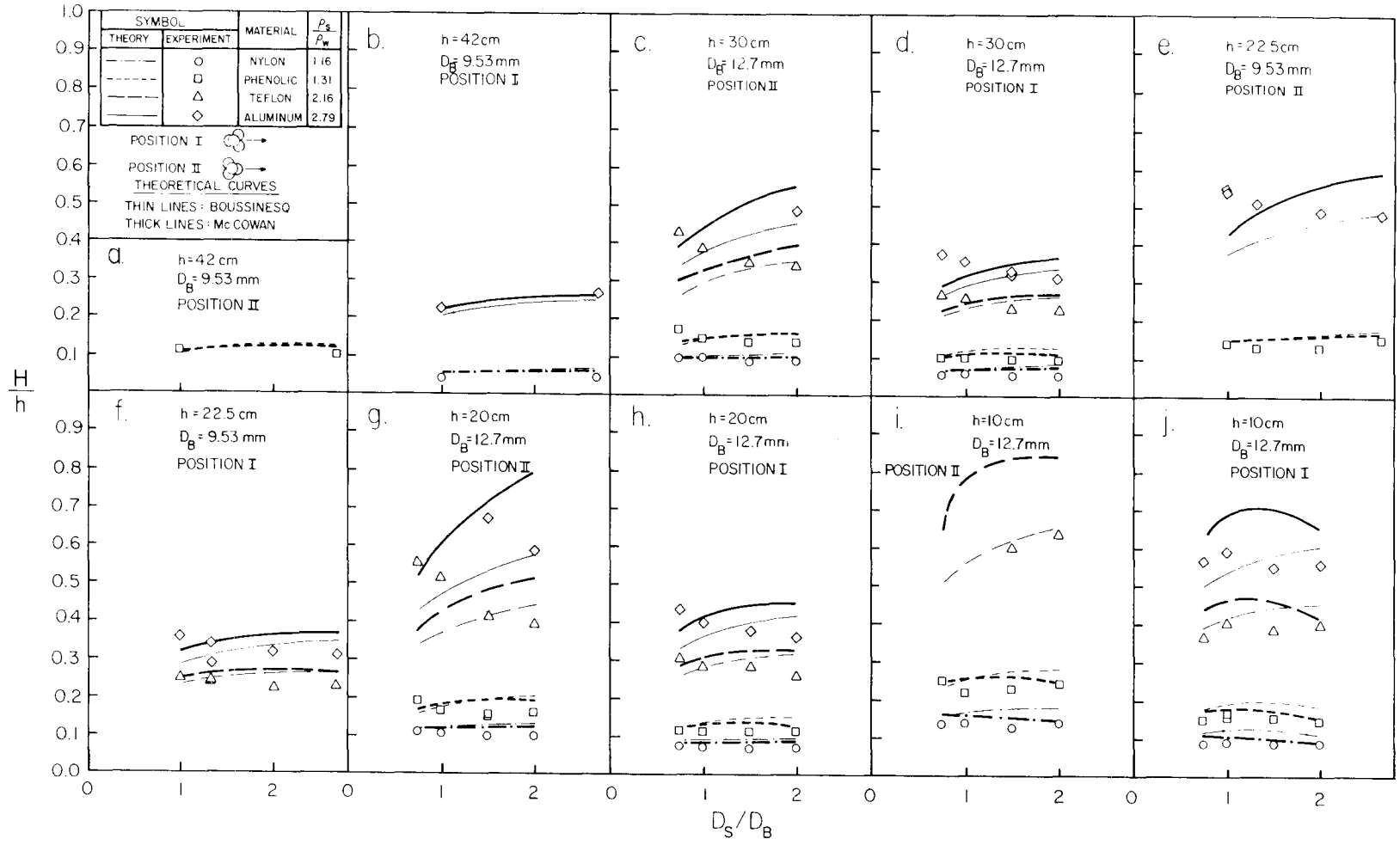

Fig. 5.23 Comparison between the experimental results of the incipient motion of spheres and between the theoretical predictions using Boussinesq's and McCowan's theories.

height for incipient motion, the differences between the two theories are small. For these cases the predicted values of H/h agree fairly well with the observed ones. For spheres made of teflon and aluminum, which require relatively large waves for incipient motion the differences in using Boussinesq's or McCowan's theory reach values of 30% of the relative height predicted by McCowan's theory. As noted earlier in this section, these differences are due to the differences between the two theories in estimating the fluid particle velocity and acceleration. The experimental results for large values of H/h appear in Fig. 5.23 to disagree with the theoretical predictions. Due to the differences between the theories of Boussinesq and McCowan it seems impossible to conclude that the theoretical considerations (i.e., the assumed point of force action, the assumed values of drag, inertia, and lift coefficients, etc.) are incorrect, as the deviations of the experimental data points from the theoretical curves are of the same order of magnitude as the differences between the two theories. However, in most of the cases shown in Fig. 5.23, the wave height at incipient motion is theoretically predicted to increase with increasing D_s/D_B (for given h, ρ_s/ρ_w, position, and D_B), and the experimental data show the opposite trend. This clearly indicates that the assumptions on which the theory is based are inaccurate. These assumptions are reviewed as follows.

First, it was assumed that the velocity distribution at the level of the sphere is given by the free stream velocity calculated from the wave theory, neglecting the effects of the boundary layer on the magnitude of this velocity in the vicinity of the bottom. This assumption was justified by the measurements of the fluid particle velocity

over a rough bed (see Section 5.1.3), which indicated that the fluid particle velocity in the proximity of the bed is represented fairly well by the free stream velocity. However, the lower portion of the isolated sphere is sheltered from the flow by the supporting bed spheres, hence, the velocity at the bottom of the sphere is not represented by the free stream velocity. This is particularly important for small values of D_s/D_B, where relatively large portion at the bottom of the sphere is sheltered from the flow. It can be seen in Fig. 5.23 that for small values of D_s/D_B at large values of H/h, the experimental values of H/h are consistently larger than the theoretical ones. A correction of the theoretical considerations for the sheltering effect should result in larger values of predicted wave height and will decrease the discrepancy of the experimental data points. However, it will increase the discrepancy at small values of H/h where the experiments appear to agree with the theory which is not corrected for sheltering effects. It is therefore assumed that the sheltering of the bottom of the sphere from the flow by the supporting spheres is not the main reason for the disagreement between the theory and the experiments.

Another assumption made was that the drag coefficient of a sphere in the proximity of a bottom is given by the drag coefficient of a sphere in an unbounded fluid. Carty (1957) measured the drag coefficient for spheres rolling down a slope submerged in a fluid, and found that the drag coefficient in this case is larger than that in an unbounded fluid. However, the spinning of the rolling spheres in his experiments (which introduces circulation to the flow) and the friction between the spheres and the plane boundary add unknown parameters to the problem. Coleman

(1972) measured the forces acting on a sphere supported above a bed of similar spheres (in a configuration similar to that of the present investigation) in a steady flow, and by measuring the velocity at the level of the center of the sphere he evaluated the drag coefficient. The values of the drag coefficient which he found are similar to those of a sphere in an unbounded fluid. Hence, it was assumed that the proximity of the isolated sphere to the bottom in the present study has no effect on the drag coefficient.

In addition, an assumption was made that the hydrodynamic forces act at the center of the sphere. It is reasonable to believe that the point of force action is located above the center, since due to the velocity profile in the boundary layer at the bottom, and due to the sheltering of the bottom of the sphere, the velocity at the top of the sphere is larger than the velocity at the bottom. Hence, the forces at the top of the sphere are larger than those at the bottom, and the resultant force is shifted upwards. Since the exact point of force action is unknown, the examination of this assumption will be based on the hypothetical possibility, considering the forces as acting on top of the sphere. Thus, when the values of H/h are estimated based on the assumptions that the forces act either at the center or at the top of the sphere (which are considered as the two extreme possibilities), it will be expected that the actual H/h at incipient motion will be between these two values. The theoretical and experimental values of H/h as a function of D_s/D_B (for given h, D_B, ρ_s/ρ_w, and position), are shown in Fig. 5.24, where the theoretical curves were evaluated using Boussinesq's theory for the solitary wave, and calculated for both cases where the

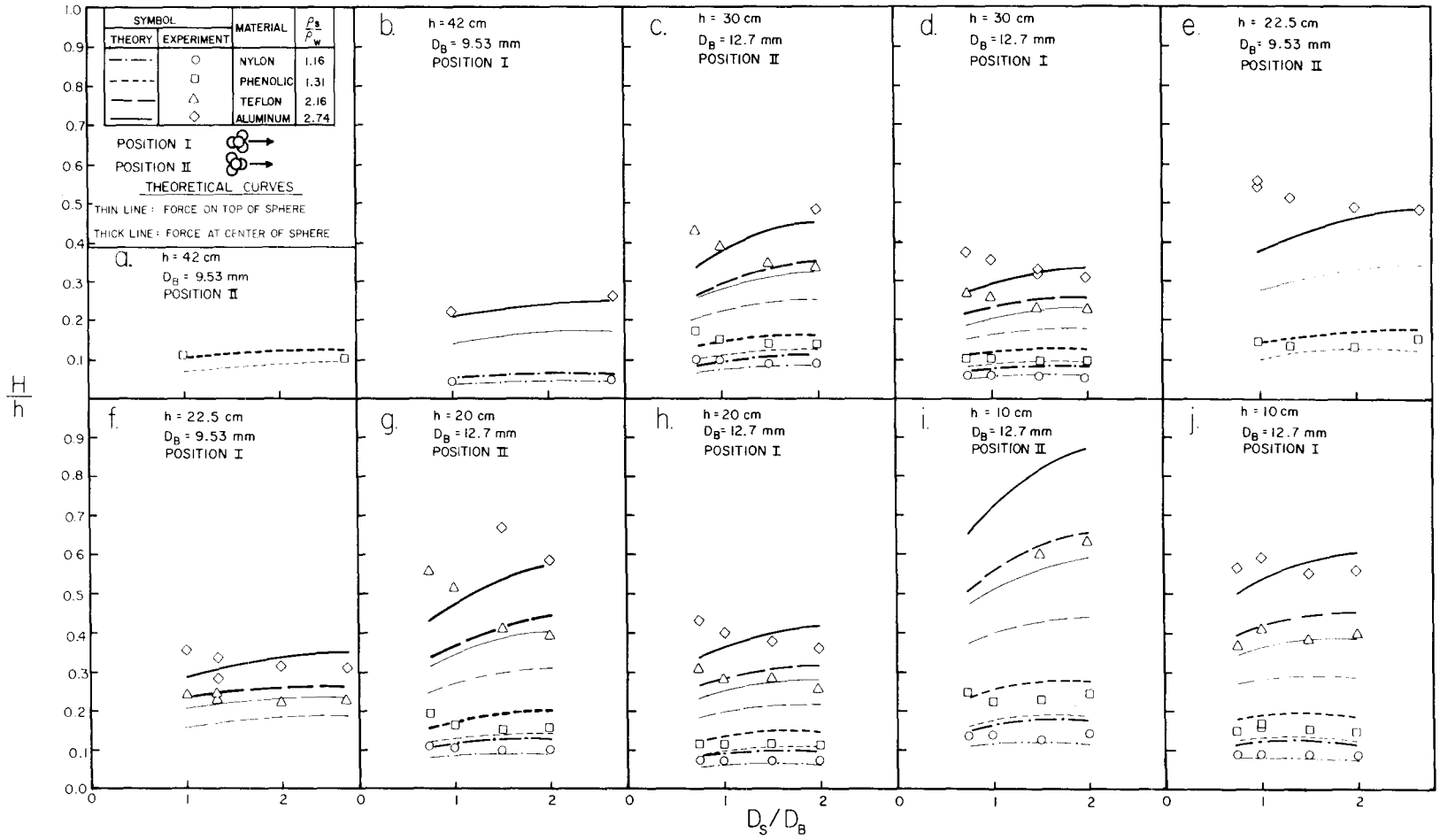

Fig. 5.24 Comparison between the experimental results of the incipient motion of spheres and the theoretical predictions (using Boussinesq's theory) assuming that the hydrodynamic forces act either at the top or at the center of the sphere.

forces are assumed to act at the center and at the top of the sphere. Fig. 5.24 indicates that when the forces are assumed to act at the top of the sphere, the wave height for incipient motion is smaller than that when the forces are assumed to act at the center. This is expected, since the arm of the hydrodynamic moment is larger when the forces act at the top of the sphere, hence the same hydrodynamic moment (at incipient motion) requires smaller hydrodynamic forces which are caused by a smaller wave. Fig. 5.24 clearly indicates that the approximation considered by assuming that the forces act at the center of the sphere is not the main reason for the discrepancy between the theory and the experiments. Assuming that the forces act above the center shifts the theoretical curve to lower values of H/h (for given h, ρ_s/ρ_w, D_B, and position), but does not change the trend of increasing H/h with D_s/D_B, which is opposite (in most cases) to the trend of the experimental data. In view of the assumptions which have been discussed so far, it appears that the only change in trend of the theoretical curves can result from the considerations of the velocity profile near the bottom and the sheltering of the bottom of the sphere. These considerations imply that the same hydrodynamic forces (as those estimated considering vertically uniform velocity distribution at the level of the sphere) require a larger wave when the velocity distribution is assumed as not being uniform vertically. This applies particularly for small values of D_s/D_B, where a large portion of the sphere is sheltered from the flow, and the other portion does not protrude above the bed as much as in cases of large D_s/D_B. However, for these cases (of small D_s/D_B) the upwards shift of the point of force action is larger than in cases of

large D_s/D_B. Hence, it results in a smaller wave at incipient motion, and the effects due to the vertically non-uniform velocity distribution at the level of the sphere seem to cancel each other.

It is concluded that the disagreement between the theory and the experiments is probably due to the inaccuracies which result from the assumptions concerning the values of the inertia, lift, and drag coefficients. The inertia and lift coefficients for a sphere resting on the top of a bed of spheres were calculated from potential flow theory, assuming that they are similar to those of a sphere touching a smooth wall. In Appendix I it is noted that these coefficients are functions of the proximity of the sphere to the wall, and the approximate theory used to estimate them is fairly accurate only when the sphere is located far away from the wall. The errors in the values of the inertia and lift coefficients may therefore result from the inaccuracy of the theory by which they are estimated (when the sphere is close to the wall). In addition, errors in these coefficients may be due to the fact that the configuration of a sphere touching a smooth wall may not represent the situation of a sphere resting on a bed of spheres, and to the fact that the fluid is real and not ideal, i.e., that there are effects of viscosity (which are described by the Reynolds number). Hence, the coefficients may not be the same as those evaluated from potential flow theory. Another assumption was that the instantaneous drag coefficient can be evaluated from charts which are usually used for steady flow. However, the development of the boundary layer and the wakes around the sphere in an unsteady flow is different from that in a steady flow, hence there are inertia effects, which are described by the dimensionless

acceleration, on the drag coefficient. Since the drag coefficient depends on both the Reynolds number and the acceleration, and since the inertia and lift coefficients are also functions of the Reynolds number, it seems impossible to assume that the hydrodynamic force can be described by a linear combination of drag, inertia, and lift components in which the drag, inertia, and lift coefficients are independent of each other.

Based on the preceding discussion, it was proposed (in Section 3.2.3) to combine inertia, drag, and lift effects into a single coefficient, C_D^*. Bugliarello (1956) proposed to combine drag and inertia effects into a similar coefficient for a sphere moving in a unidirectional unsteady motion. However, since his experiments were conducted in an essentially unbounded fluid, his considerations did not include lift effects. Furthermore, Basset (1888) showed that the resistance coefficient of a sphere in an unsteady flow of a viscous fluid depends also on the history of the flow, i.e., on the initial conditions. Keulegan and Carpenter (1958) noted that when the resistance coefficient (which includes both inertia and drag effects) is obtained for one type of flow, it is impossible to apply it to a different type of flow for this reason. This means, for example, that the resistance coefficient in a viscous oscillatory flow may be different from that in a unidirectional flow even if the Reynolds number and the dimensionless acceleration are instantaneously equal for both flows. Therefore, due to the different flow characteristics in Bugliarello's (1956) study, it was impossible to estimate the resistance coefficient of a sphere for the present study from his results. Since the variation of the resistance coefficient

with the various dimensionless parameters (i.e., the Reynolds number, the dimensionless acceleration, etc.) is unknown, it had to be obtained experimentally.

Dimensional analysis considerations which were presented in Section 3.3.2 yielded the expression

$$\left(\frac{H}{h}\right)^2 = f\left[C_D^*, \frac{(\rho_s-\rho_w)}{\rho_w}\frac{D_s}{h}\tan\phi\right] \tag{5.27}$$

for incipient motion, where $f[\ ]$ denotes a function of the terms appearing within the brackets. The values of $(H/h)^2$ obtained experimentally are plotted against the corresponding values of $\frac{\rho_s-\rho_w}{\rho_w}\frac{D_s}{h}\tan\phi$ in Fig. 5.25. The results given in Figs. 5.25a,b,c, and d represent experiments which were conducted with ratios of water depth to bed sphere diameter, h/D_B, of 44.1, 23.6, 15.7, and 7.9, respectively. The dashed lines in each of these figures represent different ratios of the test sphere diameter to the bed sphere diameter, D_s/D_B. The solid lines were obtained using a least-squares fit technique, employing all the data points for each value of h/D_B. These lines are plotted together in Fig. 5.25e. They have the form

$$\left(\frac{H}{h}\right)^2 = K_1\left[\frac{(\rho_s-\rho_w)}{\rho_w}\frac{D_s}{h}\tan\phi\right]^{\gamma_1}, \tag{5.28}$$

where K_1 and γ_1 are functions of h/D_B. Their values are given in Table 5.2.

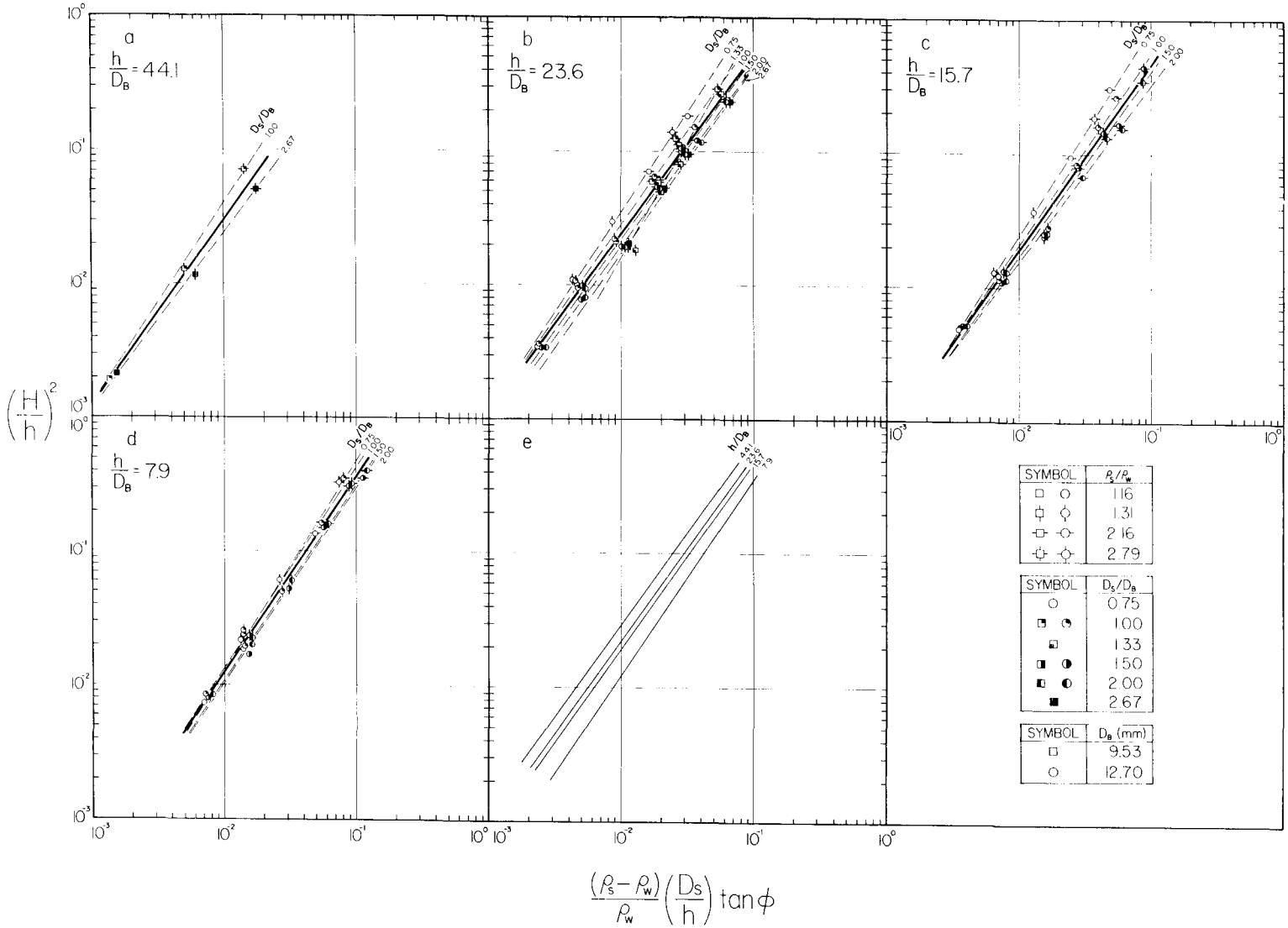

Fig. 5.25 Experimental results of the incipient motion of spheres.

Table 5.2. The values of K_1 and γ_1 (in Eq. (5.28)) as a function of h/D_B.

h/D_B	K_1	γ_1
44.1	16.3	1.37
23.6	11.4	1.34
15.7	11.2	1.38
7.9	10.7	1.47

Substituting Eq. (5.28) into Eq. (5.27) and noting from Fig. 5.25a,b,c, and d that the values of $(H/h)^2$ at incipient motion depend also on D_s/D_B indicates that C_D^* is a function of H/h, h/D_B and D_s/D_B. The dependence on h/D_B is obtained from Fig. 5.25e as follows.

A study of the variation of h/D_B with $\frac{(\rho_s-\rho_w)}{\rho_w}\left(\frac{D_s}{h}\right)\tan\phi$ for constant values of $(H/h)^2$ indicates that

$$\frac{(\rho_s-\rho_w)}{\rho_w}\left(\frac{D_s}{h}\right)\tan\phi \cong K_2\left(\frac{h}{D_B}\right)^{\gamma_2} \tag{5.29}$$

where K_2 is a function of H/h and D_s/D_B. The value of γ_2 is nearly constant since the curves in Fig. 5.25e are nearly parallel. It has the value of approximately -1/3. Multiplying both sides of Eq. (5.29) by $\left(\frac{h}{D_B}\right)^{1/3}$ yields

$$K_2\left(\frac{H}{h}, \frac{D_s}{D_B}\right) = \frac{(\rho_s-\rho_w)}{\rho_w}\left(\frac{D_s}{h}\right)\left(\frac{h}{D_B}\right)^{1/3}\tan\phi \quad . \tag{5.30}$$

The four different curves shown in Fig. 5.25e should nearly coincide when plotting the experimental values of $(H/h)^2$ against the right-hand side of Eq. (5.30). These data are shown in Fig. 5.26 where the abscissa is the right-hand side of Eq. (5.30) and the ordinate is $(H/h)^2$. The

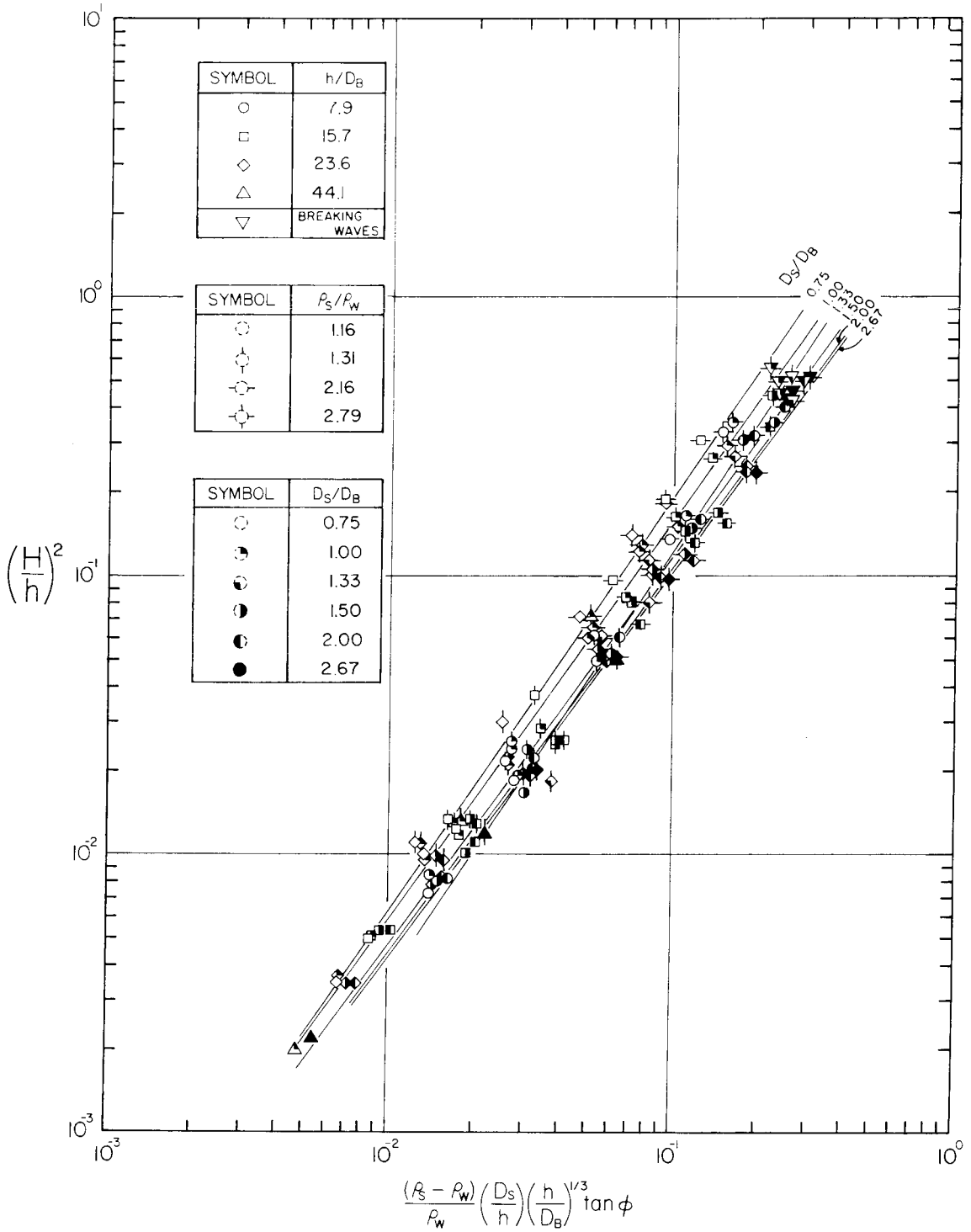

Fig. 5.26 Incipient motion of a sphere. Relationship between the wave height, the water depth, the test sphere diameter, the bed sphere diameter, the angle ϕ, and the submerged density of the sphere.

curves in this figure represent the variation of $(H/h)^2$ with $\frac{(\rho_s-\rho_w)}{\rho_w}\left(\frac{D_s}{h}\right)\left(\frac{h}{D_B}\right)^{1/3}\tan\phi$ for given D_s/D_B. These curves are nearly parallel except that corresponding to $D_s/D_B = 1.33$, which was derived from only eight data points and therefore may be inaccurate. This curve is ignored in the following analysis.

A study of the variation of D_s/D_B with $\frac{(\rho_s-\rho_w)}{\rho_w}\left(\frac{D_s}{h}\right)\left(\frac{h}{D_B}\right)^{1/3}\tan\phi$ for constant values of $(H/h)^2$ indicates:

$$\frac{(\rho_s-\rho_w)}{\rho_w}\left(\frac{D_s}{h}\right)\left(\frac{h}{D_B}\right)^{1/3}\tan\phi \cong K_3\left(\frac{D_s}{D_B}\right)^{\gamma_3} \tag{5.31}$$

where K_3 is a function of H/h. The value of γ_3 is not constant since the lines representing D_s/D_B in Fig. 5.25 are not parallel (they are nearly parallel but not quite so). The values of γ_3 vary from approximately 1/4 at $(H/h)^2 = 0.004$ to 1/2.4 at $(H/h)^2 = 0.56$ and it has the value of approximately 1/3 at the midrange of relative wave heights tested. Multiplying both sides of Eq. (5.31) by $\left(\frac{D_s}{D_B}\right)^{-1/3}$ yields

$$K_3\left[\left(\frac{H}{h}\right)^2\right] = \frac{(\rho_s-\rho_w)}{\rho_w}\left(\frac{D_s}{h}\right)\left(\frac{h}{D_B}\right)^{1/3}\left(\frac{D_s}{D_B}\right)^{-1/3}\tan\phi$$

$$= \frac{(\rho_s-\rho_w)}{\rho_w}\left(\frac{D_s}{h}\right)^{2/3}\tan\phi \quad . \tag{5.32}$$

The experimental data are now shown in Fig. 5.27 where the abscissa is the right-hand side of Eq. (5.32) and the ordinate is $(H/h)^2$. The empirical relationship for incipient motion is represented in this figure by a least-squares fit straight line through the data. An equation for this curve can be expressed by

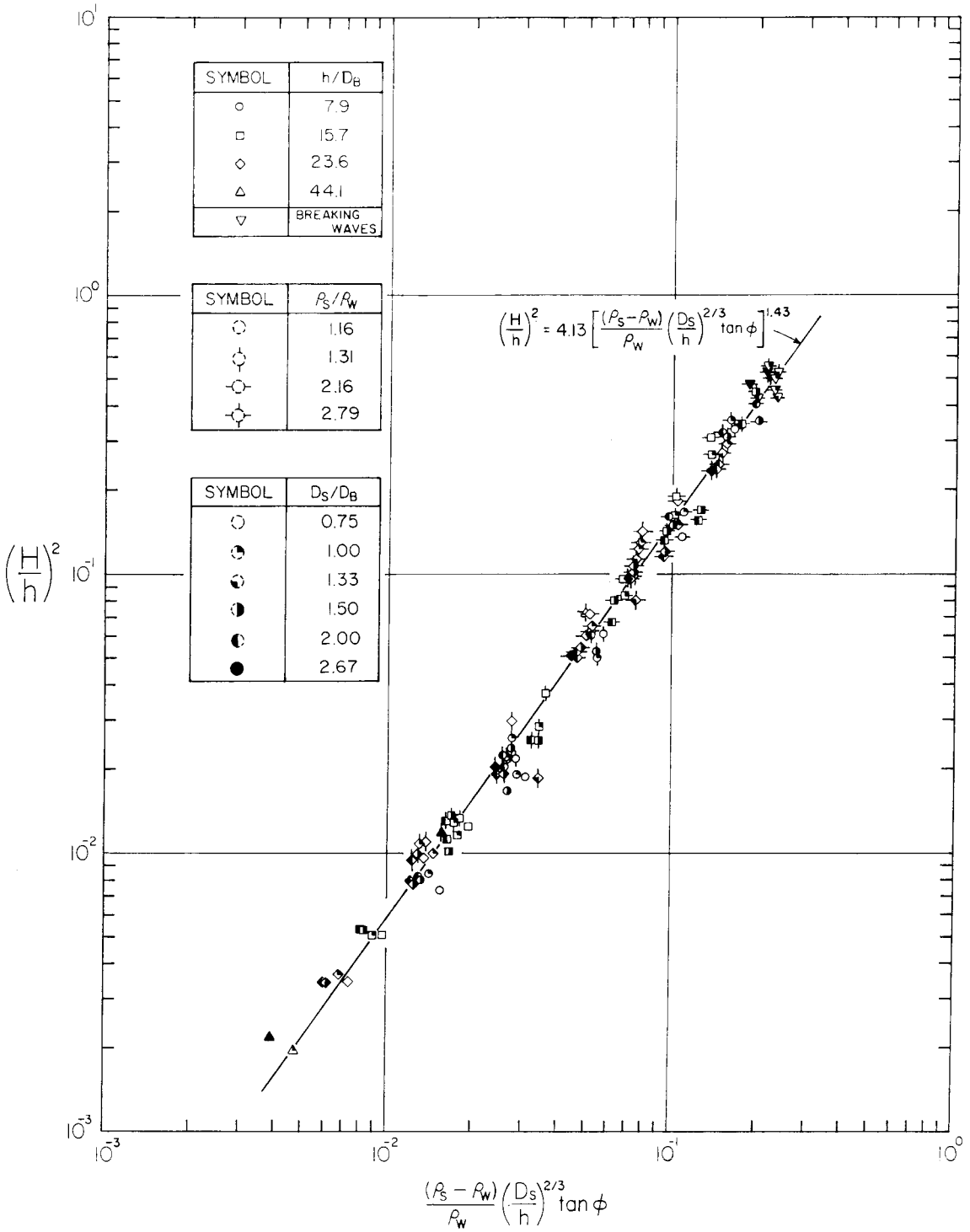

Fig. 5.27 Incipient motion of a sphere. Relationship between the wave height, the water depth, the angle ϕ, and the diameter and submerged density of the sphere.

$$(H/h)^2 = 4.13 \left[\frac{(\rho_s - \rho_w)}{\rho_w} \left(\frac{D_s}{h} \right)^{2/3} \tan\phi \right]^{1.43} . \qquad (5.33)$$

The region to the left of the line in Fig. 5.27 is the unstable region in which the sphere moves under the wave. The stable region in which there is no motion is to the right of the curve.

The value of C_D^* which is the resistance coefficient of a sphere incorporating drag, inertia and lift effects can now be derived from the relationship obtained for incipient motion. Eq. (5.33) is rewritten in the form

$$\frac{(\rho_s - \rho_w)}{\rho_w} \frac{D_s}{h} \tan\phi = 0.37 \left(\frac{H}{h} \right)^{1.40} \left(\frac{D_s}{h} \right)^{1/3} . \qquad (5.34)$$

Substituting this equation into Eq. (3.65) yields

$$C_D^* = 0.494 \left(\frac{D_s}{h} \right)^{1/3} \left(1 + \frac{H}{h} \right) \left(\frac{H}{h} \right)^{-0.60} . \qquad (5.35)$$

Eq. (5.35) implies that C_D^* is independent of lift effects since it is independent of the angle ϕ. However, it should be remembered that Eq. (5.35) displays only an approximate expression for C_D^*. It has been noted that the value of γ_3 in Eq. (5.31) is not constant. An approximate value of $\gamma_3 = 1/3$ was used to obtain the abscissa of Fig. 5.27, from which C_D^* has been derived. Assuming a value of γ_s different from 1/3, or considering it not to be constant would have led to the dependence of C_D^* on D_s/D_B. Consequently, C_D^* would have included lift effects since ϕ is a function of D_s/D_B.

In considering the dependence of C_D^* on H/h and D_s/h (Eq. (5.35)), it is noted that although the Reynolds number and the dimensionless

acceleration are functions of the parameters D_s, h, and H, it is impossible to deduce the actual physical effects quantitatively. The reasons are that the differences between the theories describing the distribution of the fluid particle velocity and acceleration along the wave are quite large, and the measurements of the fluid particle velocity under the wave (see Section 5.1.3) were not accurate enough to deduce this distribution. Hence it is impossible to define the actual Reynolds number and the dimensionless acceleration accurately. For example, inspection of Figs. 5.21 and 5.22 indicates that if the dimensionless acceleration is described in terms of the maximum acceleration and maximum velocity (hence, for constant inertia and drag coefficients, it is described by the ratio of maximum inertia force to maximum drag), then the values of this ratio calculated from McCowan's (1891) theory are significantly different from those calculated from Boussinesq's (1872) theory. However, as both the theories of McCowan and Boussinesq indicate that the dimensionless acceleration increases for increasing D_s/h and decreasing H/h, the effects of inertia may be deduced qualitatively from a study of the variation of C_D^* with respect to D_s/h and H/h. This is done by inspection of Fig. 5.28, where C_D^* is shown as a function of D_s/h and H/h. The abscissa in Fig. 5.28 is H/h, the ordinate is C_D^*, and variation with D_s/h is described by different curves, each of them calculated for a constant value of D_s/h. The values of D_s/h in Fig. 5.28 are the same as those employed in the experiments of the attenuation of waves, and they are chosen in Fig. 5.28 so that the resistance coefficient of a single sphere, C_D^*, may be compared to the mean resistance coefficient, $\overline{Cf_b}$, of a rough bed. The mean resistance coefficient of a rough

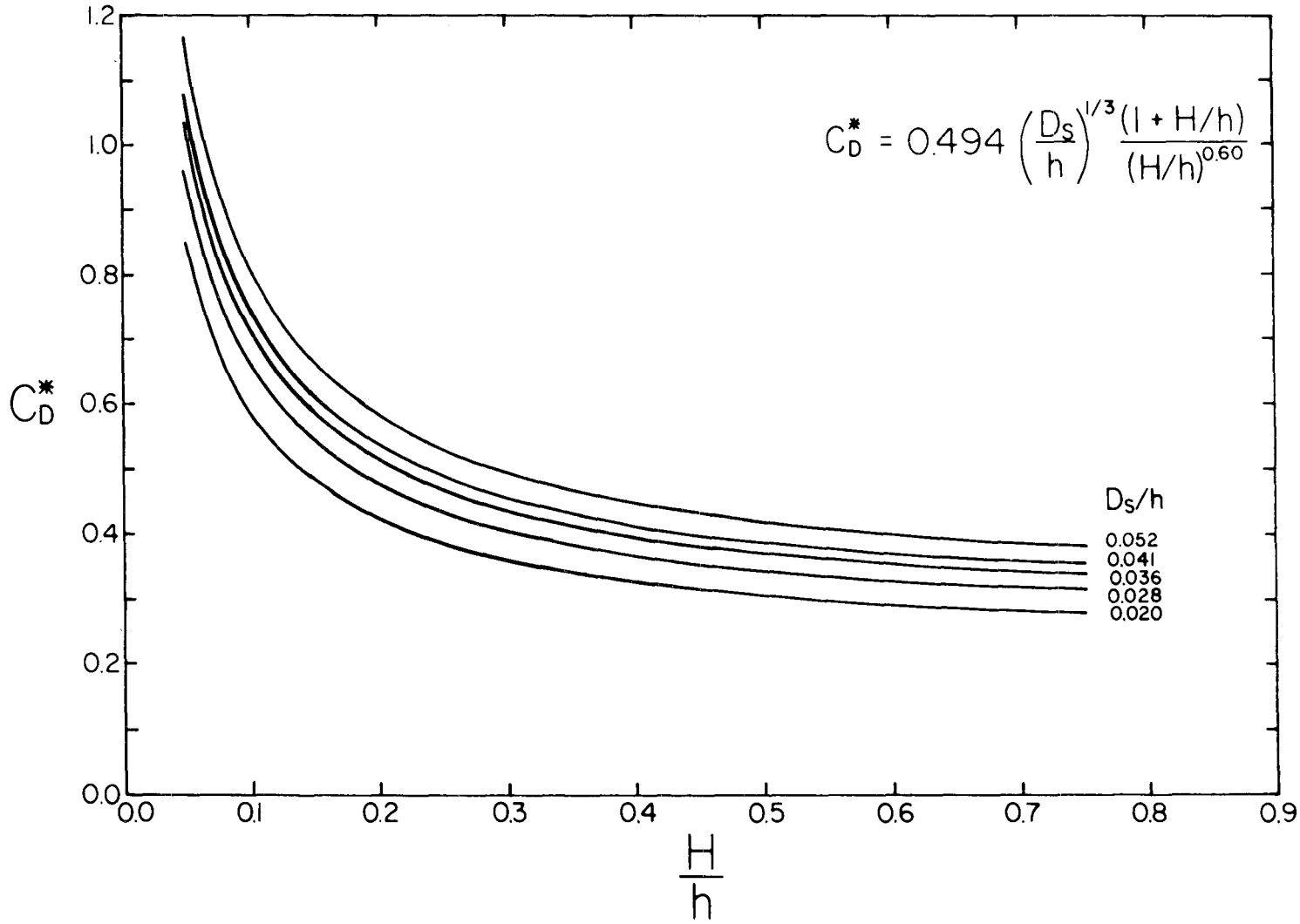

Fig. 5.28 The resistance coefficient of a sphere under solitary waves.

bed is shown in Fig. 5.14 as a function of D_s/h and H/h. Figs. 5.14 and 5.28 indicate that both the resistance coefficient of a single sphere and the mean resistance coefficient of a rough bed increase with increasing D_s/h and decreasing H/h. There are, however, three major differences between the mean resistance coefficient of a rough bed and the resistance coefficient of a single sphere. First, the values of C_D^* appear to be larger than the values of $\overline{C_{f_b}}$ by an order of magnitude for given H/h and D_s/h. Second, as indicated by Eq. (5.35), C_D^* is a linear function of $(D_s/h)^{1/3}$ for a given H/h, while $\overline{C_{f_b}}$ varies linearly with $(D_s/h)^{0.63}$, as indicated by Eq. (5.23).

The above differences are probably due to the following. First, the single sphere protrudes into an undisturbed stream and its resistance coefficient consists of inertia, drag, and lift effects. On the other hand, the roughness particles of a rough bed are sheltered from the free stream flow in the wakes behind their neighbors. The forces acting on the roughness particles are therefore much smaller than those on a single sphere, resulting in smaller resistance coefficient. Furthermore, the resistance coefficient of a single sphere is in a sense a local coefficient, obtained from measurements of the incipient motion which occurs at a specific instant under the wave. At incipient motion the force consists of both inertia, drag, and lift components whose effects are reflected by the value of C_D^*. The mean resistance coefficient is an average value for the wave which apparently excludes the lift and inertia components of the hydrodynamic force. The mean resistance coefficient

is obtained from considerations of energy dissipation by integrating the inner product of the force and the fluid particle velocity under the wave. The lift force is perpendicular to the direction of the flow, hence the inner product of the lift force and the velocity is zero, and the inertia forces are non-dissipative which cancel out when integrated over the wave. Therefore, the local coefficient, C_D^* should be larger than the average coefficient, $\overline{C_{f_b}}$. As noted in Section 5.2, the fact that inertia forces cancel out when integrated over the wave does not mean that there are no inertia effects on the mean resistance coefficient, since they probably affect the development of the boundary layer over the bed. The differences in the variation of C_D^* and $\overline{C_{f_b}}$ with H/h and D_s/h (in addition to the differences in magnitude) are probably also due to the different inertia effects. Note that for the case of a single sphere protruding into the undisturbed flow, the variation of C_D^* with D_s/h and H/h is attributed to inertia effects, where the dimensionless acceleration which describes these effects increases with increasing D_s/h and decreasing H/h. Eq. (3.56) indeed indicates that for constant drag, inertia, and lift coefficients the resistance coefficient increases with the dimensionless acceleration. For the case of the mean resistance coefficient of a rough bed, in addition to possible inertia effects, the variation of $\overline{C_{f_b}}$ with D_s/h and H/h is attributed to a parameter describing the ratio of the roughness diameter to the total displacement of a fluid particle outside the boundary layer. This parameter was derived from considerations of rough turbulent flow over a flat plate (see Sections 3.2.1 and 5.2), and although the expression describing it is similar to the expression describing the dimensionless acceleration,

its effects on the resistance coefficient may be different from the effects of inertia, resulting in a different behavior of C_D^* and $\overline{C_{f_b}}$ with respect to D_s/h and H/h.

For practical engineering purposes, where rock is used to protect offshore structures by placing it in a loose bottom pavement, the problem is to size the rock such that it will not move significantly under the action of waves. Here the rock is represented by the isolated sphere. The water depth, h, is usually given, and the relative wave height, H/h, is assumed. An empirical relationship for the incipient motion is given by Eq. (5.22), and it can be used to determine the size of the rock by rewriting Eq. (5.33) as

$$\frac{D_s}{h} = \frac{0.225\ (H/h)^{2.10}}{\left[\left(\frac{\rho_s}{\rho_w} - 1\right)\tan\phi\right]^{3/2}} \quad . \tag{5.36}$$

It is of interest to consider Eq. (5.36) for breaking waves. Breaking waves are most destructive, as at a given depth they reach their maximum height just before breaking. Shallow water waves are assumed to break at a fixed value of H/h (see, for example, Laitone (1963)). Thus, the numerator of the right-hand side of Eq. (5.36) is constant for breaking waves. The ratio of the diameter of the isolated sphere to the water depth at incipient motion then becomes a function of the specific gravity of the sphere and its placement on the bed (which defines the angle ϕ).

The results of measurements of incipient motion of spheres under breaking waves are shown in Fig. 5.29, where the abscissa is $\frac{(\rho_s - \rho_w)}{\rho_w}\tan\phi$

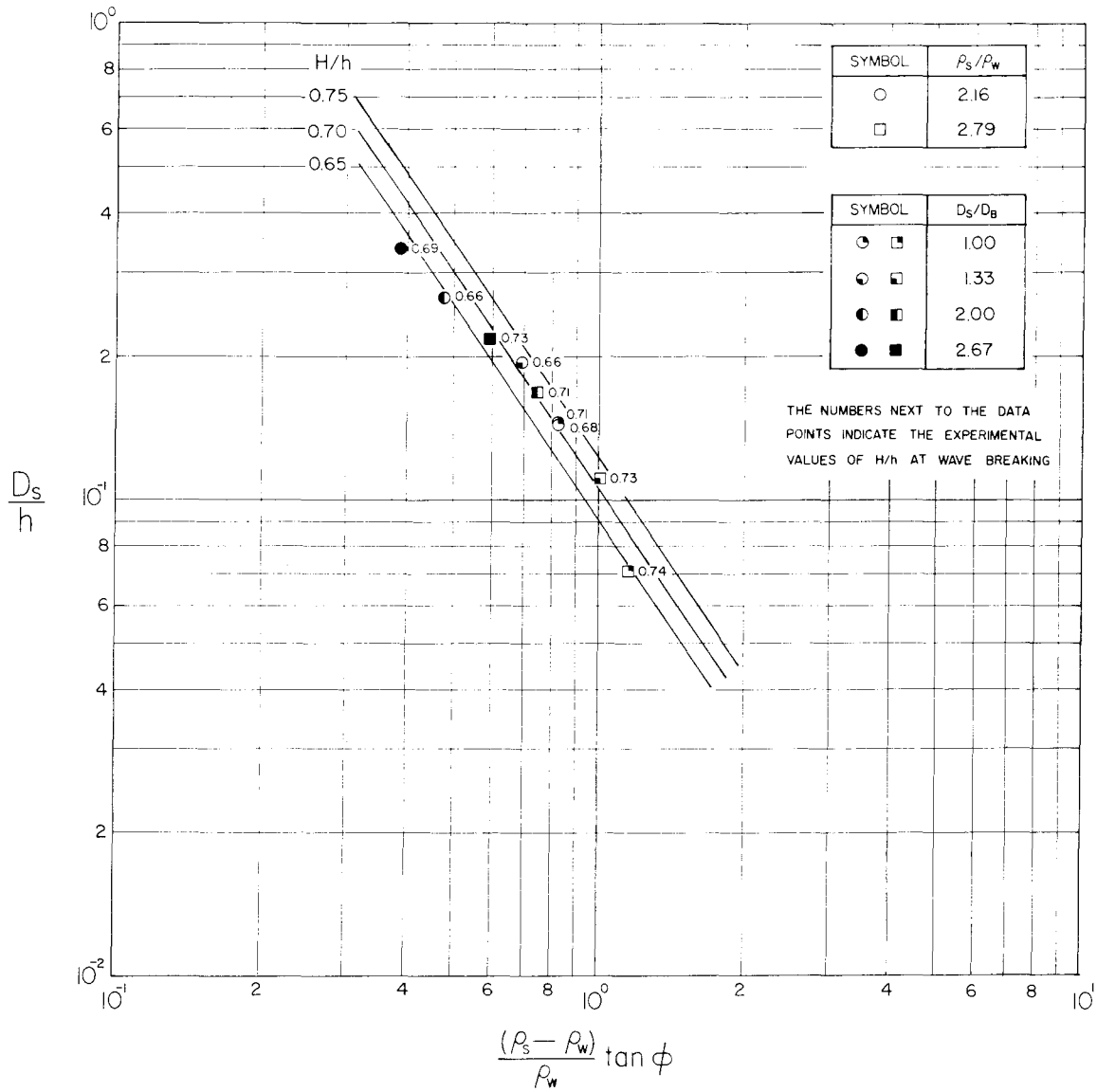

Fig. 5.29 Incipient motion of a sphere under breaking waves. Relationship between the water depth, the wave height, the angle ϕ, and the diameter and submerged density of the sphere.

and the ordinate is D_s/h. The measured values of H/h at breaking are noted in the figure for each data point, and they vary from 0.66 to 0.74. The variation of H/h for waves near breaking is probably due to the procedure by which the experiments were conducted. Since the waves were not completely damped immediately after reaching the wave dissipator at the downstream end of the tank, a waiting period between the experiments was required to let any residual waves to damp out completely. Waves were generated after waiting periods of 15 to 20 minutes when the water surface seemed completely still. Apparently, some residual, unnoticed, waves still existed in the wave tank, and depending on the phase of their current with respect to that of the solitary wave, they caused the solitary wave to break at different values of H/h. The curves representing different values of H/h in this figure were calculated from Eq. (5.36). The experimental data appear to be scattered around these waves. The reasons for the discrepancies seen in the figure are that the empirical relationship (Eq. (5.33)) from which Eq. (5.36) was derived displays an experimental scatter. This scatter, which is shown in Fig. 5.27, is due to the approximation (e.g., the value of γ_3 in Eq. (5.31)) used in obtaining Eq. (5.33), and to the imperfect conditions, where the solitary waves might be superimposed on unnoticed transient waves and currents.

Considering the isolated sphere to represent the rock used to protect offshore structures, Eq. (5.36) can now be used to determine the size of the rock for incipient motion. Most natural rocks have a specific gravity of 2.65. The angle ϕ, which is called the angle of friction, is usually considered to be constant. A value of 45° was

assumed for ϕ in the present investigation. Although this value may seem to be too large (e.g., see Lane (1955)), it was measured in the laboratory in the present study. Apparently, the value of ϕ depends on the method by which it is measured, and the problem is to determine which method more closely approximates the purpose of application. The angle ϕ is usually defined as the slope of a loose pile which is formed by the considered particles. In the present investigation this angle was obtained by tilting a tray containing a layer of loose particles. The tray was tilted until the layer of particles collapsed and rolled down the slope (see Section 4.4.3 for details). This method yields larger values for ϕ than those obtained from measurement of the slope of a loose pile, and indeed an inspection of Fig. 4.22b indicates that the slope formed by loose particles after the collapse of the layer is smaller than the slope of the tray at which the layer collapsed. It should be noted that White (1940) assumed a value of 45° for ϕ in most of the experiments conducted in his study of the stability of bottom material in a stream. However, he did not describe how he obtained this value.

Considering the example presented in Section 5.3.1, in which the value of D_s/h was sought for a rock with $\rho_s/\rho_w = 2.65$ under a wave of $H/h = 0.75$, Eq. (5.36) yields a value of 0.058 for D_s/h. This value is much smaller than that which was obtained in Section 5.3.1 from measurements of the motion of particles of arbitrary shape. However, it was noted in that section that the value of D_s/h contained large errors due to the scatter of data in these measurements and due to the uncertainties involved in estimating the mean resistance coefficient in defining incipient motion. Considering possible errors in the evaluation of

D_s/h from the results of the incipient motion of spheres, it is noted that the scatter of data points seen in Fig. 5.27 is confined within an imaginary envelope which may be used to define minimum and maximum values for D_s/h at incipient motion for a given value of H/h. For example, for H/h = 0.75 (i.e., $(H/h)^2 = 0.56$), the value of $\frac{(\rho_s-\rho_w)}{\rho_w}\left(\frac{D_s}{h}\right)^{2/3} \tan\phi$ appears to be between 0.220 and 0.275, which for $\frac{\rho_s}{\rho_w} =$ 2.65 and $\phi = 45°$ yields values of 0.049 and 0.068, respectively, for D_s/h. These values display a deviation of approximately 20% from the value 0.058 estimated from Eq. (5.36). It should also be noted that the value of 0.058 which was obtained from Eq. (5.36) was based on assuming a value of 45° for the angle of friction, ϕ, and as noted earlier, this value may seem to be too large. According to Lane (1955), the angle of friction (which is also called the angle of repose) of angular material with diameter of 5 mm to 11 mm, which is the size of the material of arbitrary shape used in the present investigation, is approximately 30° to 35°. Considering, for example, a value of 30° for ϕ for a rock with $\rho_s/\rho_w = 2.65$ under a wave of H/h = 0.75, Eq. (5.36) results in a value of 0.132 for D_s/h, instead of 0.058, when ϕ is assumed to be 45°. This example indicates that the determination of the diameter of the rock for incipient motion is largely dependent on the assumed values of the angle of friction. Note that the assumption of $\phi = 30°$ results in a value of D_s/h which is of the same order of magnitude as the value obtained in Section 5.3.1 ($D_s/h = 0.150$) from measurements of motion of particles of arbitrary shape. This may indicate that indeed assuming a value of 45° for ϕ (which results in $D_s/h = 0.058$) is too large. However, the value of D_s/h for incipient motion as obtained in Section 5.3.1 was

based on a method which contains errors of 100% order of magnitude. Hence, an indication of the magnitude of ϕ based on these results cannot be conclusive.

The incipient motion of a single sphere was considered as a valid model of the incipient motion of rocks since it was assumed the moving rock particles are those which protrude above their neighbors, thus resembling the configuration of a single isolated sphere. However, as much as this assumption seems reasonable, it was not verified. In order to investigate a possible correlation between the incipient motion of spheres and the incipient motion of particles of arbitrary shape, the results of both studies are analyzed on a similar basis as follows.

The empirical relationship defining the incipient motion of spheres is described by the straight line in Fig. 5.27. The region to the right of the line in this figure represents the stable region where no motion is expected to occur. To the left of the line is the unstable region. A point in this region indicates that the sphere is expected to move, with the amount of motion increasing with the distance from the line. The amount of motion for the case of a single sphere is different from that for the rocks where the amount of motion is represented by the number of moving particles divided by the total number of particles exposed to the flow. For a single sphere the amount of motion may be defined by the magnitude of its displacement. Nevertheless, whatever definition is used, it is expected that the points of zero amount of motion will be in the region to the right of the line in Fig. 5.27, and that the amount of motion will increase with the distance to the left of the line.

The observed values of the amount of motion of particles of arbitrary shape are shown as a function of $(H/h)^2$ and $\frac{(\rho_s-\rho_w)}{\rho_w}\left(\frac{D_s}{h}\right)^{2/3}\tan\phi$ in Fig. 5.30. The abscissa is $\frac{(\rho_s-\rho_w)}{\rho_w}\left(\frac{D_s}{h}\right)^{2/3}\tan\phi$ and the ordinate is $(H/h)^2$, both on a logarithmic scale. The average values of $(N_p/N_{p_T})\times10^4$ are printed next to each data point in this figure. The values of H/h, D_s/h, ρ_s/ρ_w, and the average N_p/N_{p_T} are also presented in Table 5.1, columns (4), (5), (2), and (8), respectively. The value of ϕ was assumed to be 45°. The solid curve in Fig. 5.30 represents the incipient motion of spheres (Eq. (5.33)), and the dashed lines represent the different values of N_p/N_{p_T}. These curves were fitted through the data assuming a first order polynomial, i.e.,

$$N_p/N_{p_T} = a + b \log (H/h)^2 + C \log\left[\frac{(\rho_s-\rho_w)}{\rho_w}\left(\frac{D_s}{h}\right)^{2/3}\tan\phi\right], \quad (5.37)$$

applying a least-square fit technique. The values of a, b, and c were found to be

$$a = -9.25\times10^{-4} \; ; \quad b = 1.593\times10^{-3} \; ; \quad c = -2.349\times10^{-3} \; .$$

Substituting these values in Eq. (5.37), it is found for incipient motion, i.e., for $N_p/N_{p_T} = 0$,

$$(H/h)^2 = 3.81\left[\frac{(\rho_s-\rho_w)}{\rho_w}\left(\frac{D_s}{h}\right)^{2/3}\tan\phi\right]^{1.47} . \quad (5.38)$$

Considering the scatter of data of both measurements of incipient motion of spheres (see Fig. 5.27) and the incipient motion of particles of arbitrary shape, a comparison of Eq. (5.38) to Eq. (5.33) and an inspection of Fig. 5.30 indicate a reasonably good correlation between the results of the two studies.

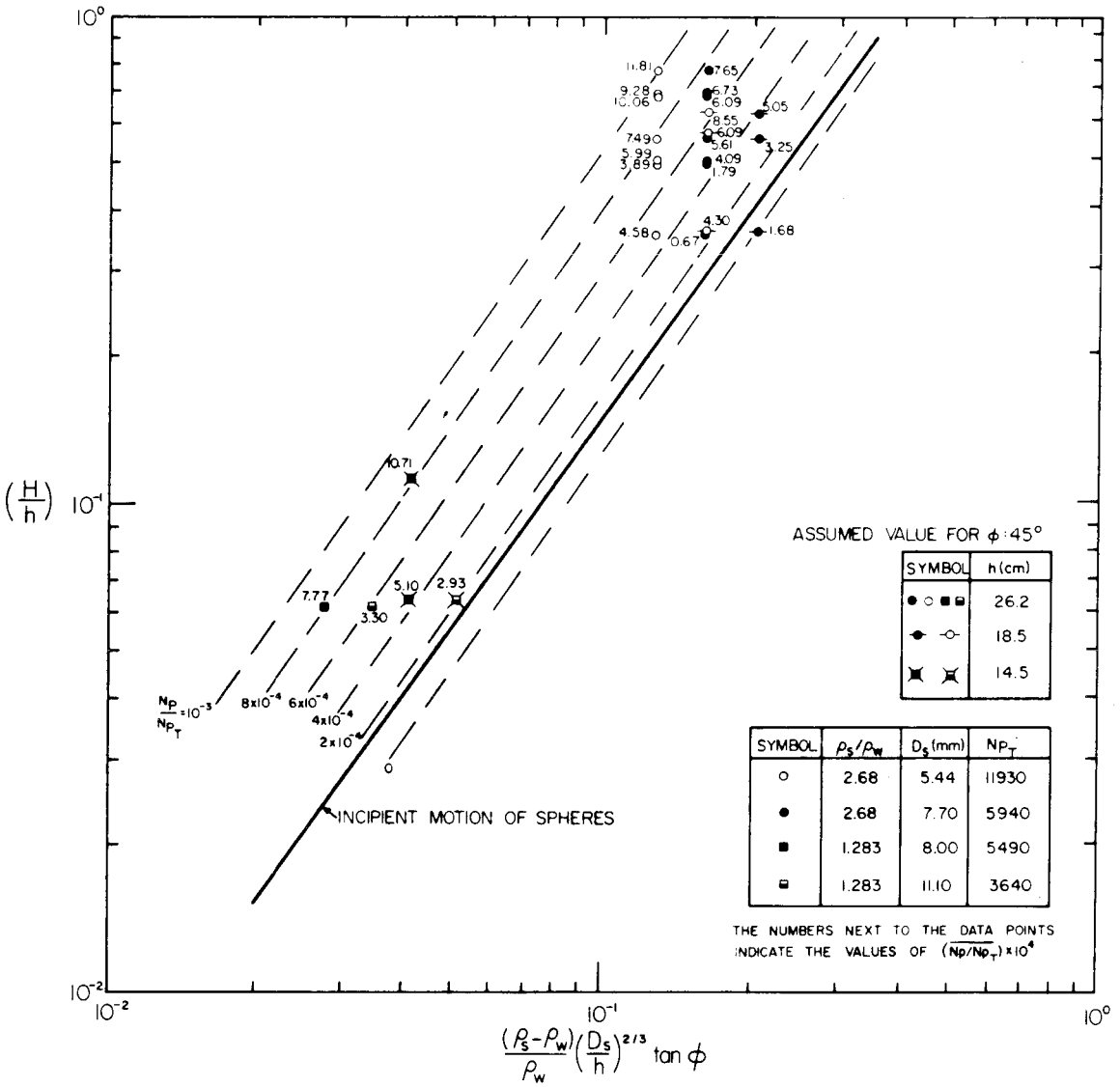

Fig. 5.30 The average amount of motion of particles of arbitrary shape as a function of the wave height, the water depth, the angle ϕ, and the mean diameter and submerged density of the particles.

Using Eq. (5.38) for the example considered earlier in this section, i.e., $\rho_s/\rho_w = 2.65$, $\tan\phi = 1$, and $H/h = 0.75$, D_s/h yields a value of 0.067. This value is closer to that predicted from the results of the incipient motion of spheres than that obtained using the relationship between the amount of motion of particles of arbitrary shape and a dimensionless shear stress. In fact $D_s/h = 0.067$ for the given conditions for the rock is within the experimental scatter of the incipient motion of spheres ($0.049 \leq D_s/h \leq 0.068$ for $\frac{\rho_s}{\rho_w} = 2.65$, $\frac{H}{h} = 0.75$).

The above example was also considered (in Section 5.3.1) for a wave with $H/h = 0.50$, and it yielded $D_s/h = 0.0255$ for incipient motion. Applying the analysis of the present section to this example, the results which were obtained for particles of arbitrary shape (Eq. (5.38)) yield $D_s/h = 0.0293$, and the results which were obtained for spheres (Eq. (5.33)) yield $D_s/h = 0.0249$. In this case the relative difference between the results of the two analyses of the incipient motion of particles of arbitrary shape is smaller than that in the preceding example. As noted in Section 5.3.1, it is expected that the error in D_s/h, due to inaccuracies in determining the bottom resistance coefficient, is small for the example with $H/h = 0.50$. Apparently, the differences between the results in the above examples are due to the different methods of analysis combined with the large scatter of data, where the results of one analysis define the incipient motion differently from the other analysis.

It is concluded that due to the uncertainties involved in the determination of the dimensionless shear stress, τ_{*max}, and due to the scatter of data observed in the measurements of motion of particles of arbitrary shape, a significant error is expected when using these results to size the rock required for incipient motion under a given wave. On the other

hand, the results obtained for the incipient motion of an isolated sphere appear to represent the incipient motion of rocks reasonably well, and they may be used to size the rock for incipient motion. While the results which were obtained from correlating the motion of particles of arbitrary shape to a dimensionless shear stress require some theoretical considerations in order to evaluate τ_{*max}, the results which were obtained in the present section are based on measurable quantities. Since it was shown here that the theoretical considerations consist of important uncertainties, it is preferred to use the empirical relationship which was obtained for spheres (Eq. (5.33)) to size the rock for incipient motion.

CHAPTER 6

CONCLUSIONS AND RECOMMENDATIONS FOR FUTURE STUDIES

6.1 CONCLUSIONS

The major objective of the study has been to investigate the stability of a bed of rocks under solitary waves. The research was limited to the investigation of the incipient motion of rocks rather than their incipient transport*. The study consisted of: (a) a review of three existing theories of the solitary wave and comparing the surface profile, the wave celerity, and the fluid particle velocity predicted by these theories to those of solitary waves generated in the laboratory; (b) an investigation of the shear stresses exerted on the bottom by these waves; (c) a study of the incipient motion of bottom material of arbitrary shape, in which the results of the investigation of the bottom shear stresses were employed; (d) an investigation of the incipient motion of a single sphere resting on top of a bed of well packed spheres.

The following are the major conclusions that were drawn from this study.

The Solitary Wave

1. The three theoretical formulations of the solitary wave due to Boussinesq (1872), McCowan (1891), and Laitone (1963) are practically

*The difference between the two definitions is that a particle may reach its incipient motion by moving slightly and falling back to its original position, but when reaching its incipient transport the particle has to be removed from its at-rest position. This difference is important from a practical engineering aspect, as the destruction of the bed is of more concern than a slight movement of a few of its rocks.

the same for very small values of H/h (wave height-to-water depth ratio). The differences between the theories increase with H/h.

2. As shown in Section 5.1, no single theory can accurately describe the surface profile, the wave celerity, and the fluid particle velocity of the solitary wave for all values of wave height-to-water depth ratio, and for both horizontal and sloping bottoms.

The Resistance Coefficient of the Bottom under Solitary Waves

3. The height of a solitary wave traveling along a horizontal channel is attenuated exponentially with distance. The decay coefficient may be considered constant for the 60 ft section of the wave tank along which the wave attenuation was measured.

4. The resistance coefficient of a smooth bottom in laminar flow is determined reasonably well from the linearized boundary layer equations.

5. For the case of rough turbulent flow, it was found that the resistance coefficient is a function of the mean diameter of the roughness particles, D_s, the water depth, h, and the wave height, H. The dimensionless parameters which were formed from these variables implied that the resistance coefficient is independent of the Reynolds number.

The Incipient Motion of Material of Arbitrary Shape

6. The amount of motion in the bed, N_p/N_{p_T}, is found to be a function of a dimensionless shear stress, τ_{*max} (similar to the Shields parameter), which is evaluated with the aid of the mean resistance coefficient under the solitary wave, and the amount of motion increases as τ_{*max} increases.

7. The relationship which is used to determine the size of the rock for incipient motion under a given wave (Eqs. (5.22) and (5.23)) shows that a ±20% error in determining $\tau_{*_{max}}$ for incipient motion (due to experimental scatter) results in an error of -40% and +85% in the diameter of the rock. It is concluded that the results presented in Fig. 5.30 are the best ones to use in sizing the rock for incipient motion.

The Incipient Motion of a Single Sphere Resting on a Bed of Spheres

8. It was found that theoretical considerations, in which the hydrodynamic forces exerted on a single sphere are assumed to be a linear combination of drag, inertia, and lift components, and where the values of the drag, inertia, and lift coefficients (which have been given in Section 5.3.2) are assumed to be independent of each other, fail to predict the incipient motion of the sphere.

9. Although the differences between Boussinesq's (1872) and McCowan's (1891) theories are small, when used to describe the surface profile and the fluid particle velocity of the solitary wave, the differences between them are significant when used to predict incipient motion.

10. Experiments demonstrate that the effect of inertia forces is to cause the incipient motion to occur under the wave front, and not under the crest where the fluid particle velocity is maximum. However, quantitative effects of inertia were not concluded due to uncertainties in the theory used to estimate them.

11. The incipient motion of an isolated sphere can be described

empirically as a relationship between the parameters H/h and $\frac{(\rho_s-\rho_w)}{\rho_w}\left(\frac{D_s}{h}\right)^{2/3}\tan\phi$, where ρ_s and ρ_w are the densities of the sphere and fluid, respectively, and ϕ is the angle between a normal to the bed and a line connecting the center of the isolated sphere and the axis around which it is forced to move.

12. The comparison between the results of the investigations of the incipient motion of spheres and the incipient motion of particles of arbitrary shape (Fig. 5.30) indicates that the empirical relationship derived from the study of the incipient motion of spheres may be used to size rock of arbitrary shape for incipient motion under waves of given height and depth.

13. In using the results which were obtained with spheres to determine the incipient motion of particles of arbitrary shape, it is necessary to assume a value of the angle of friction, ϕ, for these particles, and relatively small errors in ϕ can result in large errors in determining the size of the particles.

6.2 RECOMMENDATIONS FOR FUTURE STUDIES

The empirical relationships for incipient motion which were derived from the results of the present investigation are of limited use, from a practical engineering aspect, since they were obtained in a scaled model in the laboratory. Scaling effects have not been studied due to the uncertainties involved in quantitatively describing the physical effects which govern these relationships. The following are suggestions for future studies to resolve the uncertainties encountered in the present study.

1. Although Boussinesq's (1872) and McCowan's (1891) theories describe the solitary wave fairly well, the differences between them are large, when used to determine the hydrodynamic forces exerted on bottom particles, and when used to determine the dimensionless acceleration, which describes the effects of inertia on the resistance coefficient. With the lack of an accurate theory it was impossible in the present study to understand these effects. It is recommended for future investigations to study closely the distribution of the fluid particle velocity and acceleration under the wave, together with the distribution of forces, in order to have a better understanding of the inertia effects on the hydrodynamic forces and the resistance coefficient.

2. In order to estimate local shear stresses exerted on a rough bottom under waves it is necessary to study the development of the rough turbulent boundary layer under these waves. The stresses estimated with the aid of the mean resistance coefficient which was derived from considerations of energy dissipation do not seem to represent the actual stresses exerted on the bed.

3. A slight rocking motion of a few particles in the bed is insignificant from a practical engineering aspect. Such a motion does not endanger the bed and does not reduce the protection of the rock armoring. As the present investigation was concentrated on this kind of motion, it is recommended that a future study will be concentrated on the conditions under which the entire bed changes from a stable to an unstable condition.

4. Observations of motion of particles of arbitrary shape resulted in a large error when used to determine the size of the rock required for incipient motion under breaking waves. Since the error is partly due to the extrapolation of the data from observed motion to the point of zero motion, it is recommended to study the problem for the case where the particles are in a state of incipient motion under breaking waves.

LIST OF REFERENCES

1. Bagnold, R. A. (1946), "Motion of Waves in Shallow Water; Interaction Between Waves and Sand Bottoms," Proceedings, Royal Society of London, Vol. 187, Series A, pp. 1-15.

2. Basset, A. B. (1887), "On the Motion of Two Spheres in a Liquid and Allied Problems," Proceedings, London Mathematical Society, Vol. XVIII, pp. 369-377.

3. Basset, A. B. (1888), "On the Motion of a Sphere in a Viscous Liquid," Philosophical Transactions, Royal Society of London, Vol. 179, No. 43, pp. 43-63.

4. Bevington, P. R. (1969), Data Reduction and Error Analysis for the Physical Sciences, McGraw-Hill Book Company, New York.

5. Biesel, F. (1949), "Calcul de l'amortissement d'une Houle un Liquide Visqueux de Profondeur Finie," La Houille Blanche, Vol. 4, pp. 630-634.

6. Boussinesq, J. (1872), "Théorie des Ondes et des Remous qui se Propagent le Long d'un Canal Rectangulaire Horizontal, en Communiquant au Liquide Contenu dans ce Canal de Vitesses Sensiblement Parreilles de la Surface au Fond," Journal de Mathematiques Pures et Appliquées, 2nd Série, Vol. 17, pp. 55-108.

7. Boussinesq, J. (1878), "Complément á une Étude intitulée:<<Essai sur la Théorie des Caux Courantes>>, et á un Mémorie<<Sur l'influence des Frottements sur les Mouvements Reguliers des Fluids>>," Journal de Mathématiques Pures et Appliquées, Series 3^{c}, Vol. 4, 335 pp.

8. Bugliarello, G. (1956), "La Resista al Moto Accelerato di Sfera in Acqua," Ricerca Scientificia, Vol. 26, pp. 437-461.

9. Carty, J. J., Jr. (1957), "Resistance Coefficients for Spheres on a Plane Boundary," B.S. Thesis, Massachusetts Institute of Technology, Cambridge, Massachusetts.

10. Coleman, N. L. (1972), "The Drag Coefficient of a Stationary Sphere on a Boundary of Similar Spheres," La Houille Blanche, Vol. 27, No. 1, pp. 17-21.

11. Daily, J. W., and Stephan, S. G., Jr. (1952), "The Solitary Wave," Proceedings, 3rd Conference on Coastal Engineering, Cambridge, Massachusetts, pp. 13-30.

LIST OF REFERENCES (Cont'd)

12. Eagleson, P. S. (1962), "Laminar Damping of Oscillatory Waves," Journal of the Hydraulic Division, ASCE, Vol. 88, HY3, pp. 155-181.

13. Eagleson, P. S., Dean, R. G., and Peralta, L. A. (1958), "The Mechanics of the Motion of Discrete Spherical and Bottom Sediment Particles Due to Shoaling Waves," Beach Erosion Board, U. S. Department of the Army, Corps of Engineers, Technical Memorandum No. 104.

14. French, J. A. (1969), "Wave Uplift Pressures on Horizontal Platforms," W. M. Keck Lab. Report, KH-R-19, California Institute of Technology, Pasadena, California.

15. Grace, R. A. (1974), "Wave Forces on Submerged Objects," James K. K. Look Laboratory of Ocean Engineering, Miscellaneous Report No. 10, University of Hawaii.

16. Ippen, A. T., Kulin, G., and Raza, M. A. (1955), "Damping Characteristics of the Solitary Wave," Hydraulic Laboratory Technical Report No. 16, Massachusetts Institute of Technology, Cambridge, Massachusetts.

17. Ippen, A. T., and Kulin, G. (1957), "The Effect of Boundary Resistance on the Solitary Wave," La Houille Blanche, No. 3, pp. 390-407.

18. Ippen, A. T., and Mitchell, M. M. (1957), "The Damping of the Solitary Wave from Boundary Shear Measurements," Hydrodynamic Laboratory Technical Report No. 23, Massachusetts Institute of Technology, Cambridge, Massachusetts.

19. Iribarren Cavanilles, R. (1965), "Formule pour le Calcul des Digues en Enrochement Naturels ou Elements Artificiels," XXIst International Navigation Congress, Stockholm, Section II-1, pp. 15-32.

20. Iversen, H. W., and Balent, R. (1951), "A Correlating Modulus for Fluid Resistance in Accelerated Motion," Journal of Applied Physics, Vol. 22, No. 3, pp. 324-328.

21. Iwagaki, Y., Tsuchiya, and Sakai, M. (1965), "Basic Studies of the Wave Damping Due to Bottom Friction," Coastal Engineering in Japan, Vol. 8, pp. 37-49.

22. Iwasa, Y. (1959), "Attenuation of Solitary Waves on a Smooth Bed," Transactions, ASCE, Paper No. 2972, pp. 193-206.

LIST OF REFERENCES (Cont'd)

23. Jonsson, I. G. (1963), "Measurements in the Turbulent Wave Boundary Layers," IAHR, 10th Congress, London, Vol. 1, pp. 85-92.

24. Jonsson, I. G. (1966), "Wave Boundary Layers and Friction Factors," Proceedings, 10th Conference on Coastal Engineering, Tokyo, Vol. 1, pp. 127-148.

25. Kajiura, K. (1968), "A Model of Bottom Boundary Layer in Water Waves," Bulletin of the Earthquake Research Institute, Japan, Vol. 46, Part 1, pp. 75-123.

26. Kalkanis, G. (1957), "Turbulent Flow Near an Oscillating Wall," Beach Erosion Board, U. S. Department of the Army, Corps of Engineers, Technical Memorandum No. 97.

27. Kamphuis, J. W. (1975), "Friction Factor Under Oscillatory Waves," Journal of the Waterways, Harbors, and Coastal Engineering Division, ASCE, pp. 135-144.

28. Keulegan, G. H. (1948), "Gradual Damping of Solitary Waves," U. S. Department of Commerce, National Bureau of Standards, Research Paper RP 1895, Vol. 40, pp. 487-498.

29. Keulegan, G. H., and Carpenter, L. H. (1958), "Forces on Cylinders and Plates in an Oscillating Fluid," Journal of Research of the National Bureau of Standards, Vol. 6, No. 5, pp. 423-440.

30. Komar, P. D., and Miller, M. C. (1973), "The Threshold of Sediment Movement Under Oscillatory Waves," Journal of Sedimentary Petrology, Vol. 43, No. 4, pp. 1101-1110.

31. Komar, P. D., and Miller, M. C. (1975), "Reply. On the Comparison Between the Threshold of Sediment Motion Under Waves and Unidirectional Currents With a Discussion of the Practical Evaluation of the Threshold," Journal of Sedimentary Petrology, Vol. 45, No. 1, pp. 362-367.

32. Laitone, E. V. (1963), "Higher Order Approximation to Nonlinear Waves and the Limiting Heights of Conoidal, Solitary, and Stokes' Waves," Beach Erosion Board, U. S. Department of the Army, Corps of Engineers, Technical Memorandum No. 133.

33. Lane, E. W. (1955), "Design of Stable Channels," Transactions, ASCE, Vol. 120, Paper No. 2776, pp. 1234-1260.

LIST OF REFERENCES (Cont'd)

34. Lin, C. C. (1957), "Motion in the Boundary Layer With a Rapidly Oscillating External Flow," Proceedings, 9th International Congress on Applied Mechanics, Brussels, Vol. 4, pp. 155-167.

35. Madsen, O. S., and Grant, W. D. (1975), "The Threshold of Sediment Movement Under Oscillatory Waves: A Discussion," Journal of Sedimentary Petrology, Vol. 45, No. 1, pp. 360-361.

36. Manohar, M. (1955), "Mechanics of Bottom Sediment Movement Due to Wave Action," Beach Erosion Board, U. S. Department of the Army, Corps of Engineers, Technical Memorandum No. 75.

37. McCowan, J. (1891), "On the Solitary Wave," London, Edinburgh, and Dublin Philosophical Magazine, Vol. 32, pp. 45-58.

38. Milne-Thomson, L. M. (1960), Theoretical Hydrodynamics, Fourth Edition, The MacMillan Company, New York.

39. Morison, J. R., O'Brien, M. P., Johnson, J. W., and Schaaf, S. A. (1950), "The Force Exerted by Surface Waves on Piles," American Institute of Mixing, Metallurgical and Petroleum Engineers, Vol. 189, pp. 149-154.

40. Munk, W. H. (1949), "The Solitary Wave Theory and its Applications to Surf Problems," Annals of the New York Academy of Science, Vol. 51, pp. 376-424.

41. O'Brien, M. P., and Morison, J. R. (1952), "The Forces Exerted by Waves on Objects," Transactions, American Geophysical Union, Vol. 33, No. 1, pp. 32-38.

42. Rouse, H. (1950), Engineering Hydraulics, John Wiley & Sons, Inc., New York.

43. Schlichting, H. (1968), Boundary Layer Theory, Sixth Edition, McGraw-Hill Book Company, New York.

44. Scott-Russell, J. (1844), "On Waves," Reports to the British Association, pp. 311-390.

45. Shields, A. (1936), "Anwendung der Aehnlichkeitsmechanik und der Turbulenzforschung auf die Geschiebebewegung," Mitteilungen der Preussischen Versuchsanstalt für Wasserbau und Schiffbau, Berlin, Germany; Translated to English by W. P. Ott and J. C. van Uchelen, California Institute of Technology, Pasadena, California.

46. Vanoni, V. A. (1975), Sedimentation Engineering, ASCE Manual and Report on Engineering Practice, No. 54.

LIST OF REFERENCES (Cont'd)

47. Vanoni, V. A., Brooks, N. H., and Kennedy, J. F. (1961), "Lecture Notes on Sediment Transportation and Channel Stability," W. M. Keck Lab. Report No. KH-R-1, California Institute of Technology, Pasadena, California.

48. Vanoni, V. A., Brooks, N. H., and Raichlen, F. (1967), "A Forty Meter Precision Tilting Flume," W. M. Keck Lab. Technical Memorandum No. 67-3, California Institute of Technology, Pasadena, California.

49. Van Dorn, W. G. (1966), "Boundary Dissipation of Oscillatory Waves," Journal of Fluid Mechanics, Vol. 24, Part 4, pp. 769-779.

50. White, C. M. (1940), "The Equilibrium of Grains on the Bed of a Stream," Proceedings, Royal Society of London, Vol. 174, Series A, pp. 322-338.

LIST OF SYMBOLS

A	Area
A_{p_r}	Portion of the projected area of the bed
A_T	Total projected area of the test section
a,b	Coefficients used in fitting curves to experimental data
a_1,a_2	Radii of the spheres S_1 and S_2
a_δ	Amplitude of fluid particle displacement next to the boundary layer in oscillatory flow
B	Width of the channel
C	Wave celerity
C_D	Drag coefficient
C_D^*	Resistance coefficient (of a sphere)
C_f	Resistance coefficient (of a solid boundary)
C_{f_b}	Resistance coefficient (of the bed)
C_L	Lift coefficient
C_M	Inertia coefficient
D	Diameter (of a cylinder)
D_B	Diameter (of bed spheres)
D_s	Diameter of the particles whose incipient motion is investigated
d	Distance between the centers of the spheres S_1 and S_2
d_a,d_b,d_c	Orthogonal diameters of a particle of arbitrary shape
d_r	Distance between recorded peaks of a wave
E	Total energy in a flow domain
E_k	Total kinetic energy in a flow domain
E_l	Total energy per unit channel width

LIST OF SYMBOLS (Cont'd)

E_{k_1}	Kinetic energy per unit channel width
E_{p_1}	Potential energy per unit channel width
e	= d/2
F	Force
F_D	Drag force
F_H	Horizontal force
F_I	Inertia force
F_L	Lift force
g	Acceleration due to gravity
H	Wave height
h	Water depth
$\left(\frac{H}{h}\right)_{rep}$	Representative value of H/h
i	An integer
j	An integer
K^*, K_1, K_2, K_3	Coefficients used in fitting curves to experimental data
k	Decay coefficient
k_s	Equivalent surface roughness
L	Length of a plate
L_c	Characteristic length (of the solitary wave)
ℓ	Distance between wave gages
M,N	Parameters associated with the solitary wave due to McCowan (1891)
M_H	Hydrodynamic moment
M_R	Restoring moment

LIST OF SYMBOLS (Cont'd)

M_1, M_2	Masses of fluid displaced by the spheres S_1 and S_2
m_1, m_2	Masses of the spheres S_1 and S_2
N_{co}	Counted number
N_d	Number of data points
N_f	Number of frames (in a motion picture film strip)
N_h	Number of holes in a disk
N_p	Number of particles moved by a single wave in the test area
N_{p_r}	Total number of particles seen in the area A_{p_r}
N_{p_T}	Total number of particles in the uppermost layer in the test section
N_w	Number of waves
n	Normal to boundary
P	Point in the flow domain
P_c	Point of contact
P_r	Pulse generation rate (sec^{-1})
P_s	Recording paper speed
p	Pressure
Q_1, Q_2, Q_3, R	Parameters associated with the motion of the spheres S_1 and S_2
$\vec{q}$	Velocity vector
R_c	Wave Reynolds number used by Iwasa (1959)
R_e	Wave Reynolds number
Re_s	Particle Reynolds number
Re_*	Boundary particle Reynolds number
ΔR	Remainder force function used by Keulegan and Carpenter (1958)

LIST OF SYMBOLS (Cont'd)

r_1, r_2	Distances of the point P from the centers of the spheres S_1 and S_2
S_f	Shape factor
S_1, S_2	Spheres moving in an unbounded fluid (Appendix I)
S	Boundary of flow domain
T	Period of oscillation
T_c	Characteristic time scale (of the solitary wave)
T_{co}	Counting period
T_*	Dimensionless period
t	Time
t_1, t_2	Time displayed on a motion picture film
U_1, U_2	Velocities of the spheres S_1 and S_2
u	Horizontal component of the fluid particle velocity
u_c	Characteristic fluid particle velocity (of a solitary wave)
u_ℓ	Fluid particle velocity in the boundary layer (horizontal component)
u_{max}	Maximum fluid particle velocity
u_*	Shear velocity
V	Volume
v	Vertical component of the fluid particle velocity
v_ℓ	Fluid particle velocity in the boundary layer (vertical component)
W_{sub}	Submerged weight
X	Horizontal coordinate moving with the wave
x,y,z	Cartesian stationary coordinates

LIST OF SYMBOLS (Cont'd)

α	Parameter used in the solution of the solitary wave
α_m	Proportionality coefficient
β	Variable of integration
$\gamma_1, \gamma_2, \gamma_3$	Coefficients used in fitting curves to the experimental data
δ	Boundary layer thickness
η	Free surface elevation above still water level
θ_1, θ_2	Angles (associated with the motion of spheres S_1 and S_2)
κ	Variable of integration
μ	Dynamic viscosity
ν	Kinematic viscosity
ξ	Fluid particle displacement
π	3.14159...
ρ_s	Density of a particle
ρ_w	Density of the fluid
σ	Standard deviation
(σ_a, σ_b, etc.	Standard deviation of the parameters a,b, etc.)
σ_g	Geometric standard deviation
τ_b	Bottom shear stress
τ_w	Wall shear stress
τ_*	Dimensionless shear stress
Φ	Velocity potential
ϕ	Angle of repose

LIST OF SYMBOLS (Cont'd)

Operators

$\frac{d(\quad)}{d(\quad)}$	Total derivative
$\frac{\partial(\quad)}{\partial(\quad)}$	Partial derivative
Δ	Different (e.g., $\Delta\xi=\xi_2-\xi_1$)
∇	Gradient
∇^2	Laplacian
$f(\ldots)$	Function of...
$O(\quad)$	Order of magnitude
$(\vec{\ })$	Vector
$(\overline{\ })$	Average value

APPENDIX I

INERTIA AND LIFT COEFFICIENTS FOR A SPHERE NEAR THE BOTTOM

The following analysis is due to Milne-Thomson (1960) and is presented here for the convenience of reference.

Two spheres (shown in Fig. A.1.1) with centers at S_1 and S_2 of radii a_1 and a_2 are moving at speeds U_1 and U_2 (respectively) in a direction perpendicular to the line connecting their centers. The distance between the centers is d. A point P is located at distances r_1 and r_2 from the centers S_1 and S_2, and forms angles θ_1 and θ_2 with the directions of their motion respectively. The liquid is assumed to be ideal and the flow field satisfies Laplace's equation

$$\nabla^2\Phi = 0 \tag{A.1.1}$$

where Φ is the velocity potential and has the form

$$\Phi = U_1\Phi_1 + U_2\Phi_2 \quad . \tag{A.1.2}$$

The boundary conditions for Eq. (A.1.1) are

$$\left.\begin{aligned} -\left(\frac{\partial\Phi_1}{\partial r_1}\right)_{r_1=a_1} &= \cos\theta_1 \ , \quad -\left(\frac{\partial\Phi_1}{\partial r_2}\right)_{r_2=a_2} = 0 \ , \\ -\left(\frac{\partial\Phi_2}{\partial r_1}\right)_{r_1=a_1} &= 0 \ , \quad -\left(\frac{\partial\Phi_2}{\partial r_1}\right)_{r_2=a_2} = \cos\theta_2 \ . \end{aligned}\right\} \tag{A.1.3}$$

For a single sphere in an unbounded flow Φ_1 has the form

$$\Phi_1 = \frac{a_1^3\cos\theta_1}{2r_1^2} \tag{A.1.4}$$

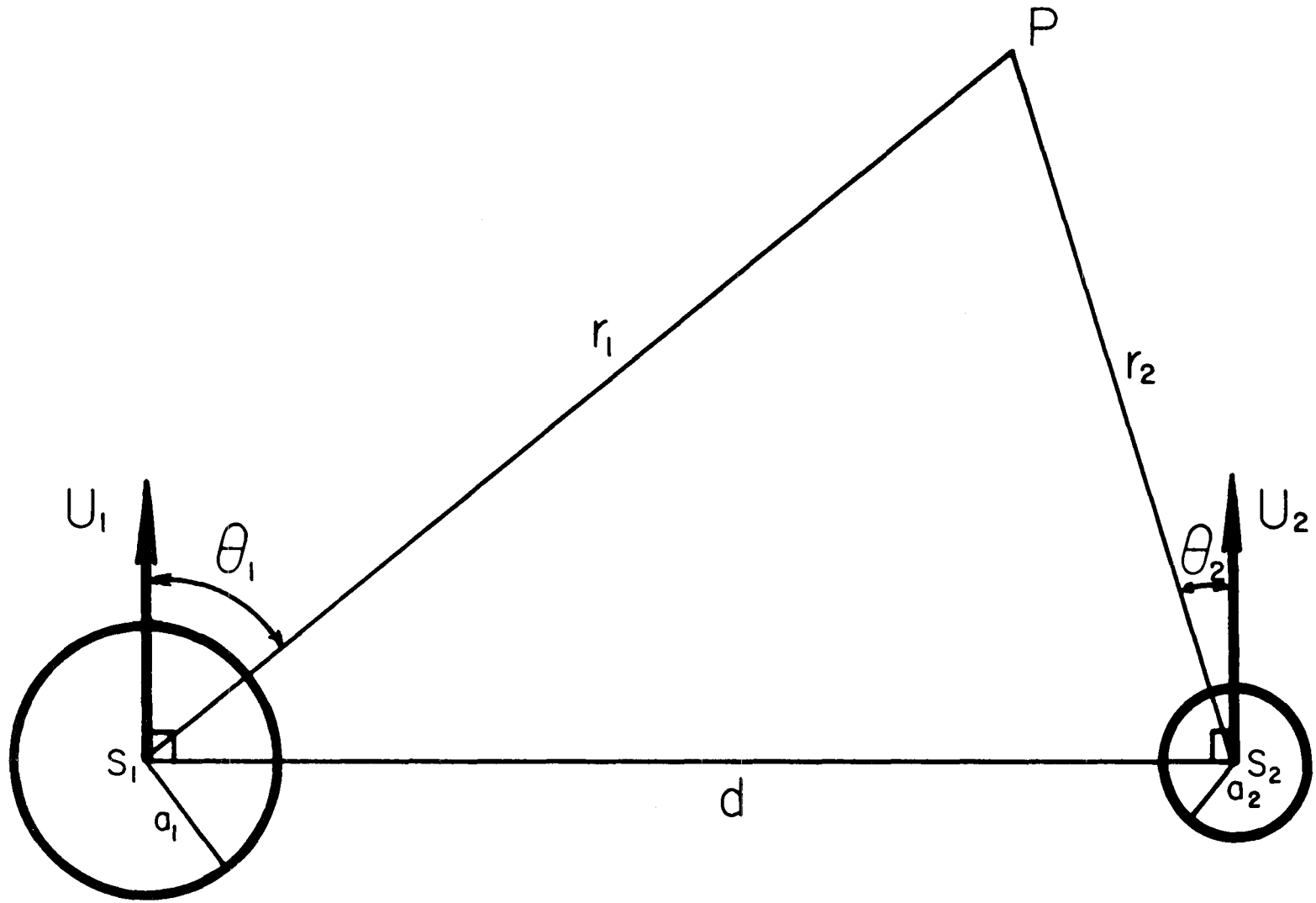

Fig. A.1.1 Definition sketch for the motion of two spheres in a fluid.

If sphere S_2 is far enough from S_1, then for a point near the surface of sphere S_2, $r_1 \simeq d$ and

$$\frac{a_1^3 \cos\theta_1}{2r_1^2} = \frac{a_1^3 r_1 \cos\theta_1}{2r_1^3} \cong \frac{a_1^3 r_1 \cos\theta_1}{2d^3} \quad . \tag{A.1.5}$$

From Eq. (A.1.5)

$$\left(\frac{\partial \Phi_1}{\partial r_2}\right)_{r_2=a_2} = -\frac{a_1^3 \cos\theta_2}{2d^3} \quad , \tag{A.1.6}$$

which is in contradiction with the requirement of Eq. (A.1.3). Writing Φ_1 in the form

$$\Phi_1 = \frac{a_1^3 \cos\theta_1}{2r_1^2} + \frac{a_1^3 a_2^3 \cos\theta_1}{4d^2 r_2^2} \tag{A.1.7}$$

satisfies the boundary conditions on sphere S_1. On sphere S_2, where $r_2 \simeq d$,

$$-\left(\frac{\partial \Phi_1}{\partial r_1}\right)_{r_1=a_1} \simeq \cos\theta_1 - \frac{a_1^3 a_2^3}{4d^6} \cos\theta_1 \, . \tag{A.1.8}$$

This satisfies the boundary conditions (A.1.3) to order d^{-6}. The expression for Φ_2 is obtained in a similar way.

The kinetic energy E_k of the system is given by

$$E_k = \frac{1}{2} \rho_w \int_V (V\Phi)^2 dV = \frac{1}{2} \rho_w \int_S \Phi \frac{\partial \Phi}{\partial n} dS \tag{A.1.9}$$

applying Stokes theorem. V is the volume of the fluid, S is its boundary and n is a normal to the boundary.

Basset (1887) carried the calculations of the flow potential to terms of higher order (than those in Eq. (A.1.7)) and obtained for the

kinetic energy

$$E_k = \frac{1}{2}(Q_1 U_1^2 + 2Q_2 U_1 U_2 + Q_3 U_2^2) \quad , \tag{A.1.10}$$

where

$$\left.\begin{aligned} Q_1 &= m_1 + \frac{1}{2} M_1 \left[1 + \frac{3a_1^3 a_2^3}{d^6}\left\{\frac{1}{4} + \frac{a_2^2}{d^2} + \frac{9a_2^4}{d^4} + \frac{a_2^3 (a_1^3 + 64a_2^3)}{16d^6}\right\}\right] \\ Q_2 &= \frac{\pi \rho_w a_1^3 a_2^3}{d^3}\left\{1 + \frac{a_1^3 a_2^3}{4d^6} + \frac{a_1^3 a_2^3 (a_1^2 + a_2^2)}{d^8}\right\} \\ Q_3 &= m_2 + \frac{1}{2} M_2 \left[1 + \frac{3a_1^3 a_2^3 a_2}{d^6}\left\{\frac{1}{4} + \frac{a_1^2}{d^2} + \frac{9a_2^4}{d^4} + \frac{a_1^3 (a_2^3 + 64a_1^3)}{16d^6}\right\}\right] \end{aligned}\right\} , \tag{A.1.11}$$

in which m_1 and m_2 are the masses of the spheres S_1 and S_2 respectively, and M_1 and M_2 are the masses of fluid displaced by them.

For a sphere near a solid boundary, using the boundary as a mirror for the image system,

$$E_k = \frac{1}{2}(Q + Q_2) U_1^2 = \frac{1}{2}\left[m_1 + \frac{1}{2} M_1 \left(1 + \frac{3a_1^3}{2d^3} + \frac{3a_1^6}{4d^6}\right)\right] U^2 \quad . \tag{A.1.12}$$

If $e = d/2$ is the distance of the center of the sphere from the boundary, and if $m_1 = M_1$ (to be used considering the sphere at rest in a flowing liquid), then

$$E_k = \frac{1}{2} M_1 U^2 \left(\frac{3}{2} + \frac{3a_1^3}{16e^3} + \frac{3a_1^6}{256e^6}\right) \quad . \tag{A.1.13}$$

Let $\frac{1}{2} M_1 \left(\frac{3}{2} + \frac{3a_1^3}{16e^3} + \frac{3a_1^3}{256e^6}\right) = R$, and let the solid boundary be horizontal (i.e., horizontal bottom). From Lagrange's equations (e.g.,

Milne-Thomson (1960) pp. 534-538), the horizontal component of the inertial force is

$$F_1 = \frac{d}{dt}\left(\frac{\partial E_k}{\partial U_1}\right) = 2R\frac{dU}{dt} \quad , \tag{A.1.14}$$

and the vertical component, or the lift force is

$$F_L = \frac{-1}{2} U_1^2 \frac{\partial R}{\partial e} = \frac{1}{4} M_1 U_1^2 \left(\frac{9a_1^3}{16e^4} + \frac{18a_1^6}{256e^6}\right) \quad . \tag{A.1.15}$$

F_I and F_L may be represented by

$$F_I = C_M \rho_w V \frac{dU_1}{dt} \quad , \tag{A.1.16}$$

and

$$F_L = \frac{1}{2} C_L \rho_w A U_1^2 \quad , \tag{A.1.17}$$

where $\rho_w V = \rho_w \frac{4}{3}\pi a^3 = M_1$ is the mass of fluid displaced by the sphere and $A = \pi a^2$ is the cross section area of the sphere. C_M is called the inertia coefficient and C_L is the lift coefficient. For a sphere resting on the bottom $e = a_1$, then C_M and C_L have the values

$$C_M = 1.699 \quad , \tag{A.1.18}$$

and

$$C_L = 0.422 \quad . \tag{A.1.19}$$

It should be noted that these are only approximate values since in the analysis of the problem it has been assumed that the distance d between the spheres is much larger than their diameters, thus the distance r_1 between a point on the surface of one sphere and the center of the other one is approximately equal to d. For a sphere touching a wall

(or, in this case, for two spheres touching each other), the values of r range from d/2 to 3d/2 and do not satisfy the required assumption $r_1 = d$. Hence, the forces evaluated with the aid of the coefficients C_L and C_M as shown in Eqs. (A.1.18) and (A.1.19) may be inaccurate.

APPENDIX II

EXPERIMENTAL DATA

Table A.2.1 Experimental data* of the incipient motion of spheres.

h = 10.0 cm; D_B = 12.700 mm			
D_s (mm)	ρ_s/ρ_w	ϕ (deg)	H/h
9.489	1.168	23.76	0.086
12.700	1.158	19.47	0.092
19.068	1.152	14.58	0.090
25.410	1.154	11.77	0.091
9.489	1.168	41.37	0.137
12.700	1.158	35.26	0.138
19.068	1.152	27.49	0.130
25.410	1.154	22.63	0.143
9.436	1.314	23.85	0.148
12.642	1.305	19.53	0.161
12.642	1.305	19.53	0.155
18.758	1.314	14.76	0.154
25.258	1.309	11.83	0.150
9.436	1.314	41.49	0.248
12.642	1.305	35.36	0.224
18.758	1.314	27.79	0.231
25.258	1.309	22.73	0.246
9.495	2.175	23.75	0.370
12.700	2.221	19.47	0.406
19.037	2.156	14.60	0.387
25.380	2.163	11.79	0.400
19.037	2.156	27.52	0.594
25.380	2.163	22.65	0.636
9.545	2.793	23.67	0.574
12.700	2.790	19.47	0.597
19.037	2.789	14.60	0.556
25.400	2.791	11.78	0.566

*The symbols appearing in this table are: h - water depth; D_B - bed sphere diameter; D_s - test sphere diameter; ρ_s/ρ_w - specific gravity of the test sphere; ϕ - angle of repose of the test sphere; H/h - height-to-depth ratio of the wave that causes incipient motion.

Table A.2.1 (cont'd)

h = 20.0 cm; D_B = 12.700 mm			
D_s (mm)	ρ_s/ρ_w	ϕ (deg)	H/h
9.489	1.168	23.76	0.071
12.700	1.158	19.47	0.071
19.068	1.152	14.58	0.073
25.410	1.154	11.77	0.073
9.489	1.168	41.37	0.111
12.700	1.158	35.26	0.108
19.068	1.152	27.49	0.101
25.410	1.154	22.63	0.106
9.436	1.314	23.85	0.115
12.642	1.305	19.53	0.114
12.642	1.305	19.53	0.114
18.758	1.314	14.76	0.116
25.258	1.309	11.83	0.114
9.436	1.314	41.49	0.193
12.642	1.305	35.36	0.169
18.758	1.314	27.79	0.160
18.758	1.314	27.79	0.158
25.258	1.309	22.73	0.160
9.495	2.175	23.75	0.310
12.700	2.221	19.47	0.290
19.037	2.156	14.60	0.284
25.380	2.163	11.79	0.260
9.495	2.175	41.35	0.555
12.700	2.221	35.26	0.519
19.037	2.156	27.52	0.409
25.380	2.163	22.65	0.392
9.545	2.793	23.67	0.435
12.700	2.790	19.47	0.402
19.037	2.789	14.60	0.382
25.400	2.791	11.78	0.364
19.037	2.789	27.52	0.671
25.400	2.791	22.64	0.588

Table A.2.1 (cont'd)

h = 30.0 cm, D_B = 12.7 mm			
D_s (mm)	ρ_s/ρ_w	ϕ (deg)	H/h
9.489	1.168	23.76	0.059
12.700	1.158	19.47	0.060
19.068	1.152	14.58	0.058
25.410	1.154	11.77	0.059
9.489	1.168	41.37	0.100
12.700	1.158	35.26	0.098
19.068	1.154	27.49	0.088
25.410	1.152	22.63	0.089
9.436	1.314	23.85	0.105
9.436	1.314	23.85	0.105
12.642	1.305	19.53	0.104
18.758	1.314	14.76	0.099
25.258	1.309	11.83	0.097
9.436	1.314	41.49	0.173
12.642	1.305	35.36	0.149
18.758	1.314	27.79	0.139
25.258	1.309	22.73	0.139
9.495	2.175	23.75	0.267
12.700	2.221	19.47	0.255
19.037	2.156	14.60	0.233
25.380	2.163	11.79	0.230
9.495	2.175	41.35	0.428
12.700	2.221	35.26	0.387
19.037	2.156	27.52	0.347
25.380	2.163	22.65	0.339
9.545	2.793	23.67	0.376
12.700	2.790	19.47	0.356
19.037	2.789	14.60	0.326
19.037	2.789	14.60	0.318
25.400	2.791	11.78	0.312
25.400	2.791	22.64	0.484

Table A.2.1 (cont'd)

h = 22.5 cm, D_B = 9.525 mm			
D_s (mm)	ρ_s/ρ_w	ϕ (deg)	H/h
9.436	1.314	35.45	0.146
12.642	1.305	29.75	0.135
18.758	1.314	22.88	0.139
25.258	1.309	18.43	0.142
9.495	2.175	19.51	0.245
12.700	2.221	15.89	0.246
12.700	2.221	15.89	0.244
19.037	2.156	11.78	0.224
25.380	2.163	9.43	0.228
9.545	2.793	19.44	0.359
12.700	2.790	15.89	0.335
12.700	2.790	15.89	0.283
19.037	2.789	11.78	0.315
25.400	2.791	9.42	0.312
9.545	2.793	35.22	0.542
9.545	2.793	35.22	0.544
12.700	2.790	29.66	0.518
19.037	2.789	22.65	0.493
25.400	2.791	18.36	0.486

Table A.2.1 (cont'd)

h = 42.0 cm, D_B = 9.525 mm			
D_s (mm)	ρ_s/ρ_w	ϕ (deg)	H/h
9.489	1.168	19.52	0.044
25.410	1.154	9.42	0.047
9.436	1.314	35.45	0.114
25.258	1.309	18.43	0.108
9.545	2.793	19.44	0.225
25.400	2.791	9.42	0.267

Table A.2.1.1 Experimental data of the incipient motion of spheres under breaking waves.

D_B = 9.525 mm				
D_s (mm)	ρ_s/ρ_w	ϕ (deg)	h (cm)	H/h
9.495	2.175	35.33	7.24	0.675
9.495	2.175	35.33	7.23	0.705
12.700	2.221	29.66	7.19	0.658
19.037	2.156	22.65	7.84	0.659
25.380	2.163	18.37	8.35	0.687
9.545	2.793	35.22	14.83	0.744
12.700	2.790	29.66	12.64	0.726
19.037	2.789	22.65	12.41	0.708
25.400	2.791	18.36	12.87	0.731

Table A.2.2 Experimental data of the resistance coefficient under solitary waves.

h = 26.2 cm, smooth bed *							
H_1 (cm)	H_2 (cm)	H_3 (cm)	H_4 (cm)	$(H/h)_{rep}$	k	$\left[\frac{d(H/h)}{d(x/h)}\right]_{rep}$	$\overline{C_{f_b}}$
5.85	5.74	5.68	5.62	0.220	5.529×10^{-4}	-1.216×10^{-4}	9.14×10^{-3}
7.52	7.39	7.34	7.30	0.280	4.051×10^{-4}	-1.134×10^{-4}	5.25×10^{-3}
8.32	8.27	8.22	8.10	0.315	3.654×10^{-4}	-1.151×10^{-4}	4.28×10^{-3}
9.31	9.17	9.09	9.00	0.350	4.663×10^{-4}	-1.632×10^{-4}	5.21×10^{-3}
10.22	10.10	10.02	9.88	0.385	4.625×10^{-4}	-1.781×10^{-4}	4.83×10^{-3}
11.17	11.16	11.02	10.87	0.420	3.985×10^{-4}	-1.674×10^{-4}	3.93×10^{-3}
12.22	12.09	12.00	11.92	0.460	3.467×10^{-4}	-1.595×10^{-4}	3.26×10^{-3}
13.34	13.29	13.16	12.98	0.505	3.884×10^{-4}	-1.961×10^{-4}	3.47×10^{-3}
14.47	14.42	14.18	14.10	0.550	3.993×10^{-4}	-2.196×10^{-4}	3.40×10^{-3}
16.08	15.96	15.85	15.67	0.610	3.567×10^{-4}	-2.176×10^{-4}	2.89×10^{-3}
16.31	16.12	15.90	15.69	0.615	5.494×10^{-4}	-3.379×10^{-4}	4.42×10^{-3}

*The symbols appearing in this table are: h - water depth; D_s and σ_g - mean size and standard deviation of the rock; H = wave height; $(H/h)_{rep.}$ = representative value of height-to-depth ratio of the wave in each experiment: k - decay coefficient (used in the relationship $\left[\frac{d(H/h)}{d(x/h)}\right]_{rep} = -k\left(\frac{H}{h}\right)_{rep}$); x - a stationary coordinate along the tank; $\overline{C_{f_b}}$ - mean resistance coefficient; the subscripts 1 through 4 refer to the four measurement stations along the tank.

For smooth bottom experiments:

$x_1 = 0.0$ cm
$x_2 = 620.0$ cm
$x_3 = 1240.0$ cm
$x_4 = 1860.0$ cm

For rough bottom experiments:

$x_1 = 0.0$ cm
$x_2 = 610.0$ cm
$x_3 = 1220.0$ cm
$x_4 = 1830.0$ cm.

Table A.2.2 (cont'd)

h = 18.5 cm, smooth bed							
H_1 (cm)	H_2 (cm)	H_3 (cm)	H_4 (cm)	$(H/h)_{rep}$	k	$\left[\frac{d(H/h)}{d(x/h)}\right]_{rep}$	$\overline{C_{f_b}}$
4.62	4.62	4.54	4.48	0.250	3.276×10^{-4}	-8.190×10^{-5}	5.09×10^{-3}
5.57	5.50	5.40	5.34	0.295	4.322×10^{-4}	-1.275×10^{-4}	6.05×10^{-3}
6.53	6.42	6.33	6.19	0.345	5.208×10^{-4}	-1.797×10^{-4}	6.60×10^{-3}
7.45	7.31	7.25	7.08	0.395	4.806×10^{-4}	-1.898×10^{-4}	5.62×10^{-3}
8.48	8.36	8.26	8.15	0.450	3.912×10^{-4}	-1.760×10^{-4}	4.20×10^{-3}
9.65	9.51	9.40	9.20	0.510	4.662×10^{-4}	-2.357×10^{-4}	4.68×10^{-3}
10.79	10.67	10.50	10.33	0.570	4.379×10^{-4}	-2.496×10^{-4}	4.18×10^{-3}
12.21	12.17	11.93	11.62	0.650	5.028×10^{-4}	-3.268×10^{-4}	4.54×10^{-3}
13.02	12.92	12.45	12.12	0.685	7.518×10^{-4}	-5.150×10^{-4}	6.55×10^{-3}
13.28	12.92	12.54	12.15	0.690	8.851×10^{-4}	-6.107×10^{-4}	7.66×10^{-3}

Table A.2.2 (cont'd)

h = 14.5 cm, smooth bed							
H_1 (cm)	H_2 (cm)	H_3 (cm)	H_4 (cm)	$(H/h)_{rep}$	k	$\left[\frac{d(H/h)}{d(x/h)}\right]_{rep}$	$\overline{C_{f_b}}$
3.37	3.26	3.18	3.07	0.220	7.123×10^{-4}	-1.567×10^{-4}	1.29×10^{-2}
4.23	4.12	4.01	3.95	0.280	5.438×10^{-4}	-1.523×10^{-4}	8.42×10^{-3}
5.11	5.04	4.91	4.77	0.340	5.442×10^{-4}	-1.850×10^{-4}	7.30×10^{-3}
5.11	5.05	4.91	4.79	0.340	5.195×10^{-4}	-1.766×10^{-4}	6.96×10^{-3}
6.08	5.99	5.85	5.72	0.405	4.835×10^{-4}	-1.958×10^{-4}	5.94×10^{-3}
7.17	7.04	6.80	6.69	0.475	5.673×10^{-4}	-2.695×10^{-4}	6.44×10^{-3}
7.13	7.07	6.86	6.75	0.480	4.548×10^{-4}	-2.183×10^{-4}	5.18×10^{-3}
8.36	8.20	8.03	7.88	0.560	4.639×10^{-4}	-2.598×10^{-4}	4.78×10^{-3}
9.68	9.46	9.11	8.81	0.640	7.489×10^{-4}	-4.793×10^{-4}	7.35×10^{-3}

Table A.2.2 (cont'd)

h = 12.8 cm, smooth bed							
H_1 (cm)	H_2 (cm)	H_3 (cm)	H_4 (cm)	$(H/h)_{rep}$	k	$\left[\frac{d(H/h)}{d(x/h)}\right]_{rep}$	$\overline{C_{f_b}}$
2.56	2.50	2.41	2.31	0.190	0.392×10^{-4}	-1.201×10^{-4}	1.27×10^{-2}
3.46	3.37	3.25	3.15	0.260	6.562×10^{-4}	-1.706×10^{-4}	1.09×10^{-2}
4.33	4.22	4.09	3.97	0.325	6.022×10^{-4}	-1.957×10^{-4}	8.76×10^{-3}
5.27	5.17	5.00	4.90	0.400	5.199×10^{-4}	-2.080×10^{-4}	6.65×10^{-3}
6.32	6.22	6.03	5.86	0.475	5.321×10^{-4}	-2.528×10^{-4}	6.16×10^{-3}
7.48	7.34	7.17	6.93	0.565	5.214×10^{-4}	-2.946×10^{-4}	5.54×10^{-3}
7.50	7.37	7.12	6.90	0.565	5.877×10^{-4}	-3.321×10^{-4}	6.25×10^{-3}
8.42	8.14	7.85	7.67	0.625	6.527×10^{-4}	-4.079×10^{-4}	6.65×10^{-3}

Table A.2.2 (cont'd)

h = 26.2 cm; D_s = 7.55 mm; σ_g = 1.15							
H_1 (cm)	H_2 (cm)	H_3 (cm)	H_4 (cm)	$(H/h)_{rep}$	k	$\left[\frac{d(H/h)}{d(x/h)}\right]_{rep}$	$\overline{C_{f_b}}$
5.28	4.96	4.79	4.57	0.190	2.011×10^{-3}	-3.821×10^{-4}	5.00×10^{-2}
5.67	5.37	5.15	4.95	0.200	1.930×10^{-3}	-3.860×10^{-4}	4.59×10^{-2}
6.08	5.73	5.48	5.28	0.215	2.009×10^{-3}	-4.319×10^{-4}	4.61×10^{-2}
6.45	6.13	5.92	5.63	0.230	1.902×10^{-3}	-4.375×10^{-4}	4.08×10^{-2}
6.47	6.13	5.87	5.62	0.230	2.001×10^{-3}	-4.602×10^{-4}	4.32×10^{-2}
6.85	6.48	6.23	5.99	0.245	1.898×10^{-3}	-4.650×10^{-4}	3.89×10^{-2}
7.37	6.97	6.67	6.38	0.260	2.048×10^{-3}	-5.325×10^{-4}	4.11×10^{-2}
7.77	7.35	7.04	6.78	0.275	1.941×10^{-3}	-5.338×10^{-4}	3.75×10^{-2}
8.21	7.78	7.47	7.18	0.295	1.902×10^{-3}	-5.611×10^{-4}	3.50×10^{-2}
8.68	8.18	7.88	7.61	0.310	1.856×10^{-3}	-5.754×10^{-4}	3.25×10^{-2}
9.12	8.63	8.31	7.97	0.325	1.899×10^{-3}	-6.172×10^{-4}	3.25×10^{-2}
9.58	9.08	8.74	8.33	0.340	1.965×10^{-3}	-6.681×10^{-4}	3.27×10^{-2}
10.02	9.57	9.17	8.82	0.360	1.827×10^{-3}	-6.577×10^{-4}	2.91×10^{-2}
10.60	10.10	9.69	9.28	0.380	1.892×10^{-3}	-7.190×10^{-4}	2.93×10^{-2}
11.08	10.55	10.11	9.62	0.395	2.004×10^{-3}	-7.916×10^{-4}	3.07×10^{-2}
11.56	11.04	10.54	10.11	0.410	1.926×10^{-3}	-7.897×10^{-4}	2.89×10^{-2}
11.62	11.07	10.58	10.13	0.415	1.963×10^{-3}	-8.146×10^{-4}	2.93×10^{-2}
12.16	11.62	11.02	10.63	0.435	1.960×10^{-3}	-8.526×10^{-4}	2.85×10^{-2}
12.08	11.60	11.05	10.58	0.435	1.917×10^{-3}	-8.339×10^{-4}	2.78×10^{-2}
12.63	12.05	11.52	11.04	0.450	1.927×10^{-3}	-8.672×10^{-4}	2.76×10^{-2}
13.14	12.48	11.94	11.41	0.470	2.009×10^{-3}	-9.442×10^{-4}	2.84×10^{-2}
13.35	12.85	12.24	11.80	0.480	1.799×10^{-3}	-8.635×10^{-4}	2.49×10^{-2}
13.65	13.13	12.55	12.04	0.490	1.811×10^{-3}	-8.874×10^{-4}	2.48×10^{-2}
14.08	13.44	12.94	12.32	0.500	1.883×10^{-3}	-9.415×10^{-4}	2.57×10^{-2}
14.52	13.91	13.17	12.68	0.520	1.981×10^{-3}	-1.030×10^{-3}	2.68×10^{-2}
15.02	14.46	13.68	13.17	0.540	1.932×10^{-3}	-1.043×10^{-3}	2.55×10^{-2}
15.54	14.82	14.13	13.53	0.550	1.989×10^{-3}	-1.094×10^{-3}	2.60×10^{-2}
16.21	15.48	14.67	14.07	0.580	2.055×10^{-3}	-1.192×10^{-3}	2.64×10^{-2}
16.81	15.97	15.17	14.55	0.600	2.081×10^{-3}	-1.249×10^{-3}	2.68×10^{-2}
16.80	16.00	15.23	14.64	0.600	1.985×10^{-3}	-1.191×10^{-3}	2.55×10^{-2}
16.86	16.00	15.16	14.38	0.600	2.282×10^{-3}	-1.369×10^{-3}	2.97×10^{-2}
16.74	15.98	15.25	14.48	0.600	2.070×10^{-3}	-1.242×10^{-3}	2.67×10^{-2}

Table A.2.2 (cont'd)

h = 26.2 cm; D_s = 5.23 mm; σ_g = 1.09							
H_1 (cm)	H_2 (cm)	H_3 (cm)	H_4 (cm)	$(H/h)_{rep}$	k	$\left[\frac{d(H/h)}{d(x/h)}\right]_{rep}$	$\overline{C_{f_b}}$
5.22	4.93	4.82	4.74	0.185	1.340×10^{-3}	-2.479×10^{-4}	3.24×10^{-2}
6.05	5.74	5.58	5.37	0.220	1.658×10^{-3}	-3.648×10^{-4}	3.66×10^{-2}
6.87	6.56	6.30	6.11	0.245	1.684×10^{-3}	-4.126×10^{-4}	3.41×10^{-2}
7.77	7.40	7.19	6.90	0.280	1.654×10^{-3}	-4.631×10^{-4}	3.10×10^{-2}
8.62	8.24	7.96	7.72	0.310	1.569×10^{-3}	-4.864×10^{-4}	2.71×10^{-2}
9.51	9.18	8.87	8.60	0.345	1.444×10^{-3}	-4.982×10^{-4}	2.29×10^{-2}
10.50	10.08	9.73	9.45	0.380	1.509×10^{-3}	-5.734×10^{-4}	2.28×10^{-2}
11.57	11.11	10.73	10.36	0.420	1.573×10^{-3}	-6.607×10^{-4}	2.28×10^{-2}
12.62	12.14	11.74	11.32	0.455	1.545×10^{-3}	-7.030×10^{-4}	2.14×10^{-2}
13.78	13.11	12.65	12.19	0.495	1.733×10^{-3}	-8.578×10^{-4}	2.35×10^{-2}
13.81	13.27	12.75	12.27	0.500	1.695×10^{-3}	-8.475×10^{-4}	2.29×10^{-2}
15.10	14.33	13.70	13.96	0.540	1.771×10^{-3}	-9.563×10^{-4}	2.31×10^{-2}
15.13	14.42	13.91	13.45	0.545	1.671×10^{-3}	-9.107×10^{-4}	2.15×10^{-2}
15.14	14.43	13.87	13.37	0.545	1.772×10^{-3}	-9.567×10^{-4}	2.30×10^{-2}
16.93	16.02	15.42	14.90	0.605	1.810×10^{-3}	-1.095×10^{-3}	2.27×10^{-2}
17.00	15.96	15.38	14.82	0.605	1.927×10^{-3}	-1.166×10^{-3}	2.44×10^{-2}
17.07	16.21	15.53	14.99	0.610	1.858×10^{-3}	-1.133×10^{-3}	2.33×10^{-2}

Table A.2.2 (cont'd)

h = 18.5 cm; D_s = 7.55 mm; σ_g = 1.15							
H_1 (cm)	H_2 (cm)	H_3 (cm)	H_4 (cm)	$(H/h)_{rep}$	k	$\left[\frac{d(H/h)}{d(x/h)}\right]_{rep}$	$\overline{C_{f_b}}$
3.25	2.94	2.85	2.50	0.155	2.481×10^{-3}	-3.846×10^{-4}	7.52×10^{-2}
3.25	2.93	2.85	2.58	0.155	2.184×10^{-3}	-3.385×10^{-4}	6.57×10^{-2}
4.07	3.68	3.50	3.20	0.195	2.340×10^{-3}	-4.563×10^{-4}	5.81×10^{-2}
4.90	4.69	4.21	3.89	0.240	2.428×10^{-3}	-5.827×10^{-4}	5.16×10^{-2}
5.80	5.31	4.95	4.60	0.280	2.322×10^{-3}	-6.502×10^{-4}	4.52×10^{-2}
6.74	6.20	5.76	5.35	0.325	2.325×10^{-3}	-7.556×10^{-4}	4.07×10^{-2}
7.75	7.17	6.60	6.13	0.375	2.385×10^{-3}	-8.944×10^{-4}	3.84×10^{-2}
8.77	8.16	7.52	6.96	0.425	2.351×10^{-3}	-9.992×10^{-4}	3.53×10^{-2}
9.93	9.19	8.46	7.87	0.480	2.366×10^{-3}	-1.136×10^{-3}	3.39×10^{-2}
11.22	10.31	9.47	8.77	0.540	2.499×10^{-3}	-1.349×10^{-3}	3.40×10^{-2}
12.58	11.20	10.19	9.48	0.590	2.861×10^{-3}	-1.688×10^{-3}	3.79×10^{-2}

Table A.2.2 (cont'd)

h = 18.5 cm; D_s = 5.23 mm; σ_g = 1.09							
H_1 (cm)	H_2 (cm)	H_3 (cm)	H_4 (cm)	$(H/h)_{rep}$	k	$\left[\frac{d(H/h)}{d(x/h)}\right]_{rep}$	$\overline{C_{f_b}}$
3.29	3.02	2.93	2.76	0.165	1.690×10^{-3}	-2.789×10^{-4}	4.69×10^{-2}
4.10	3.77	3.56	3.40	0.200	1.877×10^{-3}	-3.754×10^{-4}	4.49×10^{-2}
4.92	4.57	4.36	4.08	0.245	1.846×10^{-3}	-4.523×10^{-4}	3.81×10^{-2}
5.83	5.42	5.11	4.79	0.285	1.966×10^{-3}	-5.603×10^{-4}	3.76×10^{-2}
6.71	6.27	5.95	5.55	0.330	1.886×10^{-3}	-6.224×10^{-4}	3.21×10^{-2}
7.75	7.24	6.86	6.45	0.385	1.834×10^{-3}	-7.061×10^{-4}	2.86×10^{-2}
8.85	8.19	7.73	7.28	0.435	1.952×10^{-3}	-8.491×10^{-4}	2.86×10^{-2}
10.05	9.32	8.61	8.17	0.490	2.125×10^{-3}	-1.041×10^{-3}	2.98×10^{-2}
11.26	10.50	9.78	9.18	0.550	2.074×10^{-3}	-1.141×10^{-3}	2.75×10^{-2}
12.25	11.29	10.52	9.80	0.600	2.465×10^{-3}	-1.479×10^{-3}	3.22×10^{-2}

Table A.2.2 (cont'd)

h = 14.5 cm; D_s = 7.55 mm; σ_g = 1.15							
H_1 (cm)	H_2 (cm)	H_3 (cm)	H_4 (cm)	$(H/h)_{rep}$	k	$\left[\frac{d(H/h)}{d(x/h)}\right]_{rep}$	$\overline{C_{f_b}}$
2.24	2.04	1.83	1.68	0.135	2.310×10^{-3}	-3.119×10^{-4}	8.82×10^{-2}
3.08	2.68	2.47	2.24	0.180	2.465×10^{-3}	-4.437×10^{-4}	6.70×10^{-2}
3.595	3.18	2.86	2.57	0.210	2.646×10^{-3}	-5.557×10^{-4}	6.36×10^{-2}
4.115	3.605	3.23	2.86	0.240	2.856×10^{-3}	-6.854×10^{-4}	6.14×10^{-2}
5.16	4.53	4.06	3.61	0.300	2.808×10^{-3}	-8.424×10^{-4}	5.28×10^{-2}
5.13	4.56	4.07	3.66	0.300	2.678×10^{-3}	-8.034×10^{-4}	5.02×10^{-2}
5.70	5.08	4.515	4.02	0.335	2.770×10^{-3}	-9.280×10^{-4}	4.83×10^{-2}
6.27	5.57	4.96	4.42	0.370	2.769×10^{-3}	-1.025×10^{-3}	4.58×10^{-2}
7.60	6.72	5.98	5.30	0.445	2.848×10^{-3}	-1.267×10^{-3}	4.19×10^{-2}
8.42	7.38	6.55	5.82	0.490	2.917×10^{-3}	-1.429×10^{-3}	4.21×10^{-2}
9.02	7.85	6.96	6.14	0.520	3.029×10^{-3}	-1.575×10^{-3}	4.28×10^{-2}

Table A.2.2 (cont'd)

h = 14.5 cm; D_s = 5.23 mm; σ_g = 1.09							
H_1 (cm)	H_2 (cm)	H_3 (cm)	H_4 (cm)	$(H/h)_{rep}$	k	$\left[\frac{d(H/h)}{d(x/h)}\right]_{rep}$	$\overline{C_{f_b}}$
1.94	1.73	1.63	1.54	0.120	1.788×10^{-3}	-2.146×10^{-4}	7.19×10^{-2}
2.62	2.37	2.21	2.10	0.160	1.744×10^{-3}	-2.790×10^{-4}	5.00×10^{-2}
3.45	3.05	2.90	2.67	0.210	1.948×10^{-3}	-4.091×10^{-4}	4.55×10^{-2}
3.89	3.49	3.25	2.98	0.235	2.070×10^{-3}	-4.865×10^{-4}	4.47×10^{-2}
4.33	3.89	3.58	3.31	0.260	2.113×10^{-3}	-5.494×10^{-4}	5.26×10^{-2}
4.76	4.32	3.97	3.64	0.290	2.114×10^{-3}	-6.131×10^{-4}	4.02×10^{-2}
5.36	4.76	4.37	3.98	0.320	2.326×10^{-3}	-7.443×10^{-4}	4.16×10^{-2}
5.73	5.18	4.73	4.35	0.345	2.181×10^{-3}	-7.524×10^{-4}	3.66×10^{-2}
6.26	5.63	5.13	4.71	0.375	2.250×10^{-3}	-8.438×10^{-4}	3.62×10^{-2}
6.75	6.10	5.56	5.10	0.405	2.219×10^{-3}	-8.987×10^{-4}	3.43×10^{-2}
7.93	7.13	6.42	5.91	0.475	2.346×10^{-3}	-1.114×10^{-3}	3.38×10^{-2}
9.17	8.19	7.38	6.72	0.545	2.464×10^{-3}	-1.343×10^{-3}	3.34×10^{-2}

Table A.2.2 (cont'd)

h = 12.8 cm; D_s = 5.23 mm; σ_g = 1.09							
H_1 (cm)	H_2 (cm)	H_3 (cm)	H_4 (cm)	$(H/h)_{rep}$	k	$\left[\frac{d(H/h)}{d(x/h)}\right]_{rep}$	$\overline{C_{f_b}}$
1.92	1.78	1.64	1.50	0.135	1.726×10^{-3}	-2.330×10^{-4}	6.50×10^{-2}
2.69	2.39	2.16	2.03	0.180	1.984×10^{-3}	-3.571×10^{-4}	5.25×10^{-2}
3.57	3.13	2.84	2.57	0.235	2.273×10^{-3}	-5.342×10^{-4}	4.95×10^{-2}
4.45	3.93	3.51	3.17	0.295	2.372×10^{-3}	-6.997×10^{-4}	4.51×10^{-2}
5.41	4.70	4.31	3.84	0.360	2.340×10^{-3}	-8.424×10^{-4}	3.85×10^{-2}
6.51	5.69	5.13	4.60	0.430	2.404×10^{-3}	-1.034×10^{-3}	3.64×10^{-2}
7.66	6.75	5.99	5.33	0.505	2.534×10^{-3}	-1.280×10^{-3}	3.58×10^{-2}

Table A.2.3 Characteristics of the material used in the investigation of the incipient motion of particles of arbitrary shape.

Material	ρ_s/ρ_w Specific Gravity	D_s (mm) Mean Diameter	σ_g Geometric Standard Deviation	N_{p_T} Total Number of Particles in Upper Layer of Bed
Natural Rock #1	2.68	5.44	1.07	11930
Natural Rock #2	2.68	7.70	1.15	5940
Coal #1	1.283	8.00	1.18	5490
Coal #2	1.283	11.10	1.07	3640

Table A.2.4 Experimental data of the incipient motion of particles of arbitrary shape.

Natural Rock *							
Run No.	h (cm)	H (cm)	H/h	N_p		$(N_p/N_{p_T})\times10^4$	
				Rock #1	Rock #2	Rock #1	Rock #2
CD-121-6	26.23	22.95	.875	22	5	18.44	8.42
CD-122-6	26.23	22.95	.875	8	3	6.71	5.05
CD-123-6	26.22	22.80	.870	16	4	13.41	6.73
CD-124-6	26.22	23.08	.880	13	6	10.90	10.10
CD-125-6	26.22	22.76	.868	14	4	11.74	6.73
CD-126-6	26.22	22.94	.875	16	3	13.41	5.05
CD-127-6	26.21	22.98	.877	16	6	13.41	10.10
CD-128-6	26.21	22.87	.873	12	5	10.06	8.42
CD-129-6	26.21	22.92	.874	9	6	7.54	10.10
CD-130-6	26.21	22.97	.876	12	4	10.06	6.73
CD-131-6	26.20	23.01	.878	17	4	14.25	6.73
Average			.875			11.81	7.65
Std. dev.			.00341			3.30	1.90

*The symbols appearing in this table are h - water depth; H - wave height; N_p - number of particles moving in the bed; N_{p_T} - total number of particles in the upper layer of the bed. Rock #1, Rock #2, and Coal #1 and Coal #2 (which appear in later sections of this table) refer to the gravel whose characteristics are given in Table A.2.3.

Table A.2.4 (cont'd)

Natural Rock							
Run No.	h (cm)	H (cm)	H/h	N_p		$(N_p/N_{p_T})\times10^4$	
				Rock #1	Rock #2	Rock #1	Rock #2
CD-1-7	26.19	21.36	.816	13	7	10.90	11.78
CD-2-7	26.19	21.69	.828	12	6	10.06	10.10
CD-3-7	26.20	21.54	.822	--*	4	--	6.73
CD-4-7	26.20	21.76	.831	--	1	--	1.68
CD-5-7	26.20	21.77	.831	--	4	--	6.73
CD-6-7	26.20	21.48	.820	--	5	--	8.42
CD-7-7	26.20	21.66	.827	--	5	--	8.42
CD-8-7	26.20	21.75	.830	11	1	9.22	1.68
CD-9-7	26.20	21.69	.828	15	5	12.57	8.42
CD-10-7	26.20	21.57	.823	11	4	9.22	6.73
CD-11-7	26.20	21.56	.823	11	2	9.22	3.37
CD-12-7	26.20	21.47	.819	13	2	10.90	3.37
CD-13-7	26.21	21.52	.821	10	1	8.38	1.68
Average			.824			10.06	6.09
Std. dev.			.00493			1.34	3.40

*Bed was externally disturbed during experiment. No data were produced.

Table A.2.4 (cont'd)

Natural Rock							
Run No.	h (cm)	H (cm)	H/h	N_p		$(N_p/N_{p_T})\times10^4$	
				Rock #1	Rock #2	Rock #1	Rock #2
CD-1-8	26.19	19.54	.746	3	3	2.51	5.05
CD-2-8	26.19	19.57	.747	7	3	5.87	5.05
CD-3-8	26.20	19.48	.744	11	5	9.22	8.42
CD-4-8	26.20	19.50	.744	8	4	6.71	6.73
CD-5-8	26.20	19.60	.748	8	2	6.71	3.37
CD-6-8	26.20	19.59	.748	10	3	8.38	5.05
CD-7-8	26.20	19.51	.745	10	4	8.38	6.73
CD-8-8	26.20	19.64	.750	7	3	5.87	5.05
CD-9-8	26.20	19.60	.748	7	3	5.87	5.05
CD-10-8	26.20	19.46	.743	11	--*	9.22	--
CD-11-8	26.20	19.53	.745	9	--	7.54	--
CD-12-8	26.19	19.56	.747	12	--	10.06	--
CD-13-8	26.20	19.56	.747	14	--	11.74	--
CD-14-8	26.20	19.63	.749	10	--	8.38	--
CD-15-8	26.20	19.51	.745	7	--	5.87	--
Average			.746			7.49	5.61
Std. dev.			.00203			2.23	1.46

*Bed disturbed externally during experiments. No data produced.

Table A.2.4 (cont'd)

Natural Rock							
Run No.	h (cm)	H (cm)	H/h	N_p		$(N_p/N_{p_T})\times10^4$	
				Rock #1	Rock #2	Rock #1	Rock #2
CD-1-9	26.21	21.76	.830	10	4	8.38	6.73
CD-2-9	26.20	21.59	.824	11	5	9.22	8.42
CD-3-9	26.20	21.61	.825	11	2	9.22	3.37
CD-4-9	26.20	21.64	.826	7	4	5.87	6.73
CD-5-9	26.20	21.53	.822	7	5	5.87	8.42
CD-6-9	26.20	21.75	.830	8	3	6.71	5.05
CD-7-9	26.20	21.61	.825	12	4	10.06	6.73
CD-8-9	26.20	21.72	.829	13	4	10.90	6.73
CD-9-9	26.20	21.75	.830	7	4	5.87	6.73
CD-10-9	26.19	21.75	.830	14	3	11.74	5.05
CD-11-9	26.21	21.76	.830	14	4	11.74	6.73
CD-12-9	26.21	21.69	.828	15	3	12.57	5.05
CD-13-9	26.20	21.80	.832	17	2	14.25	3.37
CD-14-9	26.20	21.79	.832	8	5	6.71	8.42
CD-15-9	26.19	21.92	.837	12	8	10.06	13.47
Average			.829			9.28	6.73
Std. dev.			.00379			2.68	2.46

Table A.2.4 (cont'd)

Natural Rock							
Run No.	h (cm)	H (cm)	H/h	N_p		$(N_p/N_{p_T})\times10^4$	
				Rock #1	Rock #2	Rock #1	Rock #2
CD-1-10	26.22	18.40	.702	12	5	10.06	8.42
CD-2-10	26.22	18.52	.706	12	4	10.06	6.73
CD-3-10	26.21	18.54	.707	7	6	5.87	10.10
CD-4-10	26.21	18.58	.709	5	3	4.19	5.05
CD-5-10	26.21	18.50	.706	5	2	4.19	3.37
CD-6-10	26.21	18.60	.710	12	2	10.06	3.37
CD-7-10	26.20	18.61	.710	9	4	7.54	6.73
CD-8-10	26.20	18.59	.709	5	3	4.19	5.05
CD-9-10	26.20	18.57	.709	5	0	4.19	0
CD-10-10	26.19	18.52	.707	6	2	5.03	3.37
CD-11-10	26.21	--*	--	6	3	5.03	5.05
CD-12-10	26.20	--	--	7	0	5.87	0
CD-13-10	26.20	--	--	3	0	2.51	0
CD-14-10	26.20	--	--	6	0	5.03	0
Average			.708			5.99	4.09
Std. dev.			.00246			2.48	3.28

*The wave record displayed erratic reading. The wave generator, however, was set as in preceding waves.

Table A.2.4 (cont'd)

Natural Rock							
Run No.	h (cm)	H (cm)	H/h	N_p		$(N_p/N_{p_T})\times10^4$	
				Rock #1	Rock #2	Rock #1	Rock #2
CD-1-11	26.21	18.55	.708	2	1	1.68	1.68
CD-2-11	26.20	18.49	.706	5	1	4.19	1.68
CD-3-11	26.19	18.37	.701	5	1	4.19	1.68
CD-4-11	26.19	18.33	.700	4	1	3.35	1.68
CD-5-11	26.19	18.32	.700	6	1	5.03	1.68
CD-6-11	26.20	18.44	.704	5	1	4.19	1.68
CD-7-11	26.21	18.50	.706	--**	2	--	3.37
CD-8-11	26.21	18.45	.704	4	1	3.35	1.68
CD-9-11	26.20	18.40	.702	5	1	4.19	1.68
CD-10-11	26.21	18.57	.709	6	0	5.03	0
CD-11-11	26.21	18.54	.707	5	3	4.19	5.05
CD-12-11	26.21	18.60	.710	6	0	5.03	0
CD-13-11	26.22	--*	--	5	2	4.19	3.37
CD-14-11	26.22	18.33	.699	4	0	3.35	0
CD-15-11	26.21	18.37	.701	3	1	2.51	1.68
Average			.704			3.89	1.79
Std. dev.			.00365			0.96	1.35

*Erratic wave record. Wave assumed as average of all other waves.

**Erratic data, ignored.

Table A.2.4 (cont'd)

Natural Rock							
Run No.	h (cm)	H (cm)	H/h	N_p		$(N_p/N_{p_T})\times10^4$	
				Rock #1	Rock #2	Rock #1	Rock #2
CD-1-12	26.21	15.62	.596	12	0	10.06	0
CD-2-12	26.21	15.49	.591	5	0	4.19	0
CD-3-12	26.21	15.55	.593	5	0	4.19	0
CD-4-12	26.20	15.65	.597	5	0	4.19	0
CD-5-12	26.21	15.65	.597	7	1	5.87	1.68
CD-6-12	26.21	15.68	.598	10	2	8.38	3.37
CD-7-12	26.20	15.73	.600	8	1	6.71	1.68
CD-8-12	26.21	15.55	.593	5	1	4.19	1.68
CD-9-12	26.21	15.44	.589	4	0	3.35	0
CD-10-12	26.21	15.56	.594	6	0	5.03	0
CD-11-12	26.21	15.69	.599	5	0	4.19	0
CD-12-12	26.21	15.67	.598	4	0	3.35	0
CD-13-12	26.20	15.66	.598	4	0	3.35	0
CD-14-12	26.20	15.76	.602	1	0	.84	0
CD-15-12	26.20	15.78	.602	1	1	.84	1.68
Average			.596			4.58	0.673
Std. dev.			.00381			2.45	1.064

Table A.2.4 (cont'd)

Natural Rock							
Run No.	h (cm)	H (cm)	H/h	N_p		$(N_p/N_{p_T}) \times 10^4$	
				Rock #1	Rock #2	Rock #1	Rock #2
CD-1-13	18.50	15.20	.822	5	4	4.19	6.73
CD-2-13	18.51	15.60	.843	10	4	8.38	6.73
CD-3-13	18.52	15.73	.849	10	2	8.38	3.37
CD-4-13	18.52	15.52	.838	8	4	6.71	6.73
CD-5-13	18.51	15.78	.853	14	6	11.74	10.10
CD-6-13	18.51	15.90	.860	12	5	10.06	8.42
CD-7-13	18.51	15.80	.854	8	3	6.71	5.05
CD-8-13	18.50	15.93	.861	10	3	8.38	5.05
CD-9-13	18.51	16.05	.867	10	2	8.38	3.37
CD-10-13	18.51	16.14	.872	13	3	10.90	5.05
CD-11-13	18.51	16.13	.871	7	1	5.87	1.68
CD-12-13	18.51	16.12	.871	13	4	10.90	6.73
CD-13-13	18.50	16.04	.867	13	2	10.90	3.37
CD-14-13	18.51	15.70	.848	10	1	8.38	1.68
CD-15-13	18.50	15.95	.862	10	1	8.38	1.68
Average			.856			8.55	5.05
Std. dev.			.01414			2.11	2.55

Table A.2.4 (cont'd)

Natural Rock							
Run No.	h (cm)	H (cm)	H/h	N_p		$(N_p/N_{p_T}) \times 10^4$	
				Rock #1	Rock #2	Rock #1	Rock #2
CD-1-14	18.52	13.65	.737	6	4	5.03	6.73
CD-2-14	18.51	13.67	.739	9	3	7.54	5.05
CD-3-14	18.50	13.87	.750	10	3	8.38	5.05
CD-4-14	18.51	13.91	.751	7	2	5.87	3.37
CD-5-14	18.51	13.88	.750	10	1	8.38	1.68
CD-6-14	18.50	13.76	.744	9	0	7.54	0
CD-7-14	18.52	13.89	.750	4	3	3.35	5.05
CD-8-14	18.52	13.88	.749	9	2	7.54	3.37
CD-9-14	18.51	13.82	.747	7	2	5.87	3.37
CD-10-14	18.51	13.83	.747	6	2	5.03	3.37
CD-11-14	18.50	13.93	.753	5	1	4.19	1.68
CD-12-14	18.52	13.58	.733	6	1	5.03	1.68
CD-13-14	18.52	13.90	.751	5	3	4.19	5.05
CD-14-14	18.52	13.87	.749	8	0	6.71	0
CD-15-14	18.51	13.94	.753	8	2	6.71	3.37
Average			.747			6.09	3.25
Std. dev.			.00604			1.60	1.96

Table A.2.4 (cont'd)

Natural Rock							
Run No.	h (cm)	H (cm)	H/h	N_p		$(N_p/N_{p_T})\times10^4$	
				Rock #1	Rock #2	Rock #1	Rock #2
CD-1-15	18.49	11.10	.600	8	1	6.71	1.68
CD-2-15	18.51	11.22	.606	9	0	7.54	0
CD-3-15	18.52	11.12	.600	6	2	5.03	3.37
CD-4-15	18.52	11.10	.599	6	1	5.03	1.68
CD-5-15	18.51	11.16	.603	3	1	2.51	1.68
CD-6-15	18.51	11.29	.610	4	0	3.35	0
CD-7-15	18.52	10.97	.592	3	0	2.51	0
CD-8-15	18.52	11.03	.596	5	1	4.19	1.68
CD-9-15	18.51	11.05	.597	6	1	5.03	1.68
CD-10-15	18.51	11.08	.599	7	1	5.87	1.68
CD-11-15	18.51	11.08	.599	5	3	4.19	5.05
CD-12-15	18.50	11.08	.599	7	2	5.87	3.37
CD-13-15	18.50	11.08	.599	2	1	1.68	1.68
CD-14-15	18.51	11.11	.600	2	1	1.68	1.68
CD-15-15	18.50	11.10	.600	4	0	3.35	0
Average			.600			4.30	1.68
Std. dev.			.00413			1.79	1.42

Table A.2.4 (cont'd)

Coal							
Run No.	h (m)	H (cm)	H/h	N_p		$(N_p/N_{p_T})\times10^4$	
				Coal #1	Coal #2	Coal #1	Coal #2
C,2,3-1-5	26.18	6.60	.252	1	2	1.82	5.49
C,2,3-2-5	26.20	6.48	.247	4	3	7.29	8.24
C,2,3-3-5	26.21	6.49	.248	5	3	9.11	8.24
C,2,3-4-5	26.20	6.50	.248	6	1	10.93	2.75
C,2,3-5-5	26.20	6.50	.248	3	1	5.46	2.75
C,2,3-6-5	26.20	6.53	.249	5	0	9.11	0
C,2,3-7-5	26.20	6.50	.248	6	1	10.93	2.75
C,2,3-8-5	26.20	6.47	.247	4	0	7.29	0
C,2,3-9-5	26.21	6.49	.248	5	2	9.11	5.49
C,2,3-10-5	26.21	6.52	.249	6	1	10.93	2.75
C,2,3-11-5	26.21	6.52	.249	3	0	5.46	0
C,2,3-12-5	26.21	6.50	.248	4	1	7.29	2.75
C,2,3-13-5	26.20	6.54	.250	4	1	7.29	2.75
C,2,3-14-5	26.20	6.52	.249	5	1	9.11	2.75
C,2,3-15-5	26.20	6.52	.249	3	1	5.46	2.75
Average			.249			7.77	3.30
Std. dev.			.00123			2.53	2.58

Table A.2.4 (cont'd)

Coal							
Run No.	h (cm)	H (cm)	H/h	N_p		$(N_p/N_{p_T})\times 10^4$	
				Coal #1	Coal #2	Coal #1	Coal #2
C,2,3-1-6	14.50	3.65	.252	4	1	7.29	2.75
C,2,3-2-6	14.50	3.60	.248	5	2	9.11	5.49
C,2,3-3-6	14.50	3.70	.255	2	1	3.64	2.75
C,2,3-4-6	14.50	3.62	.250	3	0	5.46	0
C,2,3-5-6	14.50	3.68	.254	5	1	9.11	2.75
C,2,3-6-6	14.49	3.67	.253	3	2	5.46	5.49
C,2,3-7-6	14.48	3.70	.256	3	0	5.46	0
C,2,3-8-6	14.48	3.67	.254	3	1	5.46	2.75
C,2,3-9-6	14.50	3.67	.253	3	0	5.46	0
C,2,3-10-6	14.50	3.64	.251	1	0	1.82	0
C,2,3-11-6	14.50	3.71	.256	3	4	5.46	10.99
C,2,3-12-6	14.50	3.66	.252	2	1	3.64	2.75
C,2,3-13-6	14.51	3.70	.255	1	0	1.82	0
C,2,3-14-6	14.50	3.68	.254	2	1	3.64	2.75
C,2,3-15-6	14.50	3.67	.253	2	2	3.64	5.49
Average			.253			5.10	2.93
Std. dev.			.00214			2.20	3.02

Table A.2.4 (cont'd)

Coal							
Run No.	h (cm)	H (cm)	H/h	N_p		$(N_p/N_{p_T})\times10^4$	
				Coal #1	Coal #2	Coal #1	Coal #2
C,2,3-280-8	14.50	4.83	.333	6	5	10.93	13.74
C,2,3-290-8	14.51	4.80	.331	7	5	12.75	13.74
C,2,3-300-8	14.50	4.87	.336	8	7	14.57	19.23
C,2,3-310-8	14.50	4.95	.341	9	6	16.39	16.48
C,2,3-320-8	14.51	4.80	.330	7	4	12.75	10.99
C,2,3-330-8	14.52	4.98	.343	7	5	12.75	13.74
C,2,3-340-8	14.50	4.90	.338	4	4	7.29	10.99
C,2,3-350-8	14.47	4.81	.332	3	7	5.46	19.23
C,2,3-360-8	14.50	4.89	.337	4	--*	7.29	--
C,2,3-370-8	14.48	4.90	.338	5	8	9.11	21.98
C,2,3-380-8	14.48	4.84	.335	5	5	9.11	13.74
C,2,3-390-8	14.52	4.74	.326	4	7	7.29	19.23
C,2,3-400-8	14.51	4.90	.338	4	5	7.29	13.74
C,2,3-410-8	14.51	4.73	.326	8	3	14.57	8.24
C,2,3-420-8	14.51	4.90	.337	7	--*	12.75	--
C,2,3-430-8	14.52	4.88	.336	6	8	10.93	21.98
C,2,3-440-8	14.50	4.90	.338	6	5	10.93	13.74
Average			.335			10.71	15.38
Std. dev.			.00476			3.15	4.13

*Erratic data, ignored.